学位論文

Synthesis and Physical Properties of Multifunctional Disilane-bridged Arenes

(多様な機能を示すジシラン架橋芳香族化合物の創製と物性)

平成29年12月博士（理学）申請

東京大学大学院理学系研究科

化学専攻

島田 真樹

Abstract

In my Ph.D. thesis, the preparation of various disilane-bridged arenes *via* Pd-catalyzed arylation of hydrosilane with aryl iodide has been investigated for the development of novel materials with multifunctional properties.

In Chapter 1, as the introduction, the importance and the applications of functional molecules, especially luminescent molecules, were described. Then, recent studies and problems of donor–acceptor molecules, well-known materials showing photo- and electro-luminescent properties, were described. Then aryloligosilanes and their physical properties owing to σ–π conjugation were mentioned, and the synthetic method of aryloligosilanes *via* Pd-catalyzed arylation under mild condition was described. And my previous work, donor–Si–Si–acceptor molecules which have strong fluorescent properties and nonlinear optical properties were described. Finally, the purpose of this research was mentioned.

In Chapter 2, disilane-bridged donor–acceptor–donor (D–A–D) and acceptor–donor–acceptor (A–D–A) triads were synthesized *via* Pd-catalyzed arylation of hydrosilanes in moderate yield. These compounds showed broad UV absorption assigned to intramolecular charge transfer (ICT) and/or π–π* transition, and weak emission in the solution state whereas strong emission in the solid state described to the aggregation effect. To consider the relationship between the molecular structures and fluorescent behaviors, XRD and DFT calculation were carried out.

In Chapter 3, multifunctional disilane-bridged cyclophanes, tetrasila[2.2]cyclophanes, were investigated. *Via* Pd-catalyzed cyclization reaction, desired products containing donor–acceptor and planar chiral ones were synthesized in 20% yield. Using the structural studies such as XRD, NMR, and DFT calculation, crystal structure, molecular inversion, and inclusion into

macrocycles were investigated. Donor–acceptor tetrasila[2.2]cyclophanes showed green-colored emission assignable to intramolecular charge transfer, and some compounds showed solid state emission. OLED containing tetrasila[2.2]cyclophanes which displayed green electroluminescence was fabricated. Circular polarized luminescence was achieved using a planar chiral tetrasila[2.2]cyclophane.

Finally in Chapter 4, the conclusions throughout this work and perspectives were described.

Abbreviations

A	acceptor
a.u.	arbitrary unit
AcOH	acetic acid
ACQ	aggregation-caused quenching
AIE	aggregation-induced emission
BCP	bathocupuroin
bpy	2,2'-bipyridine
CD	circular dichroism
CI	configuration interaction
COSY	correlation spectroscopy
Cp	cyclopentadienyl
CP/MAS	cross polarization/magic angle spinning
CPL	circularly polarized luminescence
CV	cyclic voltammetry
D	donor
DFT	density functional theory
DMF	*N*,*N*-dimethylformamide
dppe	bis(diphenylphosphino)ethane
DPV	differential pulse voltammetry
dPVBi	4,4'-bis(2,2'-diphenylvinyl)-1,1'-biphenyl
EDOT	3,4-ethylenedioxythiophene
EI	electron ionization
EL	electroluminescence
ESI	electrospray ionization
Et_2O	diethyl ether
FAB	fast atom bombardment
Fc	ferrocene
GC	gas chromatography
GoF	goodness of fit
GPC	gel permeation chromatography

HOMO	highest occupied molecular orbital
HPLC	high performance liquid chromatography
HRMS	high resolution mass spectrometry
ICT	intramolecular charge transfer
ITO	Indium Tin Oxide
J	coupling constant
LUMO	lowest unoccupied molecular orbital
M	molar
Mp	melting point
MS	mass spectrometry
NIR	near-infrared
NMR	nuclear magnetic resonance
NOESY	nuclear Overhauser enhancement spectroscopy
OLED	organic light-emitting diode
ORTEP	Oak Ridge thermal-ellipsoid plot
PeT	photoinduced electron transfer
ROESY	rotating frame Overhauser effect spectroscopy
SHG	second harmonic generation
SR	synchrotron radiation
TD	time dependent
THF	tetrahydrofuran
TMEDA	*N*,*N*,*N*',*N*'-tetramethylethylenediamine
TMS	tetramethylsilane
TOCSY	total correlation spectroscopy
TOF	time of flight
TPA	two-photon absorption
UV–vis	ultraviolet-visible
VT	variable temperature
XRD	X-ray diffraction
α-NPD	*N*,*N*'-Diphenyl-*N*,*N*'-bis(1-naphthalenyl)-1,1'-biphenyl-4,4'-diamine

Table of Contents

Chapter 1

Introduction

1.1 Functional materials and their applications

Many types of functional materials, or stimuli-responsive materials, have been received much attentions in the field of chemistry, physics, and biology. By the external stimulation – light, electric field, magnetic field, heat, and chemicals (e.g. other molecules, ions, and solvents) – the peculiar physical properties of stimuli-responsive materials appear or disappear. Not only the researches in the field of basic science, but the various applications utilizing functional molecules have been developed thus far such as light-emitting diodes,[1] dye-sensitized solar cells (DSSCs),[2] field-effect transistors (FETs),[3] the light-harvesting systems,[4] photo-induced reaction,[5] receptors and recognition sensors for ions and small molecules,[6] and electrochromic devices.[7] To improve the functionalities and to expand a range of their applications, further investigation and development of functional molecules are in demand.

The main point of functionalities in this study is "photofunctionalities" – absorbing and emitting the light, controlling the character of molecules by light (e.g. photo-switching[8]), or changing the character of light with materials (e.g. optical rotation by chiral media[9]) –. As one of photofunctionalities, luminescent properties have been focused on, and an amount of fluorescent molecules have been developed for the application such as organic light-emitting diodes (OLEDs)[1,10] as well as the basis science. As shown in the following list and Figure 1.1.1, there are various types of luminophores;[11]

Organic molecules:

n–π* transition (Figure 1.1.1(a))

π–π* transition (Figure 1.1.1(b))

intramolecular charge transfer (ICT) (Figure 1.1.1(c))

excited-state intramolecular proton transfer (ESIPT) (Figure 1.1.1(d))

exciplex (Figure 1.1.1(e))

Transition metal complexes:

metal to ligand charge transfer (MLCT) (Figures 1.1.1(f) and (g))

ligand to metal charge transfer (LMCT) (Figure 1.1.1(h))

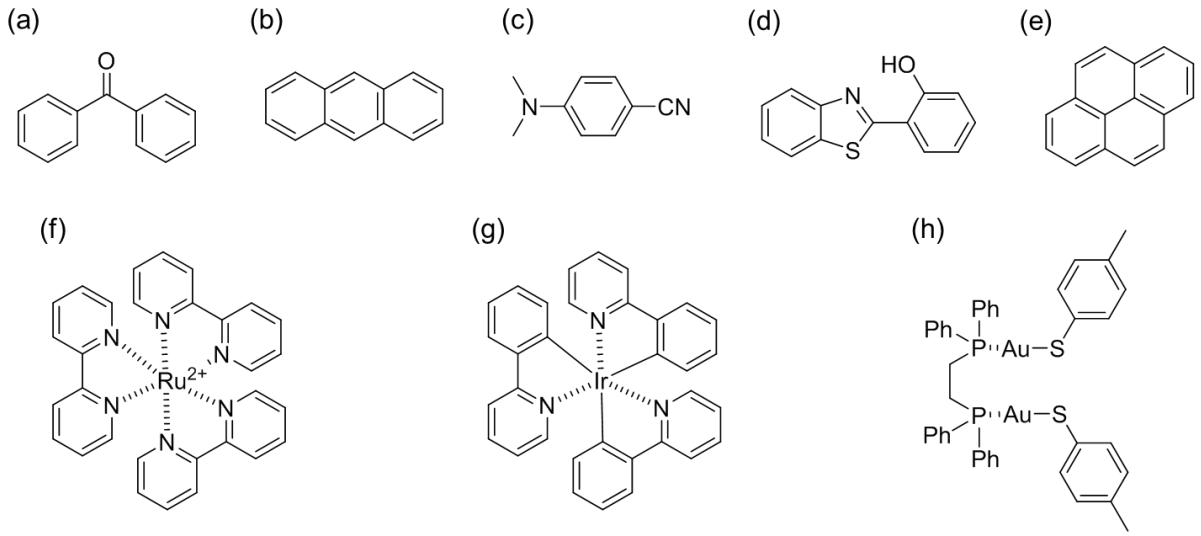

Figure 1.1.1. Representative luminescent molecules. (a) Benzophenone (n–π* phosphorescence). (b) Anthracene (π–π* fluorescence). (c) 4-(Dimethylamino)benzonitrile (ICT fluorescence). (d) 2-(Benzo[*d*]thiazol-2-yl)phenol (ESIPT fluorescence). (e) Pyrene (exciplex emission). (f) $[Ru(bpy)_3]^{2+}$ (MLCT fluorescence). (g) $Ir(ppy)_3$ (MLCT phosphorescence). (h) Au_2(*p*-thiocresol)$_2$(dppe) (LMCT phosphorescence).

In this thesis, I focused on fluorescent donor–acceptor organic molecules, which have the properties of intramolecular charge transfer. In the next section, the features of donor–acceptor molecules and their problems are described.

1.2 Donor−acceptor luminophores

Donor–acceptor (D–A) molecules have been focused in the field of physical or biological chemistry because of their applications in photonics and electronics materials.[12] The important feature of D–A molecules is intramolecular charge transfer (ICT), which can lead to remarkable absorption, emission, and nonlinear optical properties (e.g. second harmonic generation (SHG) and two-photon absorption (TPA)).[13] Excitation of D–A molecules causes charge separation state *via* ICT as shown in Figure 1.2.1, which leads emissive properties.

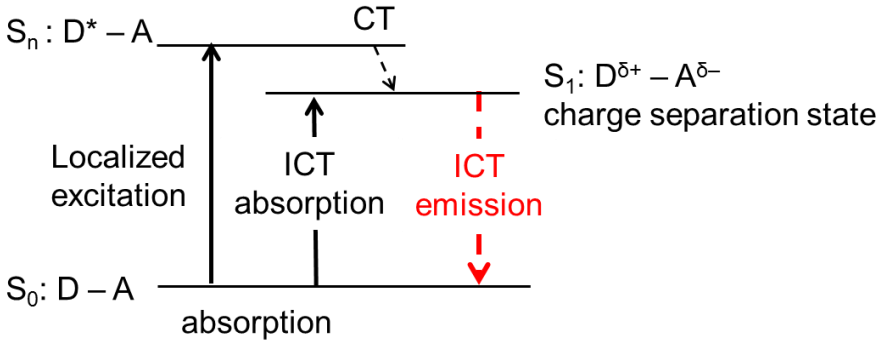

Figure 1.2.1. Jabłoński diagrams of ICT emission of donor–acceptor molecules.

D–A compounds feature the large Stocks shifts between the absorption bands and emission bands, which suppress self-absorption to improve emission intensity. Moreover, their optical properties and physical properties could be tuned with the easy modification of molecular structures, especially the combination of donor moieties, acceptor moieties, and linkers. These luminescent materials are expected for the application such as OLEDs[14] and fluorescent probes.[15] For example, Adachi and coworkers reported that OLED using D–A molecule, which showed efficient external quantum efficiency (η_{ext} = 20.5%) as shown in Figure 1.2.2.[14c] Seung and coworkers reported bioimaing probes of HeLa cell using D–A luminophores in Figure 1.2.3.[15b]

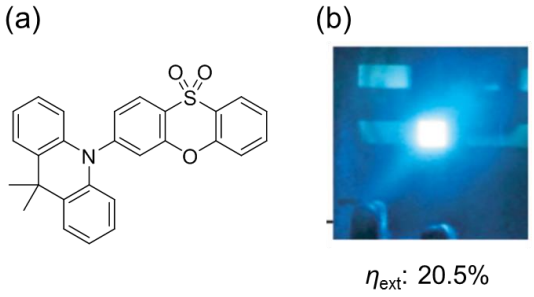

Figure 1.2.2. OLED using D–A molecules. (a) Molecular structure of emitting material. (b) Photo of its electroluminescence. From reference 14(c). Copyright © 2016 by John Wiley Sons, Inc. Adapted by permission of John Wiley & Sons, Inc.

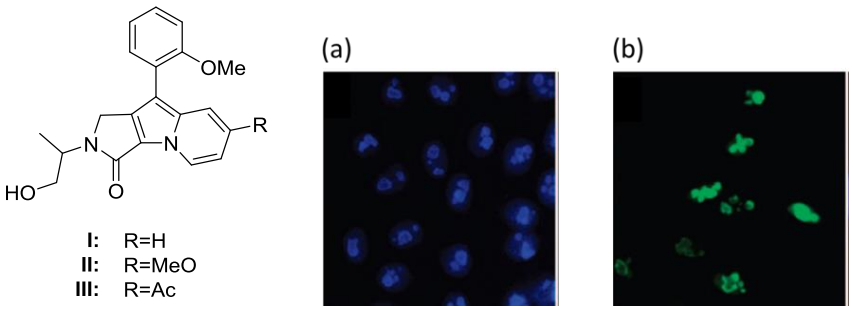

Figure 1.2.3. Fluorescence image of HeLa cell using **I** or **III**-labeled antibodies. (a) **I**–labeled HeLa cell image. (b) **III**–labeled HeLa cell image. Adapted with permission from reference 15(b). Copyright © 2008 American Chemistry Society.

Thus, an amount of molecules containing electron-push and -pull moieties have been developed and many applications in photophysical chemistry and in biochemistry have been reported. Hence introducing the donor–acceptor systems into organic molecules provides photofunctionalities.

1.3 Emissive oligosilane–arene compounds through σ–π conjugation

Oligosilane-bridged aryl compounds, which have silicon–silicon–aryl bonds, deserve attention in many fields such as luminescent materials or electron-transporting materials.[16] The most important feature of these compounds is the σ–π conjugation, σ–π interaction between aryl's π orbitals and silicon's σ orbitals.[17] It causes the extension of conjugation system as shown in Figure 1.3.1; There are the interactions of σ orbitals on Si–Si bond and π orbital on aryl (red) or those of σ* and π* (blue).

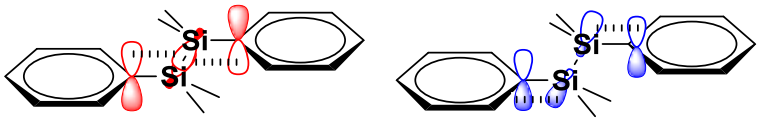

Figure 1.3.1. The schematic image of σ–π conjugation.[17a]

The σ–π conjugation affects the optical properties; maximum wavelengths of UV–vis absorption and florescence are red-shifted because of the reduction of LUMO levels, and molecular extinction coefficient increases similar to usual extended π-conjugated system.[17b] Thus, many oligosilane–arene compounds and polymers with photophysical or electron transporting properties driven from σ–π conjugation have been developed as shown in Figure 1.3.2.[18] Isobe and co-workers reported disilane-bridged anthracene derivatives (Figure 1.3.2(a)) which showed an electron-transporting properties.[18a] The preparation method and chioptical properties of chiral oligosilane-aryl compounds (Figure 1.3.2(b)) were researched by Kawakami group.[18b] And Ohshita reported several oligosilane-thiophene polymers (Figure 1.3.2(c)) which displayed electroluminescent properties with up to 2,000 cd/m^2 luminescent intensity.[18c]

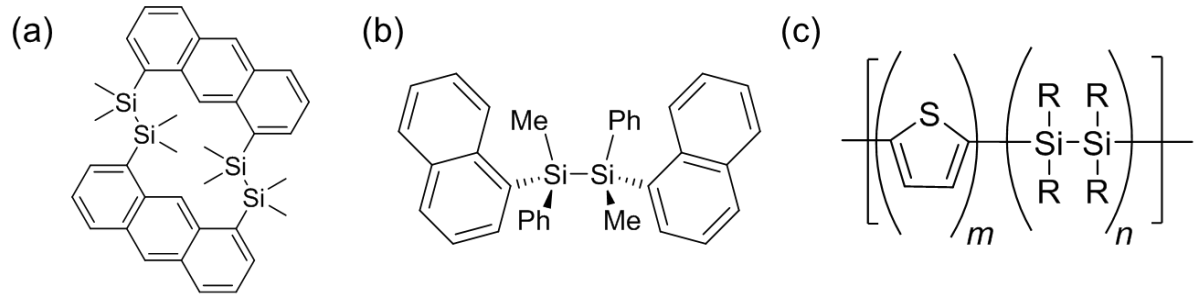

Figure 1.3.2. Examples of oligosilane-bridged arenes and polymers previously reported. (a) Disilane-bridged anthracene for electron transporting layer in OLEDs. (b) Disilane-bridged aryl compounds containing chirality. (c) Polymer including oligosilanes and thiophene moieties for EL devices.

Table 1.3.1 shows the comparison of Si–Si σ systems and C=C π systems. Both Si–Si–aryl σ–π systems and C=C π systems have energy, charge and electron transporting properties, however the chemical structures are different. C=C π system is planar and fixed structure from sp^2 orbitals of carbon atoms, while Si–Si system is "nonplanar and flexible structure" arising from sp^3 orbitals of silicon atoms and single Si–Si bond. So this structural feature of σ–π conjugation system provides unique properties different from π conjugation system, especially in the rigid phase (i.e. crystals).

Table 1.3.1. The structural comparison of Si–Si σ linker and C=C π linker.

	Si–Si σ bond	C=C π bond
	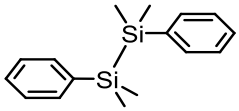	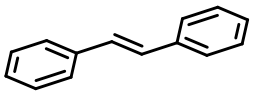
Bond style	single	double
Orbital	sp^3	sp^2
Chemical structure	nonplanar	planar

As referred above, oligosilane-bridged arenes and polymers have been developed for the application to optical or electrochemical materials with the properties not similar to mere π-conjugated ones.

1.4 Transition metal-catalyzed reaction for Si−C bond construction

In order to construct Si−C bonds for the preparation of oligosilane-arene molecules, the coupling reactions of Grignard or organolithium reagents with chlorosilanes have well been used (Scheme 1.4.1). This coupling reaction proceeds in good yield with easy operation. However, there are some problems of this reaction; one is the requirement for protecting groups to introduce the reactive functional groups, for example, ester, ketone, and nitrile groups. Another is the requirement for over chemical equivalent of Mg or organolithium reagents. To dissolve these problems and to synthesize various organosilane compounds, mild and catalytic reactions for the construction of Si−C are desired.

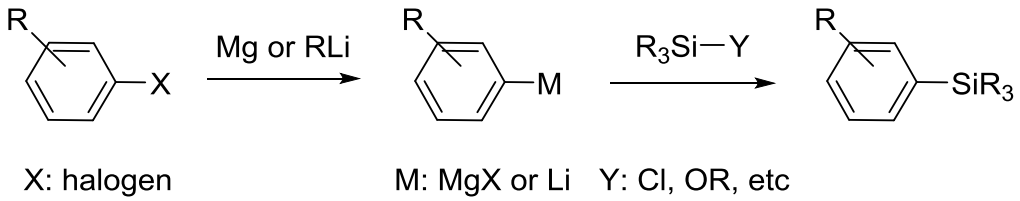

Scheme 1.4.1. Preparation of organosilanes by Grignard or organolithium reagents.

Recently our laboratory has developed the synthesis method of organosilane compounds using hydrosilanes as silicon sources under the presence of metal catalyst.[19] Previously hydrosilanes were investigated as reductant for hydride reduction or hydrosilylation under the transition-metal condition (Scheme 1.4.2(a)).[20] On the other hand, we have reported the arylation of hydrosilane with aryl iodide using palladium(0) or rhodium(I) complexes with bulky trialkylphosphine ligands (e.g. P(*t*-Bu)$_3$) as catalyst as shown in Scheme 1.4.2(b). This catalytic reaction has the following advantages; one-pot reaction, high yield, and broad scope of substrate. Moreover, this reaction did not cleave Si−Si bonds (Scheme 1.4.3),[21] which can be easily decomposed under the presence of transition metals (e.g. Pd(II)).[22] Thus, various oligosilane-arene compounds with functional groups could be prepared by Pd-catalyzed reaction of hydrosilanes.

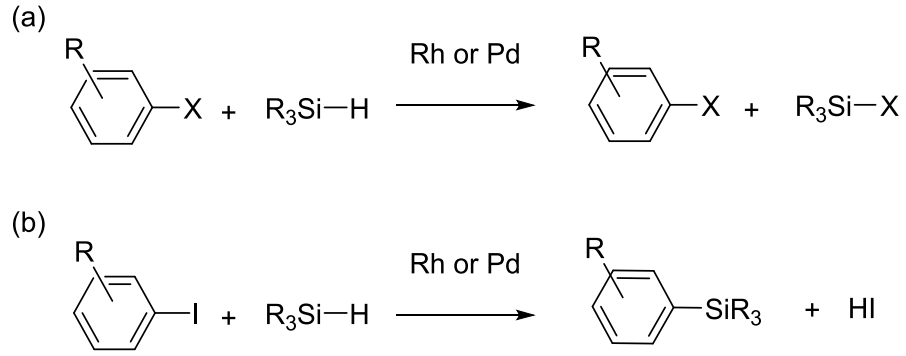

Scheme 1.4.2. (a) Hydride reduction of aryl halides by hydrosilanes. (b) Preparation of organosilanes *via* Pd-catalyzed arylation of hydrosilanes with aryl iodides.

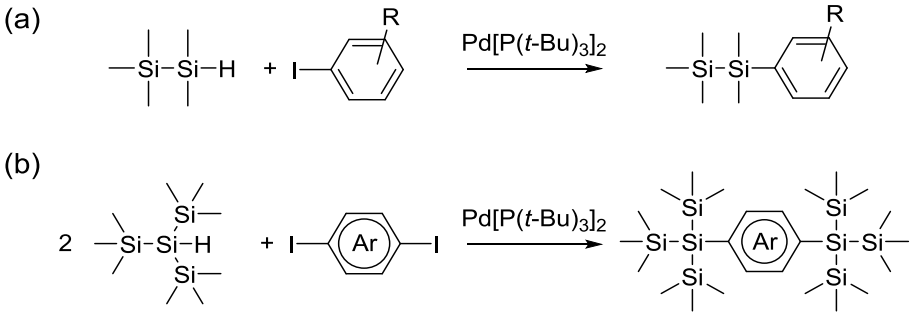

Scheme 1.4.3. Preparation of oligosilane-arene molecules *via* Pd-catalyzed arylation of hydrosilanes with aryl iodides. (a) The coupling reaction of hydrodisilane and iodoaryls.[21a] (b) The coupling reaction of tris(trimethylsilyl)silane and diiodoarene.[21b]

1.5 Previous research: disilane-bridged donor−acceptor molecules

Above the interest in donor−acceptor system and oligosilane linker, previously disilane-bridged donor−acceptor molecules, the hybridization of donor−acceptor and disilane unit (the simplest oligosilane), were investigated in my master course.[23] These molecules were expected for fluorescent materials and second harmonic generation (SHG)-active materials derived from ICT properties. Mignani,[24] Hadziioannou and van Hutten,[25] and Hiratsuka[26] have independently reported the synthesis and physical properties of donor−acceptor disilanes. However, no systematic study of the relationship between the chemical structures and physical properties of these compounds has been published, and any SHG-active disilanes in mere powder condition are not reported because Grignard reaction or lithiation as a key process of Si−C coupling cannot be allowed to prepare various 1,2-diaryldisilanes including donor−acceptor disilanes as described in Section 1.4.

Then, I designed the systematic preparation method for donor−acceptor disilanes *via* Pd-catalyzed coupling reaction of hydrosilane with aryl iodide as shown in Figure 1.5.1(a). Using this reaction, various disilane-bridged donor−acceptor molecules were synthesized in moderate yield, including compounds with reactive functional moieties. They displayed strong emission in the solid state by means of not only ICT (donor−acceptor system) but also non-planar structure (Figure 1.5.1(b)), which suppressed concentration quenching in crystalline phase. Besides, one disilane with *ortho*-substituted aryl group showed an SHG (2.9 times of urea), arising from the flexibility which allow to form the non-centrosymmetric structure (Figure 1.5.1(c)).

Hence inserting disilane units into organic molecules will provide novel functional materials utilizing the features of Si−Si bonds.

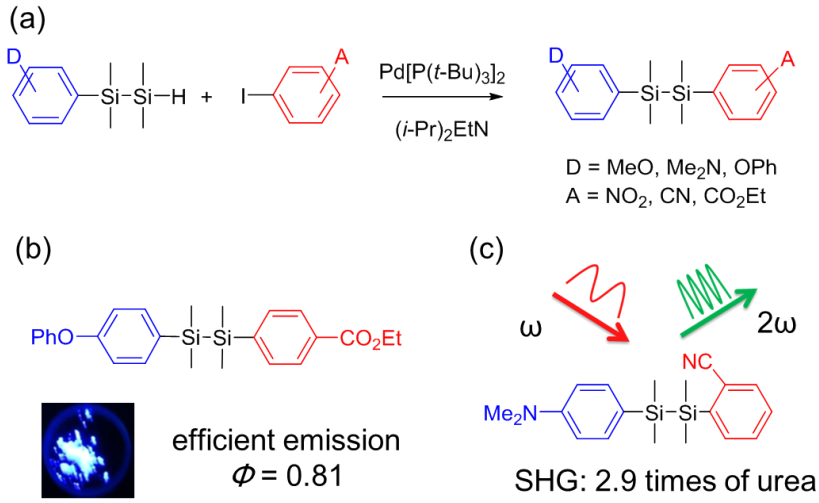

Figure 1.5.1. (a) Preparation scheme of disilane-bridged donor−acceptor compounds. (b) Molecular structure of disilane-bridged donor−acceptor molecule which shows solid-state emission. (c) Molecular structure of SHG-active disilane-bridged donor−acceptor molecule. Adapted with permission from reference 23. Copyright © 2015 American Chemistry Society.

1.6 The aim of this research

So far, inserting donor−acceptor and/or disilane linker to organic molecules will provides the novel type of functional molecules. In my Ph.D. thesis, two type of skeletons containing D−A system and/or disilane linker were investigated for the development of multifunctional molecules. One is dislane-bridged donor–acceptor–donor and acceptor–donor–acceptor triads (Figure 1.6.1(a)), and the other is disilane-bridged [2.2]cyclophanes (Figure 1.6.1(b)). By the feature of "intramolecular charge transfer" from D−A system and "σ–π conjugation, bulkiness, and flexibility" from disilane linker, these compounds display the functional properties such as aggregated-induced emission, molecular inversion, electroluminescence, and so on. This technique, providing novel functionalities by introduction of oligosilane *via* Pd-catalyzed arylation, will contribute to the development of novel functional materials in the basic chemistry and applied chemistry.

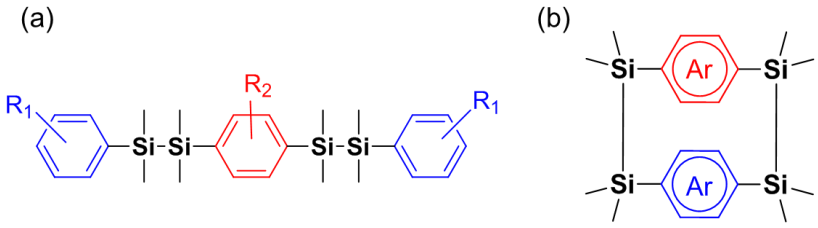

Figure 1.6.1. Prepared molecular structures in my Ph.D. thesis. (a) Disilane-bridged donor–acceptor–donor and acceptor–donor–acceptor triads. (b) Disilane-bridged [2.2]cyclophanes.

1.7 References

1. (a) Lo, S.-C.; Burn, P. L. *Chem. Rev.* **2007**, *107*, 1097–1116.
   (b) Grimsdale, A. C.; Chan, K. L.; Martin, R. E.; Jokisz, P. G.; Holmes, A. B. *Chem. Rev.* **2009**, *109*, 897–1091.
2. (a) Liang, M.; Chen, J. *Chem. Soc. Rev.* **2013**, *42*, 3453–3488.
   (b) Hagfeldt, A.; Boschloo, G.; Sun, L.; Kloo, L.; Pettersson, H. *Chem. Rev.* **2010**, *110*, 6595–6663.
3. Torsi, L.; Magliulo, M.; Manoli, K.; Palazzo, G. *Chem. Soc. Rev.* **2013**, *42*, 8612–8628.
4. (a) Frischmann, P. D.; Mahata, K.; Würthner, F. *Chem. Soc. Rev.* **2013**, *42*, 1847–1870.
   (b) Li, X.-P.; Björkman, O.; Shih, C.; Grossman, A. R.; Rosenquist, M.; Jansson, S.; Niyogi, K. K. *Nature* **2000**, *403*, 391–395.
5. (a) Hoffmann, M. R.; Martin, S. T.; Choi, W.; Bahnemann, D. W. *Chem. Rev*. **1995**, *95*, 69–96.
   (b) Hou, W.; Cronin, S. B. *Adv. Funct. Mater*. **2013**, *23*, 1612–1619.
6. (a) Bühlmann, P.; Pretsch, E.; Bakker, E. *Chem. Rev.* **1998**, *98*, 1593–1688.
   (b) Gale, P. A. *Coord. Chem. Rev.* **2003**, *240*, 191–221.
   (c) Babine, R. E.; Bender, S. L. *Chem. Rev.* **1997**, *97*, 1359–1472.
7. (a) Thakur, V. K.; Ding, G.; Ma, J. *Adv. Mater.* **2012**, *24*, 4071–4096.
   (b) Mortimer, R. J. *Chem. Soc. Rev.*, **1997**, *26*, 147–156.
   (c) Agrawal, A.; Cronin, J. P.; Zhang, R. *Sol. Energy Mater. Sol. Cells* **1993**, *31*, 9–21.
8. (a) Russew, M.-M.; Hecht, S. *Adv. Mater.* **2010**, *22*, 3348–3360.
   (b) van de Linde, S.; Sauer, M. *Chem. Soc. Rev.* **2014**, *43*, 1076–1087.
   (c) Yager, K. G.; Barrett, C. J. *J. Photochem. Photobiol. A: Chem*. **2006**, *182*, 250–261.
9. (a) Schellman, J. A. *Chem. Rev.* **1975**, *75*, 323–331.
   (b) Polavarapu, P. L. *Chirality* **2002**, *14*, 768–781.
10. Mitschke, U.; Bäuerle, P. *J. Mater. Chem.* **2000**, *10*, 1471–1507.
11. (a) *Molecular Fluorescence: Principles and Applications*, 2nd ed., Valeur, B.; Berberan-Santos, M. N. Wiley-VCH Verlag GmbH & Co. KGaA: Weinheim, **2012**.
    (b) Xu, H.; Chen, R.; Sun, Q.; Lai, W.; Su, Q.; Huang. W.; Liu, X. *Chem. Soc. Rev.* **2014**, *43*, 3259–3302.
12. Gompper, R.; Wagner, H.-U. *Angew. Chem., Int. Ed. Engl.* **1988**, *27*, 1437–1455.
13. (a) Long, N. J. *Angew. Chem., Int. Ed. Engl.* **1995**, *34*, 21–38.

(b) Kanis, D. R.; Ratner, M. A.; Marks, T. J. *Chem. Rev.* **1994**, *94*, 195–242.

(c) Pawlicki, M.; Collins, H. A.; Denning, R. G.; Ander, H. L. *Angew. Chem. Int. Ed*. **2009**, *48*, 3244–3266.

(d) Kim, H. M.; Cho, B. R. *Chem. Rev*. **2015**, *115*, 5014−5055.

14. (a) Uoyama, H.; Goushi, K.; Shizu, K.; Nomura, H.; Adachi, C. *Nature* **2012**, *492*, 234–238.

(b) Zhang, Q.; Li, B.; Huang, S.; Nomura, H.; Tanaka, H.; Adachi, C. *Nat. Photonics* **2014**, *8*, 326–332.

(c) Lee, S. Y.; Adachi, C.; Yasuda, T.; *Adv. Mater.* **2016**, *28*, 4626–4631.

(d) Grimsdale, A. C.; Chan, K. L.; Martin, R. E.; Jokisz, P. G.; Holmes, A. B. *Chem. Rev.* **2009**, *109*, 897–1091.

(e) Li, D.; Zhang, H.; Wang, Y. *Chem. Soc. Rev*. **2013**, *42*, 8416–8433.

15. (a) Gabe, Y.; Urano, Y.; Kikuchi, K.; Kojima, H.; Nagano, T. *J. Am. Chem. Soc.* **2004**, *126*, 3357–3367.

(b) Kim, E.; Koh, M.; Ryu, J.; Seung, B. P. *J. Am. Chem. Soc.* **2008**, *130*, 12206–12207.

16. Karatsu, T. *J. Photochem. Photobiol, C: Photochem. Rev.* **2008**, *9*, 111–137.

17. (a) Shimizu, M.; Oda, K.; Bando, T.; Hiyama, T. *Chem. Lett.* **2006**, *35*, 1022–1023.

(b) Kyushin, S.; Ikarugi, M.; Goto, M.; Hiratuska, H.; Matsumoto, H. *Organometallics* **1996**, *15*, 1067–1070.

(c) Tsuji, H.; Shibano, Y.; Takahashi, T.; Kumada, M.; Tamao, K. *Bull. Chem. Soc. Jpn*. **2005**, *78*, 1334–1344.

(d) Kira, M.; Miyazawa, T.; Mikami, N.; Sakurai, H. *Organometallics* **1991**, *10*, 3793–3795.

(e) Sakurai, H.; Yamamori, H.; Kumada, M. *Bull. Chem. Soc. Jpn.* **1965**, *38*, 1894–1895.

18. (a) Nakanishi, W.; Hitosugi, S.; Piskareva, A.; Shimada, Y.; Taka, H.; Kita, H.; Isobe. H. *Angew. Chem. Int. Ed*. **2010**, *49*, 7239–7242.

(b) Oh, H.-S.; Imae, I; Kawakami, Y.; S. Shanmuga, S.; Raj, S.; Yamane, T. *J. Organomet. Chem.* **2003**, *685*, 35–43.

(c) Ohshita, J.; Takata, A.; Kai, H.; Kunai, A.; Komaguchi, K.; Shiotani, M.; Adachi, A.; Sakamaki, K.; Okita, K.; Harima, Y.; Kunugi, Y.; Yamashita, K.; Ishikawa, M. *Organometallics* **2000**, *19*, 4492–4498

(d) Shimizu, M.; Tatsumi, H.; Mochida, K.; Oda, K.; Hiyama, T. *Chem. –Asian J.* **2008**, *3*, 1238–1247.

(e) Yang, D.-D. H.; Yang, N.-C. C.; Steele, I. M.; Lui, H.; Ma, Y.-Z.; Fleming, G. R. *J. Am. Chem. Soc.* **2003**, *125*, 5107–5110.

19. (a) Shimada, M.; Yamanoi, Y.; Nishihara, H. *J. Synth. Org. Chem. Jpn.* **2016**, *74*, 1098–1107.

    (b) Yamanoi, Y.; Nishihara, H. *J. Synth. Org. Chem. Jpn.* **2009**, *67*, 778–786.

20. (a) Boukherroub, R.; Chatgilialoglu, C.; Manuel, G. *Organometallics* **1996**, *15*, 1508–1510.

    (b) Esteruelas, A, M.; Herrero, J.; Lopez, M, F.; Martin, M.; Oro, A, L.; *Organometallics* **1999**, *18*, 1110–1112.

21. (a) Lesbani, A.; Kondo, H.; Sato, J.-i.; Yamanoi, Y.; Nishihara, H. *Chem. Commun*. **2010**, *46*, 7784–7786.

    (b) Inubushi, H.; Hattori, Y.; Yamanoi, Y.; Nishihara, H. *J. Org. Chem*. **2014**, *79*, 2974–2979.

22. (a) Uchimura, Y.; Tanaka, M. *J. Organomet. Chem.* **1996**, *521*, 335–341.

    (b) Naka, A.; Hayashi, M.; Okazaki, S.; Ishikawa, M. *Organometallics* **1994**, *13*, 4994–5001.

23. Shimada, M.; Yamanoi, Y.; Matsushita, T.; Kondo, T.; Nishibori, E.; Hatakeyama, A.; Sugimoto, K.; Nishihara, H. *J. Am. Chem. Soc.* **2015**, *137*, 1024–1027.

24. (a) Mignani, G.; Barzoukas, M.; Zyss, J.; Soula, G.; Balegroune, F.; Grandjean, D.; Josse, D. *Organometallics* **1991**, *10*, 3660–3668.

    (b) Mignani, G.; Krämer, A.; Puccetti, G.; Ledoux, I.; Zyss, J.; Soula, G. *Organometallics* **1991**, *10*, 3656–3659.

    (c) Mignani, G.; Soula, G. PCT Int. Appl. 1991, WO 9116329.

    (d) Soula, G.; Mignani, G. Fr. Demande, 1989, FR 2630442.

25. (a) Hissink, D.; van Hutten, P. F.; Hadziioannou, G.; van Bolhuis, F. *J. Organomet. Chem.* **1993**, *454*, 25–34.

    (b) van Hutten, P. F.; Hadziioannou, G.; Bursi, R.; Feil, D. *J. Phys. Chem*. **1996**, *100*, 85–94.

26. Hiratsuka, H.; Horiuchi, H.; Takanoha, Y.; Matsumoto, H.; Yoshihara, T.; Okitsu, T.; Negishi, K.; Kyushin, S.; Matsumoto, H. *Chem. Lett.* **2007**, *36*, 1168–1169.

Chapter 2

Disilane-bridged donor–acceptor–donor (D–A–D) and acceptor–donor–acceptor (A–D–A) triads: aggregation-induced emission and bright solid state emission

2.1 Introduction

Recently, π-conjugated triads with electron–donating (D) and –accepting (A) groups (e.g. D–π–A–π–D and A–π–D–π–A compounds) have been focused as well as D–π–A compounds because of their photofunctionalities.[1] They show strong one-photon absorption in UV–vis–NIR region with broad bands arising from intramolecular charge transfer (ICT), and the excitation of ICT bands leads to effective emission.[2] Moreover, because of quadrupole moment of these compounds and large absorption cross-section, they often display strong two-photon absorption (TPA) as shown in Figure 2.1.1.[3] Thus, π-conjugated D–A–D or A–D–A molecules have been developed for the application such as OLEDs (Figure 2.1.2),[4] photovoltaic cells,[5] and bio-imaging probes.[6] However, extinction of π-conjugated systems faces the problem "aggregation-caused quenching" (ACQ), the emission quenching in the aggregated state (for example in the solid state) due to intermolecular π–π interaction.[7] In addition, these compounds are usually a hydrophxobic, and display the low solubility in solvents or host polymer. Thus π-conjugated fluorescent molecules without quenching in the solid state and/or with high solubility are desired.

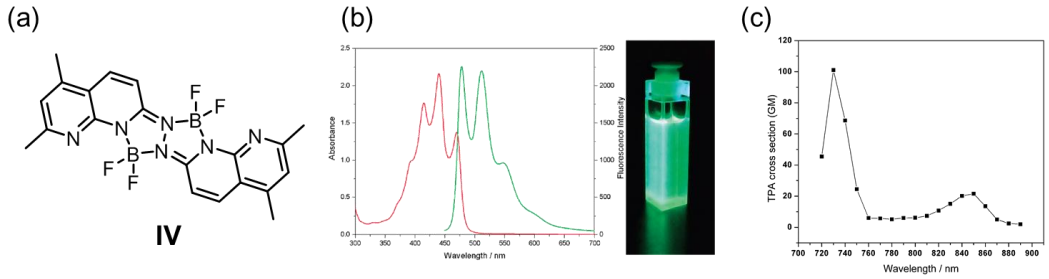

Figure 2.1.1. An example of π-conjugated A–D–A compound **IV**. (a) Molecular structure of **IV**. (b) One-photon absorption and emission spectra of **IV** in CH_2Cl_2, and photo of **IV** in CH_2Cl_2 under UV irradiation. (c) TPA spectrum of **IV** in acetonitrile. Adapted with permission from reference 3(a). Copyright © 2010 American Chemistry Society.

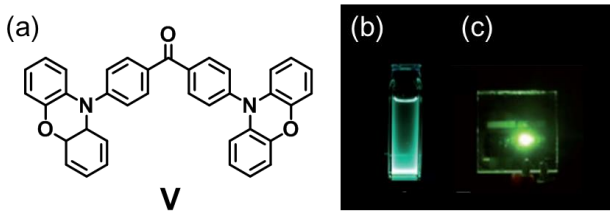

Figure 2.1.2. An example of π-conjugated D–A–D compound **V** displaying photoluminescence and electroluminescence. (a) Molecular structure of **V**. (b) Photo of luminescent **V** in toluene. (c) Photo of electroluminescence of **V**-doped OLED. From reference 4(a). Copyright © 2014 by John Wiley Sons, Inc. Adapted by permission of John Wiley & Sons, Inc.

On the other hand, oligosilane-organic compounds display light-emitting and electron-transporting properties as described in Chapter 1.[8] Moreover, they display high solubility in organic solvents. Efficient solid state emission and high solubility are derived from the suppression of intermolecular π–π interaction due to large radius of silicon atoms and their tetrahedron structures. However, no oligosilane-bridged D–A–D and A–D–A compounds, the hybridization of donor–acceptor triads and oligosilanes, have yet been realized although they are also expected to be the effectively luminophores in the solid state arising from the combination of ICT and σ–π conjugation.

In this research, disilane-bridged D–A–D and A–D–A molecules, which have the structures of D–Si–Si–A–Si–Si–D and A–Si–Si–D–Si–Si–A, and their photophysical properties were investigated.[9] These compounds were synthesized by two steps using Pd-catalyzed arylation of hydrosilane as a key step and they displayed the interesting photophysical properties in the solid state.

2.2 Results and discussion

2.2.1 Synthesis

Disilane-bridged D–A–D molecules were prepared *via* Pd-catalyzed arylation of hydrosilane (Schemes 2.2.3 and 2.2.4). 1-(4-Dimethylaminophenyl)-1,1,2,2-tetramethyldisilane (**3**), 1-(4-methoxyphenyl)-1,1,2,2-tetramethyldisilane (**4**), and 1,1,2,2-tetramethyl-1-(4-phenoxyphenyl)disilane (**5**), starting materials of this reaction, were prepared according to the literature.[8b] And the other starting materials, aryl iodides **1** and **2**, were obtained according to literatures as shown in Schemes 2.2.1 and 2.2.2, respectively.[10,11] Six disilane-bridged D–A–D compounds (**6**–**11**) were obtained in moderate yields (ca. 40%).

Disilane-bridged A–D–A molecules were also prepared *via* Pd-catalyzed arylation of hydrosilane (Scheme 2.2.8). 2,5-Bis(1,1,2,2-tetramethyldisilanyl)thiophene (**12**), 2,5-bis(1,1,2,2-tetramethyldisilanyl)-3,4-ethylenedioxythiophene (**13**) (ethylenedioxythiophene: hereinafter refer to as EDOT), and 5,5'-bis(1,1,2,2-tetramethyldisilanyl)-2,2'-bithiophene (**14**), starting materials of this reaction, were prepared as shown in Schemes 2.2.5, 2.2.6, and 2.2.7, respectively. Six disilane-bridged A–D–A compounds (**15**–**20**) were obtained in ca. 15% yield. Thus, 12 kinds of disilane-bridged triads were prepared. All compounds were characterized by ^{1}H NMR, ^{13}C NMR, and high-resolution mass spectrometry or elemental analysis, which proved the suitable purity for optical measurements.

Scheme 2.2.1. Preparation of 4,7-diiodobenzo[*c*][1,2,5]thiadiazole (**1**).[a]

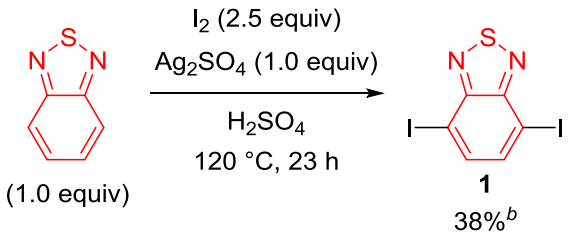

[a] Reaction conditions: benzo[*c*][1,2,5]thiadiazole (20 mmol), I_2 (50 mmol), Ag_2SO_4 (20 mmol), H_2SO_4 (30 mL), 120 °C, 23 h. [b] Isolated yield.

Scheme 2.2.2. Preparation of 5,7-diiode-2,3-dimethylthieno[3,4-*b*]pyrazine (**2**). [a]

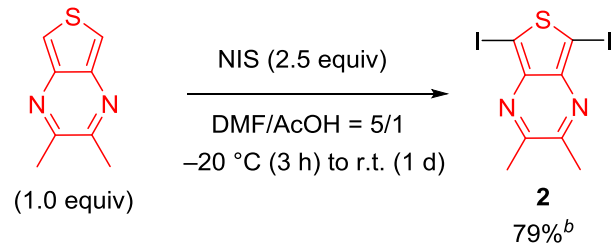

[a] Reaction conditions: 2,3-dimethylthieno[3,4-*b*]pyrazine (8.0 mmol), NIS (20 mmol), DMF (50 mL), AcOH (10 mL), –20 °C, 3 h. [b] Isolated yield.

Scheme 2.2.3. Preparation of disilane-bridged D–A–D molecules (**6**–**8**) including benzo[*c*][1,2,5]thiadiazole moiety as acceptor.[a]

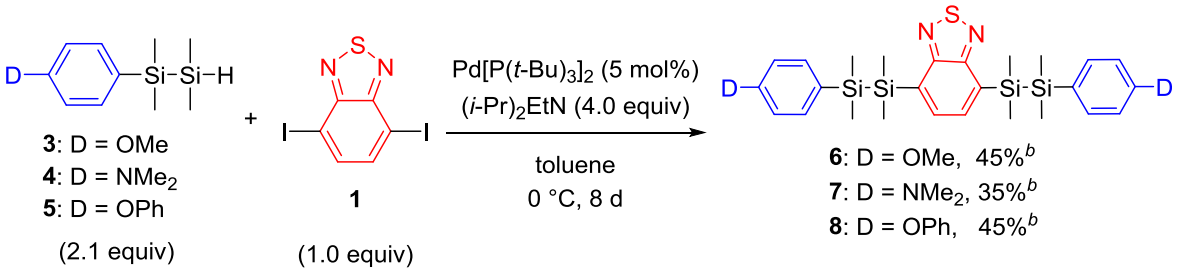

[a] Reaction conditions: 1-aryl-1,1,2,2-tetramethyldisilane (2.5 mmol), **1** (1.2 mmol), Pd[P(*t*-Bu)$_3$]$_2$ (0.06 mmol), *N*,*N*-diisopropylethylamine (4.8 mmol), toluene (10 mL), 0 °C, 8 d. [b] Isolated yield.

Scheme 2.2.4. Preparation of disilane-bridged D–A–D molecules (**9**–**11**) including 2,3-dimethylthieno[3,4-*b*]pyrazine moiety as acceptor. [a]

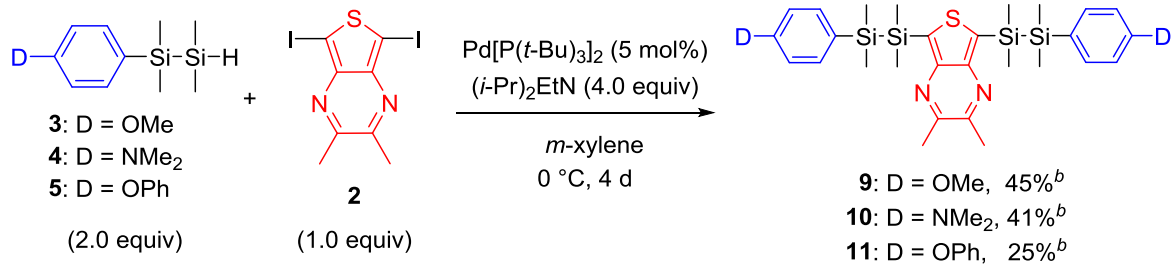

[a] Reaction conditions: 1-aryl-1,1,2,2-tetramethyldisilane (2.0 mmol), **2** (1.0 mmol), Pd[P(*t*-Bu)$_3$]$_2$ (0.05 mmol), *N*,*N*-diisopropylethylamine (4.1 mmol), *m*-xylene (7.5 mL), 0 °C, 4 d. [b] Isolated yield.

Scheme 2.2.5. Preparation of 2,5-bis(1,1,2,2-tetramethyldisilanyl)thiophene (**12**). [a]

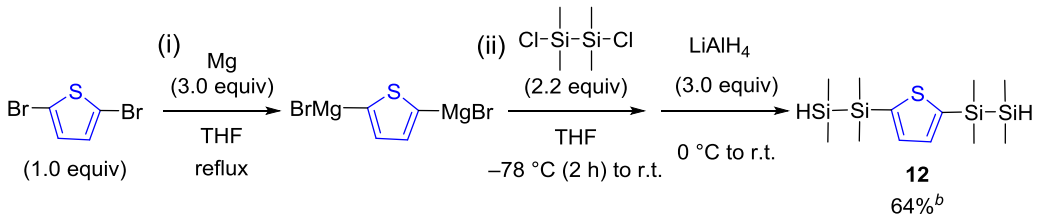

[a] Reaction conditions: (i) 2,5-dibromothiophene (30 mmol), Mg turnings (90 mmol), THF (70 mL). (ii) 1,2-Dichloro-1,1,2,2-tetramethyldisilane (66 mmol), THF (60 mL), $LiAlH_4$ (90 mmol). [b] Isolated yield.

Scheme 2.2.6. Preparation of 2,5-bis(1,1,2,2-tetramethyldisilanyl)-3,4-ethylenedioxythiophene (**13**). [a]

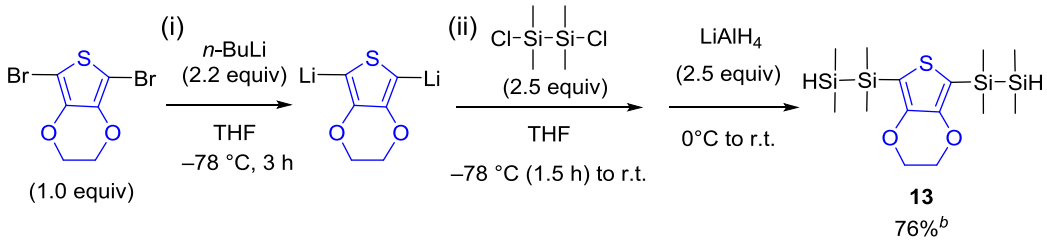

[a] Reaction conditions: (i) 2,5-dibromo-3,4-ethylenedioxythiophene (20 mmol), 1.6 M *n*-BuLi in hexane (28 mL, 44 mmol), THF (100 mL). (ii) 1,2-Dichloro-1,1,2,2-tetramethyldisilane (51 mmol), THF (200 mL), $LiAlH_4$ (50 mmol). [b] Isolated yield.

Scheme 2.2.7. Preparation of 5,5'-bis(1,1,2,2-tetramethyldisilanyl)-2,2'-bithiophene (**14**). [a]

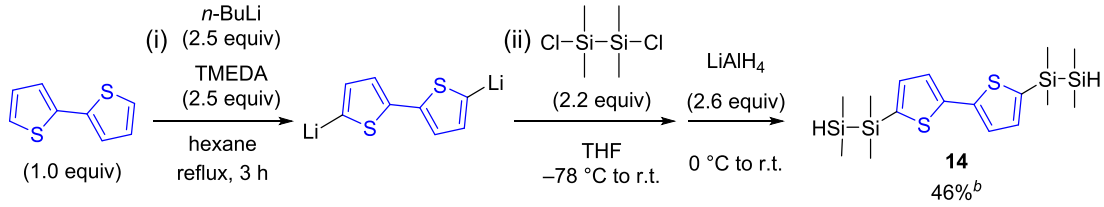

[a] Reaction conditions: (i) 2,2'-bithiophene (20 mmol), 1.6 M *n*-BuLi in hexane (24 mL, 38 mmol), TMEDA (37.5 mmol), hexane (100 mL). (ii) 1,2-Dichloro-1,1,2,2-tetramethyldisilane (33 mmol), THF (100 mL), $LiAlH_4$ (39 mmol). [b] Isolated yield.

Scheme 2.2.8. Preparation of disilane-bridged A–D–A molecules (**15**–**20**). [a]

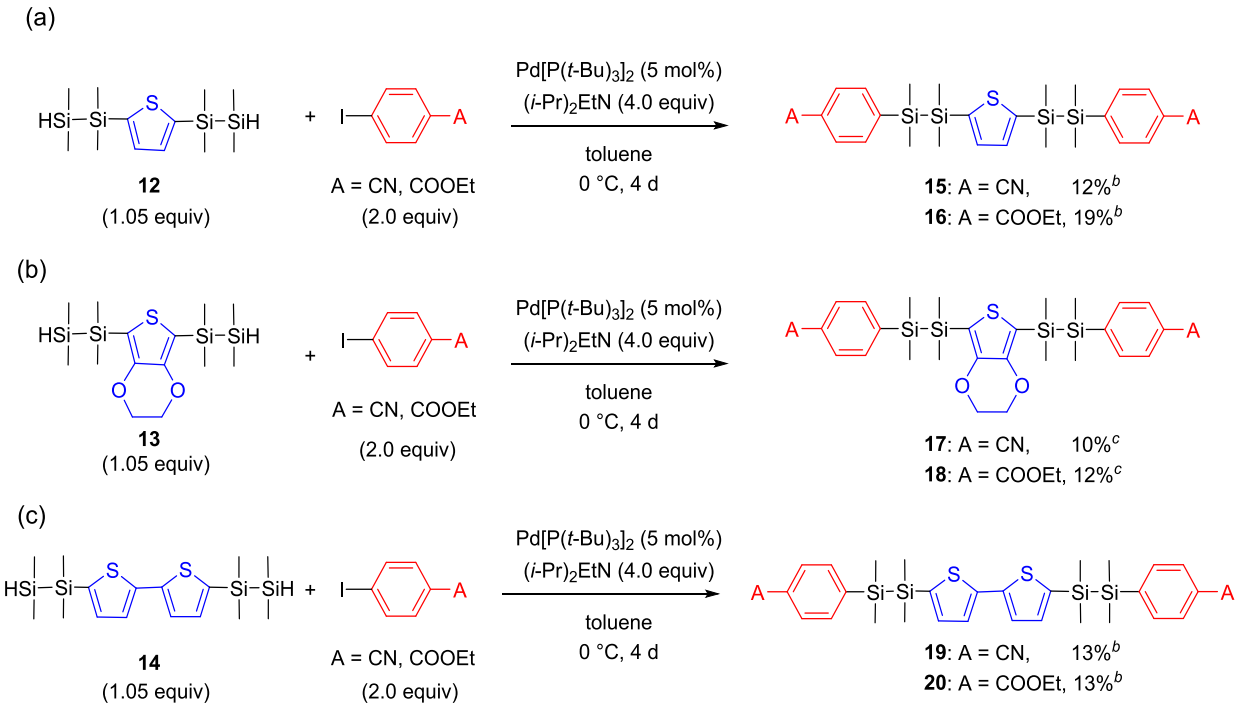

Synthesis schemes of A–D–A molecules including (a) thiophene (**15**, **16**), (b) EDOT (**17**, **18**), and (c) bithiophene (**19**, **20**) as donor moieties. [a] Reaction conditions: bis(tetramethyldisilanyl)arenes (1.05 mmol), aryl iodide (2.0 mmol), Pd[P(*t*-Bu)$_3$]$_2$ (0.050 mmol), *N*,*N*-diisopropylethylamine (4.1 mmol), toluene (7.5 mL), 0 °C, 4 d. [b] NMR yield. [c] Isolated yield.

2.2.2 UV–vis absorption and emission properties

The absorption and photoluminescence of **6**–**11** and **15**–**20** in dichloromethane and in the solid state are given in Tables 2.2.1–2.2.2 and Figures 2.3.1–2.3.12. The absorption bands of the D–A–D molecules were located at around 370 nm arising from the ICT transitions between the peripheral donor groups and the acceptor core. The absorption bands of the A–D–A molecules containing thiophene (**15**, **16**) or EDOT (**17**, **18**) were in the UV region at 270–280 nm, while those of the molecules containing the 2,2'-bithiophene moiety (**19**, **20**) were located on around 330 nm as a sharp peak. The absorption wavelength of A–D–A molecules reflects the σ–π conjugated system of the donor moiety as discussed in DFT calculation (section 2.2.5).

Table 2.2.1. Optical properties of **6–11** and **15–20** in dichloromethane [a]

Compound	λ_{abs} (nm)	ε ($\times 10^3$ $M^{-1}cm^{-1}$)	λ_{em} (nm)	Φ [b]	τ (ns) [c]
6	357	6.86	– [d]	– [d]	– [d]
7	357	6.35	509, 637	<0.01	2.7 [e]
8	353	7.54	489	<0.01	– [d]
9	383	5.10	500	0.04	1.1 [e]
10	384	4.83	500	0.01	0.63 (95%), 2.7 (5%) [e]
11	380	4.62	497	0.06	1.5 [e]
15	272	27.0	428, 460	0.18	1.9 [f]
16	272	30.8	434, 467	0.32	1.9 [f]
17	278	27.5	436, 461	0.04	1.5 [f]
18	280	28.4	461	0.09	0.29 (23%), 2.2 (77%) [f]
19	332	19.3	398	0.40	0.95 [g]
20	334	24.0	399	0.34	0.97 [g]

[a] Measured in CH_2Cl_2 purged with N_2 gas. [b] Absolute quantum yields were measured by an integrating sphere system. [c] Fluorescence lifetimes were observed at the maximum fluorescence wavelengths. [d] Under detection limit. [e] Excited at 365 nm. [f] Excited at 280 nm. [g] Excited at 340 nm. From reference 9.

Table 2.2.2. Optical properties of **6–11** and **15–20** in the solid state [a]

Compound	λ_{ex} [b] (nm)	λ_{em} (nm)	Φ [c]	τ (ns) [d]
6	370	486	0.85	7.8 [e]
7	370, 421 [f]	500	0.34	4.7 [g]
8	371	490	0.26	1.9 (50%), 4.1 (50%) [e]
9	442	491	0.44	10.2 [g]
10	450	504	0.16	3.6 (39%), 10.4 (61%) [h]
11	– [a]	– [a]	– [a]	– [a]
15	342	391	0.11	0.70 [i]
16	287	385	0.44	0.68 [j]
17	– [a]	– [a]	– [a]	– [a]
18	329	405	0.32	0.85 (99%), 12.1 (1%) [i]
19	365	410	0.66	1.7 [e]
20	370	411	0.77	2.3 [e]

[a] Measured in microcrystalline powder. Compounds **11** and **17** were oily products. [b] Excitation wavelengths in the solid phase determined by excitation spectra. [c] Absolute quantum yields were measured by an integrating sphere system. [d] Fluorescence lifetimes were observed at the maximum fluorescence wavelengths. [e] Excited at 365 nm. [f] Shoulder peak. [g] Excited at 405 nm. [h] Excited at 465 nm. [i] Excited at 340 nm. [j] Excited at 280 nm. From reference 9.

The emission spectra of the D–A–D molecules in dichloromethane expected for compound **7** showed broad bands around 500 nm; the fluorescence band of **7** was at 509 nm as small peak similar to other D–A–D molecules and at 630 nm as large peak. Besides, emission spectra of **7** and **10** (Figures 2.3.13–2.3.14 and Tables 2.2.3–2.2.4) in higher polar solvent (acetone) showed dual emission at around 500 nm and at over 600 nm (720 nm for **7** and 620 nm for **10**). These emission bands at over 600 nm in **7** and **10** were assignable to twisted ICT (TICT) emission arising from twisting amino group in the excited state as shown in Figure 2.2.1.[12]

Table 2.2.3. Optical properties of **7** in dichloromethane and acetone

solvent [a]	λ_{abs}	ε ($\times 10^3$ $M^{-1}cm^{-1}$) [b]	λ_{em}	Φ [c]	τ (ns) [d]
CH_2Cl_2	357	6.35	509, 637	<0.01	– [e]
acetone	356	5.82	498, 702	<0.01	– [e]

[a] Measured in solvent purged with N_2 gas. [b] Molar extinction coefficient. [c] Absolute quantum yields were measured by an integrating sphere system. [d] Fluorescence lifetimes were observed at the maximum fluorescence wavelengths (Excited at 365 nm). [e] Under detection limit.

Table 2.2.4. Optical properties of **10** in dichloromethane and acetone

solvent [a]	λ_{abs}	ε ($\times 10^3$ $M^{-1}cm^{-1}$) [b]	λ_{em}	Φ [c]	τ (ns) [d]
CH_2Cl_2	384	4.83	500	0.01	0.63 (95%), 2.7 (5%)
acetone	384	4.35	501, 620	<0.01	– [e]

[a] Measured in solvent purged with N_2 gas. [b] Molar extinction coefficient. [c] Absolute quantum yields were measured by an integrating sphere system. [d] Fluorescence lifetimes were observed at the maximum fluorescence wavelengths (Excited at 365 nm). [e] Under detection limit.

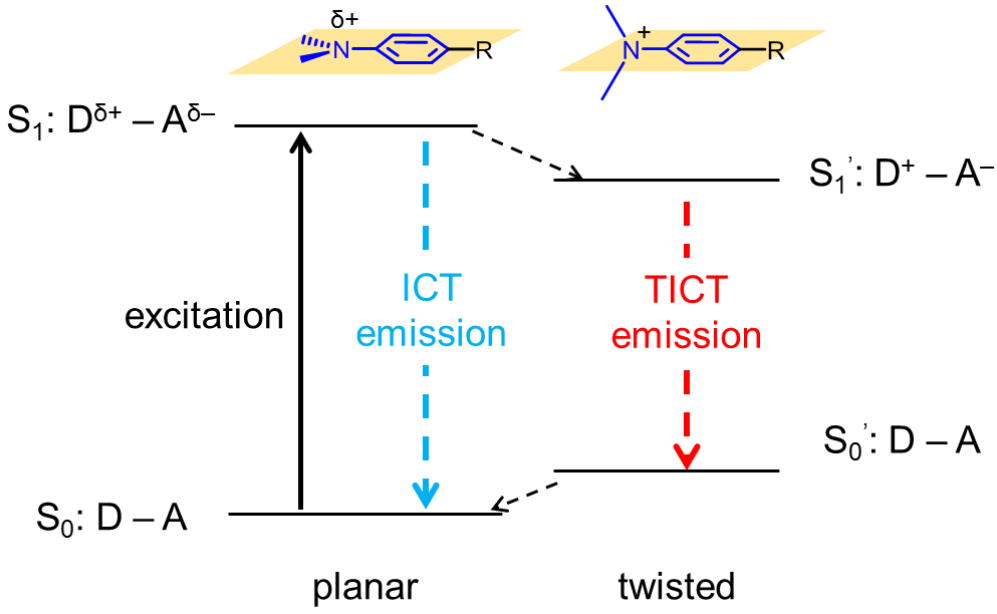

Figure 2.2.1. Jabłoński diagrams of planar ICT and twisted ICT.

The emission spectra of the A–D–A molecules with thiophene or EDOT moieties as the central aryl (**15**–**18**) emitted at around 450 nm and showed large Stokes shifts between the

absorption and emission maxima. On the other hand, the A–D–A molecules with 2,2'-bithiophene moieties (**19**, **20**) emitted with sharp bands at around 400 nm. The difference of absorption and emission behavior between **15**–**18** and **19**–**20** will be investigated from the viewpoint of computational study in Section 2.2.5.

Fluorescence quantum yields (Φ) are also summarized in Tables 2.2.1 and 2.2.2. The low quantum yields observed in dichloromethane mainly depended on the central aryl. The D–A–D molecules **6**–**8** had lower emission quantum yields ($\Phi < 0.01$) than those of **9**–**11** (Φ: up to 0.06). In the case of A–D–A molecules, quantum yields were ranked in order as 2,2'-bithiophene (**19**, **20**), thiophene (**15**, **16**), and EDOT (**17**, **18**). The lower quantum yield in solution of **17** and **18** was derived from the non-radiative relaxations induced by the flexible ethylenedioxy group.[13] Fluorescence in the solid phase was blue-green (D–A–D) or blue (A–D–A), with an emission maxima at around 500 nm (**6**–**10**) or 400 nm (**15**, **16**, **18**–**20**). All but one (**15**) displayed much higher quantum yields in the solid state than those in solution. In the solid phase, compound **6** exhibited a blue-green fluorescence at 486 nm with a high quantum yield (Φ = 0.85), and **19** and **20** also displayed strong blue emission at around 410 nm with high quantum yields (Φ = 0.66 and 0.77, respectively).

To examine the photoemission dynamics, the fluorescence rate constants (k_f) and non-radiative rate constants (k_{nr}) were calculated (Table 2.2.5) using quantum yields (Φ) and fluorescence lifetimes (τ). In the case of compounds **9**, **10**, **19**, and **20**, the fluorescence rate constants slightly had the deference between solution and the solid phase, while the non-radiative rate constant in solution was much larger than that in the solid phase. This difference indicates that non-radiative relaxation in the solid state was reduced comparing with that in solution. In addition, the solvent effect on optical properties of compound **9** was investigated as shown in Figures 2.3.15 and 2.3.16, and summarized in Table 2.2.6. Although UV–vis absorption and emission spectra did not change dramatically, the quantum yield decreased and k_{nr} increased with the increase of the polarity of the solvent, which can be ascribed to a photoinduced electron transfer (PeT) process (Table 2.2.6).[14]

Table 2.2.5. Rates of fluorescence (k_f) and non-radiative (k_{nr}) decays of selected disilane-bridged compounds in dichloromethane and in the solid state [a]

compound	dichloromethane		solid state	
	k_f ($\times 10^8$ s^{-1})	k_{nr} ($\times 10^8$ s^{-1})	k_f ($\times 10^8$ s^{-1})	k_{nr} ($\times 10^8$ s^{-1})
6	– [b]	– [b]	1.1	0.19
7	– [b]	– [b]	0.72	1.4
8	– [b]	– [b]	0.76	2.2
9	0.36	8.7	0.28	0.59
10	0.10	9.8	0.17	0.92
11	0.40	6.3	– [c]	– [c]
15	0.90	4.3	1.6	13
16	1.7	3.6	6.5	8.2
17	0.27	6.4	– [c]	– [c]
18	0.82	8.3	2.9	6.2
19	4.2	6.3	3.9	2.0
20	3.5	6.8	3.3	1.0

[a] Rate constants k_f and k_{nr} were calculated from quantum yield and fluorescence lifetime; $k_f = \Phi/\tau$ and $k_{nr} = (1-\Phi)/\tau$. [b] Low emission intensity. [c] Oily products.

Table 2.2.6. Optical properties and rates of fluorescence (k_f) and non-radiative (k_{nr}) decays of **9** in cyclohexane, toluene, dichloromethane, THF, and acetone

solvent [a]	λ_{abs} (nm)	ε ($M^{-1}cm^{-1}$) [b]	λ_{em} (nm)	Φ [c]	τ (ns) [d]	k_f ($\times 10^8$ s^{-1}) [e]	k_{nr} ($\times 10^8$ s^{-1}) [e]
cyclohexane	380	5330	479	0.08	2.1	0.38	4.4
toluene	383	4980	491	0.07	1.4	0.50	6.6
CH_2Cl_2	383	5100	500	0.04	1.2	0.33	8.0
THF	378	4540	500	0.04	1.1	0.36	8.7
acetone	380	5140	490	0.02	0.77	0.26	12.7

[a] Measured in solvent purged with N_2 gas. [b] Molar extinction coefficient. [c] Absolute quantum yields were mesured by an integrating sphere system. [d] Fluorescence lifetimes were observed at the maximum fluorescence wavelengths (excited at 365 nm). [e] Rate constants k_f and k_{nr} were calculated from quantum yield and fluorescence lifetime; $k_f = \Phi/\tau$ and $k_{nr} = (1-\Phi)/\tau$.

2.2.3 Aggregation-induced emission of **9** and **11**

The aggregation-induced emission (AIE) of **9** and **11** by THF/water method were investigated as shown in Figures 2.2.2 and 2.2.3, respectively.[15] The addition of water to a THF solution of **9** initially decreased the original fluorescence at around 500 nm caused by the PeT effect. However, when water comprised over 70% of the total solvent volume fraction, the emission intensity dramatically increased, and the photoluminescence intensity of **9** in 99% water was over three times higher than that in pure THF. This result insists that the strong emission was induced by the aggregation, which could suppress the non-radiative relaxation channels (e.g. vibration and rotation). Noted that there is no dependence of the emission and excitation spectra on the THF/water ratio (Figures 2.2.2(b) and 2.2.2(c)), and the concentration dependence on emission behavior in THF was not observed (Table 2.2.7). In addition, compound **11** also displayed AIE similar to **9** as shown in Figure 2.2.3

Table 2.2.7. Fluorescence properties of **9** in CH_2Cl_2 with different concentration

Concentration (mol/L)	λ_{em} (nm)	Φ [a]	τ (ns) [b]
1.7×10^{-3}	500	0.04	1.2
1.8×10^{-4}	500	0.04	1.2
7.3×10^{-5}	500	0.04	1.1
1.8×10^{-5}	500	0.04	1.2

[a] Absolute quantum yields were measured by an integrating sphere system. [b] Fluorescence lifetimes were observed at the maximum fluorescence wavelengths (excited at 365 nm).

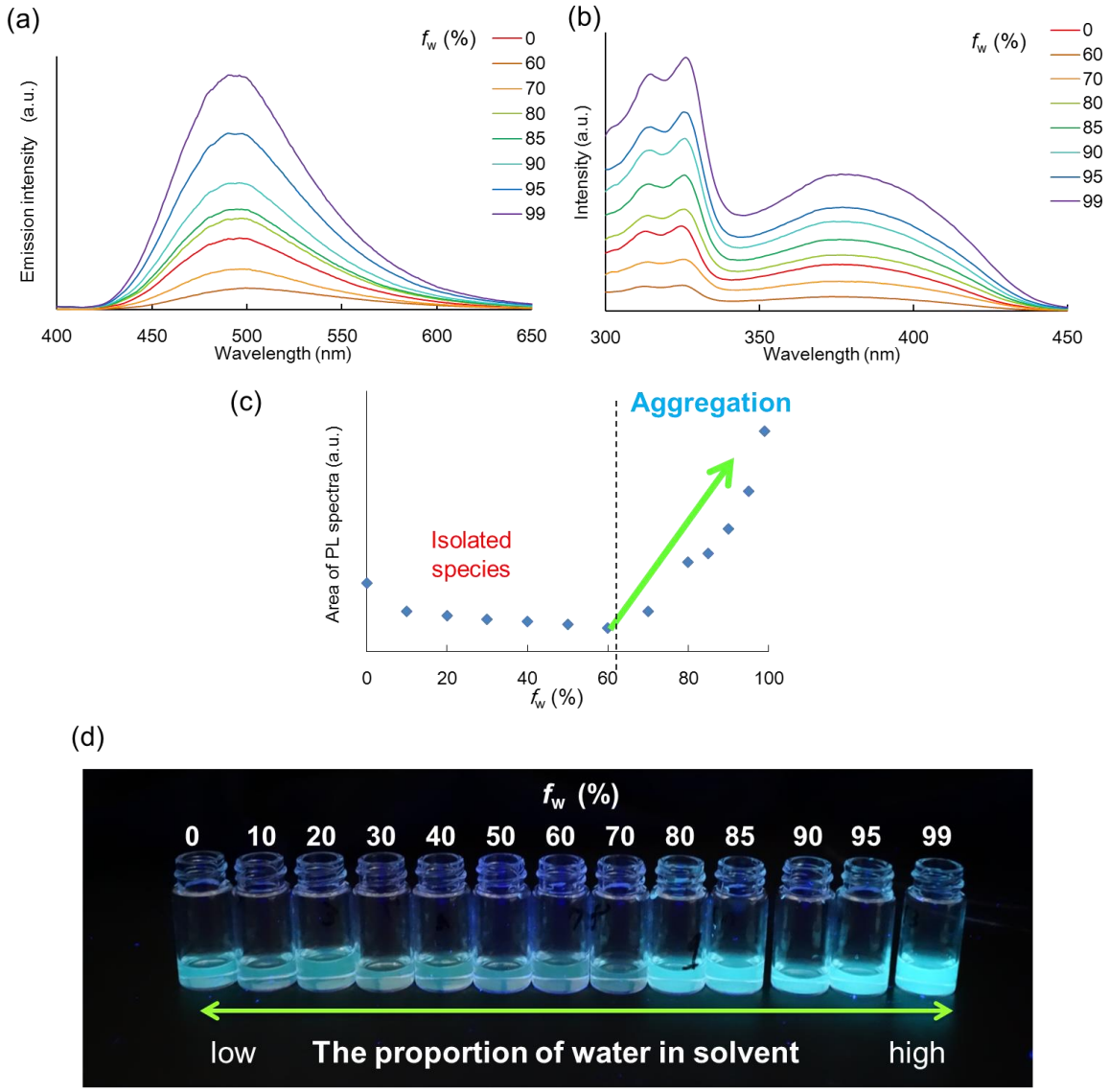

Figure 2.2.2. Measurement of the aggregation effect of **9**. f_w: the proportion of water in the total solvent volume ($f_w = V_{water}/(V_{THF} + V_{water})$, where V is volume. (a) Fluorescence spectra of **9** in various THF/water solution. (b) Excitation spectra of **9** in various THF/water solution. (c) Plot of fluorescence intensity (area) *vs* f_w. (d) Photo of the photoluminescence of **9** in various THF/water solution under UV irradiation (365 nm). From reference 9. Copyright © 2016 by John Wiley Sons, Inc. Adapted by permission of John Wiley & Sons, Inc.

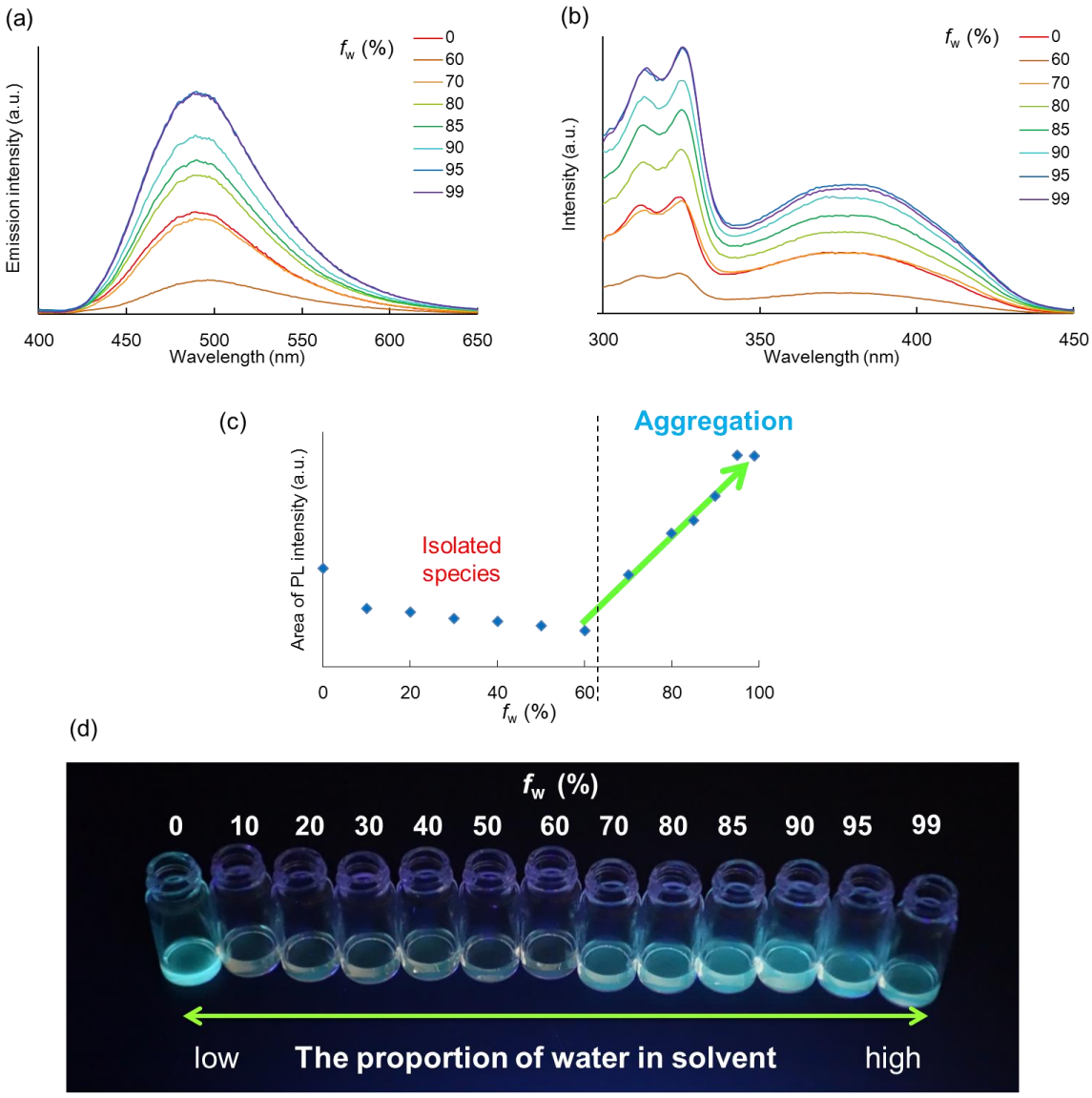

Figure 2.2.3. Measurement of the aggregation effect of **11**. f_w: the proportion of water in the total solvent volume ($f_w = V_{water}/(V_{THF} + V_{water})$, where V is volume) (a) Fluorescence spectra of **11** in various THF/water solution. (b) Excitation spectra of **11** in various THF/water solution. (c) Plot of fluorescence intensity (area) *vs* f_w. (d) Photo of the photoluminescence of **11** in various THF/water solution under UV irradiation (365 nm).

2.2.4 X-ray diffraction for crystal structures

To investigate the molecular structure, X-ray diffraction (XRD) analysis was carried out. Single crystal XRD results for **7**, **9**, **16**, and **20**, whose crystallographic data were summarized in Tables 2.3.1–2.3.8, revealed their molecular structure and packing structures as shown in Figure 2.2.4. The molecular structure of compound **7** appears almost straight and *anti* conformation (Figure 2.2.4(a)). Figure 2.2.4(b) shows that there are only CH–π intermolecular interactions (2.8–3.1 Å) and π–π stacking does not exist in the crystal packing structure. Compound **9** has a *syn*-form structure not similar to **7** (Figure 2.2.4(c)), and its crystal structure (Figure 2.2.4(d)) has the terminal donor aromatic ring (T2) and the central acceptor aromatic ring (C) located nearly parallel in the *anti*-position, and the other terminal aromatic ring (T1) and central ring (C) is distorted with ca. 110° torsion angle in the *syn*-position. There is no π–π stacking in the crystal due to the twisted structure.

A–D–A molecules **16** and **20** (Figure 2.2.4(e) and (g)) have a straight structure in the *anti*-position in crystal. The crystal packing structure of **16** (Figure 2.2.4(f)) insists that there are only CH–π intermolecular interactions (2.7–2.9 Å) without intermolecular π–π stacking. The packing structure of **20** (Figure 2.2.4(h)) suggests that there are CH–π intermolecular interactions (2.4–2.9 Å) and long intermolecular π–π distance (4.3 Å) owing to the bulkiness of disilane moieties. Thus, the crystal structure of both **16** and **20** do not have effective intermolecular π–π interactions.

Overall, the effective suppression of intermolecular π–π interactions because of the flexibility and bulkiness of Si_2Me_4 units in crystal structure affects strong solid state fluorescence of both the disilane-bridged D–A–D and the A–D–A triads in addition to the suppression of non-radiative relaxations by the aggregation.[16]

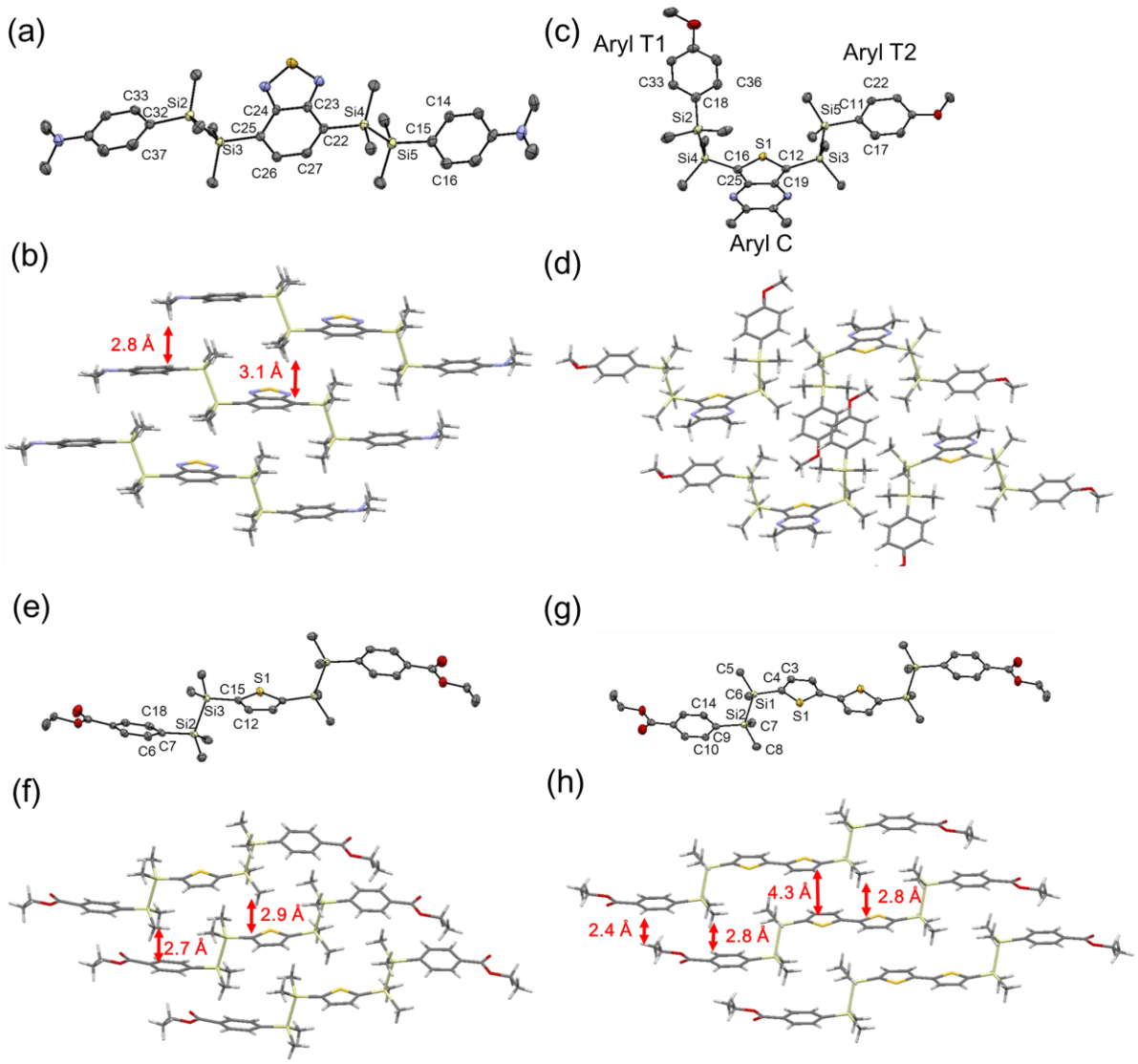

Figure 2.2.4. (a, c, e, g) ORTEP drawings (50% probability ellipsoids) and (b, d, f, h) packing structures of (a, b) **7**, (c, d) **9**, (e, f) **16**, and (g, h) **20**. Hydrogen atoms on ORTEP drawings are omitted for clarity. From reference 9. Copyright © 2016 by John Wiley Sons, Inc. Adapted by permission of John Wiley & Sons, Inc.

2.2.5 Theoretical consideration for the structural and optical properties

To investigate the combinational effects of donor, acceptor, and disilane moieties on the photophysical properties, the calculation of the molecular orbitals and transition states with density functional theory (DFT) and time-dependent DFT (TD-DFT) was carried out with Gaussian 09 Revision E.01 program.[17] The electron density of the HOMO of **6**–**8** was mainly located on the donor aryls, and the LUMO was mainly spread over the acceptor (Figure 2.2.6). Although the electron density of the LUMO of **9**–**11** was localized on the acceptor aryl and the HOMO of **10** was mainly spread over the donor and disilane units similar to **6**–**8**, the HOMO of **9** and **11** was partially localized on the thiophene and disilane units (Figure 2.2.7). Noted that compound **9** has two structure, a *syn*-form (suggested from XRD analysis) and an *anti*-form. According to their Gibbs energy, the *anti*-form and the *syn*-form by ca. 0.1 kcal/mol in vacuum (Figure 2.2.5 and Table 2.2.8), so that in solution phase the conformation of **9** should be the mix of *anti*-form and *syn*-form while in crystalline state there are only the *syn*-form. Although the frontier molecular orbitals of the *anti*-form **9** slightly differ from those of the *syn*-form, the structural difference between solution phase and solid phase affected the optical behavior such as the fluorescence rate as well as the non-radiative rate (Table 2.2.2). The TD-DFT calculation insisted that the lowest energy absorption band and the emission band of **6**–**11** represented the HOMO → LUMO transition (Tables 2.2.9–2.2.14), which was assigned to ICT (**6**–**8**, and **10**) or to a combination of ICT and π–π* transition (**9** and **11**).

Figures 2.2.8–2.2.10 show the electron density of molecular orbital and energy levels of A–D–A molecules. Compounds **15**–**18** were mainly localized on the central aromatic and disilane units, and the LUMO was localized on the acceptor aryls. Meanwhile, both the HOMO and LUMO of **19** and **20** were spread over the 2,2'-bithiophene and disilane units. TD-DFT calculations showed the lowest energy absorption band of **15**–**18** to represent the HOMO → LUMO transition mainly assigned to ICT, while that of **19** and **20** represents the π–π* excitation (Tables 2.2.15–2.2.20). Therefore, the transition of **15**–**18** can be assigned to ICT emission, whereas that of **19** and **20** can be assigned to the π–π* emission. Thus **15**–**18** showed larger Stokes shifts than **19** and **20**.

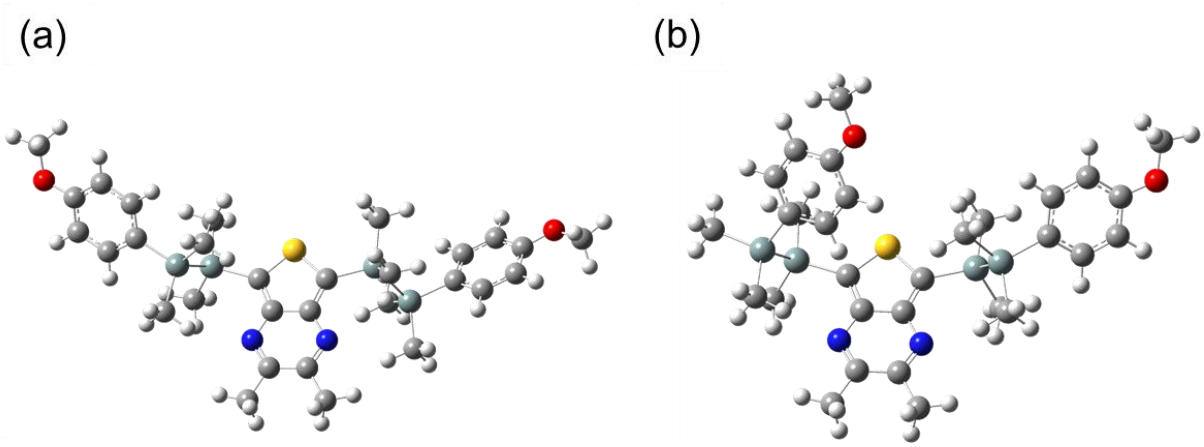

Figure 2.2.5. Molecular structures for (a) *anti*-form **9** optimized with DFT calculation at the B3LYP/6-31G(d) level and (b) *syn*-form **9** estimated with XRD analysis.

Table 2.2.8 Gibbs free energy of **9** calculated with DFT at the B3LYP/6-31G(d) level.

	Gibbs free energy (kcal/mol)
anti-form	− 1873697.824
syn-form	− 1873697.718
difference	0.11

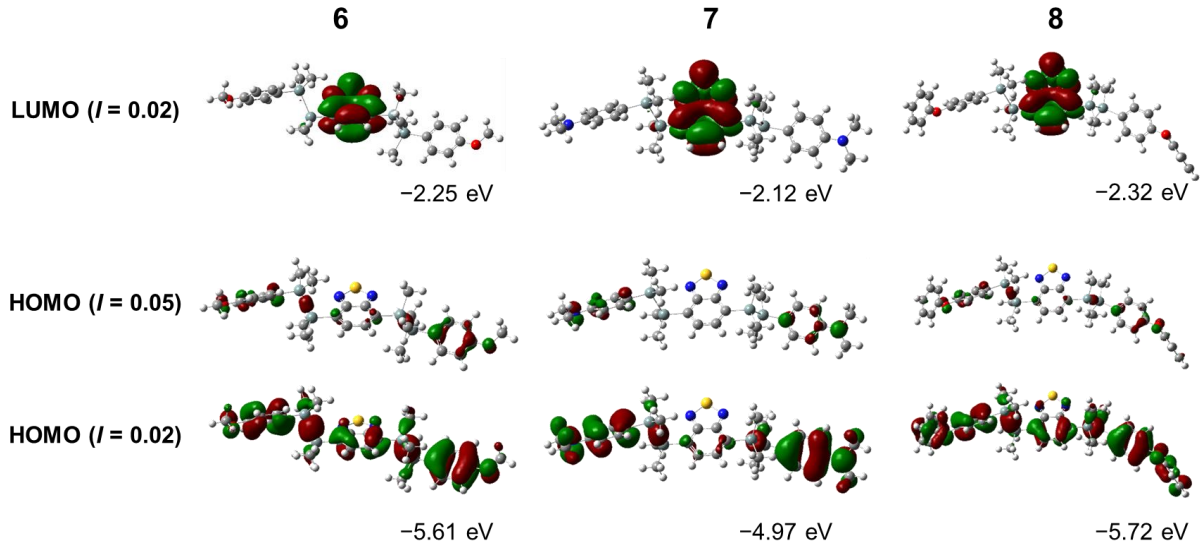

Figure 2.2.6. Frontier molecular orbitals and energy levels for **6**–**8** calculated with DFT at the B3LYP/6-31G(d) level. *I* means the probability density.

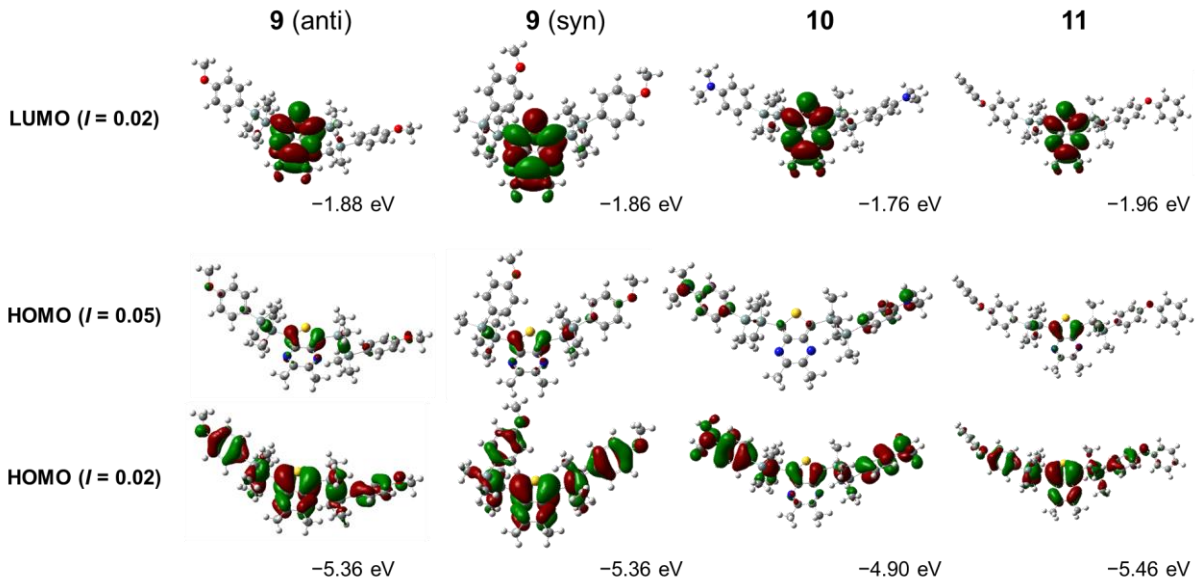

Figure 2.2.7. Frontier molecular orbitals and energy levels for *anti*-form **9**, *syn*-form **9**, **10**, and **11** calculated with DFT at the B3LYP/6-31G(d) level. *I* means the probability density.

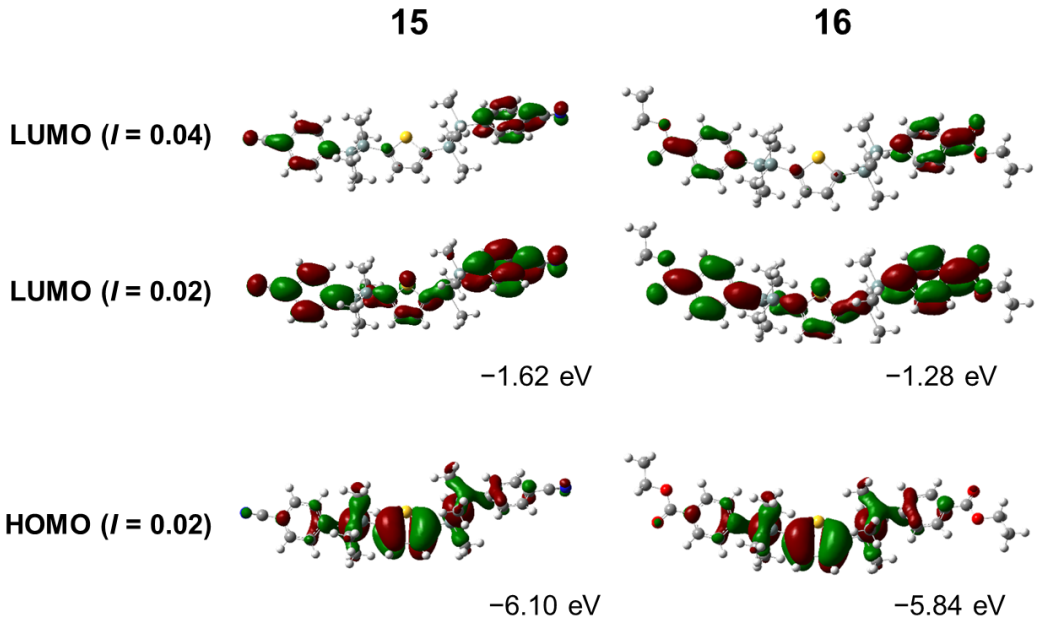

Figure 2.2.8. Frontier molecular orbitals and energy levels for **15** and **16** calculated with DFT at the B3LYP/6-31G(d) level. *I* means the probability density.

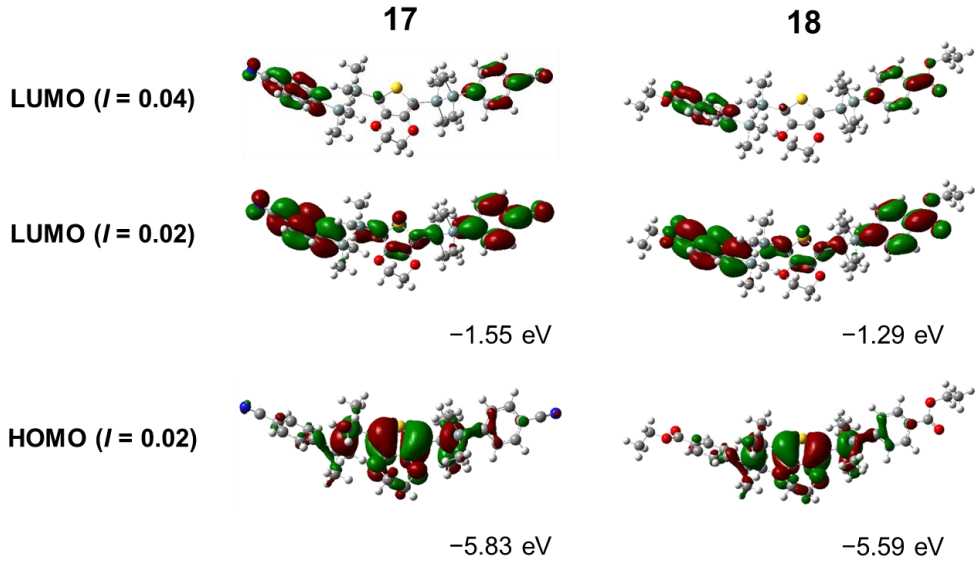

Figure 2.2.9. Frontier molecular orbitals and energy levels for **17** and **18** calculated with DFT at the B3LYP/6-31G(d) level. *I* means the probability density.

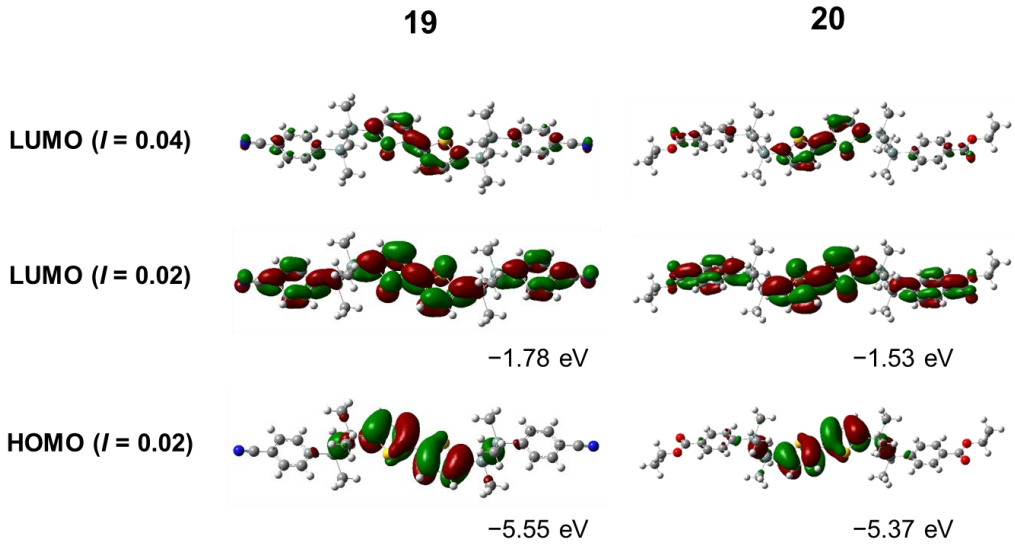

Figure 2.2.10. Frontier molecular orbitals and energy levels for **19** and **20** calculated with DFT at the B3LYP/6-31G(d) level. *I* means the probability density.

Table 2.2.9. Summary of the TD-DFT calculations of **6**

S_1: 426.53 nm			f = 0.1393 [a]
HOMO	**→**	**LUMO**	**0.69865** [b]
S_2: 401.35 nm			f = 0.0002
HOMO−1	→	LUMO	0.70269
S_3: 349.19 nm			f = 0.0752
HOMO−2	→	LUMO	0.69669

[a] Oscillator strength. [b] CI expansion coefficients for each excitation.

Table 2.2.10. Summary of the TD-DFT calculations of **7**

S_1: 498.83 nm			f = 0.0721 [a]
HOMO	**→**	**LUMO**	**0.70348** [b]
S_2: 486.84 nm			f = 0.0002
HOMO−1	→	LUMO	0.70573
S_3: 373.06 nm			f = 0.1566
HOMO−2	→	LUMO	0.69692

[a] Oscillator strength. [b] CI expansion coefficients for each excitation.

Table 2.2.11. Summary of the TD-DFT calculations of **8**

S_1: 414.09 nm			f = 0.1758 [a]
HOMO−2	→	LUMO	−0.14891 [b]
HOMO	**→**	**LUMO**	**0.68628**
S_2: 386.74 nm			f = 0.0005
HOMO−3	→	LUMO	−0.12410
HOMO−1	→	LUMO	0.69462
S_3: 351.78 nm			f = 0.0589
HOMO−2	→	LUMO	0.68291
HOMO	→	LUMO	0.14944

[a] Oscillator strength. [b] CI expansion coefficients for each excitation.

Table 2.2.12. Summary of the TD-DFT calculations of **9**

anti form				*syn* form			
S_1: 414.07 nm			f = 0.1817 [a]	S_1: 412.04 nm			f = 0.1300
HOMO	**→**	**LUMO**	**0.69646** [b]	**HOMO**	**→**	**LUMO**	**0.69892**
S_2: 368.72 nm			f = 0.0069	S_2: 426.81 nm			f = 0.0032
HOMO−3	→	LUMO	0.66344	HOMO−3	→	LUMO	0.47747
HOMO−2	→	LUMO	0.22035	HOMO−1	→	LUMO	0.51705
S_3: 365.26 nm			f = 0.0074	S_3: 426.81 nm			f = 0.0089
HOMO−1	→	LUMO	0.70113	HOMO−3	→	LUMO	0.47937
				HOMO−2	→	LUMO	0.21729
				HOMO−1	→	LUMO	−0.46091

[a] Oscillator strength. [b] CI expansion coefficients for each excitation.

Table 2.2.13. Summary of the TD-DFT calculations of **10**

S_1: 450.24 nm			f = 0.1258 [a]
HOMO	**→**	**LUMO**	**0.69667** [b]
S_2: 432.35 nm			f = 0.0044
HOMO−1	→	LUMO	0.70532
S_3: 380.88 nm			f = 0.0759
HOMO−2	→	LUMO	0.68660

[a] Oscillator strength. [b] CI expansion coefficients for each excitation.

Table 2.2.14. Summary of the TD-DFT calculations of **11**

S_1: 410.16 nm			f = 0.2159 [a]
HOMO	**→**	**LUMO**	**0.69503** [b]
S_2: 369.42 nm			f = 0.0055
HOMO−6	→	LUMO	0.16389
HOMO−3	→	LUMO	0.65882
HOMO−2	→	LUMO	−0.16763
S_3: 358.89 nm			f = 0.0072
HOMO−4	→	LUMO	0.12110
HOMO−1	→	LUMO	0.69507

[a] Oscillator strength. [b] CI expansion coefficients for each excitation.

Table 2.2.15. Summary of the TD-DFT calculations of **15**

S_1: 306.38 nm			f = 0.6906 [a]
HOMO	**→**	**LUMO**	**0.69794** [b]
S_2: 297.37 nm			f = 0.0089
HOMO	→	LUMO+1	0.70141
S_3: 261.13 nm			f = 0.5672
HOMO−3	→	LUMO	−0.14301
HOMO−1	→	LUMO+1	0.17245
HOMO	→	LUMO+2	0.65360

[a] Oscillator strength. [b] CI expansion coefficients for each excitation.

Table 2.2.16. Summary of the TD-DFT calculations of **16**

S_1: 305.45 nm			f = 0.7665 [a]
HOMO	**→**	**LUMO**	**0.69540** [b]
S_2: 296.15 nm			f = 0.0147
HOMO	→	LUMO+1	0.70081
S_3: 267.13 nm			f = 0.5862
HOMO−3	→	LUMO	0.15126
HOMO−1	→	LUMO+1	−0.20066
HOMO	→	LUMO+2	0.69673

[a] Oscillator strength. [b] CI expansion coefficients for each excitation.

Table 2.2.17. Summary of the TD-DFT calculations of **17**

S_1: 320.56 nm			f = 0.5006 [a]
HOMO	**→**	**LUMO**	**0.69800** [b]
S_2: 313.82 nm			f = 0.0140
HOMO	→	LUMO+1	0.69958
S_3: 298.52 nm			f = 0.0089
HOMO−1	→	LUMO	0.70114

[a] Oscillator strength. [b] CI expansion coefficients for each excitation.

Table 2.2.18. Summary of the TD-DFT calculations of **18**

S_1: 319.32 nm			f = 0.5350 [a]
HOMO	**→**	**LUMO**	**0.69725** [b]
S_2: 312.90 nm			f = 0.0170
HOMO	→	LUMO+1	0.70014
S_3: 295.67 nm			f = 0.0094
HOMO−1	→	LUMO	0.70163

[a] Oscillator strength. [b] CI expansion coefficients for each excitation.

Table 2.2.19. Summary of the TD-DFT calculations of **19**

S_1: 362.63 nm			f = 1.1946 [a]
HOMO	**→**	**LUMO**	**0.70104** [b]
S_2: 338.29 nm			f = 0.0000
HOMO−1	→	LUMO	0.70445
S_3: 323.91 nm			f = 0.1677
HOMO−2	→	LUMO	0.70172

[a] Oscillator strength. [b] CI expansion coefficients for each excitation.

Table 2.2.20. Summary of the TD-DFT calculations of **20**

S_1: 364.36 nm			f = 1.3435 [a]
HOMO	**→**	**LUMO**	**0.69842** [b]
S_2: 338.08 nm			f = 0.0003
HOMO	→	LUMO+1	0.70330
S_3: 326.89 nm			f = 0.0903
HOMO	→	LUMO+2	0.70124

[a] Oscillator strength. [b] CI expansion coefficients for each excitation.

2.3 Experimental section

2.3.1 General

(a) Reagents

N,*N*-Diisopropylethylamine was purchased from Tokyo Chemical Industry and was distilled before use. All solvents for synthesis were dried before use. 1,2-Dichloro-1,1,2,2-tetramethyldisilane, iodine, sulfuric acid, silver sulfate, acetic acid, lithium aluminum hydride, bis(tri-*tert*-butylphosphine)palladium(0), benzo[*c*][1,2,5]thiadiazole, *N*-iodosuccinimide (NIS), triethylamine, 1.6 M *n*-BuLi in hexane, 2,5-dibromothiophene, 2,2'-bithiophene, *N*,*N*,*N*',*N*'-tetramethylethylenediamine (TMEDA), 4-iodobenzonitrile, and ethyl 4-iodobenzoate were purchased from commercial sources and were used as received without further purification. 2,3-Dimethylthieno[3,4-*b*]pyrazine was prepared according to the literature.[11a] 2,5-Dibromo-3,4-ethylenedioxythiophene was prepared according to the literature.[18] 1-(4-Dimethylaminophenyl)-1,1,2,2-tetramethyldisilane (**3**), 1-(4-methoxyphenyl)-1,1,2,2-tetramethyldisilane (**4**), and 1,1,2,2-tetramethyl-1-(4-phenoxyphenyl)disilane (**5**) were prepared according to the literature.[8c,19] Cyclohexane, toluene, dichloromethane, and acetone for spectroscopic analysis were purchased from Wako Pure Chemical Industries and deoxygenated with nitrogen before measurements. Distilled THF for spectroscopic analysis was purchased from Kanto Chemical Co., Inc., purified through organic solvent purifier (Nikko Hansen Co., Ltd.) and deoxygenated with nitrogen before measurements. Water for synthesis and spectroscopic analysis was purified with AUTOPURE WD500 (Yamato Scientific Co., Ltd.), and Water for spectroscopic analysis was deoxygenated with nitrogen before measurements.

(b) Characterization

NMR spectra were measured with a JEOL AL-400 spectrometer, a JEOL ECX-400 spectrometer or a Bruker DRX-500 spectrometer. Tetramethylsilane ($\delta = 0.00$) was used as an internal standard for ^{1}H NMR spectra, and $CDCl_3$ ($\delta = 77.0$) was used as an internal standard for ^{13}C NMR spectra. GC-MS spectra were recorded with a Shimadzu GC-MS-QP2010 spectrometer. FAB-MS was performed with a JEOL MStation JMS-700 spectrometer. UV–vis absorption spectra were measured with a JASCO V-570 spectrometer. Fluorescence spectra and absolute quantum yields were measured with a Hitachi F-4500 spectrometer, a Shimadzu RF-5300PC spectrometer, and a Hamamatsu C9920-02 spectrometer. Fluorescence lifetimes were

measured with a Hamamatsu Quantaurus-Tau C11367 spectrometer. The most stable conformers and energy transitions identified were calculated by DFT and TD-DFT computations that were performed by the Gaussian09 revision E.01 program using B3LYP/6-31G(d).[17]

(c) X-ray crystallographic analysis

Single crystals for X-ray diffraction were prepared using the following conditions:

i. **7**: Recrystallization by vapor diffusion of benzonitrile/DMSO at room temperature
ii. **9**: Recrystallization from methanol at −30 °C
iii. **16**: Recrystallization from acetonitrile at room temperature
iv. **20**: Recrystallization from hexane at room temperature

Synchrotron radiation (SR) X-ray diffraction data of **7** were collected at 100 K on a CCD detector at SPring-8 beam line BL02B1 (Hyogo, Japan) (SR, λ = 0.3540 Å).[20] The structure was solved by direct methods using SIR-2004 program[21] and was refined by the full-matrix least-squares techniques against F^2 implementing SHELXL-2013.[22]

X-ray diffraction data of **9**, **16**, **20** were collected at 113 K with an AFC10 diffractometer coupled with a Rigaku Saturn CCD system equipped with a rotating-anode X-ray generator producing graphite-monochromated MoKα radiation (λ = 0.7107 Å). The structures were solved by the direct method using SIR-92 program (**9**, **16**)[23] or SHELX-97 program (**20**)[24] and refined against F^2 using SHELXL-97.[24]

Crystallographic data for the structure of **7**, **9**, **16**, and **20** have been deposited with the Cambridge Crystallographic Data Centre as supplementary publication nos. CCDC 1425714, 1425711, 1425712, and 1425713, respectively.

2.3.2 Synthesis

(a) An improved experimental procedure for the preparation of 4,7-diiodobenzo[*c*][1,2,5]thiadiazole.

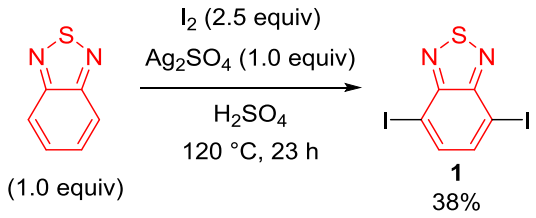

4,7-Diiodo-2,1,3-benzothiadiazole (**1**) was prepared from benzo[*c*][1,2,5]thiadiazole according to the modified method based on the literature.[8] Under an argon atmosphere, to benzo[*c*][1,2,5]thiadiazole (2.72 g, 20.0 mmol), iodine (12.7 g, 50.0 mmol) and silver(I) sulfate (6.24 g, 20 mmol), was added concentrated sulfuric acid (30 mL), and the reaction mixture was stirred at 120 °C for 23 h. After cooling to ambient temperature, the reaction mixture was quenched with water at 0 °C, and the precipitate was collected by filtration. The collected solid were extracted with CH_2Cl_2 from the precipitate three times. The organic solution was washed with saturated $NaHCO_3$ aq, water, and brine, and dried over Na_2SO_4. After evaporation of dichloromethane, the residue was recrystallized with ethyl acetate to give **1** (2.92 g, 7.54 mmol) in 38% yield.

4,7-diiodobenzo[*c*][1,2,5]thiadiazole (1):[8] Isolated yield: 38%. Yellow solid. Sublimation point: 140 °C. ^{1}H NMR (400 MHz, $CDCl_3$) δ 7.82 (s, 2H). ^{13}C NMR (100 MHz, $CDCl_3$) δ 153.9 (C_q), 139.8 (CH), 87.8 (C_q). EI-MS *m/z* 388 (M^+). Elemental analysis Calcd (%) for $C_6H_2IN_2S$: C 18.57, H 0.52, N 7.22. Found: C 18.65, H 0.68, N 7.17.

(b) An improved experimental procedure for the preparation of 5,7-diiodo-2,3-dimethylthieno[3,4-*b*]pyrazine.

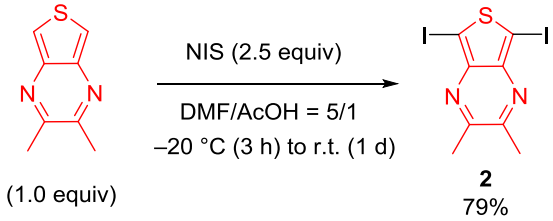

5,7-Diiodo-2,3-dimethylthieno[3,4-*b*]pyrazine (**2**) was prepared by modified method according to literature.[9] In an argon atmosphere, a solution of NIS (4.47 g, 19.9 mmol) in DMF

(100 mL) was added dropwise to a solution of 2,3-dimethylthieno[3,4-*b*]pyrazine (1.31 g, 7.97 mmol) in DMF (50 mL) and CH_3CO_2H (10 mL) at −20 °C. The reaction mixture was stirred for 3 h at −20 °C and warmed to room temperature and stirred for 1 d at room temperature. The reaction mixture was poured into water and filtered. The brown residue was washed with water and collected. The crude product was purified by flash column chromatography on silica gel (eluent: CH_2Cl_2 /hexane = 1/1) to obtain **2** (2.63 g, 6.33 mmol) as yellow solid in 79% yield.

5,7-diiodo-2,3-dimethylthieno[3,4-*b*]pyrazine (2): Isolated yield 79%. Yellow solid. Decomposition point: 147 °C. ^{1}H NMR (500 MHz, $CDCl_3$) δ 2.68 (s, 6H). ^{13}C NMR (125 MHz, $CDCl_3$) δ 155.1 (C_q), 143.8 (C_q), 73.3 (C_q), 23.3 (CH_3). FAB-MS *m/z* 417 ($[M+H]^+$). FAB-HRMS Calcd for $C_8H_7N_2SI_2$: 416.8419. Found: 416.8432 ($[M+H]^+$).

(c) A typical experimental procedure for the preparation of 6−8.

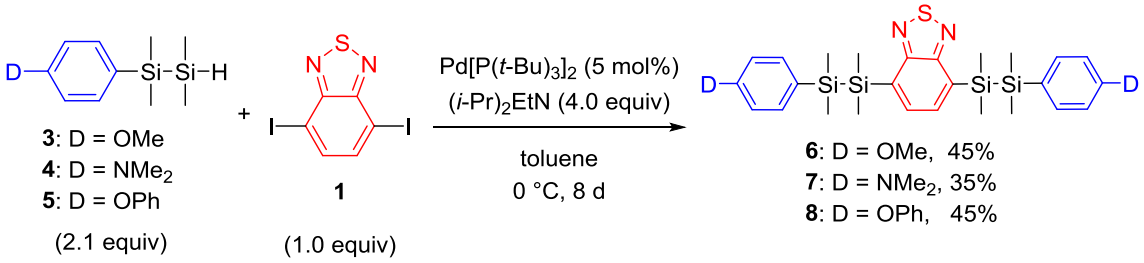

Under an argon atmosphere, to a solution of **1** (456 mg, 1.2 mmol) and $Pd[P(t\text{-}Bu)_3]_2$ (30.7 mg, 0.060 mmol) in toluene (10 mL) was added *N*,*N*-diisopropylethylamine (0.94 mL, 4.8 mmol) and **3** (0.539 mL, 2.5 mmol) for 8 d at 0 °C. The reaction mixture was poured into water and extracted with CH_2Cl_2 three times. The organic layer was washed with brine and dried over Na_2SO_4. The solvent was evaporated, and residue was roughly purified by column chromatography on silica gel (eluent: $CHCl_3$ /hexane = 1/1) and perfectly purified by HPLC with a GPC column (solvent: $CHCl_3$) to afford **6** (313 mg, 0.54 mmol) as pale yellow solid in 45% yield.

4,7-bis[2-(4-methoxyphenyl)-1,1,2,2-tetramethyldisilyl]benzo[*c*][1,2,5]thiadiazole (6): Isolated yield 45%. Pale yellow solid. Mp: 118.0−119.0 °C. ^{1}H NMR (500 MHz, $CDCl_3$) δ 7.51 (s, 2H), 7.25 (d, 4H, *J* = 8.6 Hz), 6.79 (d, 4H, *J* = 8.6 Hz), 3.78 (s, 6H), 0.48 (s, 12H), 0.31 (s, 12H). ^{13}C NMR (125 MHz, $CDCl_3$) δ 159.9 (C_q), 157.9 (C_q), 135.12 (CH), 135.06 (CH), 134.6 (C_q), 129.7 (C_q), 113.3 (CH), 54.9 (CH_3), −3.2 (CH_3), −3.6 (CH_3). EI-MS *m/z* 580 (M^+). Elemental analysis Calcd (%) for $C_{28}H_{40}N_2O_2SSi_4$: C 57.88, H 6.94, N 4.82. Found: C 57.63, H

7.21, N 4.54.

4,7-bis[2-(4-dimethylaminophenyl)-1,1,2,2-tetramethyldisilyl]benzo[*c*][1,2,5]thiadiazole (7): Isolated yield 35%. Yellow solid. Mp: 128.0−129.5 °C. ^{1}H NMR (400 MHz, $CDCl_3$) δ 7.52 (brs, 2H), 7.20 (d, 4H, *J* = 8.5 Hz), 6.63 (d, 4H, *J* = 8.5 Hz), 2.92 (s, 12H), 0.48 (s, 12H), 0.28 (s, 12H). ^{13}C NMR (100 MHz, $CDCl_3$) δ 158.0 (C_q), 150.6 (C_q), 135.2 (CH), 134.9 (C_q), 134.8 (CH), 123.9 (C_q), 111.9 (CH), 40.2 (CH_3), −3.1 (CH_3), −3.4 (CH_3). EI-MS *m/z* 606 (M^+). Elemental analysis Calcd (%) for $C_{30}H_{46}N_4SSi_4$: C 59.35, H 7.64, N 9.23. Found: C 59.20, H 7.80, N 8.98.

4,7-bis[2-(4-phenoxyphenyl)-1,1,2,2-tetramethyldisilyl]benzo[*c*][1,2,5]thiadiazole (8): Isolated yield: 45%. Pale yellow solid. Mp: 110.0−112.5 °C. ^{1}H NMR (500 MHz, $CDCl_3$) δ 7.51 (s, 2H), 7.25 (d, 4H, *J* = 8.6 Hz), 6.79 (d, 4H, *J* = 8.6 Hz), 3.78 (s, 6H), 0.48 (s, 12H), 0.31 (s, 12H). ^{13}C NMR (125 MHz, $CDCl_3$) δ 159.9 (C_q), 157.9 (C_q), 135.12 (CH), 135.06 (CH), 134.6 (C_q), 129.7 (C_q), 113.3 (CH), 54.9 (CH_3), −3.2 (CH_3), −3.6 (CH_3). FAB-MS *m/z* 704 (M^+). FAB-HRMS Calcd for $C_{38}H_{44}O_2N_2SSi_4$: 704.2200. Found: 704.2173 (M^+).

(d) A typical experimental procedure for the preparation of 9−11.

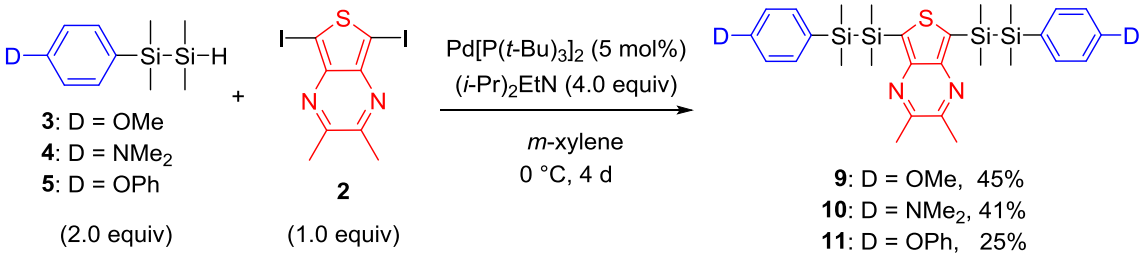

Under an argon atmosphere, to a solution of **2** (417.4 mg, 1.0 mmol) and $Pd[P(t\text{-}Bu)_3]_2$ (25.5 mg, 0.050 mmol) in *m*-xylene (7.5 mL) was added *N*,*N*-diisopropylethylamine (0.80 mL, 4.1 mmol) and **3** (0.433 mL, 2.0 mmol) at 0 °C for 4 d. The reaction mixture was poured into water and extracted with CH_2Cl_2 three times. The organic layer was washed with brine and dried over Na_2SO_4. The solvent was evaporated under a reduced pressure, and residue was roughly purified by column chromatography on silica gel (eluent: hexane/ethyl acetate = 100/1) and perfectly purified by HPLC with a GPC column (solvent: $CHCl_3$) to afford **9** (276 mg, 0.45 mmol) as yellow solid in 45% yield.

5,7-bis[2-(4-methoxyphenyl)-1,1,2,2-tetramethyldisilyl]-2,3-dimethylthieno[3,4-*b*]pyrazine (9): Isolated yield: 45%. Yellow solid. Mp: 55.1−56.2 °C. ^{1}H NMR (500 MHz, $CDCl_3$) δ 7.31 (d, 4H, *J* = 8.8 Hz), 6.81 (d, 4H, *J* = 8.6 Hz), 3.78 (s, 6H), 2.54 (s, 6H), 0.47 (s, 12H), 0.34

(s, 12H). ^{13}C NMR (125 MHz, $CDCl_3$) δ 159.9 (C_q), 150.6 (C_q), 149.8 (C_q), 135.7 (C_q), 135.3 (CH), 129.8 (C_q), 113.3 (CH), 54.9 (CH_3), 23.4 (CH_3), −2.7 (CH_3), −3.3 (CH_3). FAB-MS *m/z* 608 (M^+). FAB-HRMS Calcd for $C_{30}H_{44}O_2N_2SSi_4$: 608.2201. Found: 608.2201 (M^+).

5,7-bis[2-(4-dimethylaminophenyl)-1,1,2,2-tetramethyldisilyl]-2,3-dimethylthieno[3,4-*b*]pyrazine (10): Isolated yield: 41%. Yellow solid. Mp: 115.2−118.2 °C. ^{1}H NMR (500 MHz, $CDCl_3$) δ 7.27 (d, 4H, *J* = 8.8 Hz), 6.66 (d, 4H, *J* = 8.6 Hz), 2.93 (s, 12H), 2.55 (s, 6H), 0.48 (s, 12H), 0.32 (s, 12H). ^{13}C NMR (125 MHz, $CDCl_3$) δ 150.54 (C_q), 150.45 (C_q), 149.8 (C_q), 136.0 (C_q), 135.0 (CH), 124.0 (C_q), 111.9 (CH), 40.2 (CH_3), 23.4 (CH_3), −2.6 (CH_3), −3.2 (CH_3). FAB-MS *m/z* 634 (M^+). FAB-HRMS Calcd for $C_{32}H_{50}N_4SSi_4$: 634.2833. Found: 634.2842 (M^+).

5,7-bis[2-(4-phenoxyphenyl)-1,1,2,2-tetramethyldisilyl]-2,3-dimethylthieno[3,4-*b*]pyrazine (11): Isolated yield: 25%. Yellow oil. ^{1}H NMR (400 MHz, $CDCl_3$) δ 7.34−7.30 (m, 8H), 7.10 (t, 2H, *J* = 7.6 Hz), 6.99 (d, 4H, *J* = 7.8 Hz), 6.88 (d, 4H, *J* = 8.2 Hz), 2.54 (s, 6H), 0.48 (s, 12H), 0.34 (s, 12H). ^{13}C NMR (100 MHz, $CDCl_3$) δ 157.7 (C_q), 156.8 (C_q), 150.7 (C_q), 149.8 (C_q), 135.4 (CH), 133.1 (C_q), 123.3 (CH), 119.1 (CH), 117.8 (CH), 23.4 (CH_3), −2.7 (CH_3), −3.3 (CH_3). FAB-MS *m/z* 732 (M^+). FAB-HRMS Calcd for $C_{40}H_{48}N_2O_2SSi_4$: 732.2514. Found: 732.2534 (M^+).

(e) Preparation of 2,5-bis(1,1,2,2-tetramethyldisilanyl)thiophene (12).

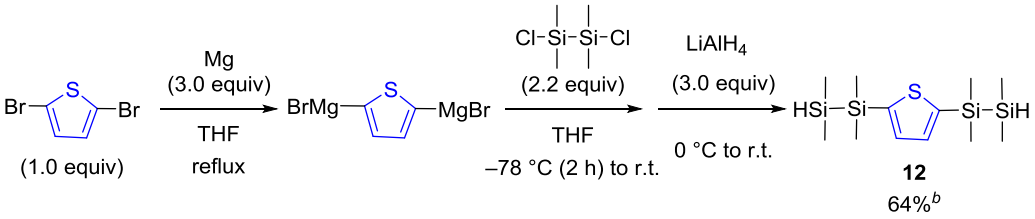

Under an argon atmosphere, a solution of 2,5-dibromothiophene (3.40 mL, 30 mmol) in THF (70 mL) was added to magnesium turning (2.19 g, 90 mmol) dropwisely, and reaction mixture was refluxed overnight to give di-Grignard reagent. This solution of the di-Grignard reagent in THF was added slowly to a solution of 1,2-dichloro-1,1,2,2-tetramethyldisilane (11.8 mL, 66 mmol) in THF (60 mL) at −78 °C for 2 h, then the reaction mixture was warmed to room temperature. The mixture was cooled to 0 °C, and $LiAlH_4$ (2.29 g, 90 mmol) was added. The reaction mixture was warmed to room temperature and stirred overnight. The reaction mixture was quenched with water and extracted with diethyl ether three times. The organic layer was washed with brine and dried over sodium sulfate. The solvent was evaporated under a reduced pressure, and residue was purified by distillation (110 °C, 1.0 mmHg) to give **12** (6.08

g, 19.2 mmol) as colorless oil in 64% yield.

2,5-bis(1,1,2,2-tetramethyldisilanyl)thiophene (12): Isolated yield: 64%. Colorless oil. ^{1}H NMR (500 MHz, $CDCl_3$) δ 7.29 (s, 2H), 3.75 (septet, 2H, *J* = 4.5 Hz), 0.41 (s, 12H), 0.16 (d, 12H, *J* = 4.6 Hz). ^{13}C NMR (125 MHz, $CDCl_3$) δ 144.4 (C_q), 135.4 (CH), −2.1 (CH_3), −6.6 (CH_3). FAB-MS *m/z* 315 ($[M-H]^+$). FAB-HRMS Calcd for $C_{12}H_{27}Si_4S$: 315.0921. Found: 315.0895 ($[M-H]^+$).

(f) Preparation of 2,5-bis(1,1,2,2-tetramethyldisilanyl)-3,4-ethylenedioxythiophene (13).

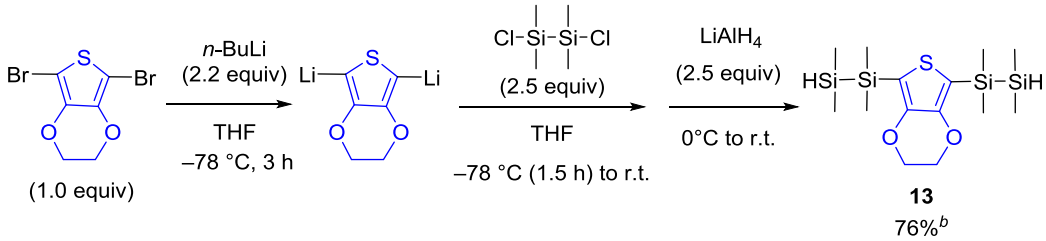

Under an argon atmosphere, a solution of 1.6 M *n*-BuLi in hexane (28 mL, 44 mmol) was added to a solution of 2,5-dibromo-3,4-ethylenedioxythiophene (6.00 g, 20 mmol) in THF (100 mL) at −78 °C for 20 min, and reaction mixture was stirred at −78 °C for 3 h to give dilithiated reagent. This solution of dilithiated reagent was added slowly to a solution of 1,2-dichloro-1,1,2,2-tetramethyldisilane (9.0 mL, 51 mmol) in THF (200 mL) at −78 °C for 1.5 h, then the reaction mixture was warmed to room temperature. The mixture was cooled to 0 °C, and $LiAlH_4$ (1.96 g, 50 mmol) was added. The reaction mixture was warmed to room temperature and stirred overnight. The reaction mixture was quenched with water and extracted with diethyl ether three times. The organic layer was washed with brine and dried over sodium sulfate. The solvent was evaporated under a reduced pressure, and residue was purified by column chromatography on silica gel (eluent: hexane) to give **13** (5.72 g, 15 mmol) as colorless oil in 76% yield.

2,5-bis(1,1,2,2-tetramethyldisilanyl)-3,4-ethylenedioxythiophene (13): Isolated yield: 76%. Colorless oil. ^{1}H NMR (500 MHz, $CDCl_3$) δ 4.14 (s, 4H), 3.73 (septet, 2H, *J* = 4.5 Hz), 0.36 (s, 12H), 0.16 (d, 12H, *J* = 4.4 Hz). ^{13}C NMR (125 MHz, $CDCl_3$) δ 148.0 (C_q), 116.0 (C_q), 64.3 (CH_2), −3.1 (CH_3), −6.4 (CH_3). FAB-MS *m/z* 373 ($[M-H]^+$). FAB-HRMS Calcd for $C_{14}H_{29}O_2Si_4S$: 373.0966. Found: 373.0971 ($[M-H]^+$).

(g) Preparation of 5,5'-bis(1,1,2,2-tetramethyldisilanyl)-2,2'-bithiophene (14).

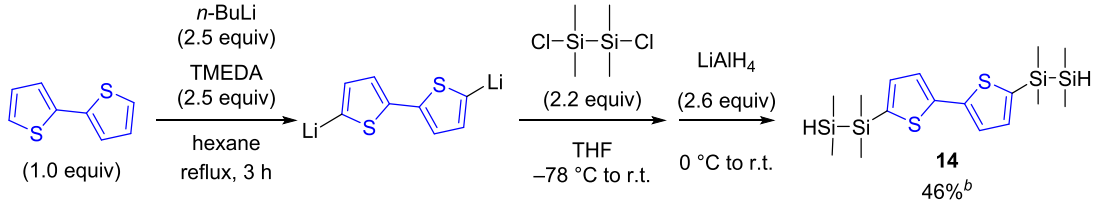

Under an argon atmosphere, a solution of 1.6 M *n*-BuLi in hexane (24 mL, 38 mmol) was added to a solution of 2,2'-bithiophene (2.50 g, 15 mmol), distilled tetramethylethylenediamine (TMEDA) (5.6 mL, 37.5 mmol) in hexane (100 mL) at 0 °C, and the reaction mixture was refluxed for 3 h to give dilithiated reagent. This solution of the dilithiated reagent in hexane was added slowly to a solution of 1,2-dichloro-1,1,2,2-tetramethyldisilane (5.90 mL, 33 mmol) in THF (100 mL) at −78 °C for 50 min, then the reaction mixture was warmed to room temperature. The mixture was cooled to 0 °C, and $LiAlH_4$ (1.48 g, 39 mmol) was added. The reaction mixture was warmed to room temperature and stirred overnight. The reaction mixture was quenched with water and extracted with diethyl ether three times. The organic layer was washed with brine and dried over sodium sulfate. The solvent was evaporated under a reduced pressure, and residue purified by column chromatography on silica gel (eluent: hexane) to give **14** (2.73 g, 6.8 mmol) as colorless oil in 46% yield.

5,5'-bis(1,1,2,2-tetramethyldisilanyl)-2,2'-bithiophene (14): Isolated yield: 46%. Colorless oil. ^{1}H NMR (500 MHz, $CDCl_3$) δ 7.24 (d, 2H, *J* = 3.5 Hz), 7.09 (d, 2H, *J* = 3.5 Hz), 3.76 (septet, 2H, *J* = 4.5 Hz), 0.41 (s, 12H), 0.17 (d, 12H, *J* = 4.7 Hz). ^{13}C NMR (125 MHz, $CDCl_3$) δ 142.6 (C_q), 138.1 (C_q), 135.0 (CH), 125.1 (CH), −2.4 (CH_3), −6.7 (CH_3). FAB-MS *m/z* 397 ($[M-H]^+$). FAB-HRMS Calcd for $C_{16}H_{29}O_2Si_4S_2$: 397.0788. Found: 397.0789 ($[M-H]^+$).

(h) A typical experimental procedure for the preparation of 15−20.

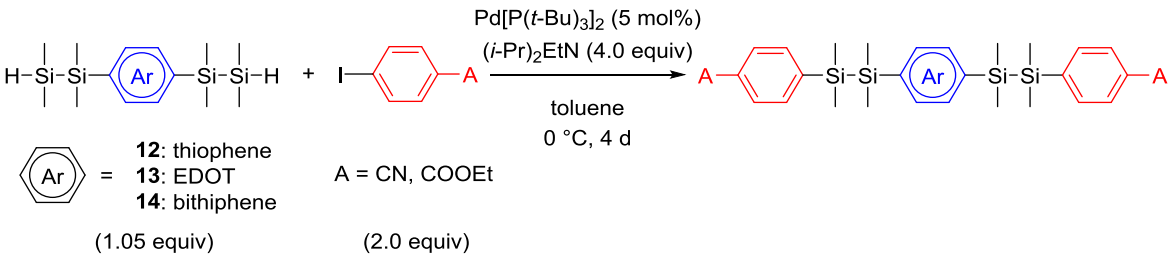

Under an argon atmosphere, to a solution of 4-iodobenzonitrile (458 mg, 2.0 mmol)

and Pd[P(*t*-Bu)$_3$]$_2$ (25.6 mg, 0.050 mmol) in toluene (7.5 mL) was added *N*,*N*-diisopropylethylamine (0.80 mL, 4.1 mmol) and **12** (333 μL, 1.05 mmol) at 0 °C for 4 d. The reaction mixture was quenched with water and extracted with CH_2Cl_2 three times. The combined organic layer was washed with brine and dried over sodium sulfate. The solvent was evaporated under a reduced pressure, and residue was purified by column chromatography on silica gel (eluent: hexane/ethyl acetate = 5/1) and HPLC with a GPC column (solvent: $CHCl_3$) to afford roughly purified **15** (62.3 mg, 0.12 mmol). This product was recrystallized with hexane and ethyl acetate to give **15** (38.3 mg, 0.074 mmol) as colorless solid in 7.4% yield.

4,4'-[thiophene-2,5-diylbis(1,1,2,2-tetramethyldisilane-2,1-diyl)]dibenzonitrile (15): Isolated yield after recrystallization from hexane/ethyl acetate: 7.4%, NMR yield: 12%. Colorless solid. Mp: 139.5−141.0 °C. ^{1}H NMR (500 MHz, $CDCl_3$) δ 7.54 (d, 4H, *J* = 8.3 Hz), 7.44 (d, 4H, *J* = 8.1 Hz), 7.12 (s, 2H), 0.37 (s, 12H), 0.35 (s, 12H). ^{13}C NMR (125 MHz, $CDCl_3$) δ 146.1 (C_q), 143.6 (C_q), 135.6 (CH), 134.2 (CH), 130.8 (CH), 119.1 (C_q), 112.0 (C_q), −2.7 (CH_3), −4.4 (CH_3). FAB-MS *m/z* 519 ([M+H]$^+$). FAB-HRMS Calcd for $C_{26}H_{35}N_2SSi_4$: 519.1598. Found: 519.1617 ([M+H]$^+$).

Diethyl 4,4'-[thiophene-2,5-diylbis(1,1,2,2-tetramethyldisilane-2,1-diyl)]dibenzoate (16): Isolated yield after recrystallization from acetonitrile: 1.2%, NMR yield: 19%. Colorless solid. Mp: 95.0−95.6 °C. ^{1}H NMR (500 MHz, $CDCl_3$) δ 7.95 (d, 4H, *J* = 8.2 Hz), 7.44 (d, 4H, *J* = 8.2 Hz), 7.13 (s, 2H), 4.73 (q, 4H, *J* = 7.1 Hz), 1.38 (t, 6H, *J* = 7.3 Hz), 0.37 (s, 12H), 0.34 (s, 12H). ^{13}C NMR (125 MHz, $CDCl_3$) δ 166.8 (C_q), 145.3 (C_q), 143.9 (C_q), 135.5 (CH), 133.8 (CH), 130.4 (C_q), 128.4 (CH), 60.9 (CH_2), 14.4 (CH_3), −2.6 (CH_3), −4.3 (CH_3). FAB-MS *m/z* 613 ([M+H]$^+$). FAB-HRMS Calcd for $C_{30}H_{45}O_4SSi_4$: 613.2116. Found: 613.2120 ([M+H]$^+$).

4,4'-[(3,4-ethylenedioxythiophene-2,5-diyl)bis(1,1,2,2-tetramethyldisilane-2,1-diyl)]dibenzonitrile (17): Isolated yield: 10%. Colorless oil. ^{1}H NMR (500 MHz, $CDCl_3$) δ 7.54 (d, 4H, *J* = 8.2 Hz), 7.48 (d, 4H, *J* = 8.5 Hz), 3.96 (s, 4H), 0.38 (s, 12H), 0.30 (s, 12H). ^{13}C NMR (125 MHz, $CDCl_3$) δ 148.0 (C_q), 146.9 (C_q), 134.3 (CH), 130.7 (CH), 119.2 (C_q), 115.5 (C_q), 111.8 (C_q), 64.1 (CH_2), −3.6 (CH_3), −4.1 (CH_3). FAB-MS *m/z* 577 ([M+H]$^+$). FAB-HRMS Calcd for $C_{28}H_{37}N_2O_2SSi_4$: 577.1654. Found: 577.1649 ([M+H]$^+$).

Diethyl 3,4'-[(3,4-ethylenedioxythiophene-2,5-diyl)bis(1,1,2,2-tetramethyldisilane-2,1-diyl)]dibenzoate (18): Isolated yield: 12%. Colorless solid. Mp: 76.0−77.7 °C. ^{1}H NMR (500 MHz, $CDCl_3$) δ 7.94 (d, 4H, *J* = 8.2 Hz), 7.47 (d, 4H, *J* = 8.2 Hz), 4.36 (q, 4H, *J* = 7.1 Hz), 3.96 (s, 4H), 1.38 (t, 6H, *J* = 7.3 Hz), 0.37 (s, 12H), 0.29 (s, 12H). ^{13}C NMR (125 MHz, $CDCl_3$) δ

166.9 (C_q), 146.1 (C_q), 133.8 (CH), 130.2 (C_q), 128.2 (CH), 115.7 (C_q), 60.8 (CH_2), 14.4 (CH_3), −3.5 (CH_3), −3.9 (CH_3). FAB-MS *m/z* 671 ($[M+H]^+$). FAB-HRMS Calcd for $C_{32}H_{47}O_6SSi_4$: 671.2170. Found: 671.2144 ($[M+H]^+$).

4,4'-[(2,2'-bithiophene)-5,5'-diylbis(1,1,2,2-tetramethyldisilane-2,1-diyl)]dibenzonitrile (19): Isolated yield after recrystallization from acetonitrile: 1.7%, NMR yield: 13%. Colorless solid. Mp: 167.8−169.0 °C. ^{1}H NMR (500 MHz, $CDCl_3$) δ 7.57 (d, 4H, *J* = 8.2 Hz), 7.48 (d, 4H, *J* = 8.1 Hz), 7.20 (d, 2H, *J* = 3.5 Hz), 6.97 (d, 2H, *J* = 3.5 Hz), 0.41 (s, 12H), 0.37 (s, 12H). ^{13}C NMR (125 MHz, $CDCl_3$) δ 145.9 (C_q), 142.7 (C_q), 137.1 (C_q), 135.4 (CH), 134.3 (CH), 130.9 (CH), 125.3 (CH), 119.0 (C_q), 112.2 (C_q), −2.9 (CH_3), −4.4 (CH_3). FAB-MS *m/z* 601 ($[M+H]^+$). FAB-HRMS Calcd for $C_{30}H_{37}N_2S_2Si_4$: 601.1475. Found: 601.1462 ($[M+H]^+$).

Diethyl 4,4'-[(2,2'-bithiophene)-5,5'-diylbis(1,1,2,2-tetramethyldisilane-2,1-diyl)]dibenzoate (20): Colorless solid. Isolated yield after recrystallization from hexane: 6.4%. NMR yield: 13%. Mp: 131.8−135.0 °C. ^{1}H NMR (500 MHz, $CDCl_3$) δ 7.98 (d, 4H, *J* = 8.2 Hz), 7.49 (d, 4H, *J* = 8.2 Hz), 7.20 (d, 2H, *J* = 3.5 Hz), 6.96 (d, 2H, *J* = 3.5 Hz), 4.38 (q, 4H, *J* = 7.1 Hz), 1.39 (t, 6H, *J* = 7.1 Hz), 0.41 (s, 12H), 0.35 (s, 12H). ^{13}C NMR (125 MHz, $CDCl_3$) δ 166.9 (C_q), 145.1 (C_q), 142.7 (C_q), 137.5 (C_q), 135.3 (CH), 133.8 (CH), 130.5 (C_q), 128.5 (CH), 125.2 (CH), 60.9 (CH_2), 14.4 (CH_3), −2.8 (CH_3), −4.2 (CH_3). FAB-MS *m/z* 695 ($[M+H]^+$). Elemental analysis Calcd (%) for $C_{34}H_{46}O_4S_2Si_4$: C 58.74, H 6.67. Found: C 58.55, H 6.66.

2.3.3 Crystallographic data

Table 2.3.1. Selected crystallographic data of **7**

Empirical formula	$C_{30}H_{46}N_4SSi_4$
Fw / g mol^{-1}	607.12
Crystal system	monoclinic
Space group	*C*2/c
Crystal size / mm	0.140 × 0.020 × 0.015
Temperature / K	100
a / Å	34.168(3)
b / Å	6.4994(4)
c / Å	31.642(2)
α / °	90
β / °	103.018(8)
γ / °	90
V / Å^3	6846.2(8)
Z	8
D_{calcd} / g cm^{-3}	1.178
λ / Å	0.35400
μ / mm^{-1}	0.052
Reflections collected	46287
Independent reflections	7865
Parameters	352
R_{int}	0.1596
R_1 ($I > 2.00\sigma(I)$) [a]	0.0644
wR_2 (All reflections) [b]	0.1807
GoF [c]	1.045

[a] $R_1 = \Sigma||Fo| - |Fc||/\Sigma|Fo|$ ($I > 2\sigma(I)$). [b] $wR_2 = [\Sigma(w(Fo^2 - Fc^2)^2/\Sigma w(Fo^2)^2]^{1/2}$ ($I > 2\sigma(I)$). [c] GoF = $[\Sigma(w(Fo^2 - Fc^2)^2/\Sigma(Nr - Np)^2]$

Table 2.3.2. Selected bond lengths, angles, and torsion angles of **7**

Bond lengths / Å	
Si2–Si3	2.3395(13)
Si4–Si5	2.3399(14)
Si2–C30	1.878(5)
Si2–C31	1.872(5)
Si2–C32	1.876(4)
Si3−C25	1.890(4)
Si3−C28	1.875(5)
Si3−C29	1.868(5)
Si4−C20	1.874(5)
Si4−C21	1.859(5)
Si4−C22	1.892(4)
Si5−C15	1.878(4)
Si5−C18	1.880(5)
Si5−C19	1.867(5)
Angles / °	
Si2−Si3−C25	110.26(11)
Si3−Si2−C32	109.16(11)
Si4−Si5−C15	108.52(13)
Si5−Si4−C22	107.54(11)
Torsion angles / °	
C32−Si2−Si3−C25	−175.50(13)
C22−Si4−Si5−C15	−177.44(13)

Table 2.3.3. Selected crystallographic data of **9**

Empirical formula	$C_{30}H_{44}N_2O_2SSi_4$
Fw / g mol^{-1}	609.09
Crystal system	triclinic
Space group	$P-1$
Crystal size / mm	0.560 × 0.490 × 0.130
Temperature / K	133
a / Å	8.020(7)
b / Å	10.182(9)
c / Å	22.21(2)
α / º	97.39(2)
β / º	99.248(13)
γ / º	105.101(11)
V / Å^3	1700(3)
Z	2
D_{calcd} / g cm^{-3}	1.190
λ / Å	0.71070
μ / mm^{-1}	0.141
Reflections collected	11011
Independent reflections	5855
Parameters	352
R_{int}	0.0519
R_1 ($I > 2.00\sigma$ (I)) [a]	0.0539
wR_2 (All reflections) [b]	0.1438
GoF [c]	1.064

[a] $R_1 = \Sigma||Fo| - |Fc||/\Sigma|Fo|$ ($I > 2\sigma$ (I)). [b] $wR_2 = [\Sigma(w(Fo^2 - Fc^2)^2/\Sigma w(Fo^2)^2]^{1/2}$ ($I > 2\sigma$ (I)). [c] GoF = $[\Sigma(w(Fo^2 - Fc^2)^2/\Sigma(Nr - Np)^2]$

Table 2.3.4. Selected bond lengths, angles, and torsion angles of **9**

Bond lengths / Å	
Si2−Si4	2.371(3)
Si3−Si5	2.349(2)
Si2−C18	1.881(4)
Si2−C35	1.883(4)
Si2−C39	1.870(4)
Si3−C12	1.876(4)
Si3−C15	1.871(4)
Si3−C30	1.877(3)
Si4−C16	1.874(4)
Si4−C21	1.881(3)
Si4−C27	1.868(4)
Si5−C11	1.878(4)
Si5−C23	1.876(3)
Si5−C29	1.886(4)
Angles / °	
Si2−Si4−C16	104.21(12)
Si4−Si2−C18	108.98(11)
Si3−Si5−C11	107.21(13)
Si5−Si3−C12	105.87(12)
Torsion angles / °	
C18−Si2−Si4−C16	110.07(13)
C12−Si3−Si5−C11	168.33(10)

Table 2.3.5. Selected crystallographic data of **16**

Empirical formula	$C_{30}H_{44}O_4SSi_4$
Fw / g mol^{-1}	613.08
Crystal system	monoclinic
Space group	$C2/c$
Crystal size / mm	0.450 × 0.200 × 0.050
Temperature / K	133
a / Å	40.78(2)
b / Å	12.358(6)
c / Å	6.643(3)
α / º	90
β / º	93.208(6)
γ / º	90
V / Å^3	3343(3)
Z	4
D_{calcd} / g cm^{-3}	1.218
λ / Å	0.71070
μ / mm^{-1}	0.141
Reflections collected	12013
Independent reflections	3810
Parameters	177
R_{int}	0.0512
R_1 ($I > 2.00\sigma$ (I)) [a]	0.0534
wR_2 (All reflections) [b]	0.1169
GoF [c]	1.075

[a] $R_1 = \Sigma||Fo| - |Fc||/\Sigma|Fo|$ ($I > 2\sigma$ (I)). [b] $wR_2 = [\Sigma(w(Fo^2 - Fc^2)^2/\Sigma w(Fo^2)^2]^{1/2}$ ($I > 2\sigma$ (I)). [c] GoF = $[\Sigma(w(Fo^2 - Fc^2)^2/\Sigma(Nr - Np)^2]$

Table 2.3.6. Selected bond lengths, angles, and torsion angles of **16**

Bond lengths / Å	
Si2−Si3	2.3388(12)
Si2−C7	1.881(3)
Si2−C16	1.864(3)
Si2−C19	1.875(3)
Si3−C9	1.867(3)
Si3−C15	1.870(3)
Si3−C17	1.863(3)
Angles / °	
Si2−Si3−C15	108.53(8)
Si3−Si2−C7	106.98(8)
Torsion angle / °	
C7−Si2−Si3−C15	171.07(8)

Table 2.3.7. Selected crystallographic data of **20**

Empirical formula	$C_{34}H_{46}O_4S_2Si_4$
Fw / g mol^{-1}	695.20
Crystal system	monoclinic
Space group	$P2_1/c$
Crystal size / mm	0.328 × 0.072 × 0.042
Temperature / K	113
a / Å	22.553(10)
b / Å	12.270(5)
c / Å	6.730(3)
α / º	90
β / º	92.726(4)
γ / º	90
V / Å^3	1860.2(13)
Z	2
D_{calcd} / g cm^{-3}	1.241
λ / Å	0.71070
μ / mm^{-1}	0.141
Reflections collected	14328
Independent reflections	4241
Parameters	177
R_{int}	0.0689
R_1 ($I > 2.00\sigma$ (I)) [a]	0.0739
wR_2 (All reflections) [b]	0.1835
GoF [c]	1.106

[a] $R_1 = \Sigma||Fo| - |Fc||/\Sigma|Fo|$ ($I > 2\sigma$ (I)). [b] $wR_2 = [\Sigma(w(Fo^2 - Fc^2)^2/\Sigma w(Fo^2)^2]^{1/2}$ ($I > 2\sigma$ (I)). [c] GoF = $[\Sigma(w(Fo^2 - Fc^2)^2/\Sigma(Nr - Np)^2]$

Table 2.3.8. Selected bond lengths, angles, and torsion angles of **20**

Bond lengths / Å	
Si1−Si2	2.3475(15)
Si1−C4	1.878(4)
Si1−C5	1.873(4)
Si1−C6	1.878(4)
Si2−C7	1.874(4)
Si2−C8	1.873(4)
Si2−C9	1.885(4)
Angles / °	
Si2−Si1−C4	108.07(12)
Si1−Si2−C9	107.19(12)
Torsion angle / °	
C4−Si1−Si2−C9	173.47(12)

2.3.4 Optical properties of **6−11** and **15−20**

(a) UV–vis absorption and fluorescence spectra of 6−11 and 15−20

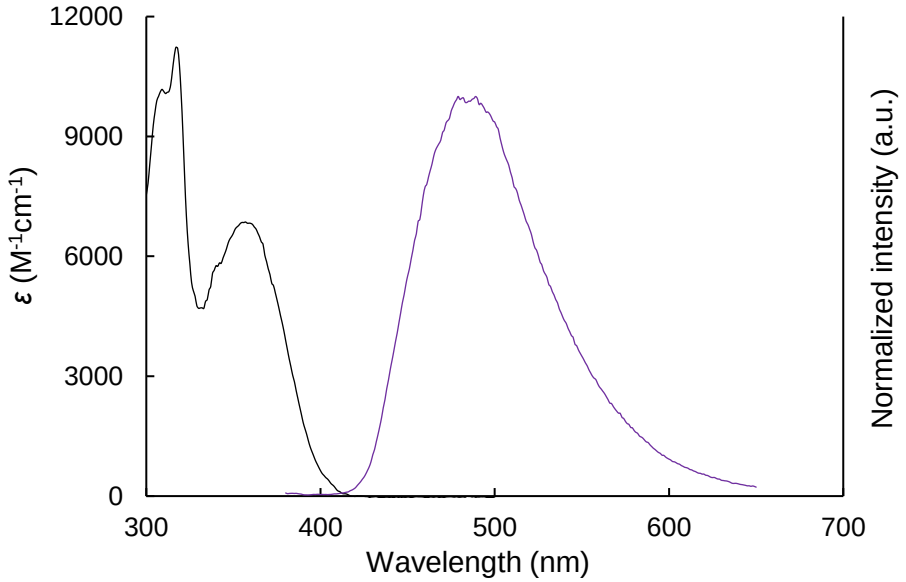

Figure 2.3.1. UV–vis absorption spectrum of **6** in cyclohexane (black line) and fluorescence spectrum of **6** in the solid state (purple line, excited at 370 nm).

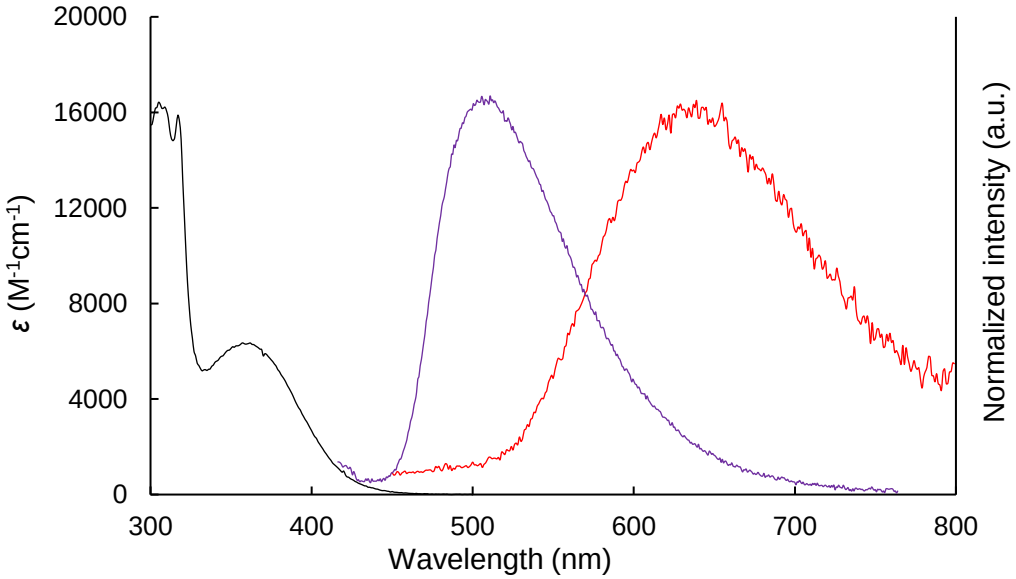

Figure 2.3.2. UV–vis absorption spectrum of **7** in dichloromethane (black line), fluorescence spectrum of **7** in dichloromethane (red line, excited at 357 nm), and fluorescence spectrum of **7** in the solid state (purple line, excited at 421 nm).

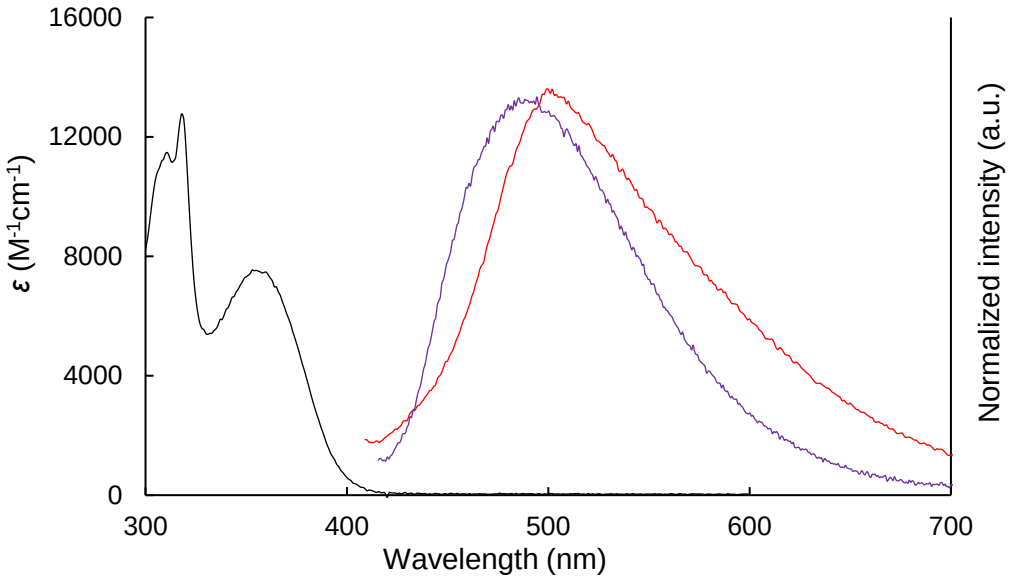

Figure 2.3.3. UV–vis absorption spectrum of **8** in dichloromethane (black line), fluorescence spectrum of **8** in dichloromethane (red line, excited at 353 nm), and fluorescence spectrum of **8** in the solid state (purple line, excited at 371 nm).

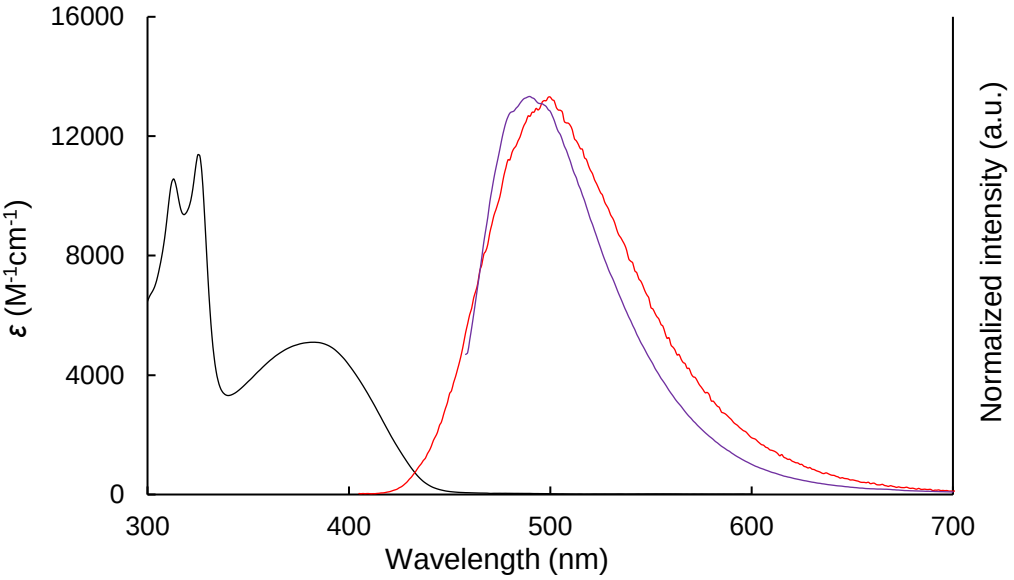

Figure 2.3.4. UV–vis absorption spectrum of **9** in dichloromethane (black line), fluorescence spectrum of **9** in dichloromethane (red line, excited at 383 nm), and fluorescence spectrum of **9** in the solid state (purple line, excited at 442 nm).

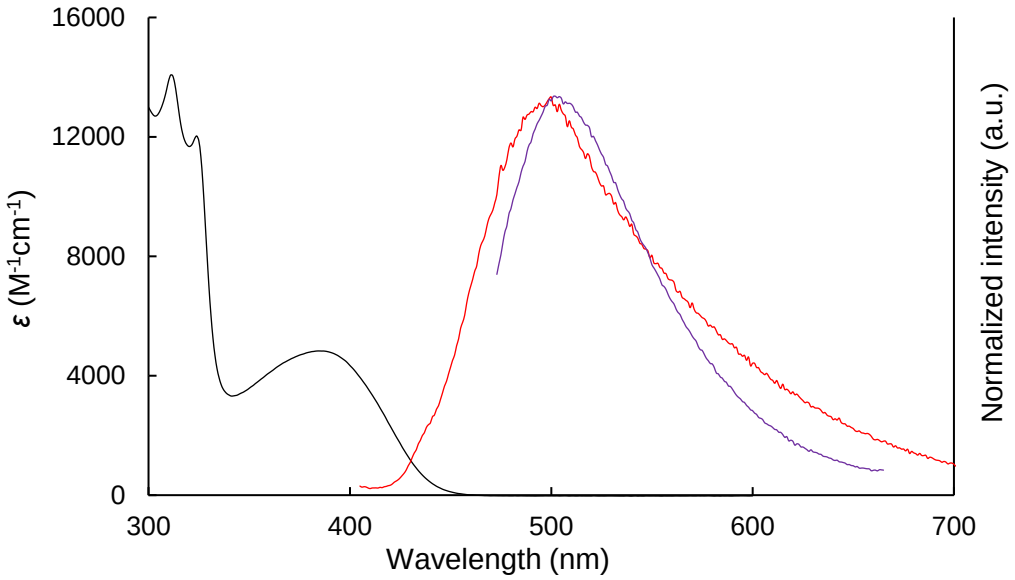

Figure 2.3.5. UV–vis absorption spectrum of **10** in dichloromethane (black line), fluorescence spectrum of **10** in dichloromethane (red line, excited at 384 nm), and fluorescence spectrum of **10** in the solid state (purple line, excited at 450 nm).

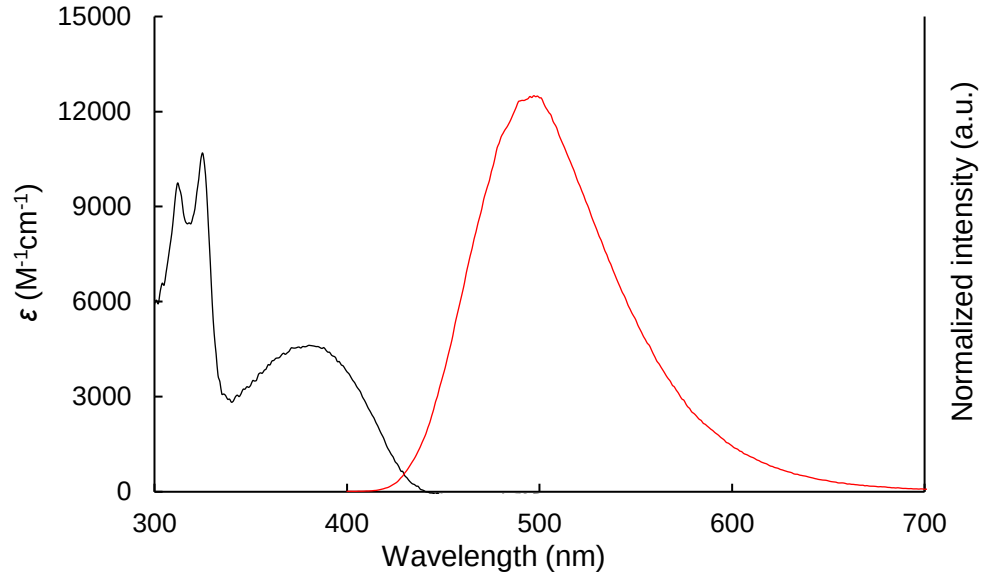

Figure 2.3.6. UV–vis absorption spectrum of **11** in dichloromethane (black line) and fluorescence spectrum of **11** in dichloromethane (red line, excited at 380 nm).

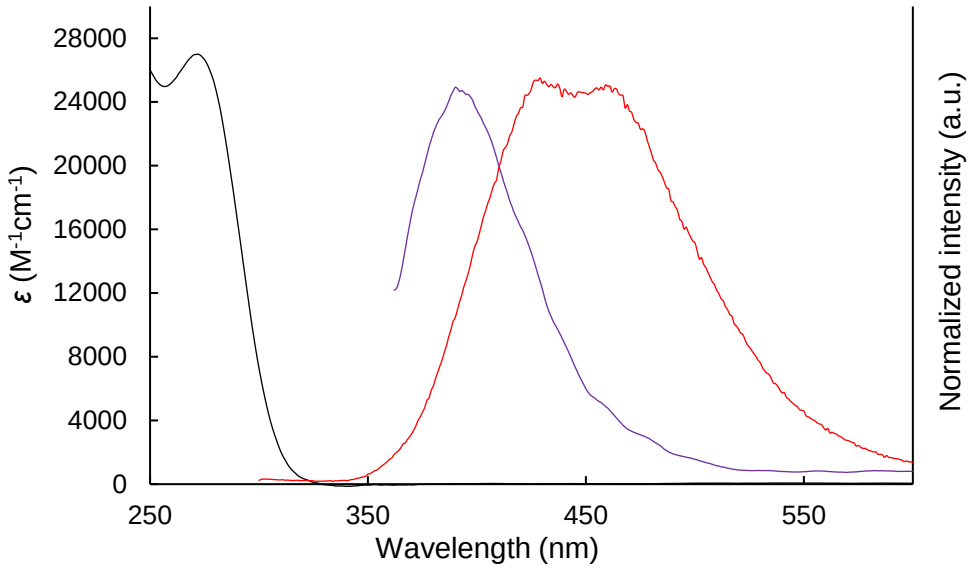

Figure 2.3.7. UV–vis absorption spectrum of **15** in dichloromethane (black line), fluorescence spectrum of **15** in dichloromethane (red line, excited at 272 nm), and fluorescence spectrum of **15** in the solid state (purple line, excited at 342 nm).

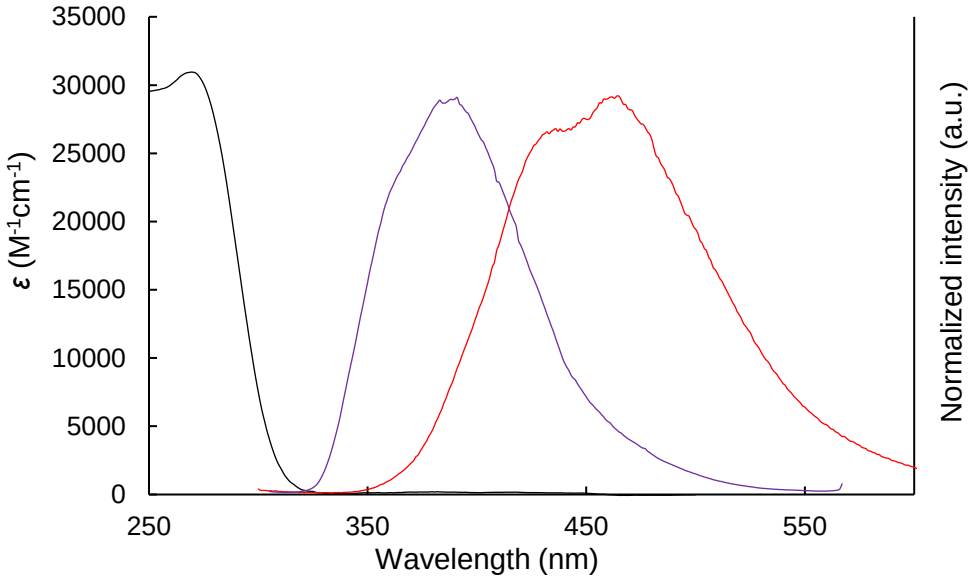

Figure 2.3.8. UV–vis absorption spectrum of **16** in dichloromethane (black line), fluorescence spectrum of **16** in dichloromethane (red line, excited at 272 nm), and fluorescence spectrum of **16** in the solid state (purple line, excited at 287 nm).

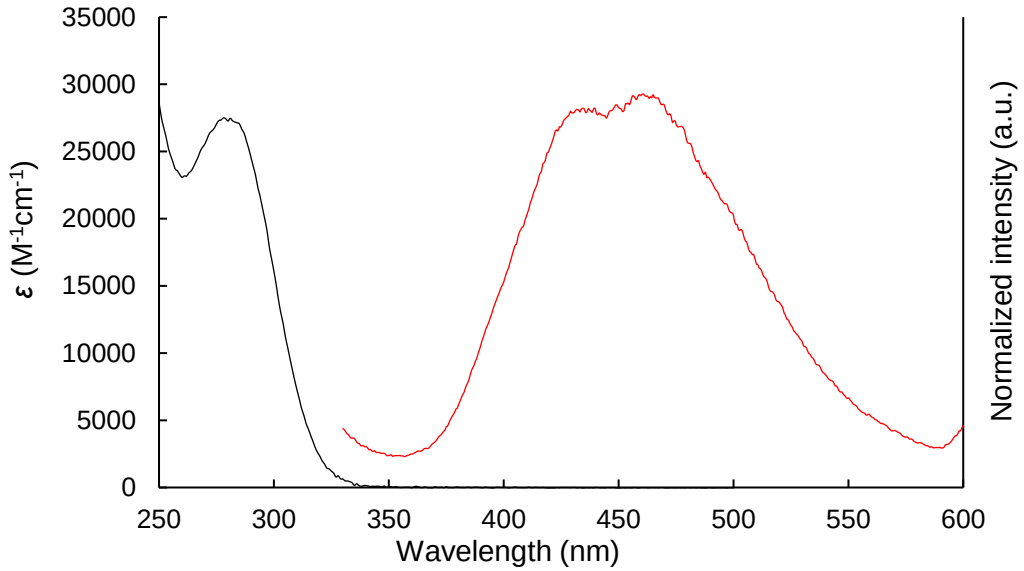

Figure 2.3.9. UV–vis absorption spectrum of **17** in dichloromethane (black line) and fluorescence spectrum of **17** in dichloromethane (red line, excited at 278 nm).

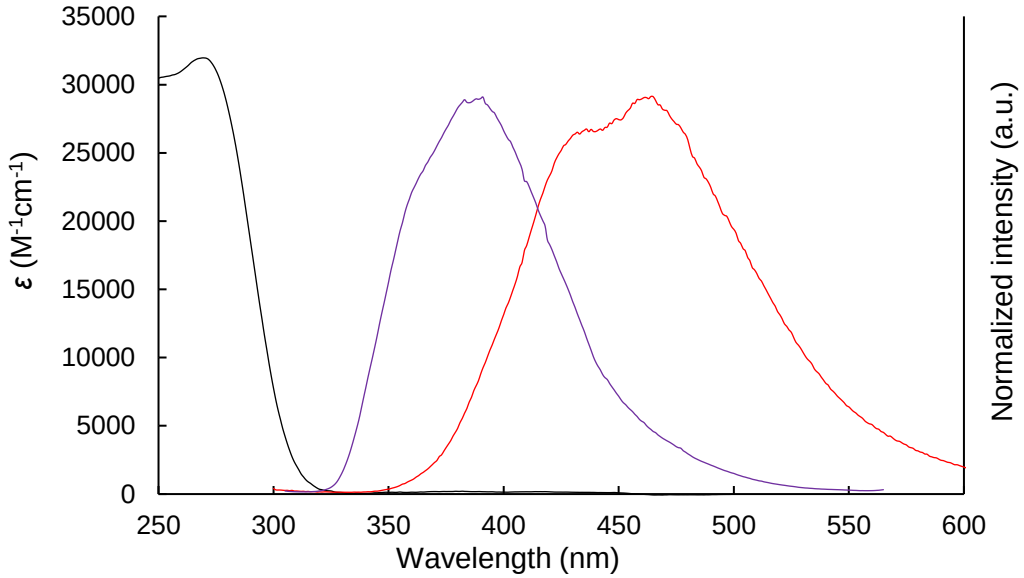

Figure 2.3.10. UV–vis absorption spectrum of **18** in dichloromethane (black line), fluorescence spectrum of **18** in dichloromethane (red line, excited at 280 nm), and fluorescence spectrum of **18** in the solid state (purple line, excited at 329 nm).

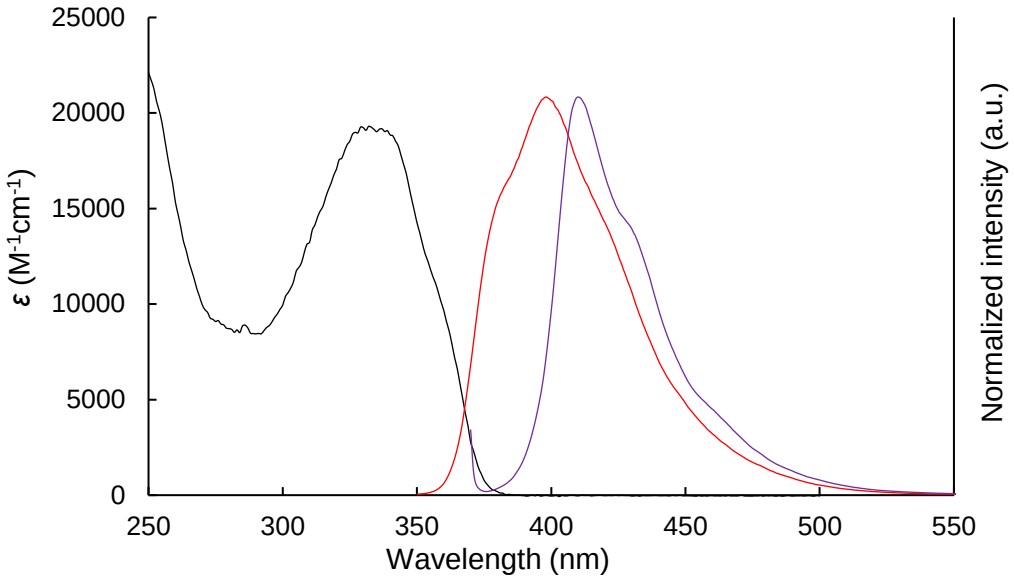

Figure 2.3.11. UV–vis absorption spectrum of **19** in dichloromethane (black line), fluorescence spectrum of **19** in dichloromethane (red line, excited at 332 nm), and fluorescence spectrum of **19** in the solid state (purple line, excited at 365 nm).

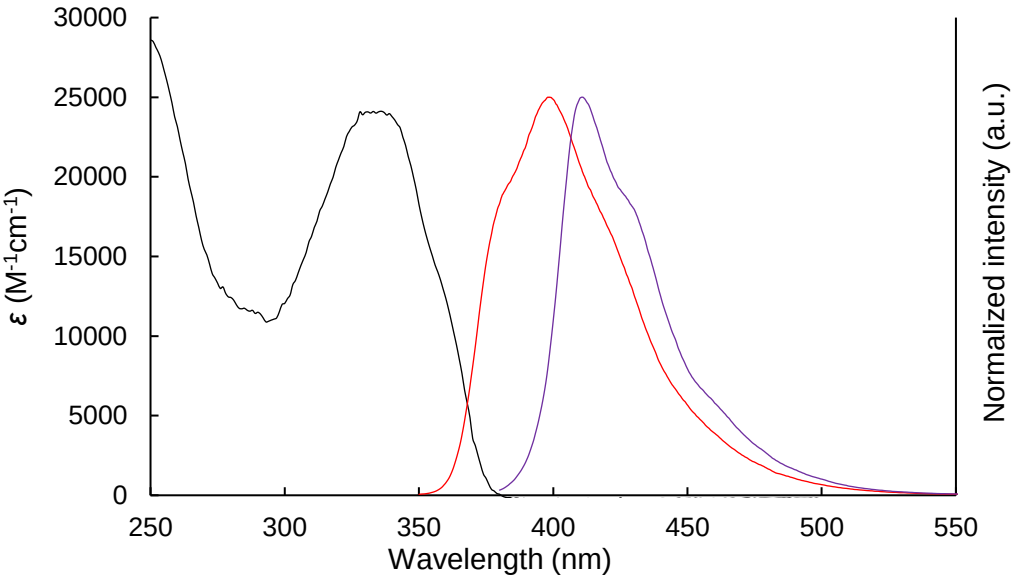

Figure 2.3.12. UV–vis absorption spectrum of **20** in dichloromethane (black line), fluorescence spectrum of **20** in dichloromethane (red line, excited at 334 nm), and fluorescence spectrum of **20** in the solid state (purple line, excited at 370 nm).

(b) UV–vis absorption and fluorescence spectra of 7 and 10 in CH_2Cl_2 and acetone

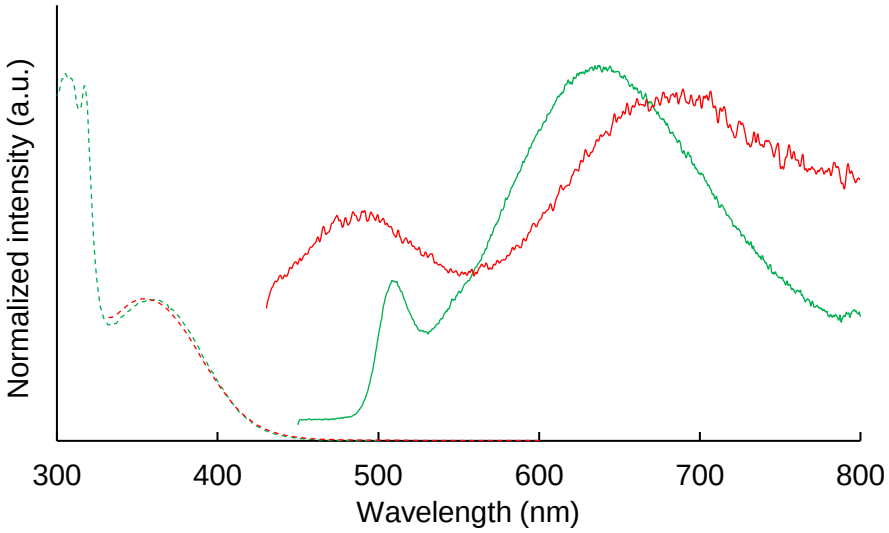

Figure 2.3.13. UV–vis absorption spectrum of **7** in dichloromethane (green dashed line) and in acetone (red dashed line), and fluorescence spectrum of **7** in dichloromethane (green solid line, excited at 357 nm) and in acetone (red solid line, excited at 356 nm).

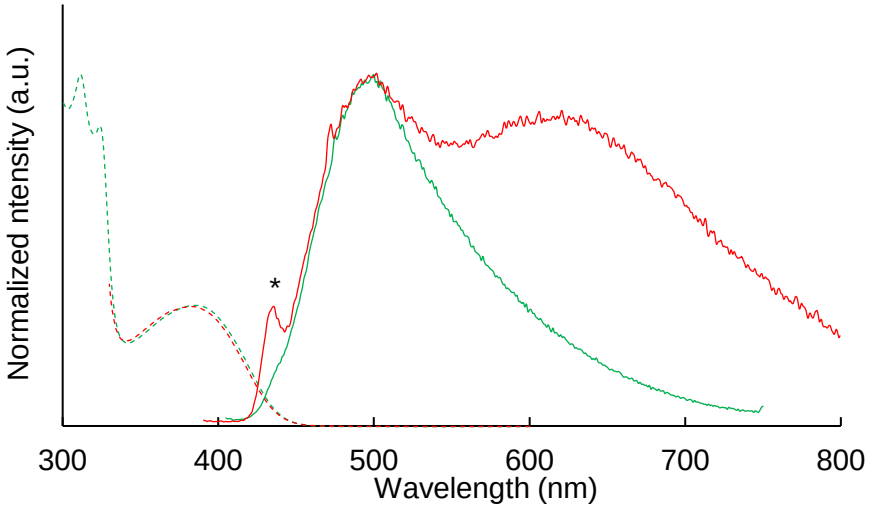

Figure 2.3.14. UV–vis absorption spectrum of **10** in dichloromethane (green dashed line) and in acetone (red dashed line), and fluorescence spectrum of **10** in dichloromethane (green solid line, excited at 357 nm) and in acetone (red solid line, excited at 356 nm). A peak denoted with an asterisk is due to Raman scatting of solvent.

(c) UV–vis absorption and fluorescence spectra of 9 in several solvents

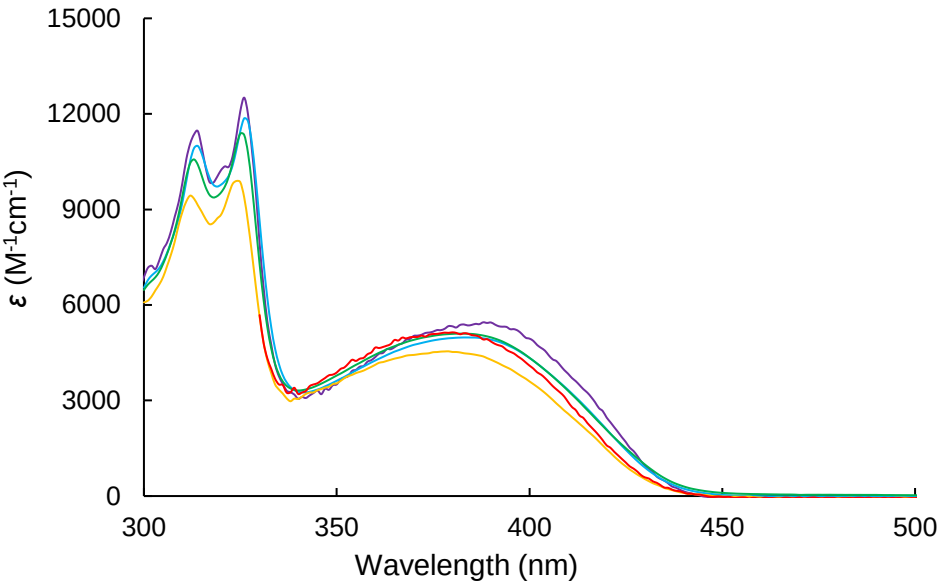

Figure 2.3.15. UV–vis absorption spectra of **9** in cyclohexane (purple line), toluene (blue line), dichloromethane (green line), THF (orange line), and acetone (red line).

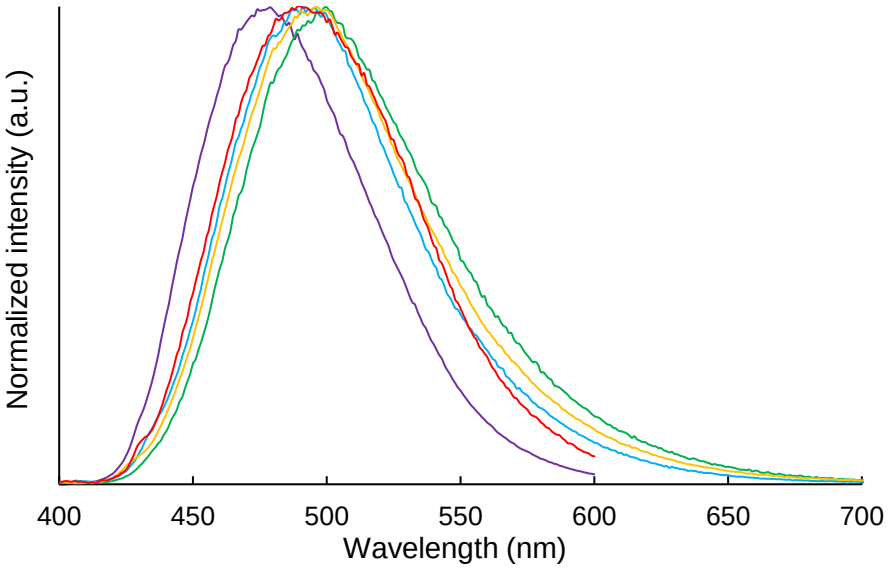

Figure 2.3.16. Fluorescence spectra of **9** in cyclohexane (purple line, excited at 380 nm), toluene (blue line, excited at 383 nm), dichloromethane (green line, excited at 383 nm), THF (orange line, excited at 378 nm), and acetone (red line, excited at 380 nm).

2.4 Summary

A series of disilane-bridged donor−acceptor−donor triads **6**−**11** and acceptor−donor−acceptor triads **15**−**20** were synthesized in acceptable to moderate yields systematically by means of Pd-catalyzed coupling reaction of hydrosilanes with aryl diiodes as a key step. They displayed unique UV–vis absorption and fluorescence properties. They displayed broad UV–vis absorption bands in around UV to visible region assignable to ICT transition (**6**−**8**, **10** and **15**−**18**), the combination of ICT transition and π–π* transition (**9**, **11**) or mere π–π* transition (**19**, **20**) according to DFT and TD-DFT calculation. D−A−D compounds displayed very weak green-colored fluorescence in the solution state (quantum yield: up to Φ = 0.08) but very strong fluorescence in the solid state (up to Φ = 0.85) due to reducing the non-radiative (e.g. vibration or rotation) quenching process by aggregation effect. A−D−A compounds showed blue-colored emission in solution phase with low to moderate quantum yields (up to Φ = 0.40) and strong emission in the solid state (up to Φ = 0.77). Single crystal X-ray diffraction revealed that the crystal structure of **7**, **9**, **16**, and **20** had no intermolecular π–π stacking which leads to quenching emission in the solid state owing to the steric hindrance of disiane units.

These compounds are expected to be used for the fluorescence probes and organic electroluminescence devices, because they have strong emissive properties without quenching emission in the aggregated condition owing to avoiding π–π stacking.

2.5 References

1. (a) Zhang, J.; Chen, W.; Rojas, J. A.; Jucov, V. E.; Timofeeva, V. E.; Parker, C. T.; Barlow, S.; Marder, R. S. *J. Am. Chem. Soc.* **2013**, *135*, 16376–16379.
   (b) Kim, M. H.; Cho, R. B. *Chem. Commun*. **2009**, *2*, 153–164.
   (c) Chen, L.; Wang, L.; Jing, X. *J. Mater. Chem.* **2011**, *21*, 10265–10267.
   (d) Liu, Y.; Zhou, J.; Wan, X.; Chen, Y.; *Tetrahedron* **2009**, *65*, 5209–5215.
2. (a) Moss, K. C.; Bourdakos, K. N.; Bhalla, V.; Kamtekar, K. T.; Bryce, M. R.; Fox, M. A.; Vaughan, H. L.; Dias, F. B.; Monkman, A. P. *J. Org. Chem*. **2010**, *75*, 6771–6781.
   (b) Hayashi, M.; Toshimitsu, F.; Sakamoto, R.; Nishihara, H. *J. Am. Chem. Soc.* **2011**, *133*, 14518–14521.
3. (a) Li, H.-J.; Fu, W.-F.; Li, L.; Gan, X.; Mu, W.-H.; Chen, W.-Q.; Duan, X.-M.; Song, H.-B. *Org. Lett.* **2010**, *12*, 2924–2927.
   (b) He, G. S.; Tan, L.-S.; Zheng, Q.; Prasad, P. N. *Chem. Rev*. **2008**, *108*, 1245−1330.
   (c) Susumu, K.; Fisher, J. A. N.; Zheng, J.; Beratan, D. N.; Yodh, A. G.; Therien, M. J. *J. Phys. Chem. A* **2011**, *115*, 5525−5539.
4. (a) Lee, S. Y.; Yasuda, T.; Yang, Y. S.; Zhang, Q.; Adachi, C. *Angew. Chem*. *Int. Ed.* **2014**, *53*, 6402–6406.
   (b) Grimsdale, A. C.; Chan, K. L.; Martin, R. E.; Jokisz, P. G.; Holmes, A. B. *Chem. Rev.* **2009**, *109*, 897−1091.
   (c) Xiao, L.; Chen, Z.; Qu, B.; Luo, J.; Kong, S.; Cong, Q.; Kido, J. *Adv. Mater.* **2011**, *23*, 926−952.
   (d) Li, D.; Zhang, H.; Wang, Y. *Chem. Soc. Rev.* **2013**, *42*, 8416−8433.
   (e) Anthony, J. E. *Chem. Rev.* **2006**, *106*, 5028−5048.
5. (a) Bai, H.; Wang, Y.; Cheng, P.; Li, Y.; Zhu, D.; Zhan, X. *ACS Appl. Mater. Interfaces* **2014**, *6*, 8426–8433.
   (b) Mercier, L. G.; Mishra, A.; Ishigaki, Y.; Henne, F.; Schulz, G.; Bäuerle, P. *Org. Lett*. **2014**, *16*, 2642–2645.
6. (a) Jiang, T.; Qu, Y.; Li, B.; Gao, Y.; Hua, J. *RSC Adv.* **2015**, *5*, 1500–1506.
   (b) Yao, S.; Ahn, H.-Y.; Wang, X.; Fu, J.; Van Stryland, E. W.; Hagan, D. J.; Belfield, K. D. *J. Org. Chem*. **2010**, *75*, 3965–3974.
   (c) Chongzhao Ran, C.; Xu, X.; Raymond, S. B.; Ferrara, B. J.; Neal, K.; Bacskai, B. J.; Medarova, Z.; Moore, A. *J. Am. Chem. Soc.* **2009**, *131*, 15257–15261.

7. (a) Beddard, G. S.; Porter, G. *Nature* **1976**, *260*, 366–367.
(b) Hong, Y.; Lam, J. W. Y.; Tang, B. Z. *Chem. Commun*. **2009**, *45*, 4332–4353.
(c) Jakubiak, R.; Collison, C. J.; Wan, W. C.; Rothberg, L. J.; Hsieh, B. R. *J. Phys. Chem. A* **1999**, *103*, 2394–2398.
(d) Ooyama, Y.; Okamoto, T.; Yamaguchi, T.; Suzuki, T.; Hayashi, A.; Yoshida, K. *Chem. Eur. J*. **2006**, *12*, 7827–7838.
8. (a) Lesbani, A.; Kondo, H.; Sato, J.-i.; Yamanoi, Y.; Nishihara, H. *Chem. Commun.* **2010**, *46*, 7784−7786.
(b) Inubushi, H.; Hattori, Y.; Yamanoi, Y.; Nishihara, H. *J. Org. Chem.* **2014**, *79*, 2974−2979.
(c) Shimada, M.; Yamanoi, Y.; Matsushita, T.; Kondo, T.; Nishibori, E.; Hatakeyama, A.; Sugimoto, K.; Nishihara, H. *J. Am. Chem. Soc.* **2015**, *137*, 1024−1027.
9. Shimada, M.; Tsuchiya, M.; Sakamoto, R.; Yamanoi, Y.; Nishibori, E.; Sugimoto, K.; Nishihara, H. *Angew. Chem. Int. Ed.* **2016**, *55*, 3022−3026.
10. Therien, J. M.; Susumu. M. *PCT Int. Appl.*, **2007**, WO 2007081991.
11. (a) Abdo, N. I.; El-Shehawy, A. A.; El-Barbary, A. A.; Lee, J.-S. *Eur. J. Org. Chem.* **2012**, 5540–5551.
(b) Lin, L.; Morisaki, Y.; Chujo, Y. *J. Polym. Sci. A* **2009**, *47*, 7003–7011.
12. (a) Cao, C.; Liu, X.; Qiao, Q.; Zhao, M.; Yin, W.; Mao, D.; Zhang, H.; Xu, Z. *Chem. Commun.* **2014**, *50*, 15811–15814.
(b) Sasaki, S.; Drummen. G. P. C.; Konishi. G. *J. Mater. Chem. C* **2016**, *4*, 2731–2743.
13. Belletête, M.; Beaupré, S.; Bouchard, J.; Blondin, P.; Leclerc, M.; Durocher, G. *J. Phys. Chem. B* **2000**, *104*, 9118–9125.
14. a) Yeh, M.-Y.; Lin, H.-C.; Lim, T.-S.; Lee, S.-L.; Chen, C.-H.; Fann, W.; Luh, T.-Y. *Macromolecules* **2007**, *40*, 9238–9243.
(b) Chen, C.-H.; Chen, W.-H.; Liu, Y.-H.; Lim, T.-S.; Luh, T.-Y. *Chem. Eur. J*. **2012**, *18*, 347–354.
(c) Ohshita, J.; Kaneko, F.; Tanaka, D.; Ooyama. Y. *Asian J. Org. Chem.* **2014**, *3*, 170–175.
15. (a) Hong, Y.; Lam, J. W. Y.; Tang, B. Z. *Chem. Soc. Rev.* **2011**, *40*, 5361–5388.
(b) Shen, X. Y.; Wang, Y. J.; Zhao, E.; Yuan, W. Z.; Liu, Y.; Lu, P.; Qin, A.; Ma, Y.; Sun, J. Z.; Tang, B. Z. *J. Phys. Chem. C* **2013**, 117, 7334–7347.
16. Kubota, Y.; Ozaki, Y.; Funabiki, K.; Matsui, M. *J. Org. Chem.* **2013**, *78*, 7058–7067.

17. Gaussian 09, Revision E.01, Frisch, M. J.; Trucks, G. W.; Schlegel, H. B.; Scuseria, G. E.; Robb, M. A.; Cheeseman, J. R.; Scalmani, G.; Barone, V.; Mennucci, B.; Petersson, G. A.; Nakatsuji, H.; Caricato, M.; Li, X.; Hratchian, H. P.; Izmaylov, A. F.; Bloino, J.; Zheng, G.; Sonnenberg, J. L.; Hada, M.; Ehara, M.; Toyota, K.; Fukuda, R.; Hasegawa, J.; Ishida, M.; Nakajima, T.; Honda, Y.; Kitao, O.; Nakai, H.; Vreven, T.; Montgomery, J. A., Jr.; Peralta, J. E.; Ogliaro, F.; Bearpark, M.; Heyd, J. J.; Brothers, E.; Kudin, K. N.; Staroverov, V. N.; Kobayashi, R.; Normand, J.; Raghavachari, K.; Rendell, A.; Burant, J. C.; Iyengar, S. S.; Tomasi, J.; Cossi, M.; Rega, N.; Millam, J. M.; Klene, M.; Knox, J. E.; Cross, J. B.; Bakken, V.; Adamo, C.; Jaramillo, J.; Gomperts, R.; Stratmann, R. E.; Yazyev, O.; Austin, A. J.; Cammi, R.; Pomelli, C.; Ochterski, J. W.; Martin, R. L.; Morokuma, K.; Zakrzewski, V. G.; Voth, G. A.; Salvador, P.; Dannenberg, J. J.; Dapprich, S.; Daniels, A. D.; Farkas, Ö.; Foresman, J. B.; Ortiz, J. V.; Cioslowski, J.; Fox, D. J. Gaussian, Inc., Wallingford CT, 2009.
18. Kerszulis, J. A.; Johnson, K. E.; Kuepfert, M.; Khoshabo, D.; Dyer, A. L.; Reynolds, J. R. *J. Mater. Chem. C* **2015**, *3*, 3211–3218.
19. Cartuledge, K. F.; Riedel, H. K. *J. Organomet. Chem*. **1972**, *34*, 11–15.
20. Sugimoto, K.; Ohsumi, H.; Aoyagi, S.; Nishibori, E.; Moriyoshi, C.; Kuroiwa, Y.; Sawa, H.; Takata, M. *AIP Conf. Proc.* **2010**, *1234*, 887–890.
21. Burla, M. C.; Caliandro, R.; Camalli, M.; Carrozzini, B.; Cascarano, G. L.; De Caro, L.; Giacovazzo, C.; Polidori, G.; Spagna R. *J. Appl. Cryst.* **2005**, *38*, 381–388.
22. Gruene, T.; Hahn, H. W.; Luebben, A. V.; Meilleur, F.; Sheldrick. G. M. *J. Appl. Cryst.* **2014**, *47*, 462–466.
23. Altomare, A.; Cascarano, G.; Giacovazzo, C.; Guagliardi, A.; Burla, M. C.; Polidori, G.; Camalli, M. *J. Appl. Cryst*. **1994**, *27*, 435.
24. Sheldrick, G. M. *Acta Cryst*. **2008**, *A64*, 112–122.

Chapter 3

Multifunctional tetrasila[2.2]cyclophanes exhibiting conformational variation, electroluminescence, and circularly polarized luminescence

3.1 Introduction

3.1.1 Circularly polarized luminescence (CPL)

Interest in circularly polarized luminescence (CPL), which is derived from the difference in emission between right- and left-circularly polarized light by chiral luminophores, has grown because of its potential for the development of advance photonic devices such as 3D displays and enantioselective chemo/biosensors.[1] In general, circularly polarized light is generated through polarizing filters from light sources. In this process, the problem is the reduction of light intensity. Thus, CPL-active materials, which generate circularly polarized light directly from light source, are desired.

To evaluate chiroptical properties, the rotational strength (R_{mn}) is determined theoretically, which is given by $Im\{\boldsymbol{\mu}_{mn}\cdot\boldsymbol{m}_{nm}\}$, where $\boldsymbol{\mu}_{mn} = \langle m|\boldsymbol{\mu}|n\rangle$ means electric transition dipole moment, $\boldsymbol{m}_{nm} = \langle n|\boldsymbol{M}|m\rangle$ means magnetic transition dipole moment, and $\boldsymbol{\mu}$ and $\boldsymbol{M}$ mean the electric and magnetic dipole moment operators, respectively.[2] When a compound or crystal phase has an achiral or centrosymmetric structure, all wave functions have the individual parities (odd or even) against the centrosymmetric inversion operation. Here $\boldsymbol{\mu}$ is odd parity while $\boldsymbol{M}$ is even parity.[2d] When the parity of ψ_m and ψ_n is different, then $\langle m|\boldsymbol{M}|n\rangle$ is zero. Meanwhile their parity is same, $\langle m|\boldsymbol{\mu}|n\rangle$ is zero. Thus the achiral compounds of $\langle m|\boldsymbol{\mu}|n\rangle\langle n|\boldsymbol{M}|m\rangle$ should be zero in all transitions, so the rotation strengths of all transition vanish (i.e. in achiral media there are no chiroptical properties). On the other hand, chiral compounds and crystals can have non-zero $\boldsymbol{\mu}_{mn}$ and non-zero $\boldsymbol{m}_{nm}$ because there is no symmetrical center. Thus they can have non-zero rotational strength ($|R_{mn}| \neq 0$), which causes chiroptical properties such as optical rotation, circular dichroism (CD) activity (e.g. $S_0 \rightarrow S_a$) and CPL activity (e.g. $S_a \rightarrow S_0$).

The degree of CPL is given by the luminescence dissymmetry ratio, $g_{lum} = 2(I_L - I_R)/(I_L + I_R)$, where I_L and I_R refer to the intensity of left and right circularly polarized emissions, respectively. Noted that g_{lum} value is given by;

$$g_{lum} \sim \frac{R_{mn}}{D_{mn}} \sim \frac{\boldsymbol{\mu}_{mn}\cdot\boldsymbol{m}_{nm}}{|\boldsymbol{\mu}_{mn}|^2} = \frac{|\boldsymbol{m}_{nm}|}{|\boldsymbol{\mu}_{mn}|}\cos\theta$$

where D_{mn} means total emission intensity (m→n) which is proportional to $|\boldsymbol{\mu}_{mn}|^2$, and θ means the angle between $\boldsymbol{\mu}_{mn}$ and $\boldsymbol{m}_{nm}$.[2a] Thus to improve the CPL activity, the enhancement of $|\boldsymbol{m}_{nm}|\cos\theta/|\boldsymbol{\mu}_{mn}|$ is important.

Intense CPL is mainly achieved from chiral lanthanide complexes.[3] Chiral lanthanide complexes display high CPL activity with $|g_{lum}|$ (up to 1.38)[3a–3b] owing to magnetic-allowed transition using its 4f orbitals, which causes high magnetic transition dipole moment (Figure 3.1.1). However there are several problems such as the use of rare earth atoms and low fluorescence quantum yield because fluorescence transition is electric-forbidden.[3c]

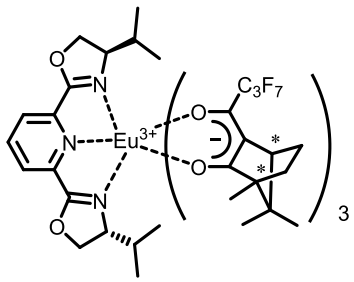

g_{lum} = –1.0
Φ_F = 8.9 x 10^{-3}

Figure 3.1.1. Examples of CPL-active lanthanide complexes.[3d]

As another approach, chiral organic molecules and polymers are also well investigated for CPL-active molecules such as shown in Figure 3.1.2.[4] The simple organic molecule with CPL activity have been much attention because they display high quantum yield and low cost to synthesize. Moreover, simple organic molecules are usually high soluble in solution and low toxic because of no metal. Thus, simple organic molecules with CPL activity have been much attention.

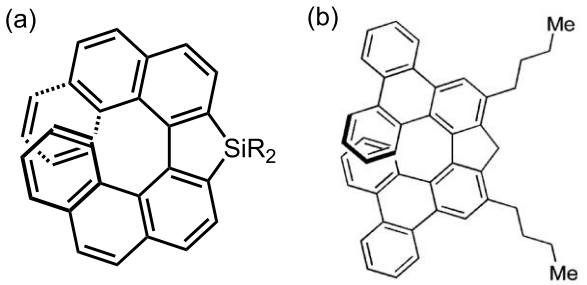

g_{lum} = –0.0035
Φ_F = 0.23

g_{lum} = –0.032
Φ_F = 0.32

Figure 3.1.2. Examples of CPL-active organic molecules.[4b,4c]

However, CPL chromophores of simple organic molecules exhibiting detectable CPL are rare and usually exhibit lower CPL ($|g_{lum}| \approx 10^{-5}$–$10^{-3}$), because the magnetic transition dipole moment of simple organic molecules is often small. There are a few examples of organic molecules with both high CPL activity and high emission intensity such as chiral macrocycles reported by Isobe's group, which show $|g_{lum}| = 0.152$ and $\Phi = 0.80$.[5] Therefore, research on simple organic molecules displaying high CPL activity is necessary for the application to advanced devices.

3.1.2 [2.2]paracyclophane derivatives

Recently, [2.2]paracyclophane derivatives also have been focused on as CPL-active simple organic molecules. [2.2]Paracyclophanes (Figure 3.1.3(a)), which were firstly reported about 70 years ago,[6] were investigated because of their interesting properties derived from unique structures, such as molecular inversion (Figure 3.1.3(b))[7] and intramolecular π–π energy transfer (Figure 3.1.3(c)).[8] And the most important feature of them is planar chirality, which can lead to the ligand or reagent for asymmetric reaction (Figure 3.1.3(d))[9] and the fabrication of chiroptical materials (e.g. CD and CPL properties) (Figure 3.1.3(e)).[10–11]

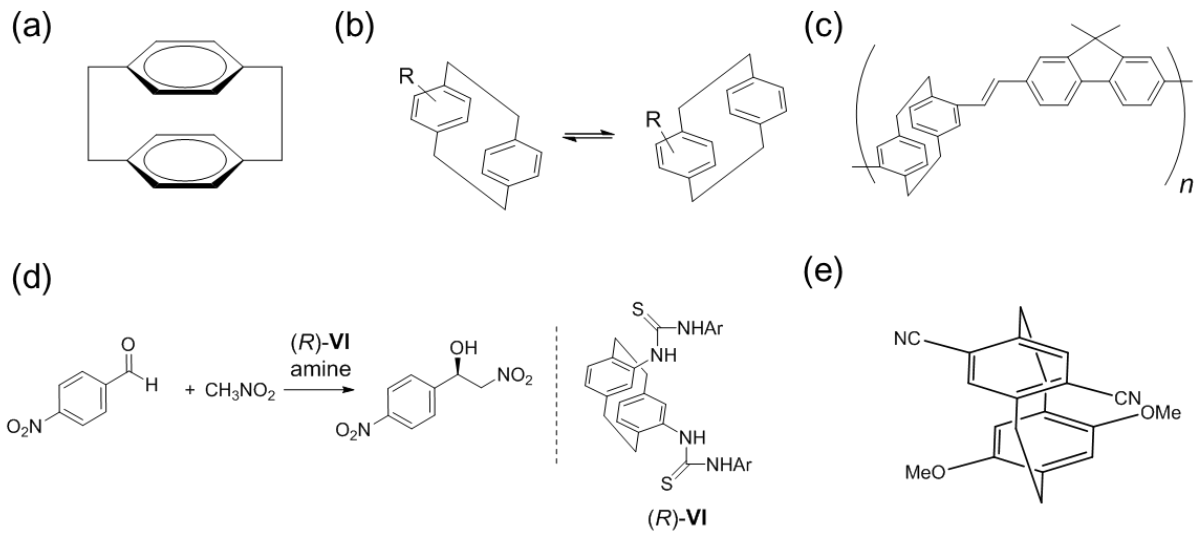

Figure 3.1.3. (a) Structure of [2.2]paracyclophane. (b) Scheme of molecular inversion of cyclophane derivatives. (c) Electroluminescent cyclophane-bridged polymer.[8a] (d) Chiral cyclophane **VI** for asymmetric reaction.[9a] (e) Planar chiral cyclophane with CD activety.[10a]

Figure 3.1.4 shows one of CPL-active cyclophanes with π-conjugated system reported by Morisaki group, which display effective luminescence quantum yield and acceptable CPL activity.[11a] However, these molecules face synthetic difficulty, multi-step reaction and low total yield (<3%) because the synthetic method of cyclophanes is less investigated.

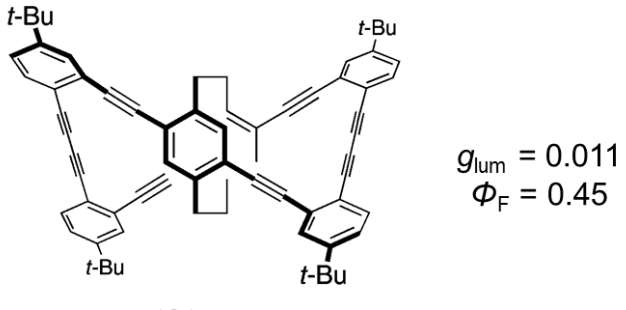

Figure 3.1.4. Examples of CPL-active cyclophanes. Adapted with permission from reference 11(a). Copyright © 2014 American Chemistry Society.

Thus, although there are few examples of planar chiral cyclophanes, they have great potential for CPL-active materials, and the systematic synthesis method for chiral cyclophanes is desired.

3.1.3 Disilane-bridged [2.2]cyclophanes

To explore the range of chiral luminophores, I focused on disilane-modified cyclophane derivatives. Introducing disilane linker(s) into arenes gives photophysical properties driven from σ–π conjugation as described in Chapter 1. Moreover, the donor–disilane–acceptor system is expected to produce solid state emission and EL arising from intramolecular charge transfer (ICT). Therefore, unsymmetrical (donor–acceptor) disilane-bridged cyclophanes, which combine Si−Si σ systems with a cyclophane skeleton, are expected to provide materials with interesting physical properties.

Despite their importance, efficient modular methods to access disilane-bridged cyclophanes remain challenging, particularly for aromatic systems except for simple, symmetrical aryls (Figure 3.1.5).[12–14] Although they displayed the functionalities such as the molecular inversion,[13] ring-opening polymerization,[14] and inclusion of chromium ion into cyclophanes,[15] the physical properties of these compounds have not been thoroughly investigated. Unsymmetrical disilane-bridged cyclophanes including donor–acceptor system have not been reported. Moreover, planar chiral ones have not been investigated despite their chiroptical properties. Thus, the development of effective and systematic synthesis method for disilane-bridged [2.2]cyclophane derivatives is desired.

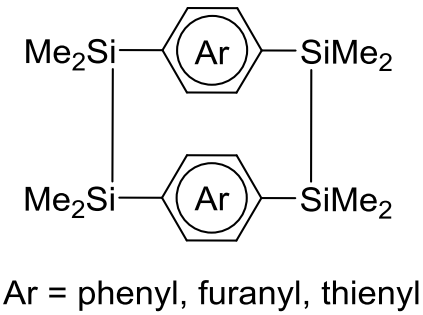

Figure 3.1.5. Molecular structure of symmetrical disilane-bridged cyclophanes.[12]

3.1.4 This work

For the development of systematic synthesis of various octamethyltetrasila[2.2]cyclophanes (hereinafter refer to as tetrasila[2.2]cyclophanes), simple structures of disilane-bridged cyclophanes, I designed Pd-catalyzed cyclization reaction as shown in Scheme 3.1.1. This reaction proceeds in only two steps, compared with ordinal unsymmetrical and planar chiral [2.2]paracyclophanes (over five steps).

Scheme 3.1.1. Designed synthetic scheme for tetrasila[2.2]cyclophanes.

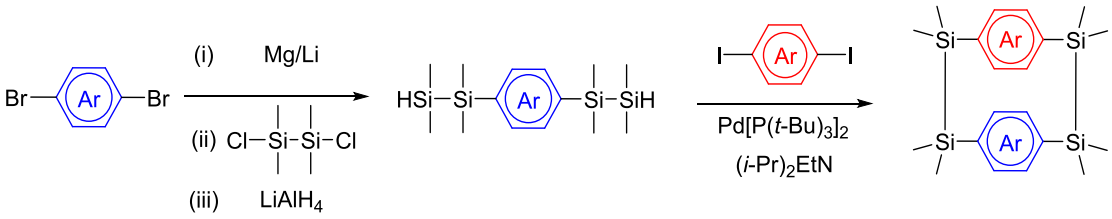

In this research, the development of this reaction and the investigation of physical properties of tetrasila[2.2]cyclophane derivatives were carried out.[16] Various tetrasila[2.2]cyclophane derivatives were prepared *via* Pd-catalyzed arylation reaction. Their physical properties such as crystal structures, molecular dynamics, thermal stabilities, electrochemical properties, and theoretically calculated structures were investigated. Moreover, an electroluminescent device containing a tetrasila[2.2]cyclophane-doped emitting layer was fabricated for the practical application. Finally the development of synthetic method of planar chiral tetrasila[2.2]cyclophanes, and the discussion of the chiroptical properties (e.g. CPL) was carried out.

3.2 Results and discussion

3.2.1 Synthesis

To construct various tetrasila[2.2]cyclophane containing donor–acceptor ones, I conducted the synthesis of tetrasila[2.2]cyclophane derivatives *via* Pd-catalyzed arylation of 2,5-bis(hydrodisilyl)thiophene derivatives (**12** and **13**, electron-donating moieties) with aryl iodides such as diiodothiophene, diiodobenzene, **1**, and **2**, including electron-withdrawing moieties as shown in Scheme 3.2.1. This reaction gave various tetrasila[2.2]cyclophanes **21**–**28**, containing donor–acceptor typed ones (**25**–**28**).

Desired compounds **21**–**28** were prepared in 15–20% yields. All compounds were characterized by ^{1}H NMR, ^{13}C NMR, MS and HRMS, and the results indicated that their purity was adequate for the spectroscopic studies.

Scheme 3.2.1. The synthetic scheme of tetrasila[2.2]cyclophane derivatives (upper row) and the structures of prepared compounds (lower rows).

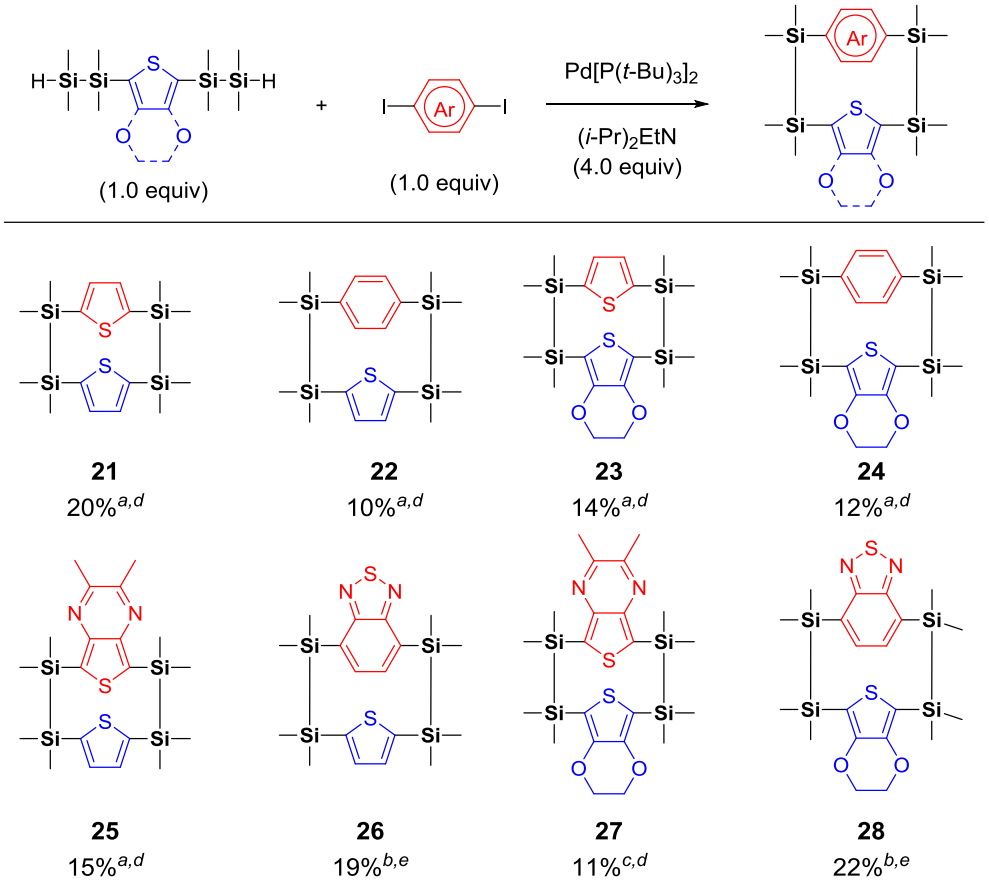

[a] Reaction conditions: bis(tetramethyldisilanyl)arenes (1.0 mmol), aryl iodide (1.0 mmol), Pd[P(*t*-Bu)$_3$]$_2$ (0.025 mmol), *N*,*N*-diisopropylethylamine (4.0 mmol), *m*-xylene (15 mL), 0 °C, 2 d. [b] Reaction conditions: bis(tetramethyldisilanyl)arenes (1.0 mmol), **1** (1.0 mmol), Pd[P(*t*-Bu)$_3$]$_2$ (0.050 mmol), *N*,*N*-diisopropylethylamine (4.0 mmol), toluene (15 mL), 0 °C, 6 d. [c] Reaction conditions: **13** (1.0 mmol), **2** (1.0 mmol), Pd[P(*t*-Bu)$_3$]$_2$ (0.025 mmol), *N*,*N*-diisopropylethylamine (4.0 mmol), *m*-xylene (15 mL), –5 °C, 5 d. [d] GC yields. [e] Isolated yields. Adapted with permission from reference 16. Copyright © 2017 American Chemistry Society.

3.2.2 Single crystal X-ray diffraction analysis

The structures of these compounds were determined by single-crystal X-ray diffraction. Suitable single crystals of compounds **21**, **25**, **26** and **28** were obtained by recrystallization (see Experimental section), allowing their structural characterization by XRD. The main crystallographic data, selected bond distances and angles are listed in Tables 3.3.1–3.3.8, and the molecular structures and packing structures were shown in Figure 3.2.1. The Si–Si bond lengths (2.36−2.38 Å) were similar to typical Si–Si bond length (2.34 Å) and the angles of aryl–Si–Si were 101°–107°. Figure 3.2.2 shows the comparison of crystal structures of **21** and corresponding carbon analog **29**.[18] Thiophene–Si–Si angle of **21** was smaller than that of **29** owing to the flexibility of disilane units and the anomeric effect of σ*–π* conjugation. Notably, a single isomer (for example, compound **21** has only *anti* conformation) was observed as the sole structure for the X-ray diffraction. The results indicate that the rotation about the two Si–Si bonds connecting the two thiophene rings was restricted in the crystal phase.

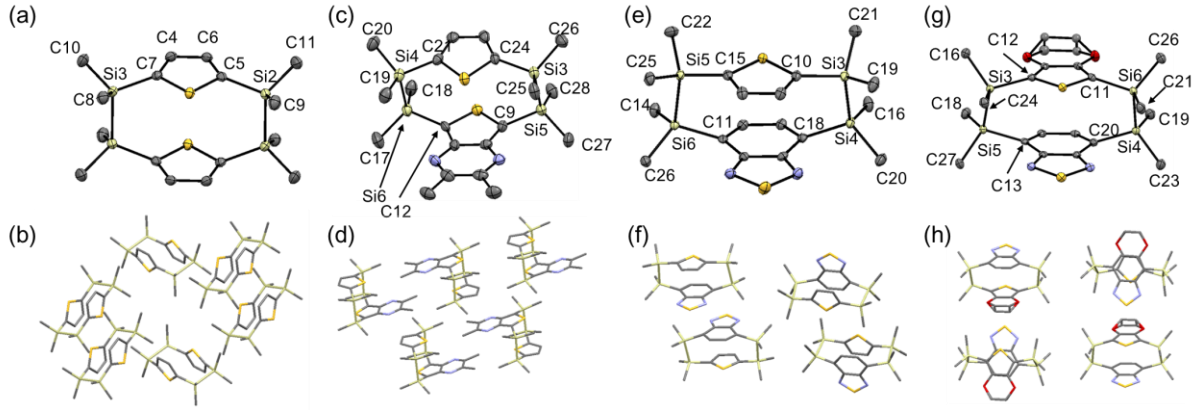

Figure 3.2.1. (a, c, e, g) ORTEP drawings (50% probability ellipsoids) and (b, d, f, h) packing structures of (a, b) **21**, (c, d) **25**, (e, f) **26**, and (g, h) **28**. Hydrogen atoms are omitted for clarity. Adapted with permission from reference 16. Copyright © 2017 American Chemistry Society.

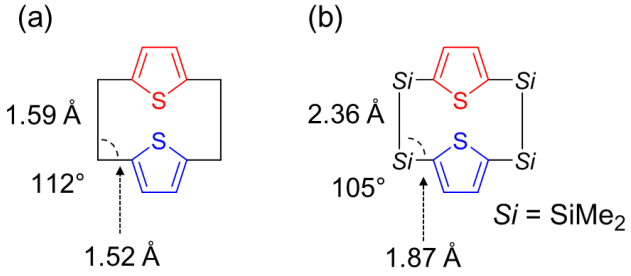

Figure 3.2.2. The comparison of crystal structures of (a) **29** and (b) **21**.

3.2.3 Molecular dynamics and conformational analysis

The molecular geometry of **21** in the conformational mobility study was investigated with theoretical calculations. Compound **21** has two conformations, *syn*- and *anti*-forms (Figures 3.2.3). Initially, the relative stability of both conformations was estimated with DFT calculation using Gaussian 09 Program.[19] The theoretical studies suggested that a Gibbs free energy of the *anti* conformation was lower than that of the *syn* conformation by 3.5 kcal/mol (Table 3.2.1). Using the equation of $K = \exp(-\Delta G/RT)$ (where ΔG, R, T, and K mean the difference of Gibbs free energy between *syn*-form and *anti*-form, gas constant, temperature, and equilibrium constant of *syn* and *anti* **21**, respectively), the ratio of *syn*/*anti* was 0.3/99.7 at 298 K. The explanation for this is that the *syn* conformation structure has electronic repulsion between two sulfur moieties. Therefore, at room temperature, almost all **21** has *anti*-conformation in solution.

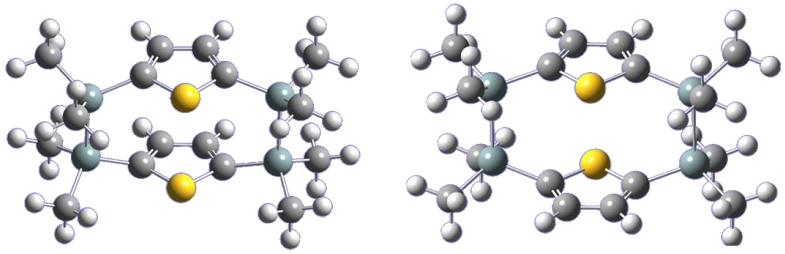

Figure 3.2.3. Optimized molecular structures for *syn*- and *anti*-forms of **21** calculated with DFT at the B3LYP/6-31G(d) level.

Table 3.2.1. Gibbs free energy of **21** calculated with DFT at the B3LYP/6-31G(d) level.

	Gibbs free energy (kcal/mol)
anti-form	−1619621.80
syn-form	−1619618.30
difference	3.5

Sakurai reported the kinetic parameters of the change in conformation of **21** between the *anti*-A and the *anti*-B forms *via* the *syn* form in solution (Scheme 3.2.2); the inversion barrier of **21** is determined to be 14.9 kcal/mol.[20] I also investigated the inversion of tetrasila[2.2]cyclophanes by variable temperature (VT) NMR in $CDCl_3$ solution in detail. Figure 3.2.4 shows the VT-NMR spectra of methyl region of **21**. At low temperature, the ^{1}H NMR showed two signals with equal intensity assigned to the Si−C$\underline{H}_3$ moiety (*a* and *b* in Figure 3.2.4).

Scheme 3.2.2. The molecular inversion of **21** in solution state.

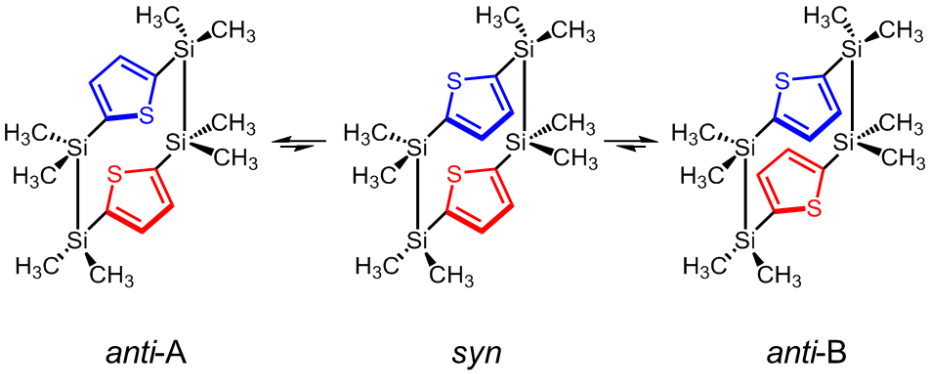

Adapted with permission from reference 16. Copyright © 2017 American Chemistry Society.

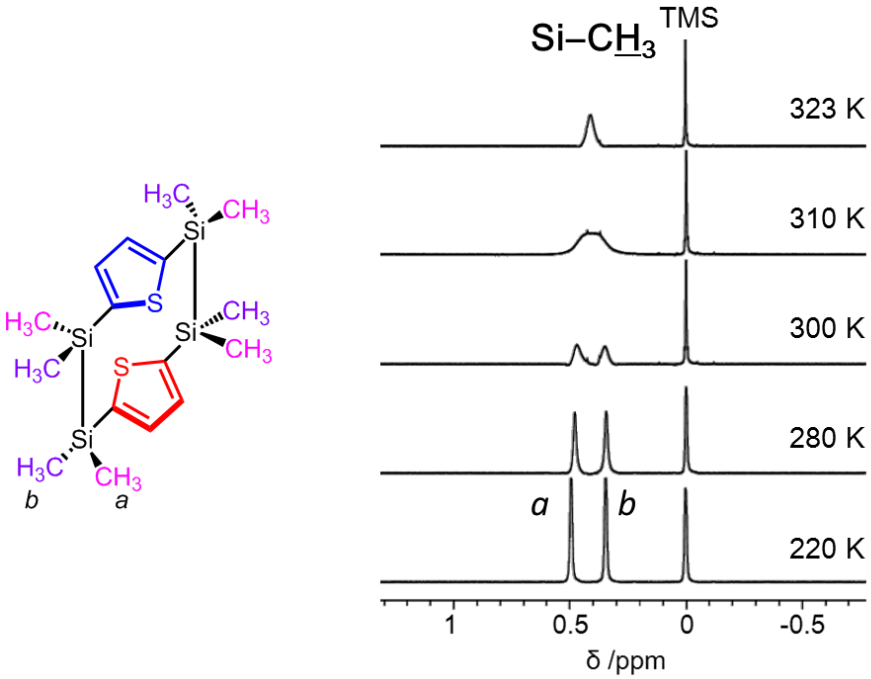

Figure 3.2.4. VT-^{1}H NMR of methyl region of compound **21**. *a* and *b* of C$\underline{H}_3$ were estimated by ^{1}H–^{1}H NOESY spectrum at 250 K (Figure 3.3.2).

As the temperature increased, these signals coalesced at around 310 K and became a broad singlet, which suggested that at over 310 K the inversion of **21** occurred. The inversion barrier of **21** between *anti*-A and *anti*-B was calculated by Eyring equation.[21] According to the Eyring equation, the flipping rate constant *k* is given by

$$k = \frac{RT}{N_a h}\exp(-\frac{\Delta G^{\neq}}{RT}) \qquad \text{(Eq. 1)}$$

where *R*, *T*, N_a, *h*, $\Delta G^{\neq}$ are gas constant, temperature, Avogadro's number, Planck's constant, and the Gibbs free energy of the inversion barrier, respectively.

The temperature at which NMR peaks are coalesced is called as coalesced temperature T_c. The inversion rate constant at coalescence temperature k_{Tc} is approximately given by $k_{T_c} = \pi\Delta\upsilon/\sqrt{2}$, where $\Delta\upsilon$ is the difference of NMR shifts between two signals under slow exchange.[21] By substituting k_{Tc} for Eq. 1, the Gibbs free energy of the inversion barrier ($\Delta G^{\neq}$) at coalescence temperature is given by

$$\Delta G^{\neq} = RT_c \ln\frac{RT_c\sqrt{2}}{\pi N_a h \Delta\upsilon} \qquad \text{(Eq. 2)}$$

According to VT-^{1}H NMR spectra of **21** (Figure 3.2.4), T_c and Δν were estimated to 310 K and 74.1 Hz, respectively. Then, by substituting these values for Eq. 2, the inversion barrier energy of **21** in $CDCl_3$ ($\Delta G^{\neq}$) was estimated to 15.0 kcal/mol. This value was lower than that of **29**, 27 kcal/mol, which reflected the large Si atoms and long and flexible Si–Si bond.[18]

The VT-^{13}C NMR of **21** in $CDCl_3$ also showed the Si−$\underline{C}H_3$ peak(s) as two signals at 300 K, which coalesced above 310 K, similar to the ^{1}H NMR (Figure 3.2.5). Moreover, solid-state VT-^{13}C NMR measurements of crystalline **21** were performed (Figure 3.2.6). The Si−$\underline{C}H_3$ peaks in the crystalline state showed a set of signals that did not coalesce below 323 K, demonstrating that the thiophene rings of **21** did not flip in the crystalline state.

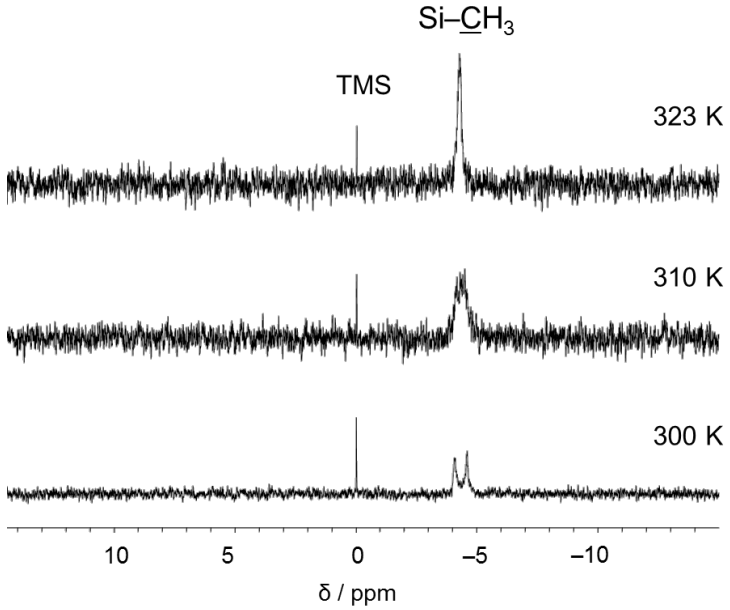

Figure 3.2.5. VT-^{13}C NMR spectra of the methyl region of compound **21** in $CDCl_3$ at 300, 310 and 323 K.

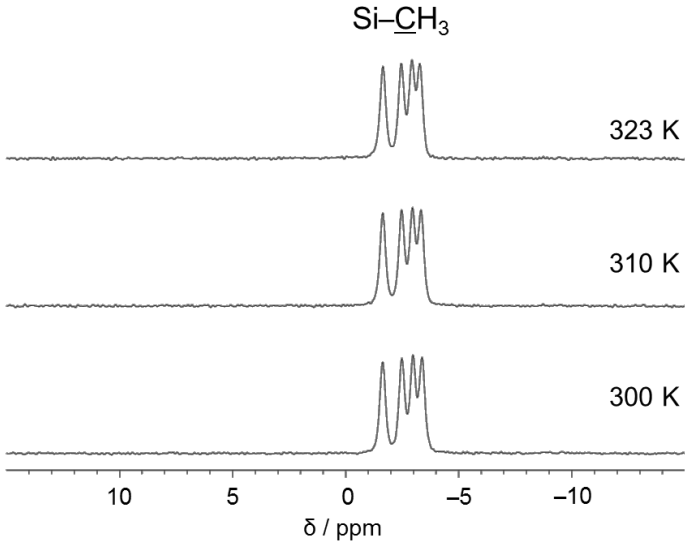

Figure 3.2.6. VT-^{13}C NMR spectra of the methyl region of compound **21** in crystalline phase at 300, 310 and 323 K.

Si−C$\underline{H}_3$ peaks of compounds **23**, **25**, and **27** were also broad and coalesced at higher temperature, which indicates that the inversion occurred in solution similarly to **21**. (Figures 3.3.3, 3.3.5, and 3.3.6) According to the Si−C$\underline{H}_3$ peaks of **22**, the flipping is in the fast limit at 300 K, and broad Si−C$\underline{H}_3$ peaks of **22** at 220 K were observed (Figure 3.2.7(a)). VT-^{1}H NMR of compound **24** displayed similar spectra (Figures 3.3.4). These results suggest that the inversion energy of **22** and **24** in solution at room temperature was lower than that of **21**. On the other hand, Si−C$\underline{H}_3$ peaks of **26** displayed sharp Si−C$\underline{H}_3$ peaks, and these signals did not depend on the temperature (Figure 3.2.7(b))). Si−C$\underline{H}_3$ peaks of **28** are also four sharp signals and independent of temperature (Figures 3.3.7). These results insist that the flipping inversion of **26** and **28** did not occur below 323 K owing to high inversion energy derived from the greater steric hindrance of the aryl substituents (thiadiazole moiety). Thus, the inversion of tetrasila[2.2]cyclophane could be controlled by the bulkiness of substituents.

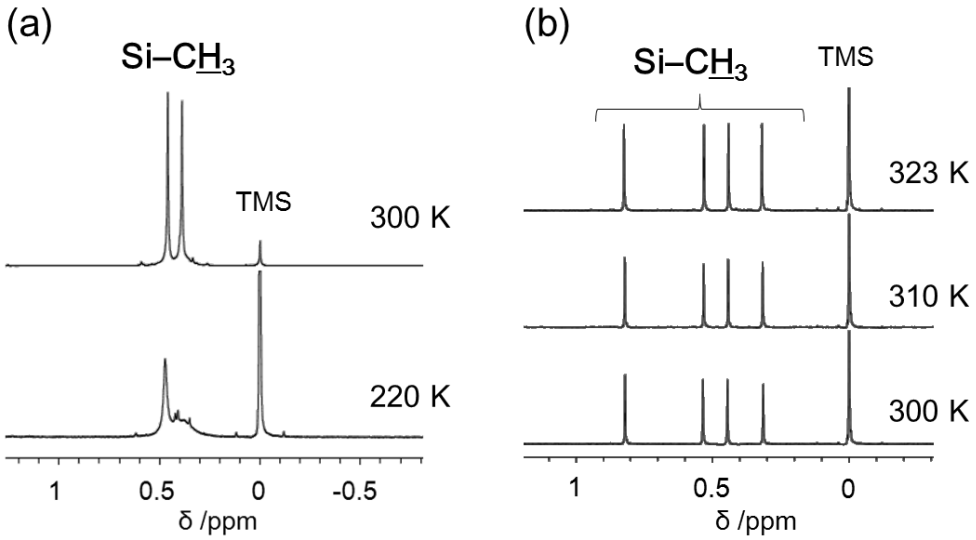

Figure 3.2.7. VT-^{1}H NMR spectra of the methyl region of (a) **22** and (b) **26** in $CDCl_3$.

3.2.4 Inversion control by host macrocycles

Cyclic host molecules that entrap small metals and/or organic molecules strongly in solution are important for selective extraction of chemical species,[22] or control of molecular motion.[23] Previously Shionoya and coworkers reported that macrocycles included small organic molecules as guests;[24] for example, macrocycle $[Ag_2\mathbf{L}X_2]^{2+}$ (in Scheme 3.2.3) included [2.2]paracyclophane and ferrocene.[24c] In this research, I demonstrated that the control of the inversion motions of **21** by the interaction between tetrasila[2.2]cyclophane **21** and $[Ag_2\mathbf{L}]^{2+}$.

21$\subset[Ag_2\mathbf{L}]^{2+}$ complex was fabricated by the mixing of **21** and $[Ag_2\mathbf{L}X_2](SbF_6)_2$ in $CDCl_3$ at room temperature as shown in Scheme 3.2.3. The NMR titration of **21** in $[Ag_2\mathbf{L}]^{2+}$ produced peaks at 3.8, −0.5, and −1.1 ppm, which was the characteristic of the inclusion of **21**. And the original peaks of **21** appeared (0.42 and 0.38 ppm) with over 1 eq addition, which indicated that **21** bound to $[Ag_2\mathbf{L}]^{2+}$ in a 1:1 ratio (Figure 3.2.8). ESI-MS also showed that **21** $\subset[Ag_2\mathbf{L}]^{2+}$ complex was fabricated (Figure 3.3.8). Moreover, 1D and 2D NMR analyses of **21** $\subset[Ag_2\mathbf{L}]^{2+}$ (Figures 3.3.9−3.3.15) showed that **21**$\subset[Ag_2\mathbf{L}]^{2+}$ had a C_{2h}-symmetrical structure, which insisted that the guest molecule included in the host cavity was only in an *anti* conformation.

Scheme 3.2.3. Preparation of **21**$\subset[Ag_2\mathbf{L}](SbF_6)_2$.[a]

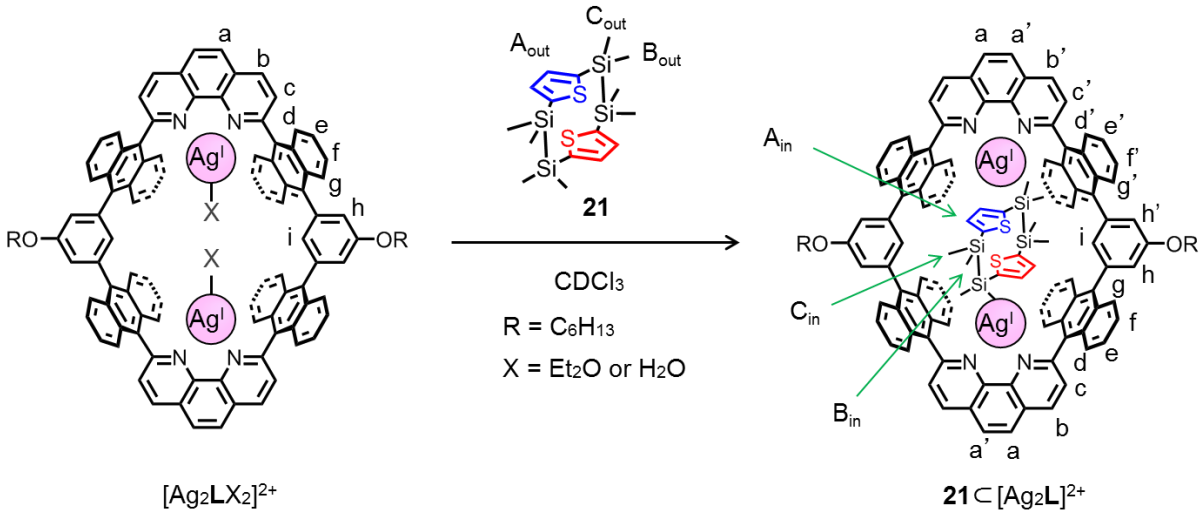

[a] To the solution of $[Ag_2\mathbf{L}X_2](SbF_6)_2$ (0.06 mM, 475 μL, 0.03 μmol, 1.0 eq) in $CDCl_3$ was added a $CDCl_3$ solution of **21** (20 mM). *p*-Dimethoxybenzene (0.025 μmol) was added as an internal standard for NMR analysis.

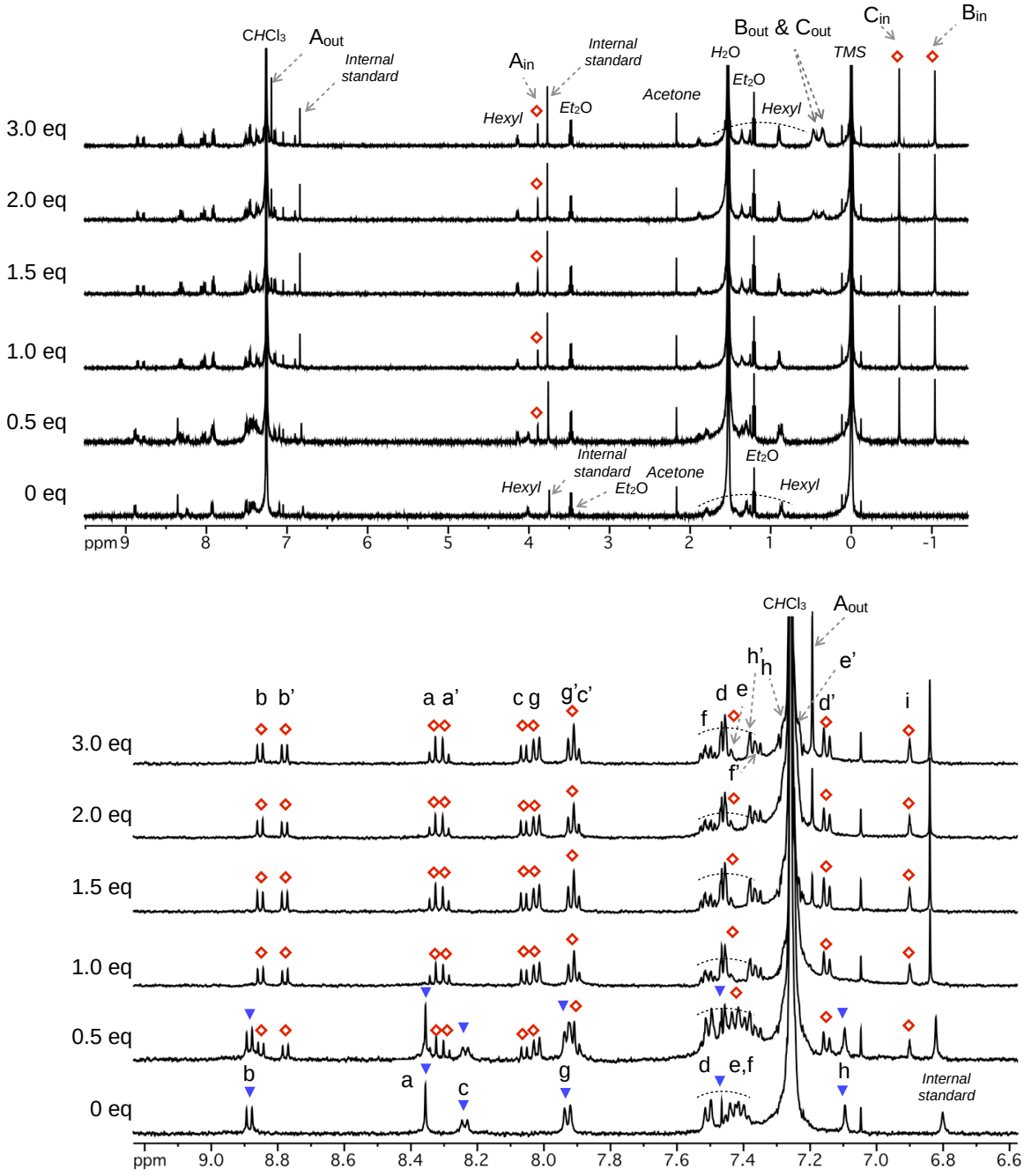

Figure 3.2.8. ^{1}H NMR spectra of mixtures of $[Ag_2\mathbf{L}X_2](SbF_6)_2$ (0.06 mM) and different amounts of **21** (500 MHz, $CDCl_3$, 300 K). Whole spectra (top) and partial spectra of an aromatic region (bottom). Diethyl ether (Et_2O) comes from X in $[Ag_2\mathbf{L}X_2](SbF_6)_2$. Internal standard: Peaks from *p*-dimethoxybenzene. ◇: Peaks from **21**⊂$[Ag_2\mathbf{L}](SbF_6)_2$. ▼: Peaks from $[Ag_2\mathbf{L}X_2](SbF_6)_2$.

The binding affinity of **21** to the dinuclear Ag(I)-macrocycle $[Ag_2\mathbf{L}X_2](SbF_6)_2$ was evaluated by ^{1}H NMR titration experiment. As the affinity between **21** and the dinuclear Ag(I)-macrocycle was too strong to directly determine from ^{1}H NMR, it was estimated from guest competing experiment using ferrocene as a completing guest (Scheme 3.3.1). However, even if an excess (100 eq) of ferrocene was added to **21**$\subset[Ag_2\mathbf{L}]^{2+}$, no guest exchange was observed (Figure 3.3.16). This result indicates that the association constant between **21** and $[Ag_2\mathbf{L}]^{2+}$ (K_a(**21**)) is higher than 10^{10} M^{-1} in $CDCl_3$ at 300 K (Eq. 14, see Section 3.3.7), suggesting there was a strong intermolecular interaction between them.

VT-^{1}H NMR of **21**$\subset[Ag_2\mathbf{L}]^{2+}$ was carried out to investigate the difference of molecular motion between free **21** and included **21** in solution phase. This result indicated that the peaks from the included **21** did not depend on the temperature and did not coalesce at 323 K, owing to the restriction of the thiophene ring rotation in the cavity (Figure 3.2.9). Encapsulation is an effective and simple approach to conformational rigidification of tetrasila[2.2]cyclophanes. From this result, it is proposed that the guest spinning motion was restricted by the interaction between thiophene and Ag^+.

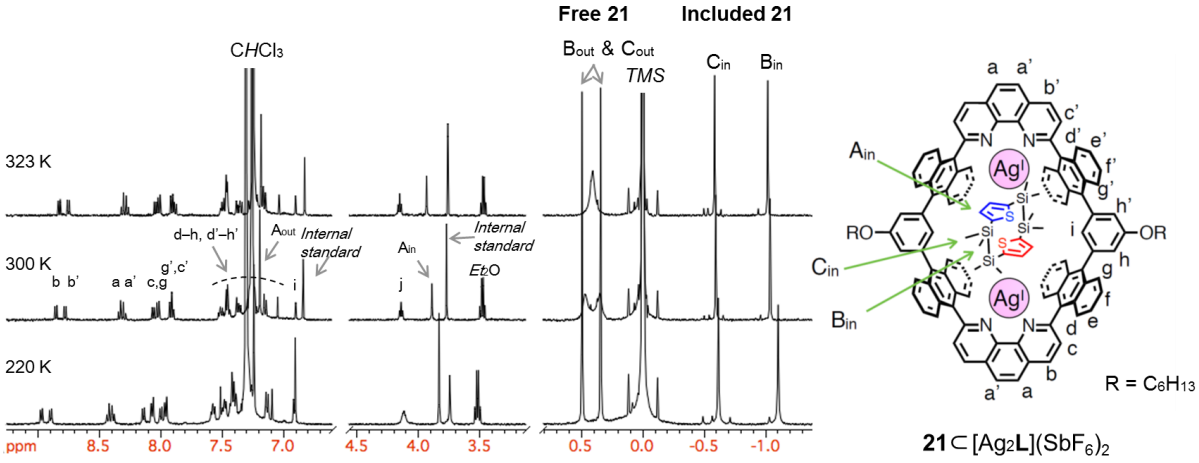

Figure 3.2.9. VT-^{1}H NMR spectra of a mixture of $[Ag_2\mathbf{L}X_2](SbF_6)_2$ (0.06 mM) and **21** (3.0 eq) at 220, 300, and 323 K.

A single crystal of **21**$\subset[Ag_2\mathbf{L}](SbF_6)_2$ suitable for X-ray crystallography was obtained by slow vapor diffusion of ether into CH_2Cl_2 solution of an equimolar mixture of $[Ag_2\mathbf{L}X_2](SbF_6)_2$ and **21**. Details of the molecular structure determination are given in Figures 3.2.10 and 3.3.1, and Tables 3.3.11−3.3.12. The structure of **21** in macrocyclic host was in an

anti conformation similar to single-crystal **21**. Moreover, the intermolecular interaction between host **L** and guest **21** were observed. Both Ag^+ ions were in η^2-typed Ag–π coordination geometries and were bridged by a side-on bound aromatic moiety with Ag−C bond lengths of ca. 2.3−2.4 Å, which were comparable to Ag−C bond lengths of a similar inclusion complex, [2.2]paracyclophane ⊂ $[Ag_2\mathbf{L}](SbF_6)_2$,[24c] and previous Ag–thiophene[25] or Ag–arene complexes.[26] This strong Ag–π interaction allowed the coordination between host and guest, and suppressed the flipping motion of guest **21** in the host, $[Ag_2\mathbf{L}]^{2+}$.

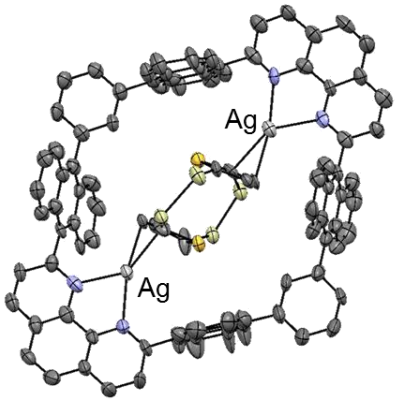

Figure 3.2.10. ORTEP drawing (30% probability ellipsoids) of one disordering pattern of **21**⊂$[Ag_2\mathbf{L}](SbF_6)_2$. Side alkyl-chains of **L**, counter anions, methyl groups of **21**, solvent molecules, and hydrogen atoms are omitted for clarity.

3.2.5 Photophysical properties of **21–28**

Photophysical properties of **21**–**28** were investigated. The results were shown in Figures 3.3.17–3.3.24 and summarized in Tables 3.2.2–3.2.3. The UV–vis absorption bands of **21**–**24** in cyclohexane are observed at around 270 nm with 15,000−30,000 $M^{-1}cm^{-1}$ molecular extinction coefficient. These compounds hardly showed any fluorescence in cyclohexane (Φ: <0.01). Therefore, there was little difference in the absorption and emission spectra among **21**–**24**. On the other hand, donor−acceptor typed tetrasila[2.2]cyclophanes **25**–**28** displayed broad and weak absorption bands at around 400 nm in cyclohexane, which are assignable to intramolecular charge transfer (ICT) absorption. By the excitation of their absorption band, they displayed green-colored emission at around 500 nm as shown in Figures 3.2.11. While the quantum yields of compounds **26** and **28** (containing thiadiazole as acceptor) was very low (Φ: <0.05), those of compounds **25** and **27** (containing thienopyrazine as acceptor) was improved (Φ: up to 0.42). The fluorescence decays of all compounds are in the nanosecond timescale.

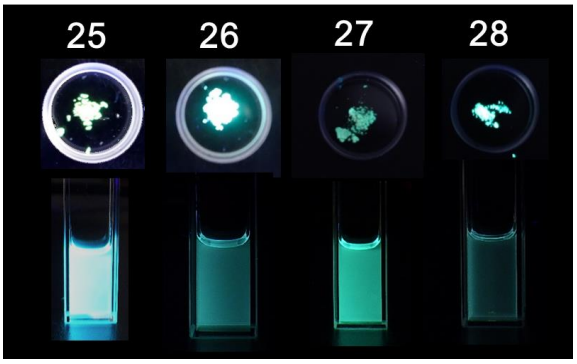

Figure 3.2.11. Photographs of **25**–**28** under UV irradiation at 365 nm: (top) in the solid state; (bottom) in cyclohexane solution. Adapted with permission from reference 16. Copyright © 2017 American Chemistry Society.

Several tetrasila[2.2]cyclophanes displayed more efficient emission in the solid phase than that in solution. Especially compound **26** displayed relatively strong solid-state emission (Φ = 0.49), which is about ten times efficiency comparing with that in solution. On the other hand, compound **25** faces concentration quenching not similar to compound **26**. Table 3.2.4 shows the rate constants of fluorescence (k_f) and non-radiative (k_{nr}) decays. Both radiative rate constants of **25** and **26** in solution are slightly different from those in the solid phase, while non-radiative rate constants are not; k_{nr} of **25** in solution is smaller than that in the solid phase, and

k_{nr} of **26** in solution is larger than that in the solid phase.

Figure 3.2.12 shows the details of crystal packing of **25** and **26**. In the case of compound **25**, there are clear π–π stacking with 3.3 Å distance in crystal structure, which causes quenching emission in the solid state. Meanwhile, because intermolecular π–π distance is 3.6 Å and two molecules are at slipped parallel position in crystal structure of **26** due to the steric hindrance of Si_2Me_4 units, there is small intermolecular π–π interaction, which suppresses concentration quenching. This structural difference affects the non-radiative rate constant in solution and in the solid state. Improvement of the quantum yield of compound **26** in the solid state was achieved by the disilane units which suppressed the radiative relaxation of intermolecular π–π interaction.

Table 3.2.2. Optical properties of **21**–**28** in cyclohexane

compound	λ_{abs} (nm)	ε (10^4 $M^{-1}cm^{-1}$) [a]	λ_{em} (nm)	Φ [b]	τ (ns) [c]
21	271	2.41	398	<0.01	– [d]
22	265	1.54	395	0.01	0.33 [e]
23	278	3.01	388	<0.01	0.35 [e]
24	286	1.62	362	<0.01	– [d]
25	329, 400	0.95, 0.30	489	0.42	11.3 [f]
26	321, 370	0.75, 0.33	490	0.05	4.2 [g]
27	341, 400	0.61, 0.33	495	0.20	9.6 [f]
28	293, 352	2.23, 0.50	503	0.04	2.8 [g]

[a] Molar extinction coefficient at λ_{abs}. [b] Absolute quantum yields determined by an integrating sphere system. [c] Fluorescence lifetime detected at the maximum fluorescence wavelengths. [d] Fluorescence lifetime below the detection limit. [e] Excited at 280 nm. [f] Excited at 405 nm. [g] Excited at 365 nm. Adapted with permission from reference 16.

Table 3.2.3. Optical properties of **21**–**28** in the solid state [a]

compound	λ_{ex} (nm) [b]	λ_{em} (nm)	Φ [c]	τ (ns) [d]
21	312	395	0.04	1.1 [e]
22	324	363	0.12	0.79 [e]
23	312	360	0.05	0.50 [e]
24	352	399	0.02	0.52 [f]
25	368, 435	483	0.25	6.2 [g]
26	371, 406	490	0.49	16.1 [g]
27	386, 443	501	0.25	11.9 [g]
28	389, 437	501	0.01	1.8 [g]

[a] Measured in microcrystalline powder. [b] Excitation wavelength in the solid state determined from the excitation spectra. [c] Absolute quantum yields determined by an integrating sphere system. [d] Fluorescence lifetime detected at the maximum fluorescence wavelengths. [e] Excited at 280 nm. [f] Excited at 340 nm [g] Excited at 405 nm. Adapted with permission from reference 16. Copyright © 2017 American Chemistry Society.

Table 3.2.4. Rates of fluorescence (k_f) and non-radiative (k_{nr}) decays of donor–acceptor typed disilane-briged compounds in cyclohexane and in the solid state. [a]

compound	in cyclohexane		in the solid state	
	k_f ($\times 10^7$ s^{-1})	k_{nr} ($\times 10^7$ s^{-1})	k_f ($\times 10^7$ s^{-1})	k_{nr} ($\times 10^7$ s^{-1})
25	3.7	5.1	4.0	12.1
26	1.2	22.6	3.0	3.2
27	2.1	8.3	2.1	6.3
28	1.4	34.3	0.56	55.0

[a] Rate constants k_f and k_{nr} were calculated from quantum yield and fluorescence lifetime; $k_f = \Phi/\tau$ and $k_{nr} = (1-\Phi)/\tau$.

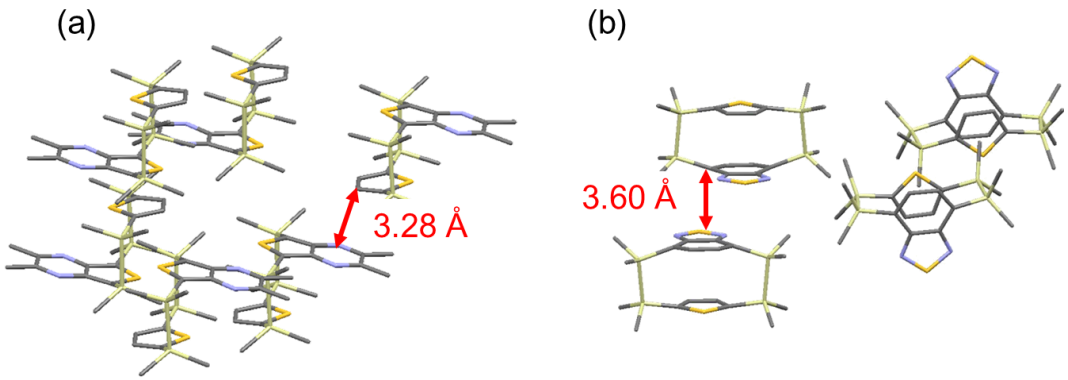

Figure 3.2.12. Details of crystal packing structures of (a) compound **25** and (b) compound **26**. Hydrogen atoms are omitted for clarify.

3.2.6 Thermal stability

The thermal stability of **25**−**28** was evaluated by thermogravimetric analysis (TGA) at a heating rate of 10 °C/min. From TGA measurement, compounds **25**−**28** remain unchanged upon heating to 200 °C (**25**, **26**) and 230 °C (**27**, **28**) under a nitrogen atmosphere (Figures 3.2.13). The results showed that these compounds had good thermal stability and were suitable for vacuum deposition to prepare optoelectronic device applications such as OLEDs.

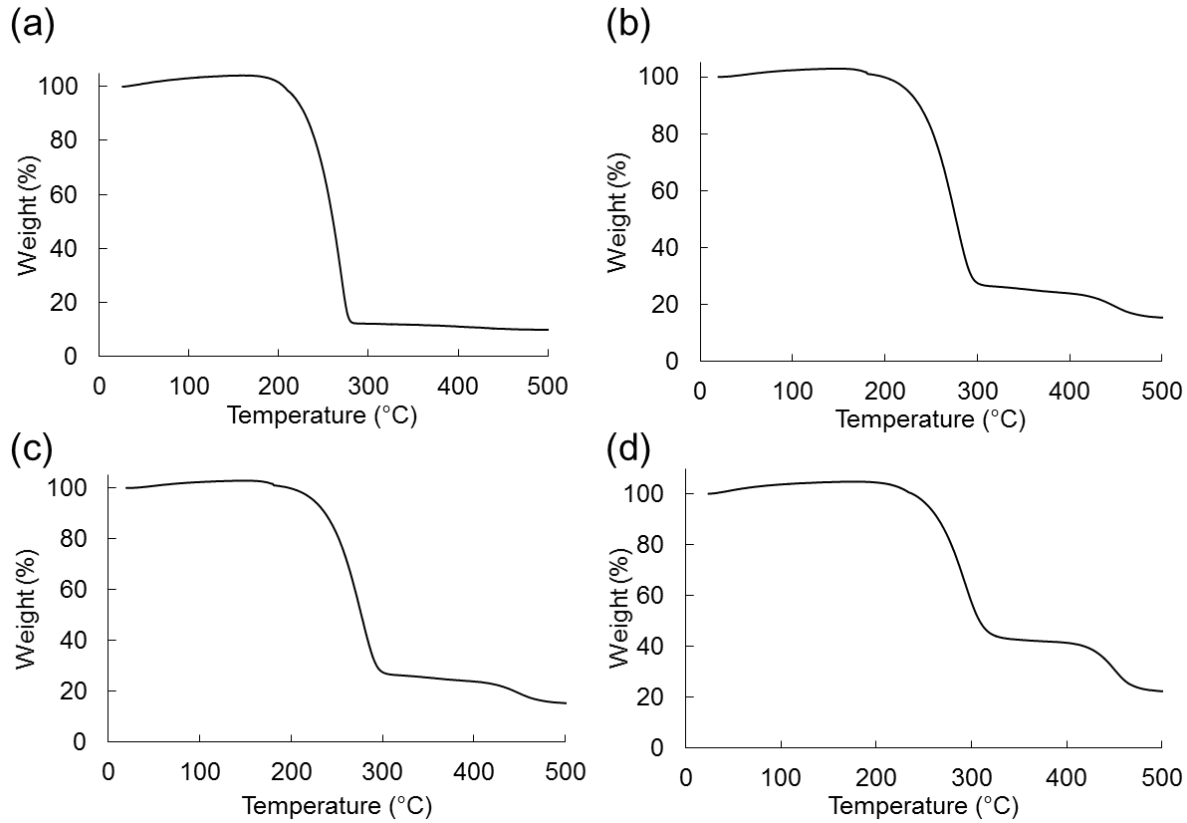

Figure 3.2.13. TGA curves of (a) compound **25**, (b) compound **26**, (c) compound **27**, and (d) compound **28**.

3.2.7 Electrochemical behavior

The electrochemical behavior of **25**–**28** in CH_2Cl_2 was investigated by cyclic voltammetry (CV) and differential pulse voltammetry (DPV). The redox potentials were calibrated by ferrocene as an internal standard. The obtained electrochemical results were presented in Table 3.2.5 and Figure 3.2.14. Compounds **25** and **27** showed an irreversible electron oxidation wave and an irreversible electron reductive wave, corresponding to donor and acceptor units, respectively. In contrast, compounds **26** and **28** displayed a partially reversible reduction wave corresponding to benzo[*c*][1.2.5]thiazole as acceptor unit although an oxidation wave for donor group was also irreversible. HOMO and LUMO levels of **25**–**28** were estimated with the electrochemical oxidation and reduction potentials (E_{ox} and E_{red}, respectively) on the basis of energy level of ferrocenium/ferrocene (4.8 eV) below vacuum level,[27] and HOMO−LUMO energy gaps of them were estimated to be 2.7−2.9 eV.

Table 3.2.5. Electrochemical data of **25**−**28**.[a]

compound	E_{ox} (V) [b]	HOMO (eV) [c]	E_{red} (V) [b]	LUMO (eV) [c]	HOMO−LUMO gap (eV)
25 [d]	0.52	−5.3	−2.27	−2.6	2.7
26 [e]	0.81	−5.6	−2.15	−2.7	2.9
27 [d]	0.46	−5.3	−2.29	−2.5	2.8
28 [d]	0.52	−5.3	−2.18	−2.6	2.7

[a] Measured in CH_2Cl_2 at room temperature in the presence of *n*-Bu_4NPF_6 (0.1 mol/L) as an electrolyte with scan rate of 100 mV/s. [b] Peaks were determined by differential pulse voltammetry with calibration of Fc^+/Fc. [c] The energy levels were calculated from oxidation and reduction peaks and referenced to Fc/Fc^+ (4.8 eV) below the vacuum level. [d] Concentration: 0.5 mmol/L. [e] Concentration: 1.0 mmol/L.

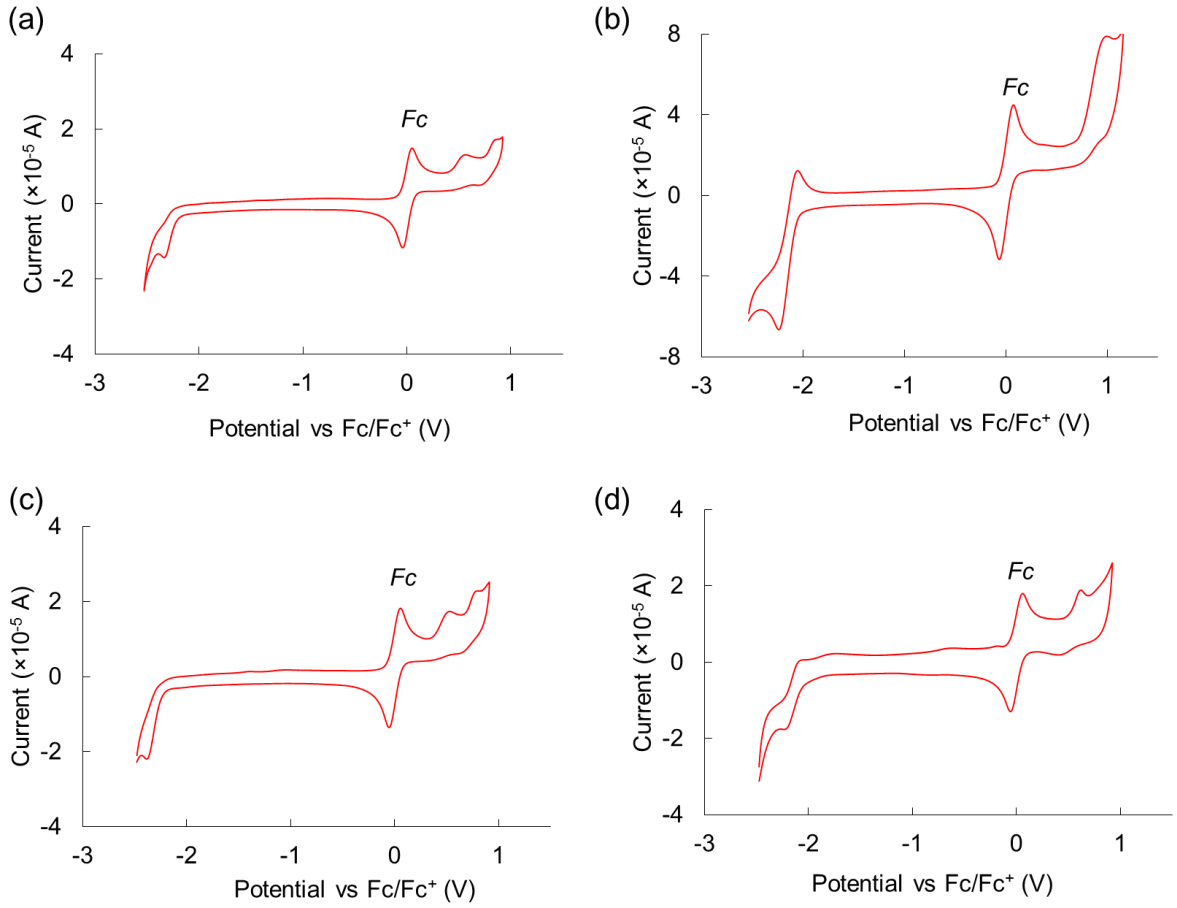

Figure 3.2.14. Cyclic voltammograms of (a) compound **25**, (b) compound **26**, (c) compound **27**, and (d) compound **28**. *Fc*: redox peaks from ferrocene.

3.2.8 Theoretical calculations

To shed light on the electronic characters and transition energies, density functional theory (DFT) and time-dependent DFT (TD-DFT) were conducted using a Gaussian09 package with the B3LYP/6-31G(d) model.[19] Frontier molecular orbitals and their energy level are listed in Figures 3.2.15 and 3.2.16, and the main orbital transitions and oscillator strength *f* are in Tables 3.2.6−3.2.13. The main transition of **21** and **23** was from HOMO to LUMO+1, and that of **22** and **24** was from HOMO to LUMO. As shown in Figure 3.2.15, electron densities of HOMO and LUMO+1 of **21** and **23** were spread overall, and those of HOMO and LUMO of **22** and **24** were located on thiophene or EDOT ring and Si atom. These results insisted that the lowest absorption and emission of **21**−**24** was assignable to π–π* transition.

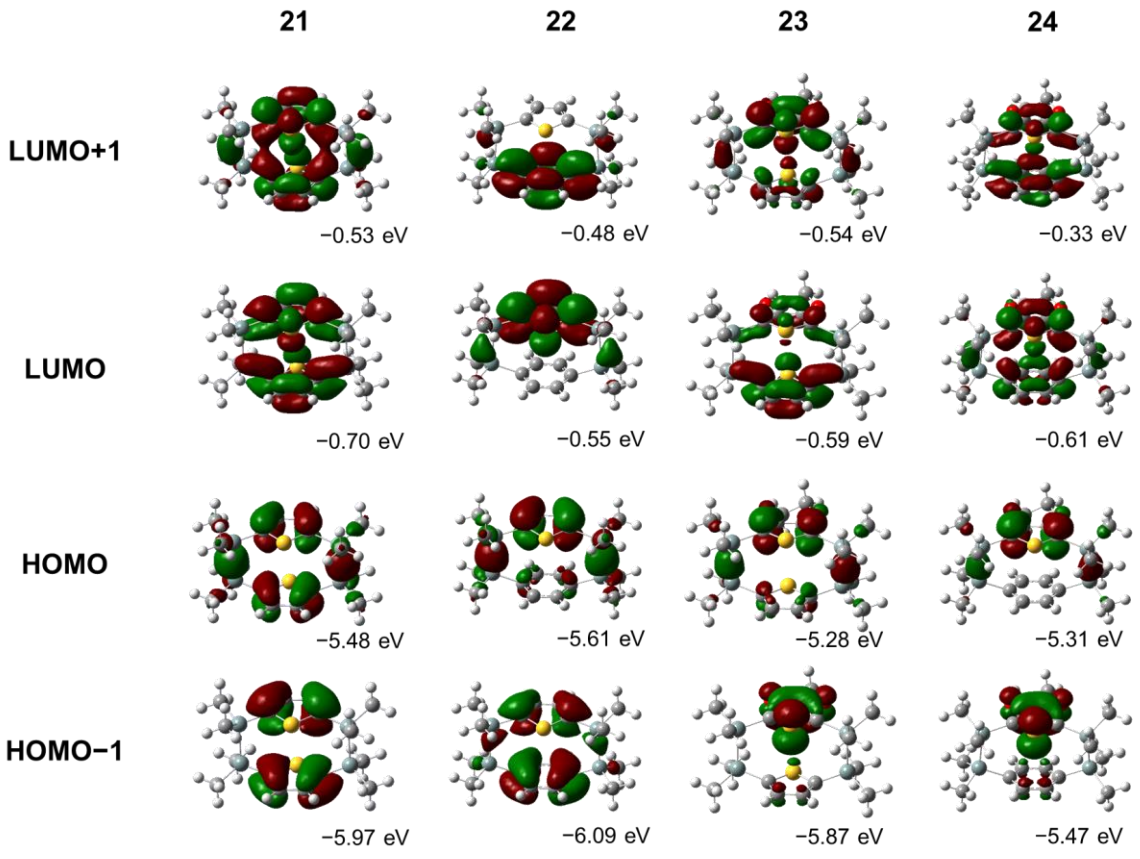

Figure 3.2.15. Frontier molecular orbitals and energy levels for **21**−**24** calculated with DFT at the B3LYP/6-31G(d) level.

In the case of **25** and **27** bearing donor and acceptor moieties, the electron density of HOMO was located on whole molecules, while that of LUMO on acceptor unit (Figure 3.2.16). In both **26** and **28**, HOMO and LUMO are spatially separated to a great extent. The HOMO is located at the donor-substituted thiophene ring with a partial overlap of orbitals at Si–Si bonds, whereas the LUMO is primarily situated on the acceptor-substituted aromatic ring with no contribution of Si–Si bonds. According to TD-DFT calculations, the lowest absorption bands of **25**−**28** were the transition from HOMO to LUMO, assignable to ICT. The lowest-energy vertical transition trends are in good agreement with the UV–vis experimental λ_{max} data trends, giving the following order for dyes from high to low wavelength: **25**, **27** > **26**, **28** > **21**−**24**. The lowest calculated HOMO values of them was –5.65 eV (**26**), roughly consistent with the values estimated from electrochemical measurements. This energy level matched with commonly used hole injection/transport layers such as *N*,*N*'-di-1-naphthyl-*N*,*N*'-diphenylbenzidine (α-NPD) (HOMO level: –5.4 eV).[28]

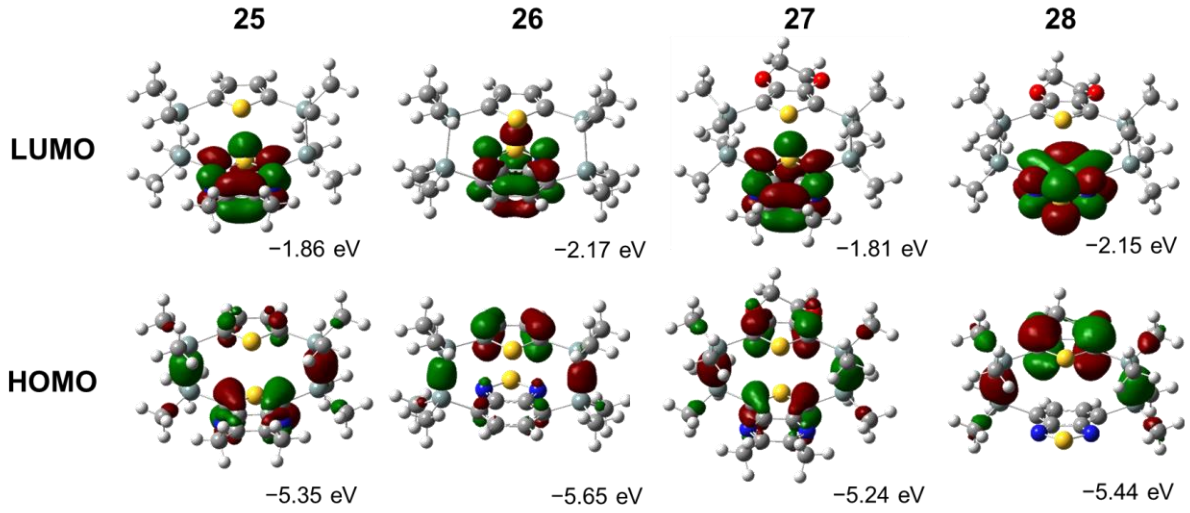

Figure 3.2.16. Frontier molecular orbitals and energy levels for **25**−**28** calculated with DFT at the B3LYP/6-31G(d) level.

Table 3.2.6. Summary of the TD-DFT calculations for **21**

S_1: 304.98 nm			f = 0.0000 [a]
HOMO	→	LUMO	0.69668 [b]
S_2: 283.02 nm			f = 0.1171
HOMO−1	→	LUMO	−0.34037
HOMO	→	**LUMO+1**	**0.61833**
S_3: 256.19 nm			f = 0.4639
HOMO−1	→	LUMO	0.60840
HOMO	→	LUMO+1	0.32855

[a] Oscillator strength. [b] CI expansion coefficients for each excitation.

Table 3.2.7. Summary of the TD-DFT calculations for **22**

S_1: 282.09 nm			f = 0.0015 [a]
HOMO	→	LUMO	0.37138 [b]
HOMO	→	LUMO+1	0.59482
S_2: 273.24 nm			f = 0.1875
HOMO−1	→	LUMO	0.16165
HOMO−1	→	LUMO+1	0.17524
HOMO	→	**LUMO**	**0.54764**
HOMO	→	LUMO+2	−0.37279
S_3: 259.12 nm			f = 0.0042
HOMO−3	→	LUMO+1	0.15630
HOMO−2	→	LUMO+1	−0.39131
HOMO−1	→	LUMO+2	0.21862
HOMO	→	LUMO+2	0.51705

[a] Oscillator strength. [b] CI expansion coefficients for each excitation.

Table 3.2.8. Summary of the TD-DFT calculations for **23**

S_1: 310.26 nm			f = 0.0019 [a]
HOMO	→	LUMO	0.70355 [b]
S_2: 293.62 nm			f = 0.1448
HOMO−2	→	LUMO	0.28322
HOMO	**→**	**LUMO+1**	**0.64042**
S_3: 288.74 nm			f = 0.0101
HOMO−1	→	LUMO	0.59092
HOMO−1	→	LUMO+1	−0.38143

[a] Oscillator strength. [b] CI expansion coefficients for each excitation.

Table 3.2.9. Summary of the TD-DFT calculations for **24**

S_1: 298.72 nm			f = 0.1040 [a]
HOMO	**→**	**LUMO**	**0.61162** [b]
HOMO	→	LUMO+1	−0.34456
S_2: 292.17 nm			f = 0.0080
HOMO−1	→	LUMO	0.66179
HOMO−1	→	LUMO+1	−0.22325
S_3: 284.50 nm			f = 0.0948
HOMO−2	→	LUMO+2	0.14816
HOMO	→	LUMO	0.31969
HOMO	→	LUMO+1	0.60377

[a] Oscillator strength. [b] CI expansion coefficients for each excitation.

Table 3.2.10. Summary of the TD-DFT calculations for **25**

S_1: 420.42 nm			f = 0.0455 [a]
HOMO	**→**	**LUMO**	**0.69273** [b]
HOMO−1	→	LUMO	0.69273
S_2: 375.55 nm			f = 0.0008
HOMO−3	→	LUMO	0.58460
HOMO−2	→	LUMO	0.38335
S_3: 365.63 nm			f = 0.0101
HOMO−1	→	LUMO	0.69285

[a] Oscillator strength. [b] CI expansion coefficients for each excitation.

Table 3.2.11. Summary of the TD-DFT calculations for **26**

S_1: 436.34 nm			f = 0.0205 [a]
HOMO	**→**	**LUMO**	**0.69922** [b]
S_2: 357.75 nm			f = 0.0493
HOMO−1	→	LUMO	0.62162
S_3: 347.64 nm			f = 0.0008
HOMO−2	→	LUMO	0.70482

[a] Oscillator strength. [b] CI expansion coefficients for each excitation.

Table 3.2.12. Summary of the TD-DFT calculations for **27**

S_1: 434.09 nm			f = 0.0351 [a]
HOMO−1	→	LUMO	−0.12884 [b]
HOMO	**→**	**LUMO**	**0.68003**
S_2: 389.78 nm			f = 0.0323
HOMO−2	→	LUMO	0.66977
HOMO−1	→	LUMO	−0.20155
S_3: 386.71 nm			f = 0.0241
HOMO−2	→	LUMO	0.20093
HOMO−1	→	LUMO	0.65728
HOMO	→	LUMO	0.11765

[a] Oscillator strength. [b] CI expansion coefficients for each excitation.

Table 3.2.13. Summary of the TD-DFT calculations for **28**

S_1: 468.66 nm			f = 0.0109 [a]
HOMO	**→**	**LUMO**	**0.70598** [b]
S_2: 430.36 nm			f = 0.0057
HOMO−1	→	LUMO	0.70584
S_3: 372.63 nm			f = 0.0607
HOMO−2	→	LUMO	0.69539

[a] Oscillator strength. [b] CI expansion coefficients for each excitation.

3.2.9 Electroluminescent performance

Organic luminophores have been the hot topic for their applications in OLEDs as described in Chapter 1. Because donor−acceptor tetrasila[2.2]cyclophanes possess good thermal stabilities and satisfactory fluorescence quantum yield in the solid state, especially compound **26**, a preliminary study of electroluminescence characteristics was performed to investigate the usefulness of the compounds. For the fabrication of OLED, compound **26** was selected as a dopant in emitting layer with 4,4'-bis(2,2'-diphenylvinyl)-1,1'-biphenyl (dPVBi), which is widely used as a host material and acts to improve the carrier mobility. Light-emitting devices with the structure ITO/α-NPD/**26**-doped dPVBi/BCP/LiF/Al was fabricated using vapor deposition processes, where α-NPD and BCP were *N*,*N*'-Diphenyl-*N*,*N*'-bis(1-naphthalenyl)-1,1'-biphenyl-4,4'-diamine and bathocupuroin, respectively (chemical structures are shown in Figure 3.2.17). Detailed preparation method is described in Experimental section 3.3.9. ITO acts as anode, α-NPD as hole-injection/transporting layer, **26**-doped dPVBi as emissive layer, BCP as electron-injection/transporting layer, and Al as cathode (Figure 3.2.18). The LiF layer reduced the work function of Al. Figure 3.2.19 shows the schematic energy diagram of the multilayer device.[28−29] The organic materials in emission layer were co-evaporated from two resistively heated evaporation cells. The doping ratio (in weight %) was optimized to be 3% of **26** in the dPVBi matrix (Figure 3.2.20). The effective size of the device was 2 mm × 3 mm.

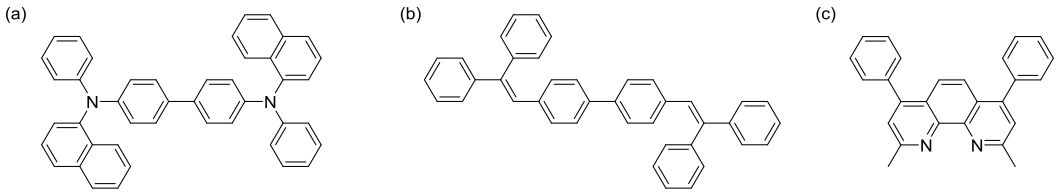

Figure 3.2.17. Molecular structures of organic mateials used for doped OLED; (a) *N*,*N*'-Diphenyl-*N*,*N*'-bis(1-naphthalenyl)-1,1'-biphenyl-4,4'-diamine (α-NPD), (b) 4,4'-bis(2,2'-diphenylvinyl)-1,1'-biphenyl (dPVBi), and (c) bathocupuroin (BCP).

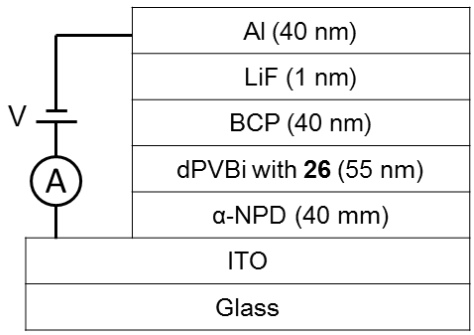

Figure 3.2.18. OLED structure with the detail of the thickness and original material used in each layer.

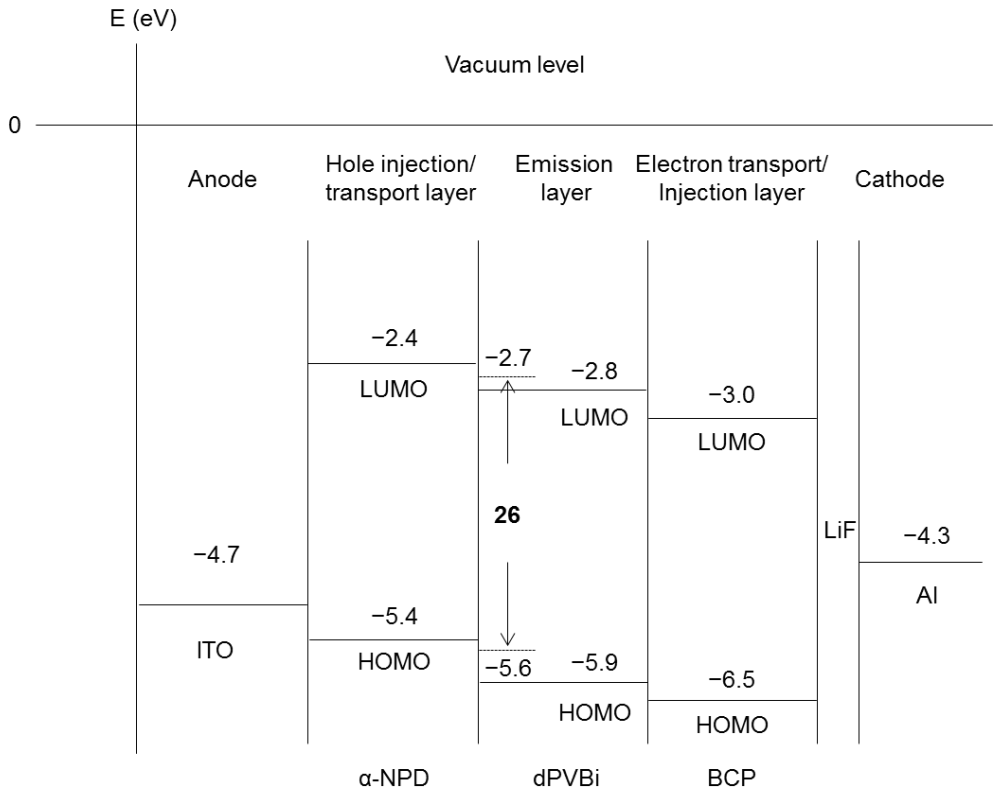

Figure 3.2.19. HOMO−LUMO energy levels of the chemicals and work functions of electrodes of ITO/α-NPD/dPVBi:**26**/BCP/LiF/Al device. The energy level values of α-NPD, and LiF/Al were quoted from the literature.[28a] The energy level values of ITO and BCP were quoted from the literature.[28b] The energy level value of dPVBi was quoted from the literature.[29]

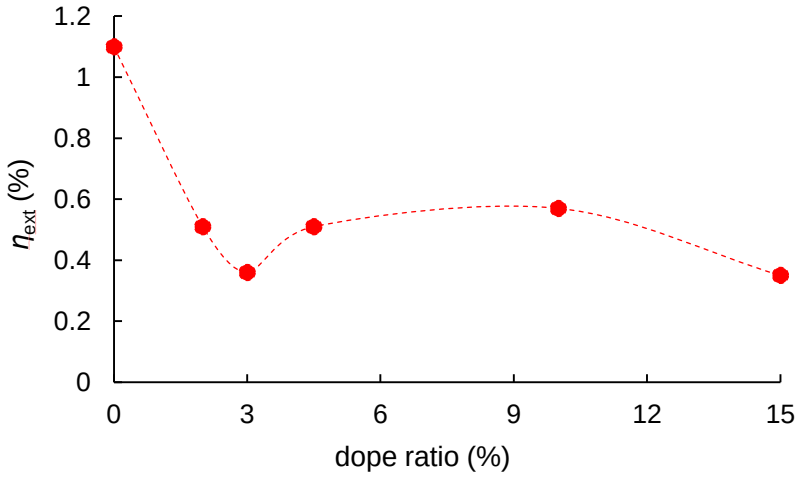

Figure 3.2.20. External quantum efficiency (η_{ext}) *vs* dope ratio of **26** in the ITO/α-NPD /dPVBi:**26**(x%)/BCP/LiF/Al.

The device was characterized based on *I–V* characteristics and emission properties as a function of voltage (Figure 3.3.26). The onset voltage of the electroluminescent device was 10 V, the external quantum efficiency (η_{ext}) was 0.36%, and the power was 90 μW/cm^2 at a current density of 9 mA/cm^2 and a voltage of 18 V. The electroluminescence from dPVBi, which is one of the standard blue fluorescence materials and emits at 470 nm, was not completely eliminated (Figure 3.3.27), because the LUMO level of **26** was slightly higher than that of dPVBi (Figure 3.2.19). Nevertheless, the electroluminescence spectra showed a blue–green emission at 495 nm similar to the corresponding photoluminescence spectra in the solid phase (Figure 3.2.21). As the external quantum efficiency of **26**-undoped OLED was 1.1%, the electroluminescence of **26**-doped OLED with acceptable efficiency (η_{ext} = 0.36%) was achieved with an effective energy transfer from the host material. These results suggested that compound **26** is a promising candidate for the manufacture of electroluminescent devices.

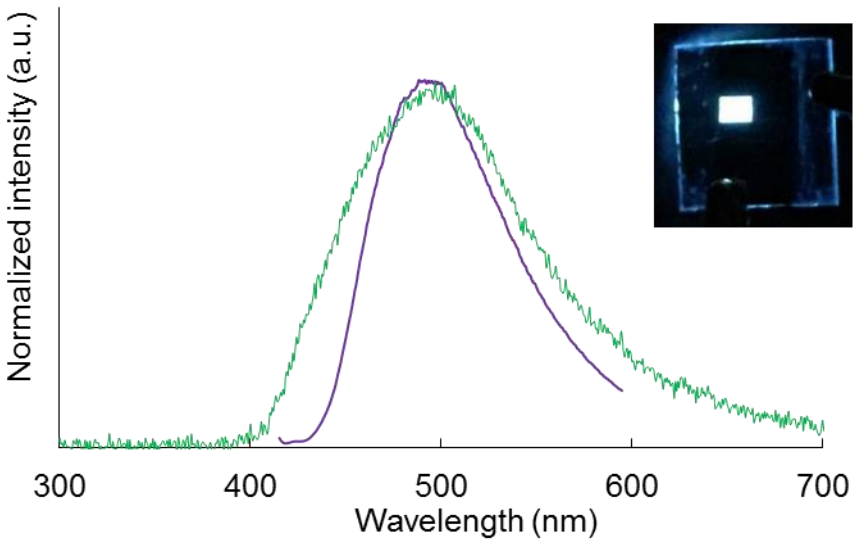

Figure 3.2.21. Electroluminescence spectrum of ITO/α-NPD /dPVBi: **26**(3%)/BCP/LiF/Al (green line) and solid-state emission spectrum of **26** (purple line). Inset: Photograph of electroluminescence from the OLED at 18 V. Reprinted with permission from reference 16. Copyright © 2017 American Chemistry Society.

3.2.10 Planar chiral tetrasila[2.2]cyclophane for CPL materials

Considering the potential for the application of tetrasila[2.2]cyclophanes, optically active compounds with planar chirality would be valuable for CPL materials. As described in previous section, donor−acceptor tetrasila[2.2]cyclophanes with thiadiazole (e.g. **26**) displayed emissive property and no inversion in solution at room temperature according to NMR results, which meant that optically active compounds were not racemized by the inversion. Then I designed planar chiral tetrasila[2.2]cyclophane **31** (in Scheme 3.2.4) for CPL-active compounds, which inserted methyl group into compound **26** for planar chirality.

Racemic **31** was prepared by Pd-catalyzed coupling reaction of **1** and 1,1'-(3-methylthiophene-2,5-diyl)bis(1,1,2,2-tetramethyldisilane) (**30**), which was prepared according to the literature (see experimental section),[17] in 21% yield as shown in Scheme 3.2.4.

Scheme 3.2.4. Preparation scheme of *rac*-**31** by Pd-catalyzed arylation.[a]

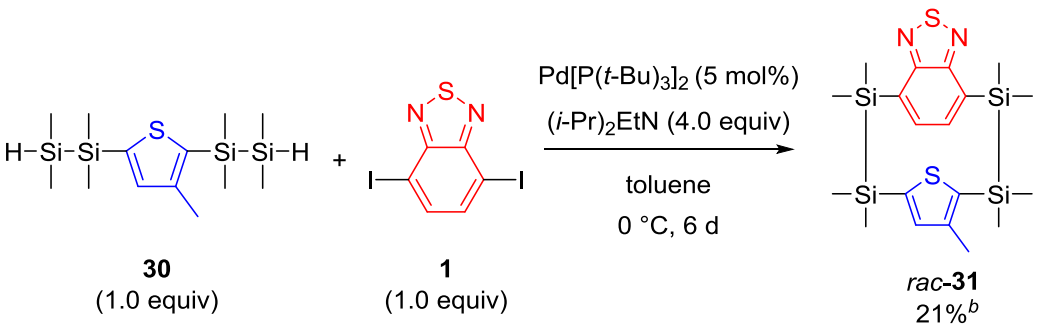

[a] Reaction conditions: **30** (1.0 mmol), **1** (1.0 mmol), Pd[P(*t*-Bu)$_3$]$_2$ (0.050 mmol), *N*,*N*-diisopropylethylamine (4.0 mmol), toluene (15 mL), 0 °C, 6 d. [b] Isolated yields.

Optical pure (*S*)- and (*R*)-**31** (>99% enantiomeric excess) was obtained with a Chiralcel OJ-H column (Figure 3.2.22(a)). The sign of (+) and (−) were determined by optical rotation measurement. By XRD analysis of enantiopure crystals, the absolute structures of (+)-**31** and (−)-**31** were determined as (*S*) and (*R*), respectively (Figures 3.2.22(b), and Tables 3.3.9 and 3.3.10).

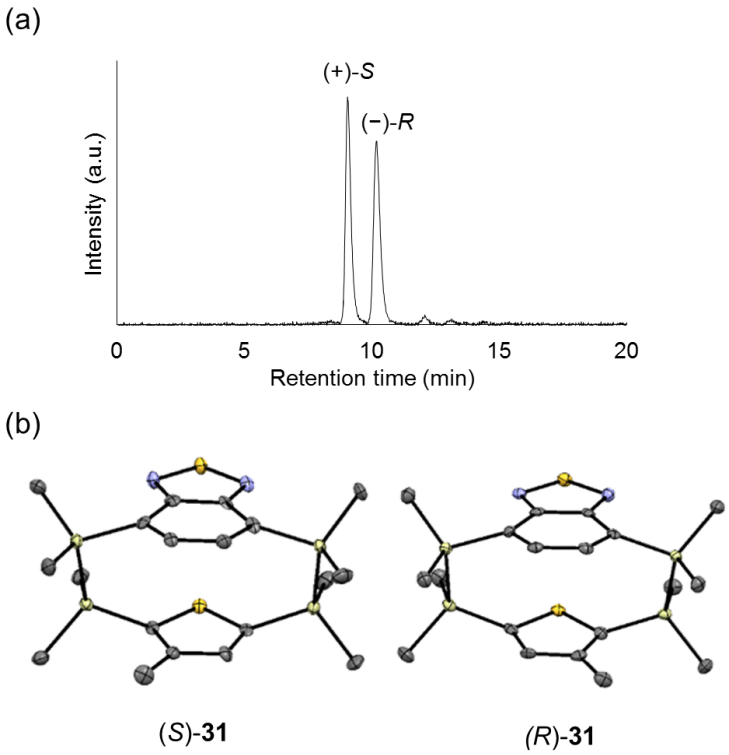

Figure 3.2.22. (a) HPLC chart of *rac*-**31** (eluent: MeOH, flow rate: 1.0 mL/min, detection wavelength of UV absorption: 260 nm). (b) ORTEP drawings (50% probability ellipsoids) of one pattern of (*S*)-**31** and (*R*)-**31**. Hydrogen atoms are omitted for clarity. Adapted with permission from reference 16. Copyright © 2017 American Chemistry Society.

The optical and chiroptical properties of **31** were investigated (Figures 3.2.25 and 3.3.25), and are summarized in Table 3.2.14. In the UV–vis spectrum in cyclohexane, *rac*-**31** exhibited maximum absorbance at 324 and 370 nm, and they emitted green photoluminescence in a cyclohexane solution (496 nm, Φ = 0.05) and in the solid state (507 nm, Φ = 0.09). DFT calculation suggests that the absorption/emission transition was assignable to ICT, similar to compound **26** and **28** (Figure 3.2.24 and Table 3.2.15).

Next, the chiroptical properties, CD and CPL, were investigated. The circular dichroism (CD) spectra of (*S*)-**31** and (*R*)-**31** was a mirror image and displayed clear Cotton effects (Figure 3.2.23(a)). The degree of CD is given by the absorption dissymmetry factor, $g_{abs} = 2(\varepsilon_L - \varepsilon_R)/(\varepsilon_L + \varepsilon_R) = \Delta\varepsilon/\varepsilon$, where ε_L and ε_R are the molar extinction coefficients of the two polarizations, respectively. The maximum g_{abs} values of (*S*)-**31** and (*R*)-**31** at ca. 380 nm were calculated to be $+8.5 \times 10^{-4}$ and -7.8×10^{-4}, respectively.

The CPL spectra of (*S*)-**31** and (*R*)-**31** in cyclohexane are also shown in Figure

3.2.23(b). Opposite CPL signals were observed, and the g_{lum} values were measured as +1.7 × 10^{-3} for (*S*)-**31** and −1.6 × 10^{-3} for (*R*)-**31** at 500 nm. The emitted light was equally polarized in opposite directions by each enantiomer, confirming that the constructed simple organic produced luminescence in solution. The values (the order of $|10^{-3}|$), were comparable to those reported for simple organic chiral molecules.[4,30] It is noted that in the solid phase, there are no detectable CPL peaks. Nevertheless, this compounds (**31**) is the first example of intrinsic CPL from a disilane-bridged planar chiral compound, and this skeleton can be extended for the development of other chiroptical materials.

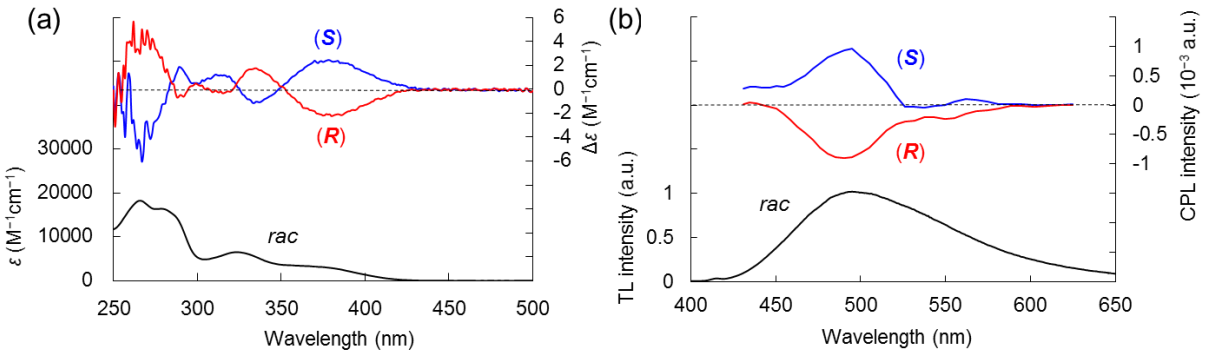

Figure 3.2.23. (a) UV–vis absorption of *rac*-**31** (black line) and CD spectra of (*S*)-**31** (blue line) and (*R*)-**31** (red line) in cyclohexane. Δε: molar CD value. (b) Emission (total luminescence (TL)) of *rac*-**31** (black line) and CPL spectra of (*S*)-**31** (blue line) and (*R*)-**31** (red line) in cyclohexane. TL: I_L+I_R. CPL: I_L−I_R. I_L and I_R: Emission intensity of left and right circularly polarized light. Excitation wavelength for CPL measurements: 370−380 nm. Concentration for CPL measurement: ca. 1.5 × 10^{-5} M. Adapted with permission from reference 16. Copyright © 2017 American Chemistry Society.

Table 3.2.14. Photophysical properties of **31** in cyclohexane

λ_{abs} (nm)	ε (10^4 $M^{-1}cm^{-1}$) [a]	λ_{em} (nm)	Φ [b]	τ (ns) [c]	g_{abs}	g_{lum}
324, 370	0.64, 0.32	496	0.05	1.0 (56%)	+8.5×10^{-4} (*S*, 379 nm)	+1.7×10^{-3} (*S*, 500 nm)
				7.4 (44%)	−7.8×10^{-4} (*R*, 380 nm)	−1.6×10^{-3} (*R*, 500 nm)

[a] Molar extinction coefficient at λ_{abs}. [b] Absolute quantum yields determined by an integrating sphere system. [c] Fluorescence lifetime detected at the maximum fluorescence wavelengths excited at 365 nm.

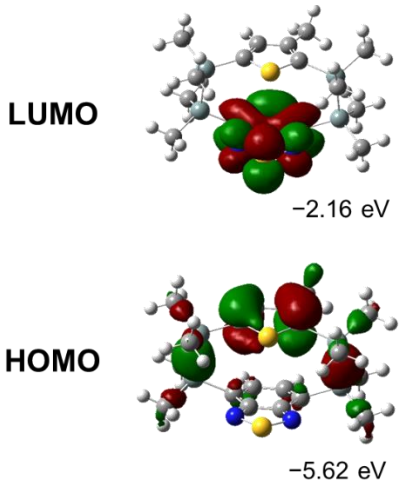

Figure 3.2.24. Frontier molecular orbitals and energy levels for **31** calculated with DFT at the B3LYP/6-31G(d) level.

Table 3.2.15. Summary of the TD-DFT calculations for **31**

S_1: 438.65 nm			f = 0.0153 [a]
HOMO	**→**	**LUMO**	**0.70490** [b]
S_2: 368.35 nm			f = 0.0540
HOMO−1	→	LUMO	0. 68964
S_3: 356.17 nm			f = 0.0194
HOMO−2	→	LUMO	0. 69326

[a] Oscillator strength. [b] CI expansion coefficients for each excitation.

3.3 Experimental section

3.3.1 General

(a) Materials.

Chemicals were purchased from commercial sources and used as received unless otherwise noted. All reactions were carried out under argon atmosphere. Solvents for the synthesis were used from a solvent purification system. Spectroscopically pure cyclohexane was used for measurement of optical spectra of samples. *N*,*N*-Diisopropylethylamine was distilled before use. **1**, **2**, **12**, and **13** were prepared according to the previous work described in Chapter 2.[17] $[Ag_2\mathbf{L}X_2](SbF_6)_2$ (X = Et_2O or H_2O) was prepared according to previously reported procedures.[24c]

(b) Characterization.

Melting points (Mp) were recorded on a Yanaco melting point apparatus and were uncorrected. NMR spectra were recorded on a Bruker US-500 spectrometer for compound **21**−**28**, **30**, and **31**, and a Bruker AVANCE 500 spectrometer for **21**⊂$[Ag_2\mathbf{L}](SbF_6)_2$, respectively. Tetramethylsilane ($\delta = 0.00$) was used as an internal standard for ^{1}H NMR spectra, and $CDCl_3$ ($\delta = 77.0$) was used as an internal standard for ^{13}C NMR spectra. Gel permeation chromatographic (GPC) separation was carried out with a JAI LC-9210II NEXT Recycling Preparative HPLC equipped a JAIGEL-GPC 1H+2H column. HPLC for chiral analysis and chiral separation of **31** was carried out using a JASCO LC-2000Plus with a Daicel OJ-H column and a LC-9210II NEXT equipped with a Daicel OJ-H semi-preparative column, respectively. GC-MS spectra were recorded with a Shimadzu GC-MS-QP2010 spectrometer. FAB-MS was performed with a JEOL MStation JMS-700 spectrometer. ESI-TOF mass spectra were recorded on a Micromass LCT spectrometer. UV–vis absorption spectra were measured with a JASCO V-570 spectrometer. Fluorescence spectra and absolute quantum yields were measured with a Hitachi F-4500 spectrometer, a JASCO F-8600 spectrometer, and a Hamamatsu C9920-02 spectrometer. Fluorescence lifetimes were measured with a Hamamatsu Quantaurus-Tau C11367 spectrometer. Circular Dichroism spectra were recorded with a JASCO J-1500 spectrometer. Optical rotation was measured with a JASCO P-1030 Polarimeter. The CPL spectra were recorded by using a lab-made CPL measurement system, the details of which have been reported previously.[31] The sample solution was circulated through a 10-mm-thick quartz cell. Cyclic voltammograms were recorded with BAS ALS-650DT using Ag^+/Ag reference, glassy-carbon

working, and Pt wire counter electrodes. Potentials are reported with reference to an internal standard of ferrocenium/ferrocene. Thermogravimetric analyses (TGA) were measured with a Rigaku Thermoplus TG-8120. The thermal stability of the samples under nitrogen atmosphere was determined by measuring their weight loss while heating at a rate of 10 °C/min from room temperature to 500 °C. The most stable conformers and energy transitions identified were calculated by DFT and TD-DFT computations that were performed by the Gaussian09 revision E.01 program using B3LYP/6-31G(d).[19]

(c) ^{13}C CP/MAS NMR measurement of compound 21.

The compound **21** sample (47.4 mg) was packed into a 4 mm zirconia rotor and measured with ^{13}C cross polarization/magic angle spinning (CP/MAS) NMR at 300, 310, and 323 K using a spectrometer (Bruker AVANCE III HD 600WB) at Larmor frequency of 150 MHz. Bruker MAS probe head was used with a 4 mm zirconia rotor and a sample spin rate was 8 kHz. The frequency of the spectra was expressed with respective to pure tetramethylsilane (TMS). Experimentally, glycine was used as a second reference material, the carbonyl signal of which was set at 176.46 ppm.

(d) X-ray crystallographic analysis.

Single crystals for X-ray diffraction were prepared using the following conditions:

i. **21** and **28**: Recrystallization from hexane at room temperature
ii. **25** and **26**: Recrystallization from CH_3CN at room temperature
iii. (*S*)-**31** and (*R*)-**31**: Recrystallization from methanol at −30 °C
iv. **21**⊂$[Ag_2\mathbf{L}](SbF_6)_2$: Recrystallization by vapor diffusion of Et_2O/CH_2Cl_2 at room temperature

X-ray diffraction data of **21** and **25** were collected at 113 K with an AFC10 diffractometer coupled with a Rigaku Saturn CCD system equipped with a rotating-anode X-ray generator producing graphite-monochromated MoKα radiation (λ = 0.7107 Å). Lorentz-polarization and empirical absorption corrections were performed with the program Crystal Clear 1.3.6. X-ray diffraction data of **26**, **28**, (*S*)-**31**, and (*R*)-**31** were collected at 93 K on a Rigaku Saturn724 (Varimax dual) diffractometer with multi-layer mirror monochromated MoKα radiation (λ = 0.71075 Å). Lorentz-polarization and empirical absorption corrections were performed with the program Crystal Clear 2.0. The structures were solved by the direct method using SIR-

92 program (**21**, **26**, **28**, and (*R*)-**31**),[32] SHELX-97 program (**25**),[33] or SIR-2004 program ((*S*)-**31**),[34] and refined by full-matrix least-squares techniques against F^2 using SHELXL-97.[33]

Single-crystal X-ray crystallographic analyses of **21**⊂[Ag_2**L**](SbF_6)$_2$ were performed at 93 K using a Rigaku RAXIS-RAPID imaging plate diffractometer with MoKα radiation (λ = 0.7107 Å), and the obtained data were calculated with a Crystal Structure crystallographic software package except for refinement, which was refined by full-matrix least-squares techniques against F^2 using SHELXL-2013.[35]

Crystallographic data for the structure of **21**, **25**, **26**, **28**, **21**⊂[Ag_2**L**](SbF_6)$_2$, (*S*)-**31** and (*R*)-**31** have been deposited with the Cambridge Crystallographic Data Centre as supplementary publication nos. CCDC 1510008, 1510009, 1509992, 1510012, 1510024, 1510174, and 1510175, respectively.

3.3.2 Synthesis

(a) Experimental procedure for the preparation of 1,1'-(3-methylthiophene-2,5-diyl)bis(1,1,2,2-tetramethyldisilane) (30).

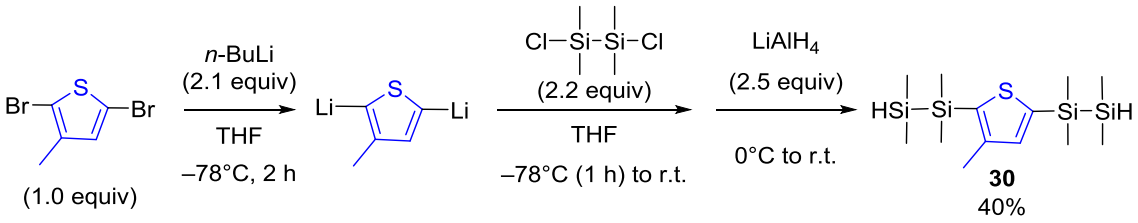

The starting material **30** was prepared by the modification method based on the literature.[17] Under an argon atmosphere, a solution of 1.6 M *n*-BuLi in hexane (29.1 mL, 46.6 mmol) was added dropwise to a solution of 2,5-dibromo-3-methylthiophene (5.0 g, 22.2 mmol) in THF (100 mL) at –78 °C for 20 min, and reaction mixture was stirred at –78 °C for 2 h to give dilithiated reagent. This solution was added slowly to a solution of 1,2-dichloro-1,1,2,2-tetramethyldisilane (8.75 mL, 49 mmol) in THF (100 mL) at –78 °C for 1 h, then the reaction mixture was warmed to room temperature. The mixture was cooled to 0 °C, and $LiAlH_4$ (2.1 g, 55 mmol) was added. The reaction mixture was warmed to room temperature and stirred overnight. The reaction mixture was quenched with water and extracted with diethyl ether three times. The organic layer was washed with brine and dried over sodium sulfate. The solvent was evaporated in vacuo and the residue was purified by distillation (120 °C, 1.0 mmHg) to give **30** (2.93 g, 8.9 mmol) as colorless oil in 40% yield.

1,1'-(3-methylthiophene-2,5-diyl)bis(1,1,2,2-tetramethyldisilane) (30): Isolated yield of analytically pure product: 40%. Colorless oil. ^{1}H NMR (500 MHz, $CDCl_3$) δ 7.06 (s, 1H), 3.80 (septet, 1H, *J* = 4.5 Hz), 3.74 (septet, 1H, *J* = 4.5 Hz), 2.33 (s, 3H), 0.42 (s, 6H), 0.38 (s, 6H), 0.16–0.15 (m, 12H). ^{13}C NMR (125 MHz, $CDCl_3$) δ 146.0 (C_q), 143.2 (C_q), 139.1 (CH), 137.5 (C_q), 16.4 (CH_3), –2.1 (CH_3), –2.3 (CH_3), –6.4 (CH_3), –6.6 (CH_3). FAB–MS *m/z* 329 ($[M–H]^+$). FAB–HRMS Calcd for $C_{13}H_{29}Si_4S$: 329.1067. Found: 329.1089 ($[M–H]^+$).

(b) Experimental procedure for the preparation of octamethyltetrasila[2.2]cyclophanes.

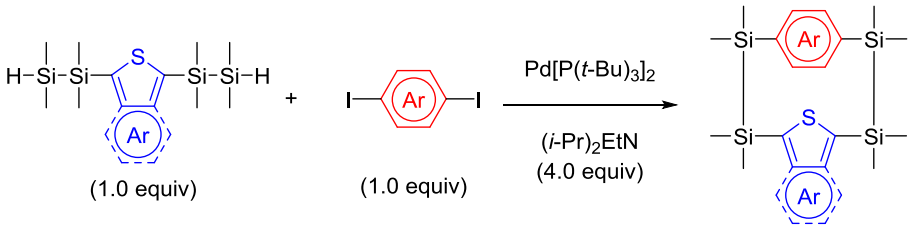

Condition A: Bis(1,1,2,2-teramethyldisilylanyl)arenes (1.0 mmol), aryl iodide (1.0 mmol) and *N*,*N*-diisopropylethylamine (4.0 mmol) was added to solution of Pd[P(*t*-Bu)$_3$]$_2$ (0.025 mmol) in *m*-xylene (15 mL) under Ar. The reaction mixture was stirred at 0 °C for 2 d. After the disappearance of starting materials, the reaction was quenched with water, extracted with CH_2Cl_2, and dried over Na_2SO_4. Solvent was removed under reduced pressure, and the residue was purified by preparative TLC (SiO_2) to afford crude product of octamethyltetrasila[2.2]cyclophanes. Analytically pure product was obtained by the purification with GPC (eluent: $CHCl_3$).

Condition B: similar to condition A but with Pd[P(*t*-Bu)$_3$]$_2$, 0.050 mmol; solvent, toluene (15 mL); reaction temperature, 0 °C; reaction time, 6 d.

Condition C: similar to condition A but with Pd[P(*t*-Bu)$_3$]$_2$, 0.025 mmol; solvent, *m*-xylene (15 mL); reaction temperature, –5 °C; reaction time, 5 d.

1,1,2,2,8,8,9,9-octamethyl-1,2,8,9-tetrasila[2.2](2.5)thiophenophane (21): Prepared under condition A. Colorless solid. GC yield: 20%. Isolated yield of analytically pure product: 9%. Colorless solid. Decomposition point: 172.0 °C. ^{1}H NMR (500 MHz, $CDCl_3$) δ 7.20 (s, 4H), 0.47 (brs, 12H), 0.35 (brs, 12H). ^{13}C NMR (125 MHz, $CDCl_3$) δ 148.1 (C_q), 134.6 (CH), –4.1 (CH_3), –4.6 (CH_3). FAB–MS *m/z* 396 (M^+). FAB–HRMS Calcd for $C_{16}H_{28}S_2Si_4$: 396.0710. Found: 396.0695 (M^+).

1,1,2,2,9,9,10,10-octamethyl-1,2,9,10-tetrasila[2.2]paracyclo(2.5)thiophenophane (22): Prepared under condition A. Colorless solid. GC yield: 10%. Isolated yield of analytically pure product: 4%. Decomposition point: 175.0 °C. ^{1}H NMR (500 MHz, $CDCl_3$) δ 6.95 (s, 4H), 6.90 (s, 2H), 0.46 (s, 12H), 0.39 (s, 12H). ^{13}C NMR (125 MHz, $CDCl_3$) δ 148.8 (C_q), 138.0 (C_q), 133.4 (CH), 132.7 (CH), –3.3 (CH_3), –5.3 (CH_3). FAB–MS *m/z* 391 ($[M+H]^+$). FAB–HRMS Calcd for $C_{18}H_{31}SSi_4$: 391.1224. Found: 391.1214 ($[M+H]^+$).

1,1,2,2,8,8,9,9-octamethyl-1,2,8,9-tetrasila[2.2](2.5)thiopheno(2.5)3,4-ethylenedioxythiophenophane (23): Prepared under condition A. Colorless solid. GC yield: 14%. Isolated yield

of analytically pure product: 9%. Mp: 235.0−237.8 °C. ^{1}H NMR (500 MHz, $CDCl_3$) δ 7.15 (s, 2H), 4.21 (brs, 4H), 0.46 (brs, 18H), 0.22 (brs, 6H). ^{13}C NMR (125 MHz, $CDCl_3$) δ 149.4 (C_q), 147.3 (C_q), 134.4 (CH), 119.3 (C_q), 64.4 (CH_2), –3.4 (CH_3), –3.9 (CH_3), –4.4 (CH_3), –5.4 (CH_3). FAB–MS *m/z* 454 (M^+). FAB–HRMS Calcd for $C_{18}H_{30}O_2S_2Si_4$: 454.0765. Found: 454.0761 (M^+).

1,1,2,2,9,9,10,10-octamethyl-1,2,9,10-tetrasila[2.2]paracyclo(2.5)3,4-ethylenedioxythiophenophane (24): Prepared under condition A. Colorless solid. GC yield: 12%. Isolated yield of analytically pure product: 8%. Mp: 215.0−218.0 °C. ^{1}H NMR (500 MHz, $CDCl_3$) δ 7.10 (s, 4H), 4.15 (s, 4H), 0.48 (s, 12H), 0.33 (s, 12H). ^{13}C NMR (125 MHz, $CDCl_3$) δ 148.0 (C_q), 138.6 (C_q), 132.5 (CH), 118.7 (C_q), 64.1 (CH_2), –4.0 (CH_3), –5.1 (CH_3). FAB–MS *m/z* 448 (M^+). FAB–HRMS Calcd for $C_{20}H_{32}O_2SSi_4$: 448.1200. Found: 448.1224 (M^+).

1,1,2,2,8,8,9,9-octamethyl-1,2,8,9-tetrasila[2.2](2.5)thiopheno(5.7)2,3-dimethylthieno[3,4-*b*]pyrazinophane (25): Prepared under condition A. Yellow solid. GC yield: 15%. Isolated yield of analytically pure product: 5%. Mp: 192.0−198.0 °C. ^{1}H NMR (500 MHz, $CDCl_3$) δ 7.08 (s, 2H), 2.63 (s, 6H), 0.64 (brs, 12H), 0.38 (brs, 12H). ^{13}C NMR (125 MHz, $CDCl_3$) δ 151.5 (C_q), 150.4 (C_q), 146.8 (C_q), 138.8 (C_q), 134.3 (CH), 23.6 (CH_3), –2.7 (CH_3), –3.9 (CH_3). FAB–MS *m/z* 476 (M^+). FAB–HRMS Calcd for $C_{20}H_{32}N_2S_2Si_4$: 476.1084. Found: 476.1099 (M^+).

1,1,2,2,8,8,9,9-octamethyl-1,2,8,9-tetrasila[2.2](2.5)thiopheno(4.7)2,1,3-benzothiadiazolophane (26): Prepared under condition B. Pale yellow solid. Isolated yield of analytically pure product: 19%. Mp: 182.0−183.6 °C. ^{1}H NMR (500 MHz, $CDCl_3$) δ 7.30 (s, 2H), 6.47 (s, 2H), 0.82 (s, 6H), 0.53 (s, 6H), 0.45 (s, 6H), 0.31 (s, 6H). ^{13}C NMR (125 MHz, $CDCl_3$) δ 158.9 (C_q), 144.6 (C_q), 135.5 (CH), 134.3 (C_q), 133.3 (CH), –2.8 (CH_3), –3.1 (CH_3), –3.3 (CH_3), –5.2 (CH_3). FAB–MS *m/z* 449 ($[M+H]^+$). FAB–HRMS Calcd for $C_{18}H_{29}N_2S_2Si_4$: 449.08249. Found: 449.0825 ($[M+H]^+$).

1,1,2,2,8,8,9,9-octamethyl-1,2,8,9-tetrasila[2.2](2.5)3,4-ethylenedioxythiopheno(5.7)2,3-dimethylthieno[3,4-*b*]pyrazinophane (27): Prepared under condition C. Yellow solid. GC yield: 11%. Isolated yield of analytically pure product: 5%. Mp: 228.0−231.0 °C. ^{1}H NMR (500 MHz, $CDCl_3$) δ 4.22 (brs, 4H), 2.60 (s, 6H), 0.76−0.22 (m, 24H). ^{13}C NMR (125 MHz, $CDCl_3$) δ 151.2 (C_q), 150.2 (C_q), 148.6 (C_q), 138.2 (C_q), 118.4 (C_q), 64.4 (CH_2), 23.6 (CH_3), −3.8 (br, 2CH_3). FAB−MS *m/z* 534 (M^+). FAB-HRMS Calcd for $C_{22}H_{34}N_2O_2S_2Si_4$: 534.1139. Found: 534.1129 (M^+).

1,1,2,2,8,8,9,9-octamethyl-1,2,8,9-tetrasila[2.2](2.5)3,4-ethylenedioxythiopheno(4.7)2,1,3-

benzothiadiazolophane (28): Prepared under condition B. Yellow solid. Isolated yield of analytically pure product: 22%. Mp: 239.0−240.5 °C. ^{1}H NMR (500 MHz, $CDCl_3$) δ 7.28 (s, 2H), 4.12–4.02 (m, 4H), 0.80 (s, 6H), 0.58 (s, 6H), 0.36 (s, 6H), 0.31 (s, 6H). ^{13}C NMR (125 MHz, $CDCl_3$) δ 159.5 (C_q), 147.7 (C_q), 134.7 (CH), 134.3 (C_q), 116.3 (C_q), 64.1 (CH_2), −3.36 (CH_3), −3.42 (CH_3), −3.6 (CH_3), −4.5 (CH_3). FAB−MS *m/z* 507 ($[M+H]^+$). FAB-HRMS Calcd for $C_{20}H_{31}N_2O_2S_2Si_4$: 507.0904. Found: 507.0880 ($[M+H]^+$).

1,1,2,2,8,8,9,9-octamethyl-1,2,8,9-tetrasila[2.2](2.5)3,4-ethylenedioxythiopheno(4.7)-5-methyl-2,1,3-benzothiadiazolophane (31): Prepared under condition B. Pale yellow solid. Isolated yield of analytically pure product (racemate): 21%. Mp: 151.3−154.0 °C (racemic compound), 158.5–160.8 °C (chiral compound). ^{1}H NMR (500 MHz, $CDCl_3$) δ 7.30 (d, 1H, *J* = 6.3 Hz), 7.24 (d, 1H, *J* = 6.3 Hz), 6.28 (s, 1H), 2.07 (s, 3H), 0.88 (s, 3H), 0.82 (s, 3H), 0.57 (s, 3H), 0.52 (s, 3H), 0.419 (s, 3H), 0.417 (s, 3H), 0.37 (s, 3H), 0.30 (s, 3H). ^{13}C NMR (125 MHz, $CDCl_3$) δ 159.13 (C_q), 159.07 (C_q), 144.9 (C_q), 143.5 (C_q), 138.6 (C_q), 137.4 (CH), 135.6 (CH), 134.9 (CH), 134.1 (C_q), 134.0 (C_q), 16.3 (CH_3), −2.0 (CH_3), −2.5 (CH_3), −2.65 (CH_3), −2.71 (CH_3), −3.2 (CH_3), −3.3 (CH_3), −4.5 (CH_3), −5.2 (CH_3). FAB−MS *m/z* 463 ($[M+H]^+$). FAB−HRMS Calcd for $C_{19}H_{31}N_2S_2Si_4$: 463.1006. Found: 463.1010 ($[M+H]^+$). HPLC (OJ-H, methanol, flow rate = 1.0 mL/min) t_1 = 9.0 min (+, *S*) and t_2 = 10.2 min (–, *R*). (*S*)-**9**: $[\alpha]_D^{25}$ = +41.9 (*c* = 3.0 g/L, CH_2Cl_2). (*R*)-**9**: $[\alpha]_D^{25}$ = –38.5 (*c* = 3.1 g/L, CH_2Cl_2).

3.3.3 Crystallographic data

(a) Crystal structures of **21**⊂[Ag_2**L**](SbF_6)$_2$

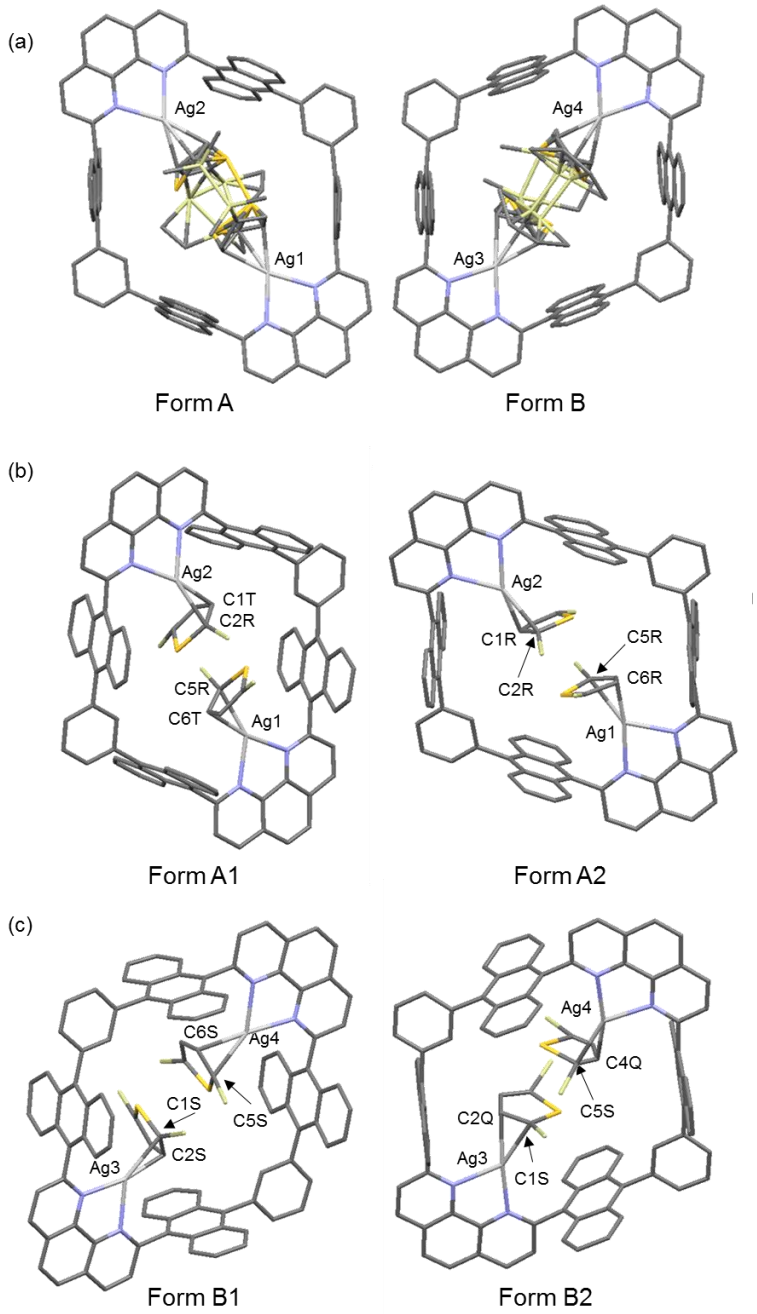

Figure 3.3.1. (a) Lattice structure of **21**⊂[Ag_2**L**](SbF_6)$_2$. (b) Two disordering patterns of Form A. Occupancies of A1 and A2 is 0.538 and 0.462, respectively. (c) Two disordering patterns of Form B. Occupancies of B1 and B2 is 0.707 and 0.293, respectively. Side alkyl-chains of **L**, several Si–Si bonds and methyl groups of **21**, counter anions, solvent molecules, and hydrogen atoms are omitted for clarity.

(b) Crystallographic data

Table 3.3.1. Selected crystallographic data of **21**

Empirical formula	$C_{16}H_{28}S_2Si_4$
Fw / g mol^{-1}	396.86
Crystal system	monoclinic
Space group	$P2_1/n$
Crystal size / mm	0270 × 0.160 × 0.120
Temperature / K	113
a / Å	6.8068(5)
b / Å	13.8764(10)
c / Å	11.7221(8)
α / º	90
β / º	97.501(5)
γ / º	90
V / Å^3	1097.7(2)
Z	2
D_{calcd} / g cm^{-3}	1.201
λ / Å	0.71070
μ / mm^{-1}	0.4561
Reflections collected	8405
Independent reflections	2504
Parameters	100
R_{int}	0.0357
R_1 ($I > 2.00\sigma$ (I)) [a]	0.395
wR_2 (All reflections) [b]	0.0830
GoF [c]	1.099

[a] $R_1 = \Sigma||Fo| - |Fc||/\Sigma|Fo|$ ($I > 2\sigma$ (I)). [b] $wR_2 = [\Sigma(w(Fo^2 - Fc^2)^2/\Sigma w(Fo^2)^2]^{1/2}$ ($I > 2\sigma$ (I)). [c] GoF = $[\Sigma(w(Fo^2 - Fc^2)^2/\Sigma(Nr - Np)^2]$

Table 3.3.2. Selected bond lengths and angles of **21**

Bond lengths / Å	
Si2−Si3	2.3621(8)
Si2−C5	1.868(2)
Si2−C9	1.872(3)
Si2−C11	1.869(3)
Si3−C7	1.8727(19)
Si3−C8	1.869(3)
Si3−C10	1.868(3)
Angles / °	
Si2−Si3−C7	104.45(7)
Si3−Si2−C5	105.80(7)

Table 3.3.3. Selected crystallographic data of **25**

Empirical formula	$C_{20}H_{32}N_2S_2Si_4$
Fw / g mol^{-1}	476.95
Crystal system	triclinic
Space group	$P\bar{1}$
Crystal size / mm	0.300 × 0.100 × 0.050
Temperature / K	133
a / Å	8.327(5)
b / Å	11.182(6)
c / Å	14.842(9)
α / º	74.59(2)
β / º	88.77(3)
γ / º	79.46(3)
V / Å^3	1309.4(13)
Z	2
D_{calcd} / g cm^{-3}	1.210
λ / Å	0.71070
μ / mm^{-1}	0.3958
Reflections collected	9639
Independent reflections	5233
Parameters	253
R_{int}	0.0643
R_1 ($I > 2.00\sigma$ (I)) [a]	0.0798
wR_2 (All reflections) [b]	0.2085
GoF [c]	1.090

[a] $R_1 = \Sigma||Fo| - |Fc||/\Sigma|Fo|$ ($I > 2\sigma$ (I)). [b] $wR_2 = [\Sigma(w(Fo^2 - Fc^2)^2/\Sigma w(Fo^2)^2]^{1/2}$ ($I > 2\sigma$ (I)). [c] GoF = $[\Sigma(w(Fo^2 - Fc^2)^2/\Sigma(Nr - Np)^2]$

Table 3.3.4. Selected bond lengths and angles of **25**

Bond lengths / Å	
Si3−Si5	2.363(3)
Si4−Si6	2.361(3)
Si3−C24	1.865(5)
Si3−C25	1.865(6)
Si3−C26	1.864(7)
Si4−C19	1.869(6)
Si4−C20	1.871(7)
Si4−C21	1.871(5)
Si5−C9	1.877(5)
Si5−C27	1.848(6)
Si5−C28	1.879(6)
Si6−C12	1.874(6)
Si6−C17	1.863(6)
Si6−C18	1.873(6)
Angles / °	
Si6−Si4−C21	102.58(16)
Si4−Si6−C12	103.93(17)
Si3−Si5−C9	102.84(16)
Si5−Si3−C24	104.27(17)

Table 3.3.5. Selected crystallographic data of **26**

Empirical formula	$C_{18}H_{28}N_2S_2Si_4$
Fw / g mol^{-1}	448.89
Crystal system	monoclinic
Space group	$P2_1/n$
Crystal size / mm	0.350 × 0.180 × 0.130
Temperature / K	93
a / Å	8.437(3)
b / Å	11.874(4)
c / Å	23.696(8)
α / º	90
β / º	98.704(4)
γ / º	90
V / Å^3	2346.5(14)
Z	4
D_{calcd} / g cm^{-3}	1.271
λ / Å	0.71075
μ / mm^{-1}	0.4374
Reflections collected	17536
Independent reflections	5328
Parameters	235
R_{int}	0.0467
R_1 ($I > 2.00\sigma$ (I)) [a]	0.0364
wR_2 (All reflections) [b]	0.0904
GoF [c]	1.062

[a] $R_1 = \Sigma||Fo| - |Fc||/\Sigma|Fo|$ ($I > 2\sigma$ (I)). [b] $wR_2 = [\Sigma(w(Fo^2 - Fc^2)^2/\Sigma w(Fo^2)^2]^{1/2}$ ($I > 2\sigma$ (I)). [c] GoF = $[\Sigma(w(Fo^2 - Fc^2)^2/\Sigma(Nr - Np)^2]$

Table 3.3.6. Selected bond lengths and angles of **26**

Bond lengths / Å	
Si3−Si4	2.3761(9)
Si5−Si6	2.3711(9)
Si3−C10	1.8702(17)
Si3−C19	1.867(2)
Si3−C21	1.869(2)
Si4−C16	1.8748(19)
Si4−C18	1.8822(18)
Si4−C20	1.873(2)
Si5−C15	1.8678(19)
Si5−C22	1.870(2)
Si5−C25	1.8700(18)
Si6−C11	1.8817(17)
Si6−C14	1.872(2)
Si6−C26	1.8724(19)
Angles / °	
Si3−Si4−C18	103.45(6)
Si4−Si3−C10	107.12(6)
Si5−Si6−C11	103.32(6)
Si6−Si5−C15	106.82(6)

Table 3.3.7. Selected crystallographic data of **28**

Empirical formula	$C_{20}H_{30}N_2O_2S_2Si_4$
Fw / g mol^{-1}	506.93
Crystal system	monoclinic
Space group	$P2_1/n$
Crystal size / mm	0.170 × 0.160 × 0.050
Temperature / K	93
a / Å	8.156(4)
b / Å	13.965(6)
c / Å	22.5205(10)
α / º	90
β / º	94.157(8)
γ / º	90
V / Å^3	2558(2)
Z	4
D_{calcd} / g cm^{-3}	1.316
λ / Å	0.71075
μ / mm^{-1}	0.4151
Reflections collected	18742
Independent reflections	5503
Parameters	269
R_{int}	0.0476
R_1 ($I > 2.00\sigma$ (I)) [a]	0.0501
wR_2 (All reflections) [b]	0.1128
GoF [c]	1.097

[a] $R_1 = \Sigma||Fo| - |Fc||/\Sigma|Fo|$ ($I > 2\sigma$ (I)). [b] $wR_2 = [\Sigma(w(Fo^2 - Fc^2)^2/\Sigma w(Fo^2)^2]^{1/2}$ ($I > 2\sigma$ (I)). [c] GoF = $[\Sigma(w(Fo^2 - Fc^2)^2/\Sigma(Nr - Np)^2]$

Table 3.3.8. Selected bond lengths and angles of **28**

Bond lengths / Å	
Si3−Si5	2.3873(15)
Si4−Si6	2.3799(16)
Si3−C12	1.868(3)
Si3−C16	1.870(3)
Si3−C24	1.872(3)
Si4−C19	1.872(3)
Si4−C20	1.886(3)
Si4−C23	1.873(3)
Si5−C13	1.884(3)
Si5−C17	1.871(3)
Si5−C27	1.873(3)
Si6−C11	1.868(3)
Si6−C21	1.871(4)
Si6−C26	1.871(3)
Angles / °	
Si6−Si4−C20	102.75(9)
Si4−Si6−C11	103.21(9)
Si3−Si5−C13	101.63(9)
Si5−Si3−C12	102.93(9)

Table 3.3.9. Selected crystallographic data of (*S*)-**31**

Empirical formula	$C_{19}H_{30}N_2S_2Si_4$
Fw / g mol^{-1}	462.92
Crystal system	triclinic
Space group	*P*1
Crystal size / mm	0.190 × 0.100 × 0.050
Temperature / K	93
a / Å	7.911(3)
b / Å	11.840(5)
c / Å	13.499(6)
α / º	81.369(11)
β / º	88.853(12)
γ / º	78.737(10)
V / Å^3	1226.0(9)
Z	2
D_{calcd} / g cm^{-3}	1.254
λ / Å	0.71075
μ / mm^{-1}	0.4206
Reflections collected	9469
Independent reflections	7336
Parameters	507
R_{int}	0.0532
R_1 ($I > 2.00\sigma$ (I)) [a]	0.0896
wR_2 (All reflections) [b]	0.2435
GoF [c]	1.055
Friedel pairs	2004
Flack Parameter	0.2(2)

[a] $R_1 = \Sigma||Fo| - |Fc||/\Sigma|Fo|$ ($I > 2\sigma$ (I)). [b] $wR_2 = [\Sigma(w(Fo^2 - Fc^2)^2/\Sigma w(Fo^2)^2]^{1/2}$ ($I > 2\sigma$ (I)). [c] GoF = $[\Sigma(w(Fo^2 - Fc^2)^2/\Sigma(Nr - Np)^2]$

Table 3.3.10. Selected crystallographic data of (*R*)-**31**

Empirical formula	$C_{19}H_{30}N_2S_2Si_4$
Fw / g mol^{-1}	462.92
Crystal system	triclinic
Space group	*P*1
Crystal size / mm	0.150 × 0.120 × 0.070
Temperature / K	93
a / Å	7.912(2)
b / Å	11.836(3)
c / Å	13.510(4)
α / º	81.434(8)
β / º	88.885(9)
γ / º	78.740(6)
V / Å^3	1226.9(6)
Z	2
D_{calcd} / g cm^{-3}	1.253
λ / Å	0.71075
μ / mm^{-1}	0.4203
Reflections collected	8598
Independent reflections	6539
Parameters	487
R_{int}	0.0671
R_1 ($I > 2.00\sigma$ (I)) [a]	0.0406
wR_2 (All reflections) [b]	0.1034
GoF [c]	1.044
Friedel pairs	1854
Flack Parameter	0.14(8)

[a] $R_1 = \Sigma||Fo| - |Fc||/\Sigma|Fo|$ ($I > 2\sigma$ (I)). [b] $wR_2 = [\Sigma(w(Fo^2 - Fc^2)^2/\Sigma w(Fo^2)^2]^{1/2}$ ($I > 2\sigma$ (I)). [c] GoF = $[\Sigma(w(Fo^2 - Fc^2)^2/\Sigma(Nr - Np)^2]$

Table 3.3.11. Selected crystallographic data of **21**⊂$[Ag_2\mathbf{L}](SbF_6)_2$

Empirical formula	$C_{251}H_{234}Ag_4Cl_6F_{24}N_8O_6S_4Sb_4Si_8$
Fw / g mol^{-1}	5398.74
Crystal system	triclinic
Space group	*P*−1
Crystal size / mm	0.300 × 0.100 × 0.100
Temperature / K	93
a / Å	23.3109(9)
b / Å	23.5067(8)
c / Å	24.2410(9)
α / º	111.0626(9)
β / º	100.2965(10)
γ / º	92.7909(11)
V / Å^3	12103.5(8)
Z	2
D_{calcd} / g cm^{-3}	1.481
λ / Å	0.71075
μ / mm^{-1}	0.970
Reflections collected	40928
Independent reflections	2863
Parameters	494
R_{int}	0.0926
R_1 ($I > 2.00\sigma(I)$) [a]	0.1052
wR_2 (All reflections) [b]	0.2923
GoF [c]	1.056

[a] $R_1 = \Sigma||Fo| - |Fc||/\Sigma|Fo|$ ($I > 2\sigma(I)$). [b] $wR_2 = [\Sigma(w(Fo^2 - Fc^2)^2/\Sigma w(Fo^2)^2]^{1/2}$ ($I > 2\sigma(I)$). [c] GoF = $[\Sigma(w(Fo^2 - Fc^2)^2/\Sigma(Nr - Np)^2]$

Table 3.3.12. Selected bond lengths of **21**⊂[Ag_2**L**](SbF_6)$_2$

Bond lengths / Å	
Ag1−C5R	2.428(13)
Ag1−C6R	2.21(3)
Ag1−C6T	2.35(2)
Ag2−C1T	2.30(2)
Ag2−C1R	2.43(4)
Ag2−C2R	2.428(13)
Ag3−C1S	2.445(14)
Ag3−C2S	2.344(16)
Ag3−C2Q	2.39(4)
Ag4−C4Q	2.33(6)
Ag4−C5S	2.429(15)
Ag4−C6S	2.307(19)

3.3.4 2D NMR spectra of **21**

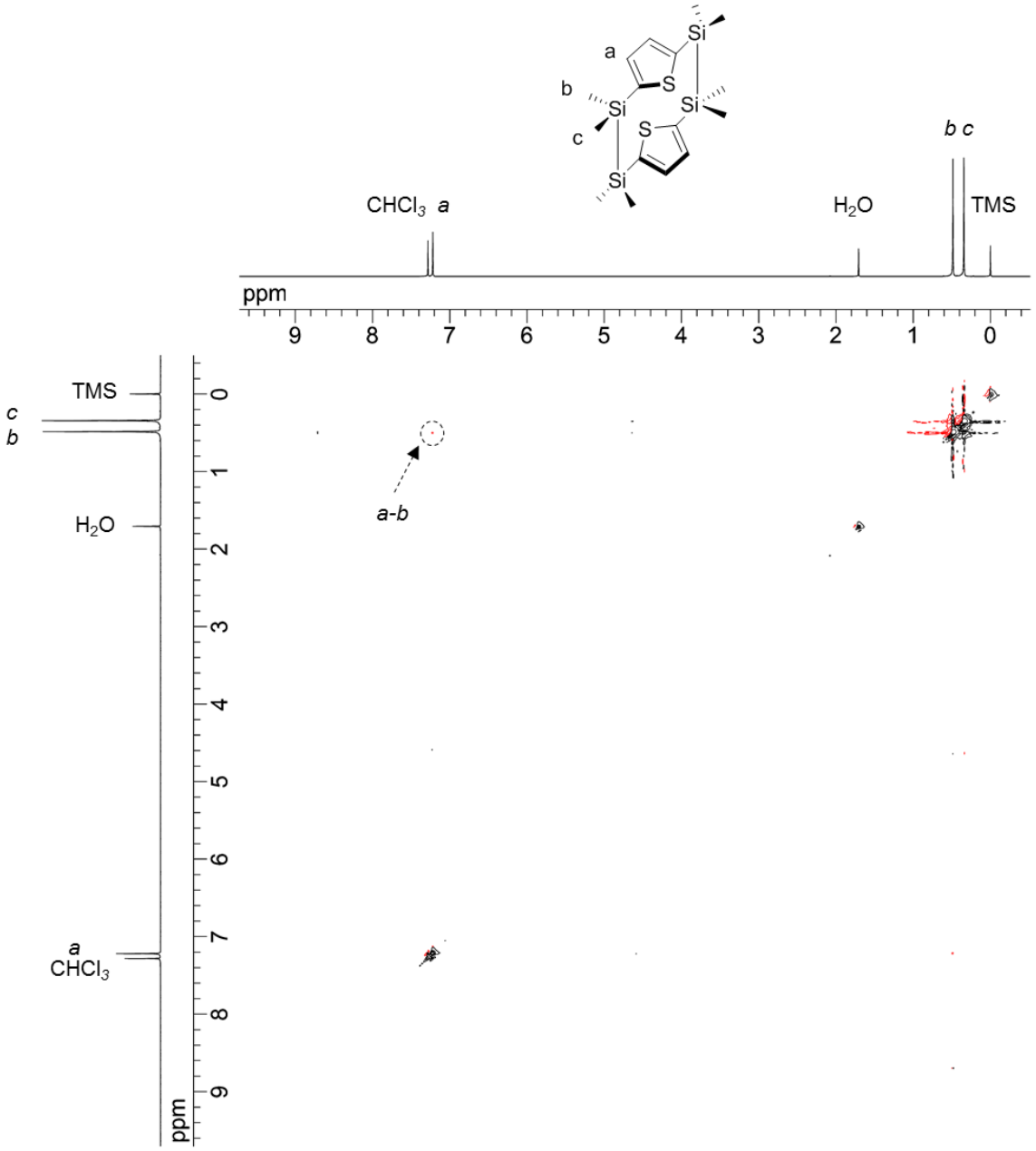

Figure 3.3.2. ^{1}H–^{1}H NOESY spectrum of **21** (500 MHz, $CDCl_3$, 250 K).

3.3.5 Variable Temperature NMR spectra of **23**, **24**, **25**, **27**, and **28**

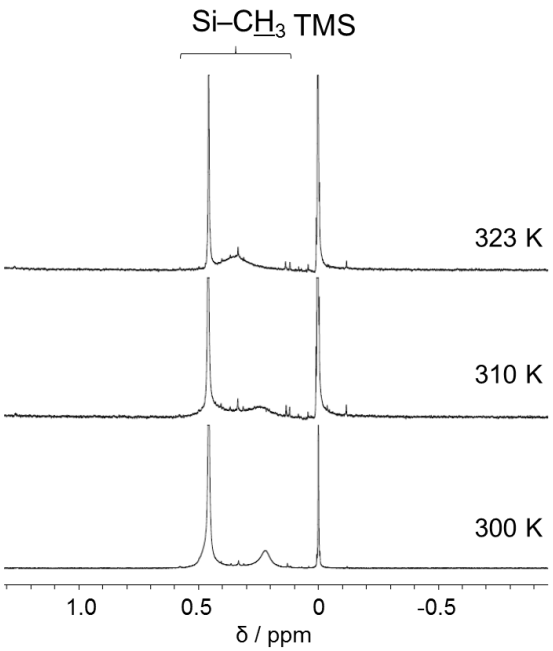

Figure 3.3.3. VT-^{1}H NMR spectra of the methyl region of compound **23** in $CDCl_3$ at 300, 310, and 323 K.

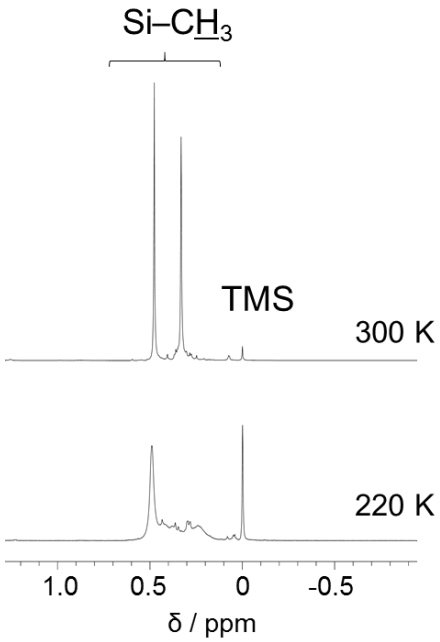

Figure 3.3.4. VT-^{1}H NMR spectra of the methyl region of compound **24** in $CDCl_3$ at 220 and 300 K.

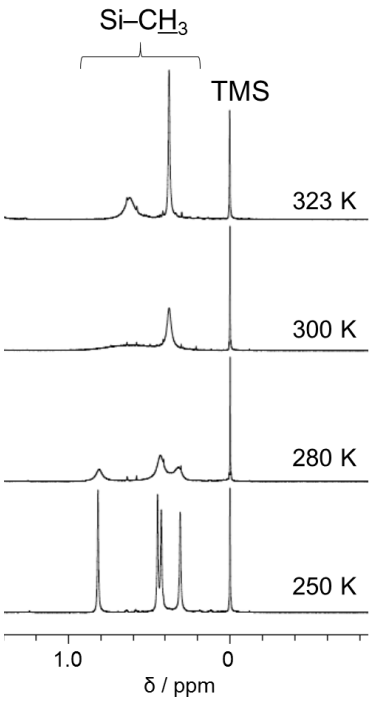

Figure 3.3.5. VT-^{1}H NMR spectra of the methyl region of compound **25** in $CDCl_3$ at 250, 280, 300, and 323 K.

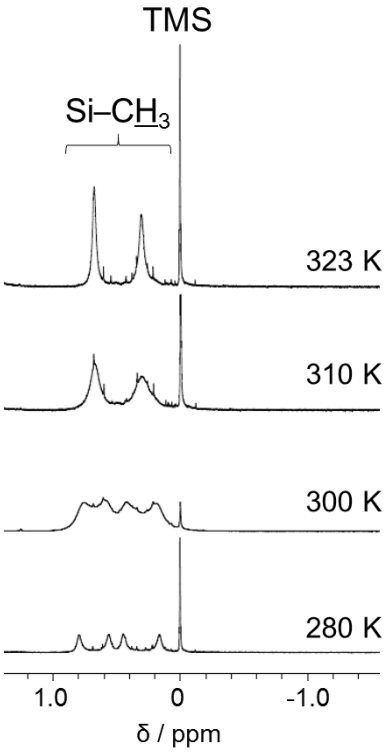

Figure 3.3.6. VT-^{1}H NMR spectra of the methyl region of compound **27** in $CDCl_3$ at 280, 300, 310, and 323 K.

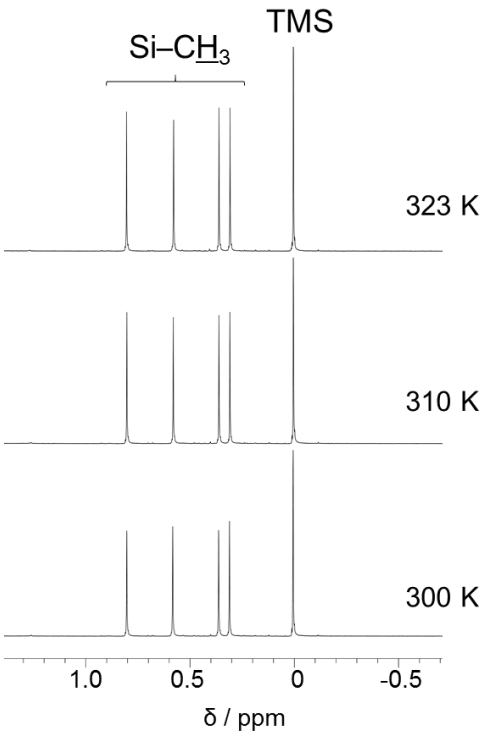

Figure 3.3.7. VT-^{1}H NMR spectra of the methyl region of compound **28** in $CDCl_3$ at 300, 310, and 323 K.

3.3.6 Inclusion of **21** into $[Ag_2\mathbf{L}](SbF_6)_2$

(a) ESI-MS measurement of $\mathbf{21}\subset[Ag_2\mathbf{L}]^{2+}$

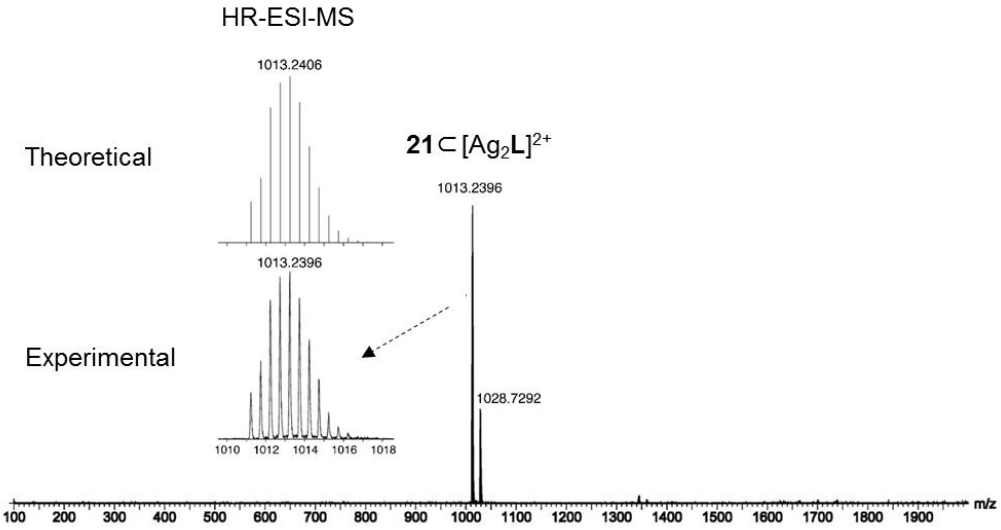

Figure 3.3.8. HR-ESI-MS of a mixture of $[Ag_2\mathbf{L}X_2](SbF_6)_2$ (0.04 mM) and **21** (1.0 eq) in $CDCl_3/CHCl_3$. Calcd for $\mathbf{21}\subset[Ag_2\mathbf{L}]^{2+}$: 1013.2406. Found: 1013.2396.

(b) Detailed ^{1}H NMR spectrum of $\mathbf{21}\subset[Ag_2\mathbf{L}]^{2+}$

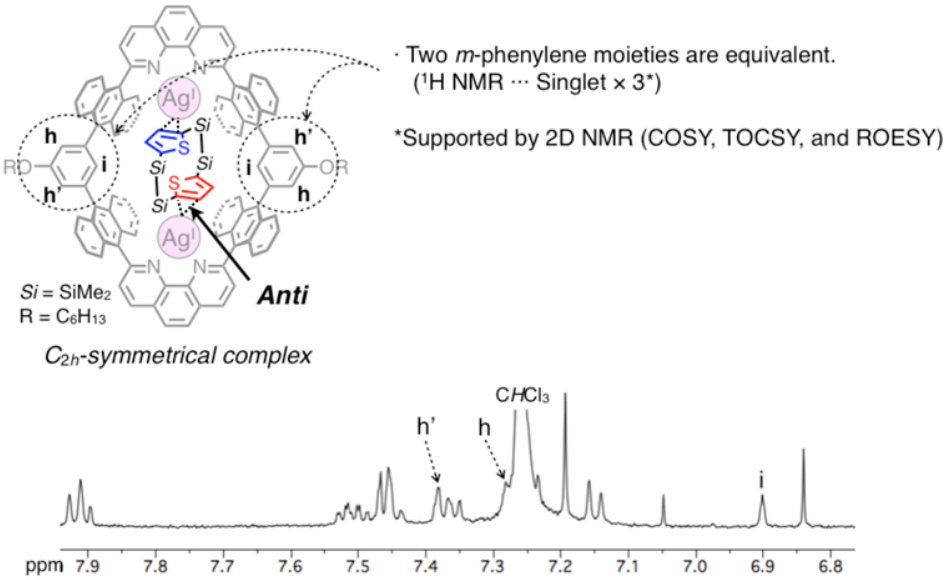

Figure 3.3.9. Partial ^{1}H NMR spectrum of a mixture of $[Ag_2\mathbf{L}X_2](SbF_6)_2$ (0.06 mM) and **21** (3.0 eq) (500 MHz, $CDCl_3$, 300 K).

(c) 2D NMR of 21⊂[Ag$_2$L](SbF$_6$)$_2$

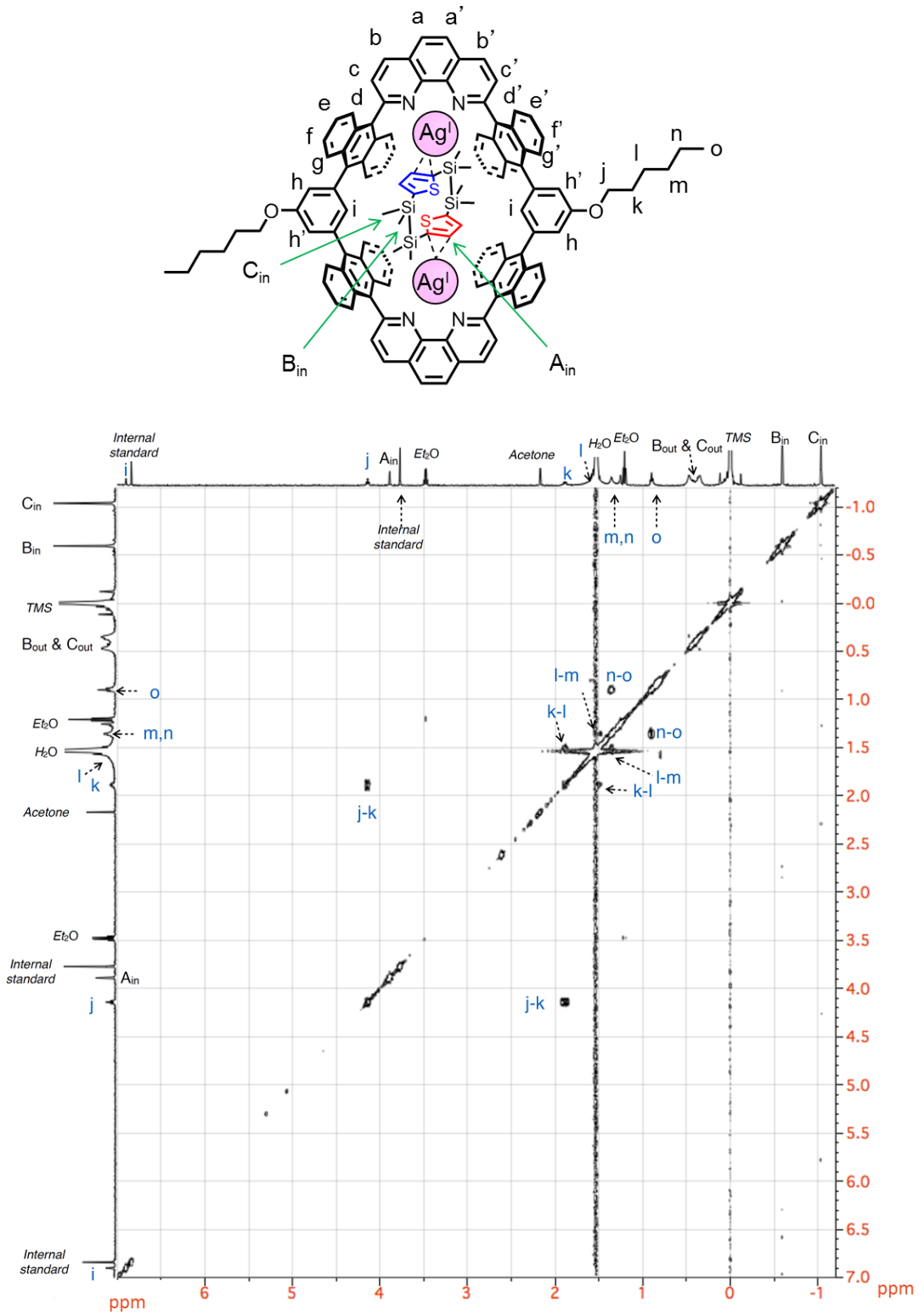

Figure 3.3.10. Partial spectrum of ^{1}H–^{1}H COSY of a mixture of [Ag$_2$**L**X$_2$](SbF$_6$)$_2$ (0.06 mM) and **21** (3.0 eq) (500 MHz, CDCl$_3$, 300 K). Signals of the protons of the macrocyclic skeleton are marked with blue letters for clarity.

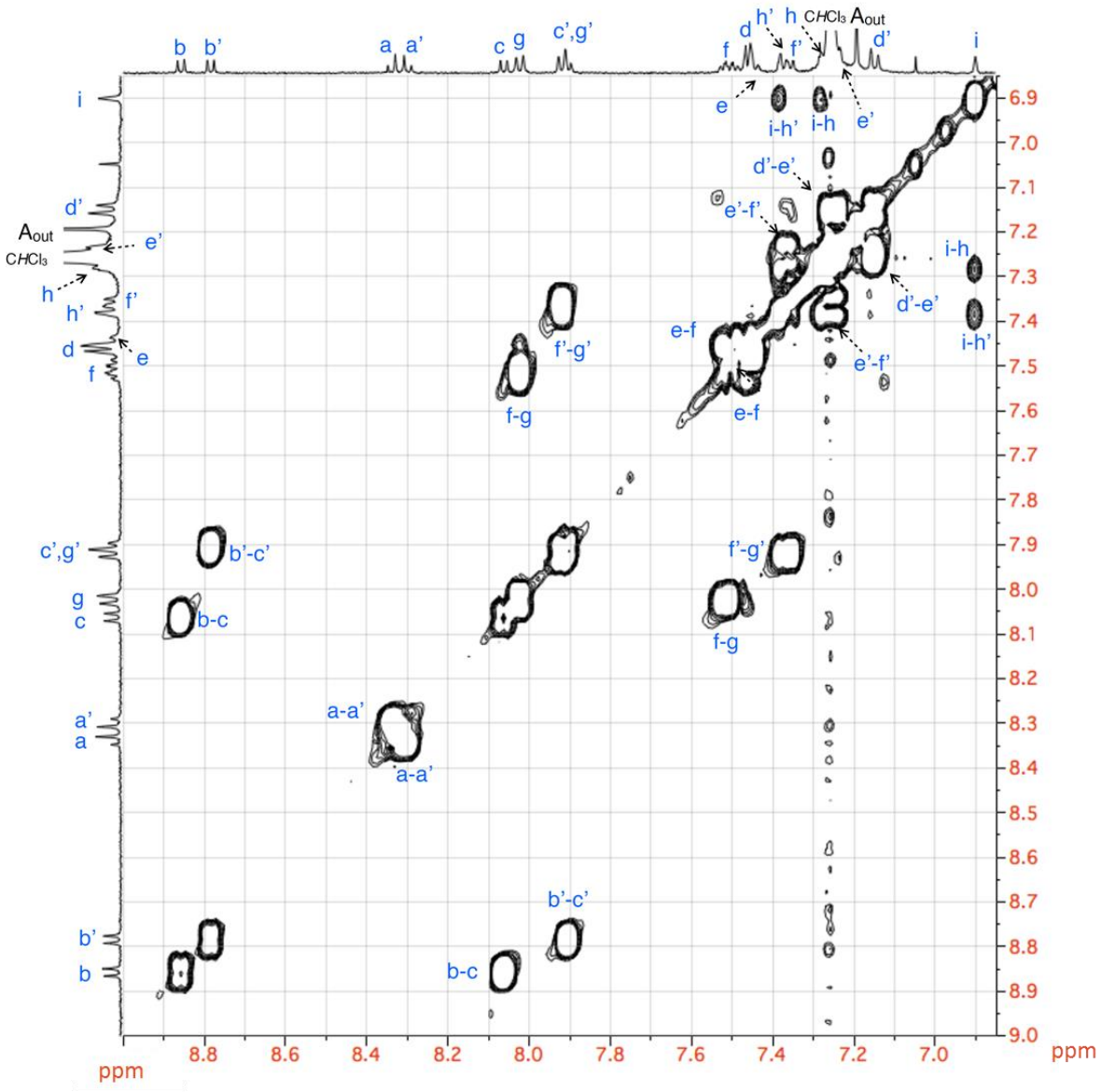

Figure 3.3.11. Partial spectrum of ^{1}H–^{1}H COSY of a mixture of $[Ag_2\mathbf{L}X_2](SbF_6)_2$ (0.06 mM) and **21** (3.0 eq) (500 MHz, $CDCl_3$, 300 K). Signals of the protons of the macrocyclic skeleton are marked with blue letters for clarity.

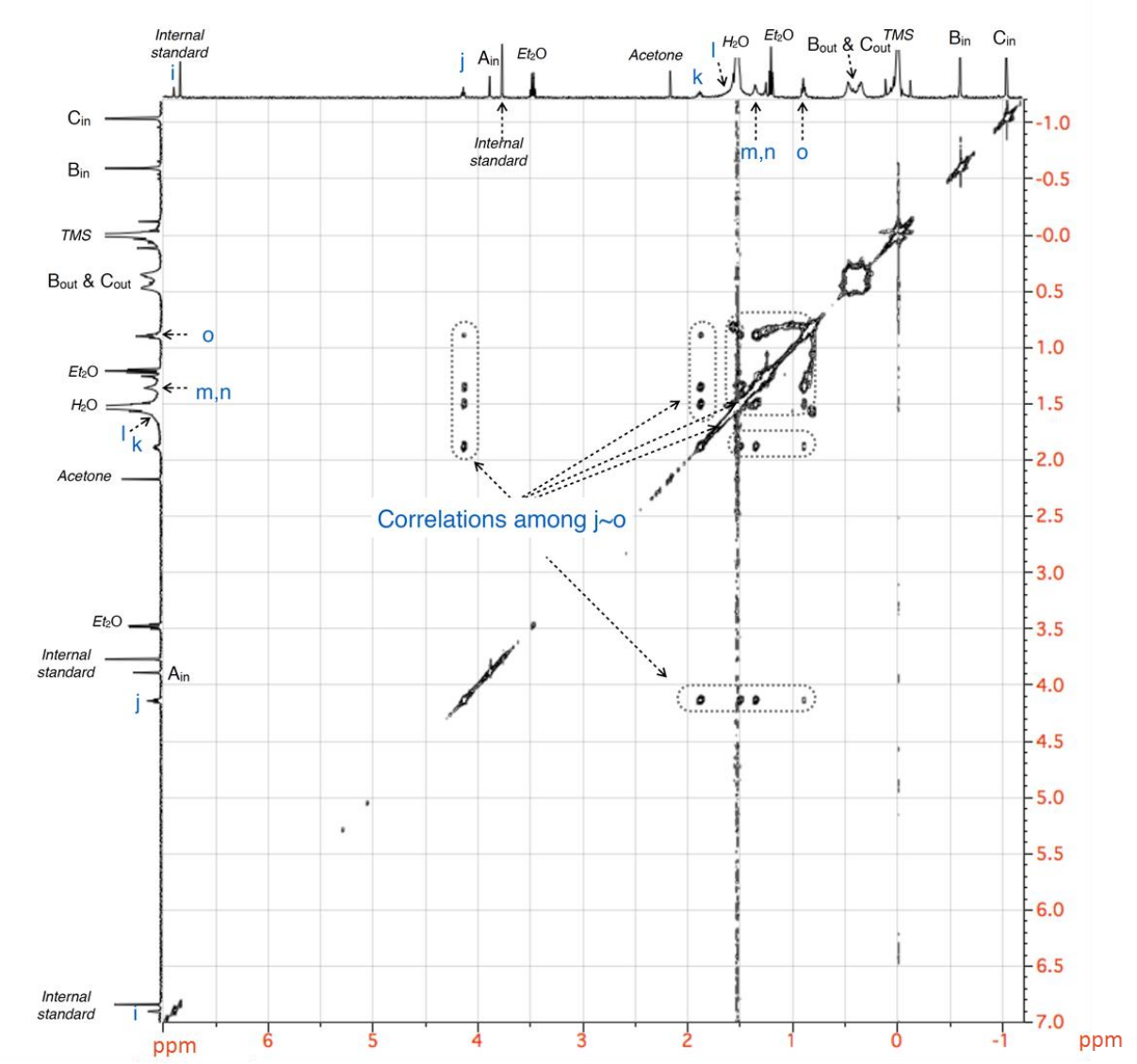

Figure 3.3.12 Partial spectrum of ^{1}H–^{1}H TOCSY of a mixture of $[Ag_2\mathbf{L}X_2](SbF_6)_2$ (0.06 mM) and **21** (3.0 eq) (500 MHz, $CDCl_3$, 300 K). Signals of the protons of macrocyclic skeleton are marked with blue letters for clarity.

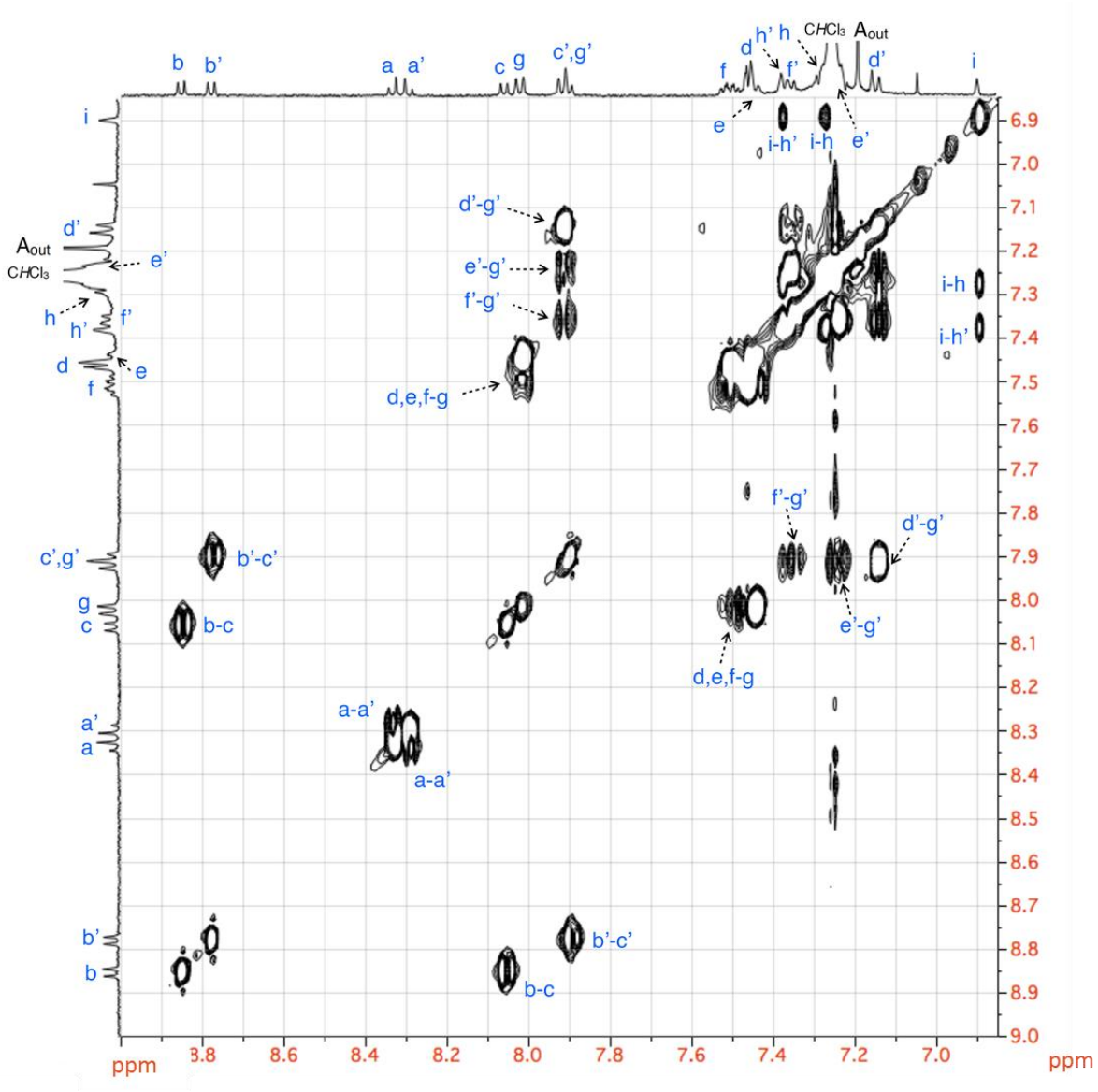

Figure 3.3.13. Partial spectrum of ^{1}H–^{1}H TOCSY of a mixture of $[Ag_2\mathbf{L}X_2](SbF_6)_2$ (0.06 mM) and **21** (3.0 eq) (500 MHz, $CDCl_3$, 300 K). Signals of the protons of macrocyclic skeleton are marked with blue letters for clarity.

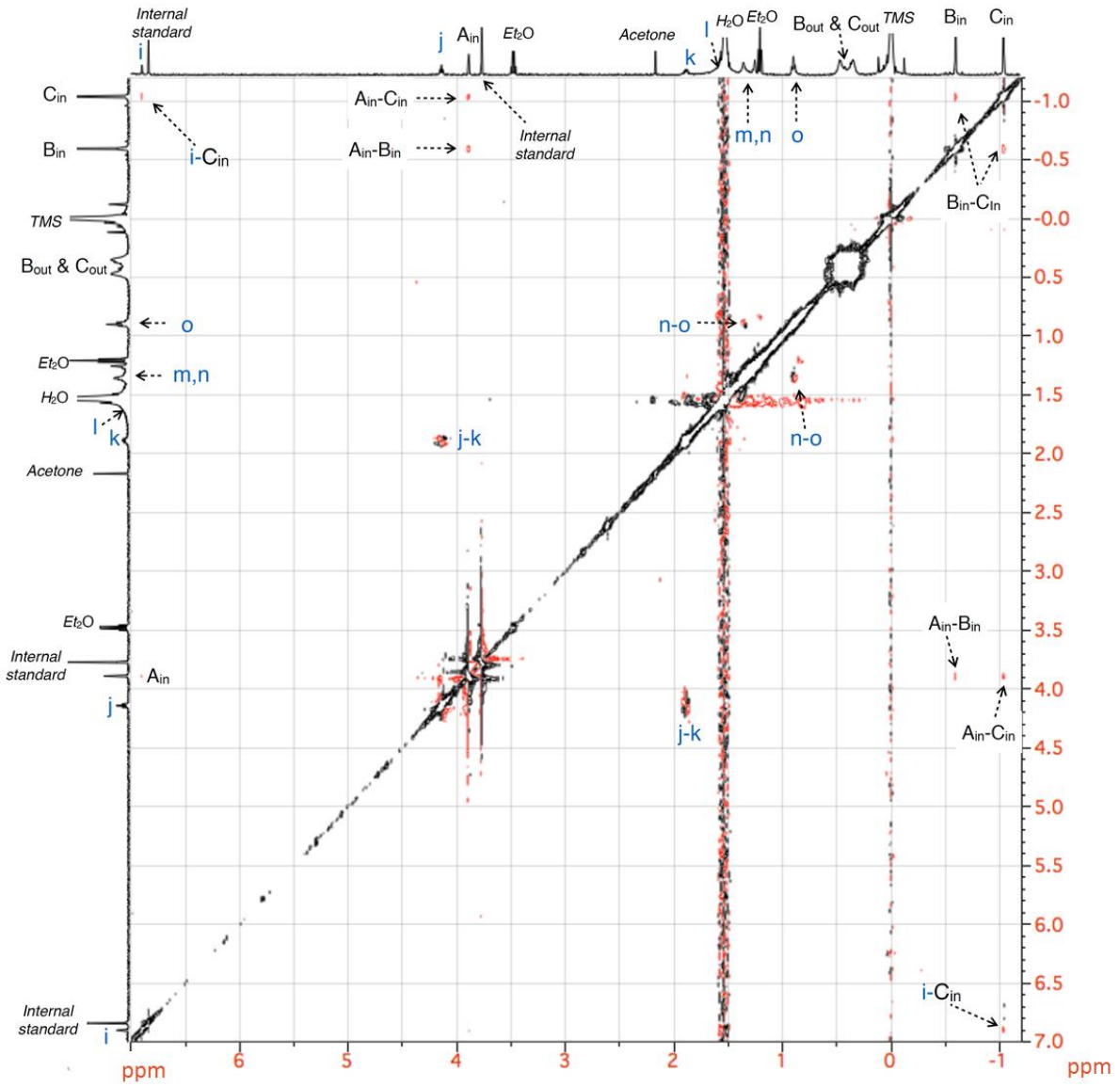

Figure 3.3.14. Partial spectrum of ^{1}H–^{1}H ROESY of a mixture of $[Ag_2\mathbf{L}X_2](SbF_6)_2$ (0.06 mM) and **21** (3.0 eq) (500 MHz, $CDCl_3$, 300 K). Signals of the protons of macrocyclic skeleton are marked with blue letters for clarity. Signals B_{in} and C_{in} were assigned based on an intramolecular ROE correlation, i–C_{in}, and a comparison between two ROE signal intensities (A_{in}–B_{in} and A_{in}–C_{in}).

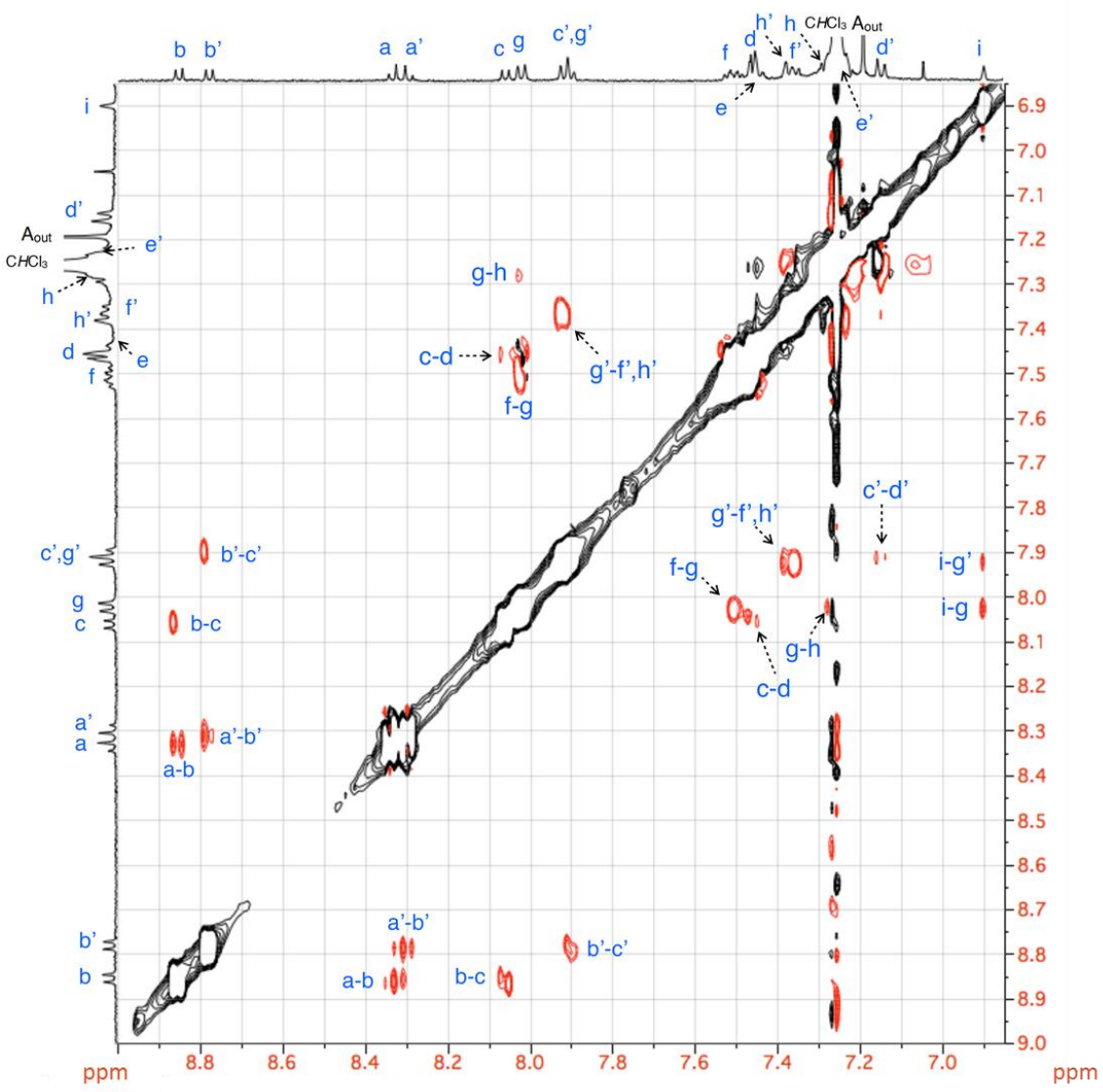

Figure 3.3.15. Partial spectrum of ^{1}H–^{1}H ROESY of a mixture of $[Ag_2\mathbf{L}X_2](SbF_6)_2$ (0.06 mM) and **21** (3.0 eq) (500 MHz, $CDCl_3$, 300 K). Signals of the protons of macrocyclic skeleton are marked with blue letters for clarity.

3.3.7 Estimation of the binding constant between $[Ag_2\mathbf{L}X_2](SbF_6)_2$ and **21**

To investigate the binding constant between $[Ag_2\mathbf{L}X_2](SbF_6)_2$ and **21** (K_a(**21**)), a guest competition experiment with ferrocene was demonstrated as shown in Scheme 3.3.1, and the results of guest change were investigated with ^{1}H NMR spectra (Figure 3.3.16).

Scheme 3.3.1. The equilibrium reaction between **21**⊂$[Ag_2\mathbf{L}](SbF_6)_2$ and ferrocene ($FeCp_2$).

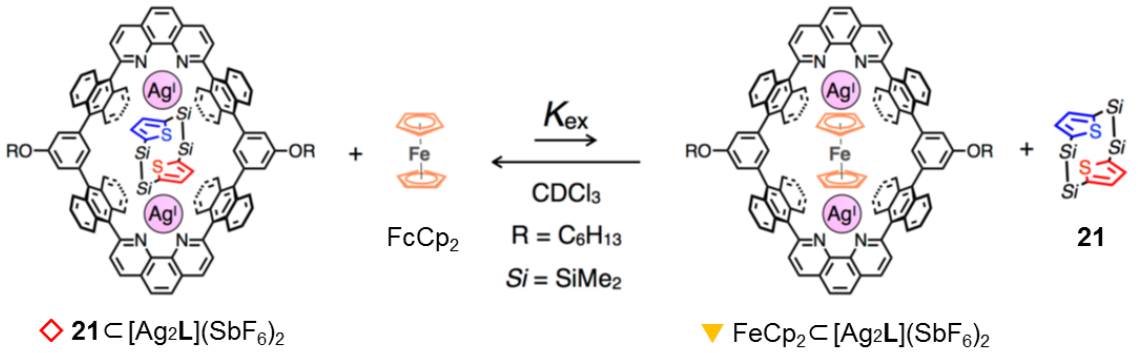

To a 1:1 mixture of $[Ag_2\mathbf{L}X_2](SbF_6)_2$ (0.05 mM, 450 μL, 0.023 μmol) and **21** (1 eq) in $CDCl_3$ was added a solution of $FeCp_2$ in $CDCl_3$ (100 eq).

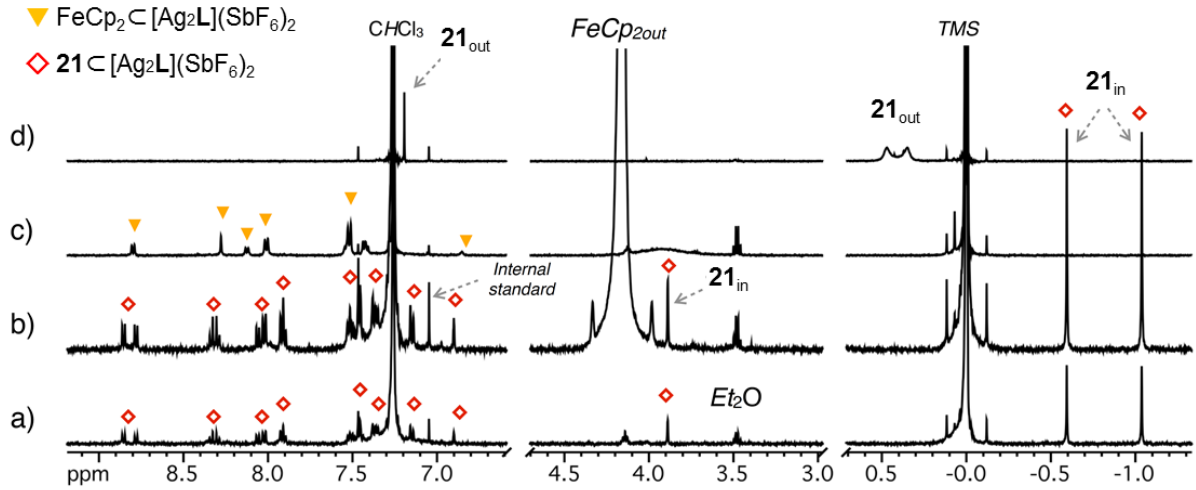

Figure 3.3.16. ^{1}H NMR spectra of 1:1 mixtures of $[Ag_2\mathbf{L}X_2](SbF_6)_2$ and **21** (0.05 mM, 450 μL, 0.022 μmol, 1.0 eq) in the presence of (a) 0 eq and (b) 100 eq of $FeCp_2$, (c) a mixture of $[Ag_2\mathbf{L}X_2](SbF_6)_2$ (0.11 mM) and $FeCp_2$ (5 eq), and (d) **21** only (500 MHz, $CDCl_3$, 300 K). *p*-Dimethoxybenzene (0.025 μmol) was added as an internal standard.

The binding constants for guest inclusion of the dinuclear Ag(I)-macrocycle $[Ag_2\mathbf{L}X_2]^{2+}$ with **21** (K_a(**21**)) and $FeCp_2$ ($K_a(FeCp_2)$), and the equilibrium constant of the guest exchange reaction (K_{ex}) were defined as shown below. ($K_a(FeCp_2)$ was determined to be $(6.2 \pm 0.9) \times 10^4$ M^{-1} in $CDCl_3$ at 300 K (Eq. 4).[24c]

$$[Ag_2\mathbf{L}X_2]^{2+} + \mathbf{21} \overset{Ka(\mathbf{21})}{\underset{\leftarrow}{\longrightarrow}} \mathbf{21}\subset[Ag_2\mathbf{L}]^{2+}$$

$$[Ag_2\mathbf{L}X_2]^{2+} + FeCp_2 \overset{Ka(FeCp2)}{\underset{\leftarrow}{\longrightarrow}} FeCp_2\subset[Ag_2\mathbf{L}]^{2+}$$

$$\mathbf{21}\subset[Ag_2\mathbf{L}]^{2+} + FeCp_2 \overset{Kex}{\underset{\leftarrow}{\longrightarrow}} FeCp_2\subset[Ag_2\mathbf{L}]^{2+} + \mathbf{21}$$

$$K_a(\mathbf{21}) = \frac{[\mathbf{21}\subset[Ag_2\mathbf{L}]^{2+}]}{[[Ag_2\mathbf{L}X_2]^{2+}][\mathbf{21}]} \quad \text{(Eq. 3)}$$

$$K_a(FeCp_2) = \frac{[FeCp_2\subset[Ag_2\mathbf{L}]^{2+}]}{[[Ag_2\mathbf{L}X_2]^{2+}][FeCp_2]} = (6.2 \pm 0.9) \times 10^4\ M^{-1} \quad \text{(Eq. 4)}$$

$$K_{ex} = \frac{[FeCp_2\subset[Ag_2\mathbf{L}]^{2+}][\mathbf{21}]}{[\mathbf{21}\subset[Ag_2\mathbf{L}]^{2+}][FeCp_2]} \quad \text{(Eq. 5)}$$

Using Eqs. 3–5, K_{ex} was represented by

$$K_{ex} = \frac{[FeCp_2\subset[Ag_2\mathbf{L}]^{2+}][\mathbf{21}]}{[\mathbf{21}\subset[Ag_2\mathbf{L}]^{2+}][FeCp_2]} = \frac{[Ag_2\mathbf{L}X_2]^{2+}][\mathbf{21}]}{[\mathbf{21}\subset[Ag_2\mathbf{L}]^{2+}]} \times \frac{[FeCp_2\subset[Ag_2\mathbf{L}]^{2+}]}{[[Ag_2\mathbf{L}X_2]^{2+}][FeCp_2]} = \frac{K_a(FeCp_2)}{K_a(\mathbf{21})} \quad \text{(Eq. 6)}$$

When an excess $FeCp_2$ (100 eq) was added to a solution of **21**⊂$[Ag_2\mathbf{L}]^{2+}$ in $CDCl_3$ at 300 K, no guest exchange reaction between **21**⊂$[Ag_2\mathbf{L}]^{2+}$ and $FeCp_2$ was observed (Figure 3.3.16). Then, assuming that less than 1% of included **21** was replaced by $FeCp_2$ under this condition, the concentration of each guest or complex was described as shown below (Eqs. 7–10). Noted that as the total volume of the solution was increased from 450 μL to 470 μL due to the addition of a solution of $FeCp_2$ to $CDCl_3$, the total concentration of **21**⊂$[Ag_2\mathbf{L}]^{2+}$ decreased from 50 μM to 48 μM.

$$[\mathbf{21}\subset[Ag_2\mathbf{L}]^{2+}] > 47.5\ \mu M \quad \text{(Eq. 7)}$$

$$[\mathbf{21}] < 0.5\ \mu M \quad \text{(Eq. 8)}$$

$$[FeCp_2\subset[Ag_2\mathbf{L}]^{2+}] < 0.5\ \mu M \quad \text{(Eq. 9)}$$

$$[FeCp_2] \approx 4.8\ mM \quad \text{(Eq. 10)}$$

In this case, by substituting Eqs. 7–10 for Eq. 5,

$$K_{ex} < 1.1 \times 10^{-6} \quad \text{(Eq. 11)}$$

Therefore, from Eq. 6 and Eq. 11,

$$K_{ex} = \frac{K_a(FeCp_2)}{K_a(\mathbf{21})} < 1.1 \times 10^{-6} \quad \text{(Eq. 12)}$$

$$\therefore\ K_a(\mathbf{21}) > \frac{K_a(FeCp_2)}{1.1 \times 10^{-6}} \quad \text{(Eq. 13)}$$

In conclusion, by substituting Eq. 4 for Eq. 13,

$$K_a(\mathbf{21}) > 10^{10}\ M^{-1} \quad \text{(Eq. 14)}$$

(in $CDCl_3$ at 300 K)

3.3.8 UV–vis absorption and fluorescence spectra of **21**−**28** and **31**

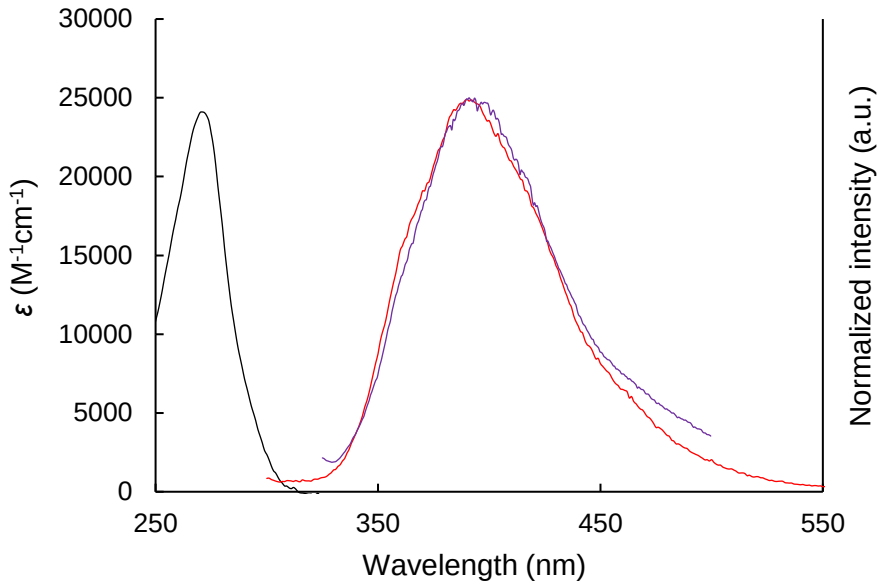

Figure 3.3.17. UV–vis absorption spectrum of **21** in cyclohexane (black line), fluorescence spectrum of **21** in cyclohexane (red line, excited at 271 nm), and fluorescence spectrum of **21** in the solid state (purple line, excited at 312 nm).

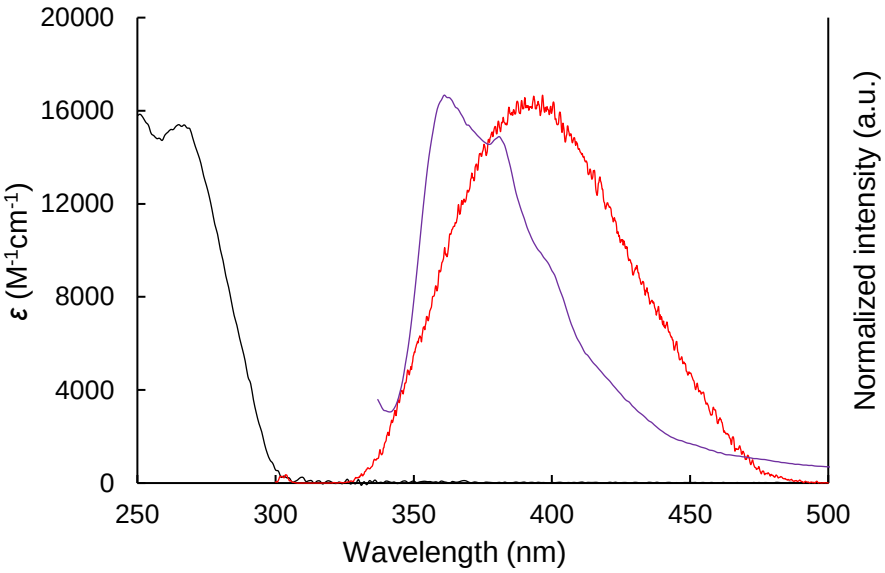

Figure 3.3.18. UV–vis absorption spectrum of **22** in cyclohexane (black line), fluorescence spectrum of **22** in cyclohexane (red line, excited at 265 nm), and fluorescence spectrum of **22** in the solid state (purple line, excited at 324 nm).

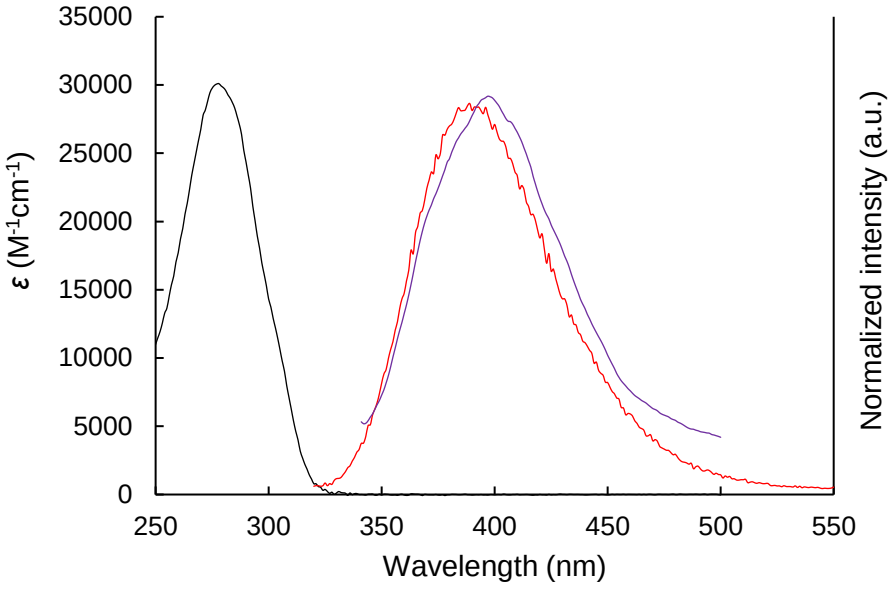

Figure 3.3.19. UV–vis absorption spectrum of **23** in cyclohexane (black line), fluorescence spectrum of **23** in cyclohexane (red line, excited at 278 nm), and fluorescence spectrum of **23** in the solid state (purple line, excited at 312 nm).

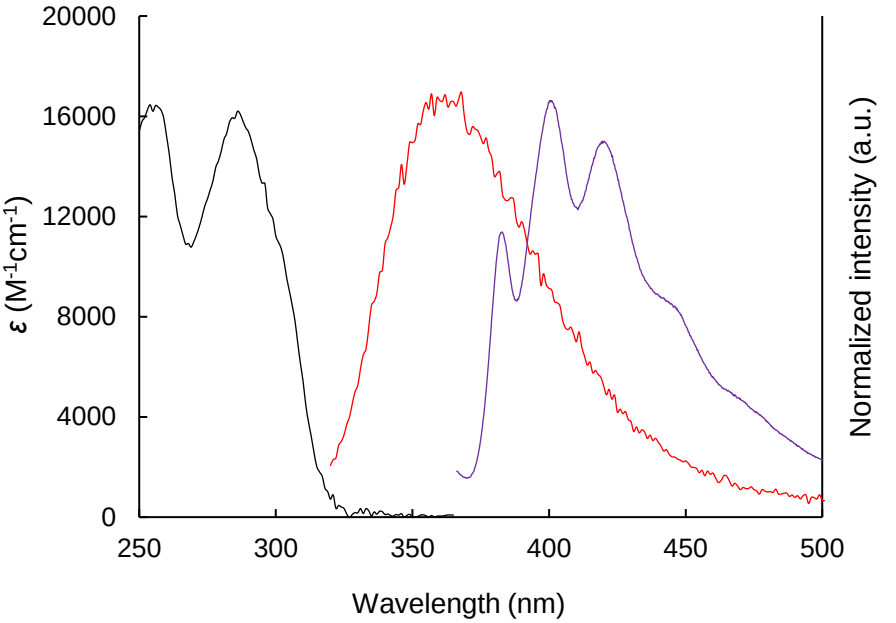

Figure 3.3.20. UV–vis absorption spectrum of **24** in cyclohexane (black line), fluorescence spectrum of **24** in cyclohexane (red line, excited at 286 nm), and fluorescence spectrum of **24** in the solid state (purple line, excited at 353 nm).

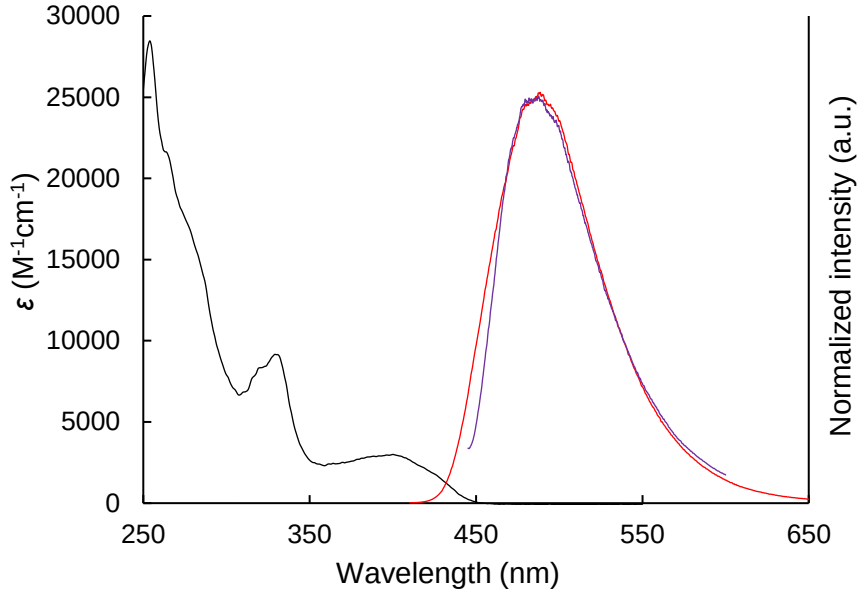

Figure 3.3.21 UV–vis absorption spectrum of **25** in cyclohexane (black line), fluorescence spectrum of **25** in cyclohexane (red line, excited at 400 nm), and fluorescence spectrum of **25** in the solid state (purple line, excited at 435 nm).

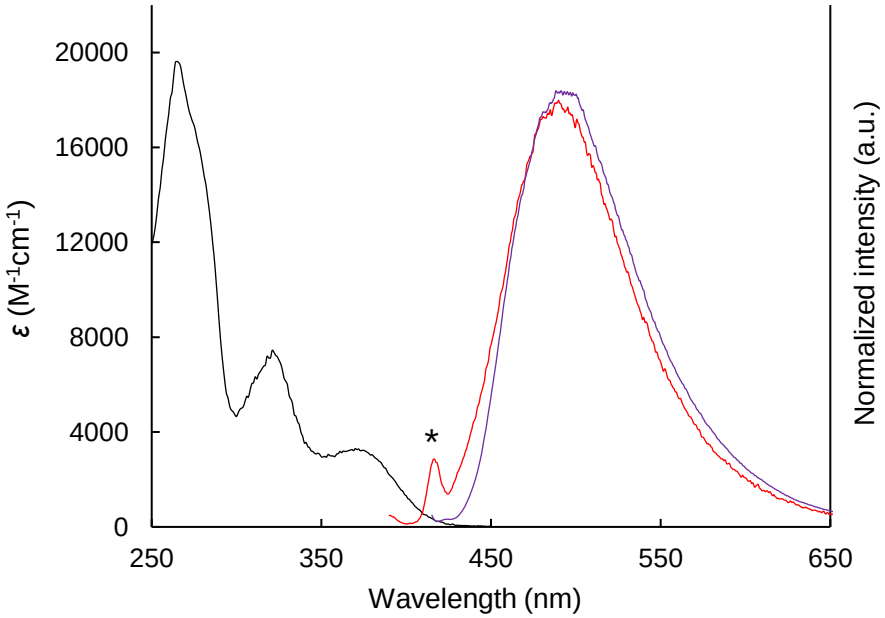

Figure 3.3.22. UV–vis absorption spectrum of **26** in cyclohexane (black line), fluorescence spectrum of **26** in cyclohexane (red line, excited at 370 nm), and fluorescence spectrum of **26** in the solid state (purple line, excited at 406 nm). A peak denoted with an asterisk is due to Raman scattered light of solvent.

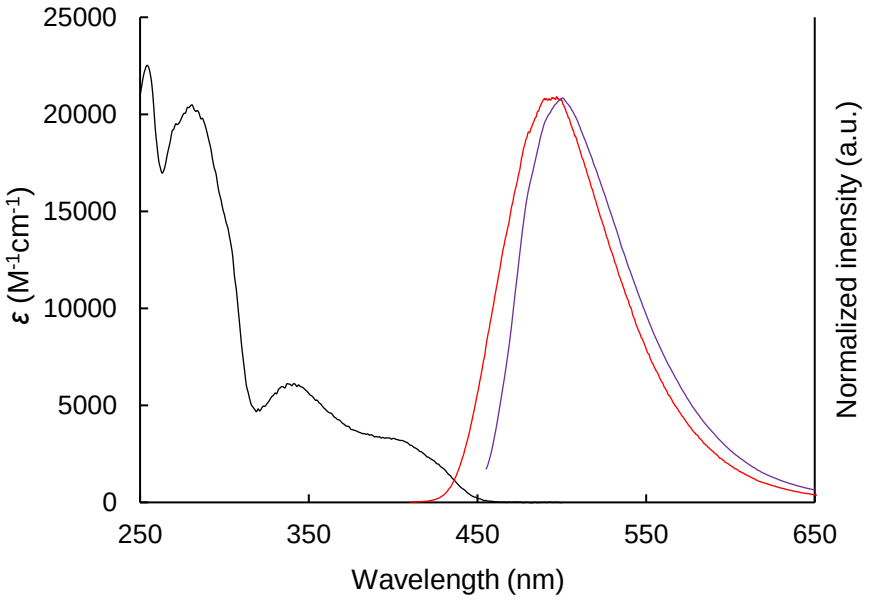

Figure 3.3.23. UV–vis absorption spectrum of **27** in cyclohexane (black line), fluorescence spectrum of **27** in cyclohexane (red line, excited at 400 nm), and fluorescence spectrum of **27** in the solid state (purple line, excited at 443 nm).

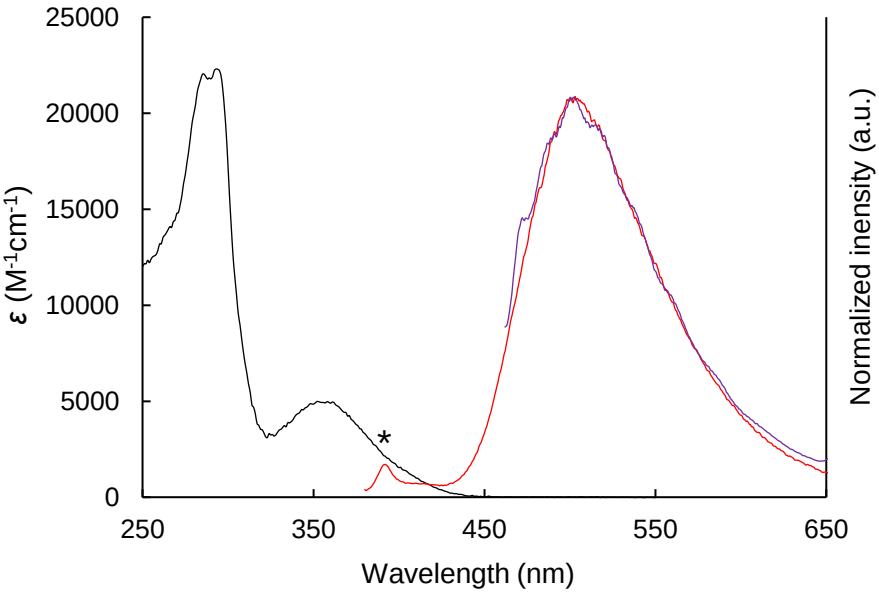

Figure 3.3.24. UV–vis absorption spectrum of **28** in cyclohexane (black line), fluorescence spectrum of **28** in cyclohexane (red line, excited at 352 nm), and fluorescence spectrum of **28** in the solid state (purple line, excited at 437 nm). A peak denoted with an asterisk is due to Raman scattered light of solvent.

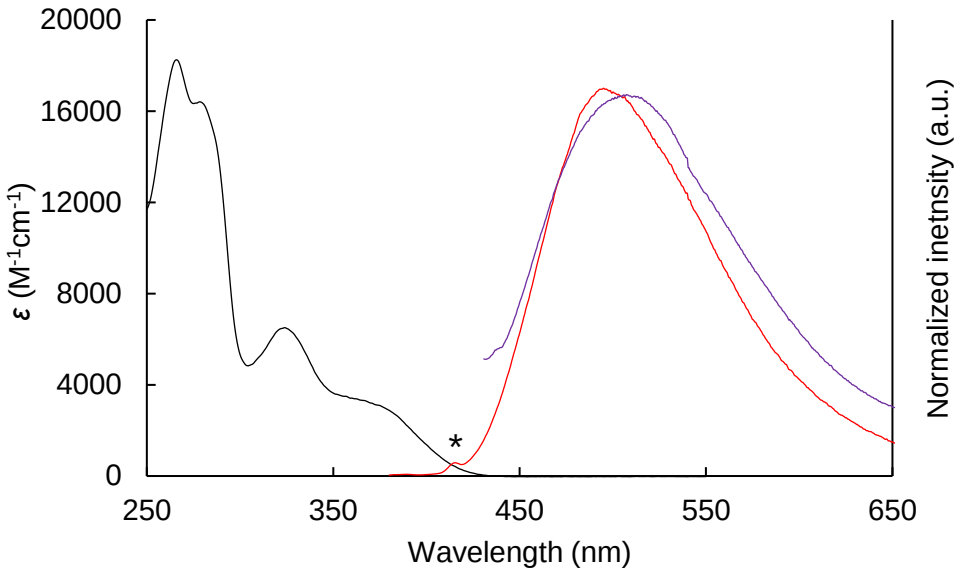

Figure 3.3.25. UV–vis absorption spectrum of *rac*-**31** in cyclohexane (black line), fluorescence spectrum of *rac*-**31** in cyclohexane (red line, excited at 370 nm), and fluorescence spectrum of *rac*-**31** in the solid state (purple line, excited at 398 nm). A peak denoted with an asterisk is due to Raman scattered light of solvent.

3.3.9 Electroluminescence data

(a) Fabrication of OLED

The OLEDs were developed on a glass substrate coated with a 200-nm-thick Indium Tin Oxide (ITO) layer. ITO film was etched with zinc powder and HCl to obtain the 2-mm-width electrode pattern. The substrate was cleaned by sonication in successively detergent, ultrapure water, acetone and isopropanol, and then treated with ozone under UV. The OLED was prepared by the sequential vapor deposition of organic materials onto ITO at a deposition rate of 1 Å/s. The emitter layer of **26** and dPVBi was vacuum deposited by simultaneous evaporation from two separate sources. The substrate was transferred to a metal-evaporation chamber through the glove box to avoid exposure to ambient air. Al was deposited at a rate of 10 Å/s. The effective area of the emitting diode was 6.0 mm^2. The optical fiber guided the EL light to a spectrograph (Oriel, model FICS 77441) connected to CCD camera (Andor, model DU420-OE) to measure the spectra. The current-voltage characteristics of the devices were measured with Keithley 2400. The power of EL light was measured with Thorlabs S120 Optical Power Meter simultaneously with the electric current. The external quantum efficiency of EL devices was estimated by considering the area of detection (solid angle of 32.34°). All measurements were carried out at room temperature under ambient atmosphere.

(b) Electroluminescence properties of the device

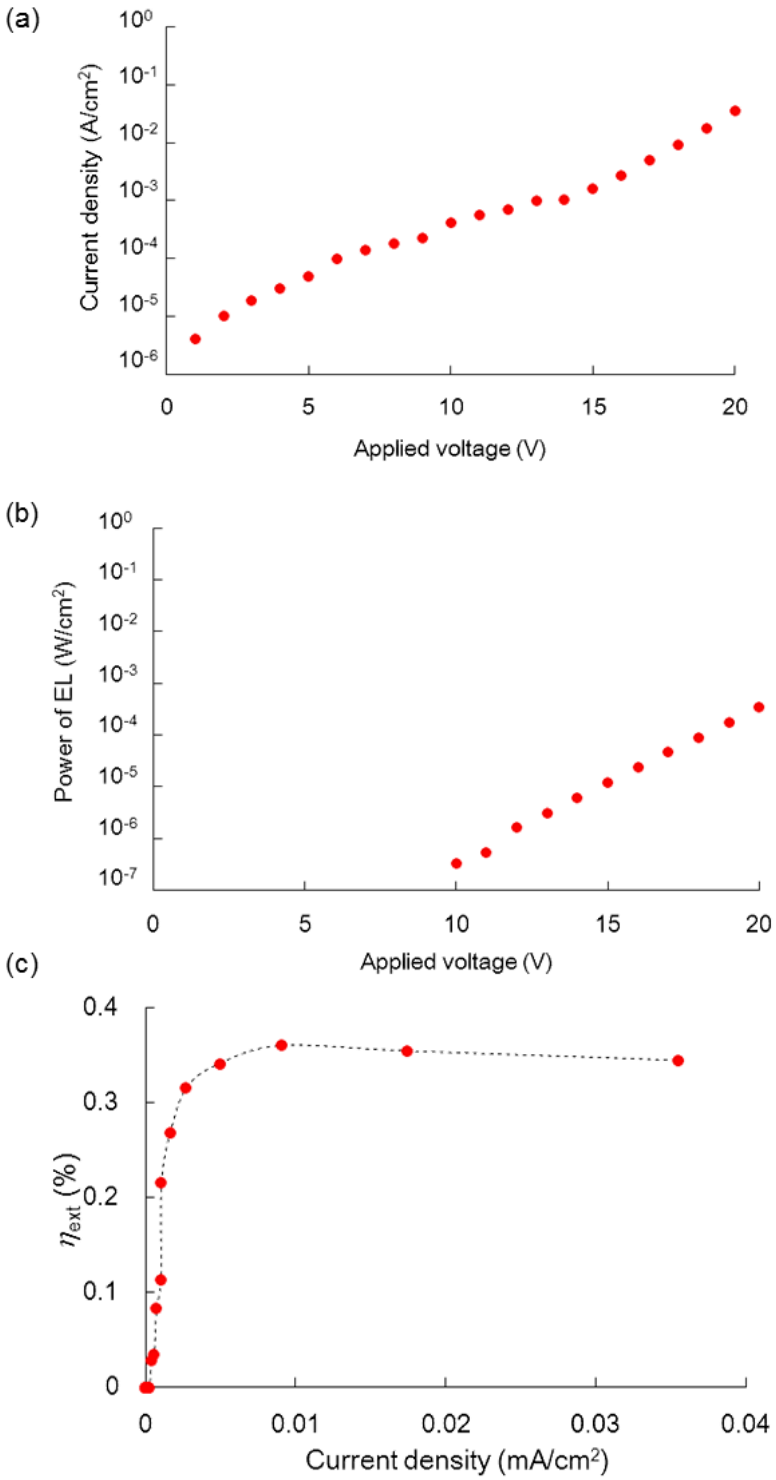

Figure 3.3.26. (a) Voltage *vs* current density, (b) voltage *vs* power of EL (Onset: 10 V), and (c) current density *vs* external quantum yield characteristics of the ITO/α-NPD/dPVBi:**26**(3%)/BCP/LiF/Al device.

(c) Electroluminescence spectra of the ITO/α-NPD/dPVBi:26/BCP/LiF/Al device

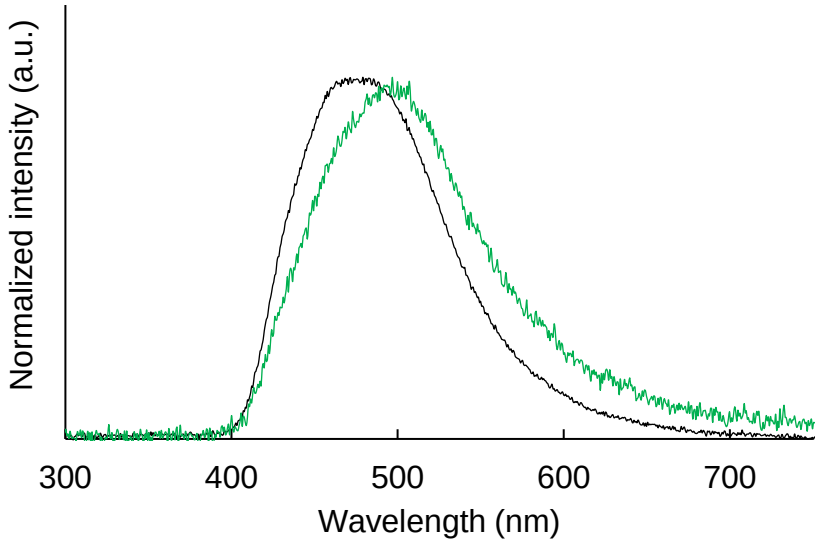

Figure 3.3.27. Electroluminescence spectra of the undoped ITO/α-NPD/dPVBi/BCP/LiF/Al device (black line) and the ITO/α-NPD/dPVBi:**26**(3%)/BCP/LiF/Al device (green line). Applied voltage: 18 V.

3.4 Summary

In Chapter 3, I developed an easily accessible synthetic route to provide disilane-bridged cyclophanes, tetrasila[2.2]cyclophanes, *via* Pd-catalyzed cyclization reaction. Some of the compounds displayed the inversion motion in solution at room temperature, and this inversion was controlled by altering the phase (solid *vs* solution), the bulkiness of substituent, and the inclusion into a host molecule. The photophysical and electrochemical properties of these molecules were investigated by UV–vis absorption and fluorescence spectroscopies as well as cyclic voltammetry. The donor–acceptor tetrasila[2.2]cyclophanes (**25**–**28**) showed green emission derived from ICT transition. In particular, compound **26** displayed strong solid-state emission (Φ = 0.49), because of the suppression of intermolecular π–π stacking in crystal structure according to XRD analysis. Physical properties of these compounds were rationalized by the results of DFT calculations. Moreover, **26**-doped multilayered OLEDs exhibited green electroluminescence at around 500 nm with an efficiency of ca. 0.4% at 18 V. Furthermore, the preparation of planar chiral tetrasila[2.2]cyclophane was achieved. Optically active (*R*)-**31** and (*S*)-**31** displayed CPL activity, which was comparable to those of reported low-molecular-weight organic molecules.

Thus, the synthetic method demonstrated in this work provide a new route for functionalizing disilane-bridged cyclophanes. These findings of multi-functional tetrasila[2.2]cyclophanes could contribute to provide a new molecular design strategy for functional organosilanes, donor–acceptor systems, and planar chiral systems.

3.5 References

1. (a) Grell, M.; Bradley, D. D. C. *Adv. Mater.* **1999**, *11*, 895–905.
   (b) *Circular Dichroism: Principles and Applications*, 2nd ed.; Berova, N.; Nakanishi, K.; Woody, R. W., Eds.; Wiley-VCH: New York, 2000.
   (c) Maeda, H.; Bando, Y. *Pure Appl. Chem.* **2013**, *85*, 1967–1978.
   (d) Furumi, S. *Chem. Rec.* **2010**, *10*, 394–408.
2. (a) Riehl, J. P.; Richardson, F. S. *Chem. Rev.* **1986**, *86*, 1−16.
   (b) Carr, R.; Evans, N. H.; Parker, D. *Chem. Soc. Rev.* **2012**, *41*, 7673−7686.
   (c) Woody, R. W. "Aromatic side-chain contributions to protein circular dichroism" In *Methods in Protein Structure and Stability Analysis: Luminescence Spectroscopy and Circular Dichroism*; Uversky, V. N.; Permyakov, E. A., Eds; Nova Science Publishers: NewYork, 2007, 291−344.
   (d) 小林諶三 「光と物質の相互作用−X　光学活性」光学, **1988**, *17*, 530−539.
   (e) 森田眞「円偏光ルミネッセンスの原理とその応用」分光研究, **1980**, *29*, 357−374.
3. (a) Lunkley, J. L.; Shirotani, D.; Yamanari, K.; Kaizaki, S.; Muller, G. *J. Am. Chem. Soc.* **2008**, *130*, 13814–13815.
   (b) Lunkley, J. L.; Shirotani, D.; Yamanari, K.; Kaizaki, S.; Muller, G. *Inorg. Chem.* **2011**, *50*, 12724−12732.
   (c) Pietro, S. D.; Bari, L. D. *Inorg. Chem.* **2012**, *51*, 12007−12014.
   (d) Harada, T.; Tsumatori, H.; Nishiyama, K.; Yuasa, J.; Hasegawa, Y.; Kawai, T. *Inorg. Chem.* **2012**, *51*, 6476−6485.
   (e) Muller, G. *Dalton Trans.* **2009**, 9692−9707.
   (f) Okutani, K.; Nozaki, K.; Iwamura M. *Inorg. Chem.* **2014**, *53*, 5527−5537.
   (g) Uchida, T.; Nozaki, K.; Iwamura, M. *Chem. –Asian J.* **2016**, *11*, 2415−2422.
4. (a) Sánchez-Carnerero, E. M.; Agarrabeitia, A. R.; Moreno, F.; Maroto, B. L.; Muller, G.; Ortiz, M. J.; de la Moya, S. *Chem. –Eur. J.* **2015**, *21*, 13488−13500.
   (b) Oyama, H.; Nakano, K.; Harada, T.; Kuroda, R.; Naito, M.; Nobusawa, K.; Nozaki, K. *Org. Lett.* **2013**, *15*, 2104–2107.
   (c) Nakamura, K.; Furumi, S.; Takeuchi, M.; Shibuya, T.; Tanaka, K. *J. Am. Chem. Soc.* **2014**, *136*, 5555–5558.
   (d) Wang, Y.; Li, X.; Li, F.; Sun, W.-Y.; Zhu, C.; Cheng, Y. *Chem. Commun.* **2017**, *53*, 7505−7508.

5. Sato, S.; Yoshii, A.; Takahashi, S.; Furumi, S.; Takeuchi, M.; Isobe, H. *Proc. Natl. Acad. Sci. U.S.A.* **2017**, *114*, 13097−13101.
6. (a) Brown, C. J.; Farthing, A. C. *Nature* **1949**, *164*, 915−916.
(b) Cram, D. J.; Steinberg, H. *J. Am. Chem. Soc.* **1951**, *73*, 5691−5704.
7. Kannen, N.; Otsubo, T.; Sakata, Y.; Misumi, S. *Bull. Chem. Soc. Jpn.* **1976**, *49*, 3203–3207.
8. (a) Morisaki, Y.; Chujo Y. *Angew. Chem. Int. Ed*. **2006**, *45*, 6430−6437.
(b) Morisaki, Y.; Kawakami, N.; Nakano, T.; Chujo Y. *Chem.–Eur. J.* **2013**, *19*, 17715−17718.
(c) Morisaki, Y.; Kawakami, N.; Shibata, S.; Chujo Y. *Chem. –Asian J*. **2014**, *9*, 2891–2895.
9. (a) Kitagaki, S.; Ueda, T.; Mukai, C. *Chem. Commun.* **2013**, *49*, 4030–4032.
(b) Pye, P. J.; Rossen, K.; Reamer, R. A.; Tsou, N. N.; Volante, R. P.; Reider, P. J. *J. Am. Chem. Soc.* **1997**, *119*, 6207–6208.
(c) Ma, Y.; Song, C.; Ma. C.; Sun, Z.; Chai, Q.; Andrus, M. B. *Angew. Chem. Int. Ed*. **2003**, *42*, 5871–5874.
10. (a) Abbate, S.; Lebon, F.; Gangemi, R.; Longhi, G.; Spizzichino, S.; Ruzziconi, R. *J. Phys. Chem. A* **2009**, *113*, 14851–14859.
(b) Furo, T.; Mori, T.; Wada, T.; Inoue, Y. *J. Am. Chem. Soc.* **2005**, *127*, 8242–8243.
(c) Shimizu, A.; Inoue, Y.; Mori, T. *J. Phys. Chem. A* **2017**, *121*, 8389−8398.
11. (a) Morisaki, Y.; Gon, M.; Sasamori, T.; Tokitoh, N.; Chujo, Y. *J. Am. Chem. Soc.* **2014**, *136*, 3350−3353.
(b) Gon, M.; Sawada, R.; Morisaki, Y.; Chujo, Y. *Macromolecules* **2017**, *50*, 1790−1802.
(c) Gon, M.; Kozuka, H.; Morisaki, Y.; Chujo, Y. *Asian J. Org. Chem.* **2016**, *5*, 353−359.
(d) Morisaki, Y.; Sawada, R.; Gon, M.; Chujo, Y. *Chem. –Asian J.* **2016**, *11*, 2524−2527.
12. (a) Gleiter, R.; Schäfer, W.; Krennrich, G.; Sakurai, H. *J. Am. Chem. Soc.* **1988**, *110*, 4117−4126.
(b) Sakurai, H. *Pure Appl. Chem.* **1987**, *59*, 1637−1646.
(c) Sekiguchi, A.; Yatabe, T.; Kabuto, C.; Sakurai, H. *Angew. Chem., Int. Ed.* **1989**, *28*, 757−758.
(d) Sakurai, H.; Hoshi, S.; Kamiya, A.; Hosomi, A.; Kabuto, C. *Chem. Lett.* **1986**, *15*, 1781−1784.
(e) Sakurai, H.; Nakadaira, Y.; Hosomi, A.; Eriyama, Y. *Chem. Lett.* **1982**, *11*, 1971−1974.
13. Nishiyama, K.; Sugawara, T. *Chem. Lett.* **1992**, *21*, 1409−1412.
14. Kira, M.; Tokura, S. *Organometallics* **1997**, *16*, 1100−1102.

15. (a) Dyson, P. J.; Hulkes, A. G.; Suman, P. *Chem. Commun.* **1996**, 2223−2224.
(b) Braunschweig, H.; Buggisch, N.; Englert, U.; Homberger, M.; Kupfer, T.; Leusser, D.; Lutz, M.; Radacki, K. *J. Am. Chem. Soc.* **2007**, *129*, 4840−4846.
16. Shimada, M.; Yamanoi, Y.; Ohto, T.; Pham, S.-T.; Ryo Yamada, R.; Tada, H.; Omoto, K.; Tashiro, S.; Shionoya, M.; Hattori, M.; Jimura, K.; Hayashi, S.; Koike, H.; Iwamura, M.; Nozaki, K.; Nishihara, H. *J. Am. Chem. Soc.* **2017**, *139*, 11214–11221.
17. Shimada, M.; Tsuchiya, M.; Sakamoto, R.; Yamanoi, Y.; Nishibori, E.; Sugimoto, K.; Nishihara, H. *Angew. Chem. Int. Ed.* **2016**, *55*, 3022−3026.
18. Pahor, N. B.; Calligaris, M.; Randaccio, L. *J. Chem. Soc., Perkin Trans. 2* **1978**, 42–45.
19. Gaussian 09, Revision E.01, Frisch, M. J.; Trucks, G. W.; Schlegel, H. B.; Scuseria, G. E.; Robb, M. A.; Cheeseman, J. R.; Scalmani, G.; Barone, V.; Mennucci, B.; Petersson, G. A.; Nakatsuji, H.; Caricato, M.; Li, X.; Hratchian, H. P.; Izmaylov, A. F.; Bloino, J.; Zheng, G.; Sonnenberg, J. L.; Hada, M.; Ehara, M.; Toyota, K.; Fukuda, R.; Hasegawa, J.; Ishida, M.; Nakajima, T.; Honda, Y.; Kitao, O.; Nakai, H.; Vreven, T.; Montgomery, J. A., Jr.; Peralta, J. E.; Ogliaro, F.; Bearpark, M.; Heyd, J. J.; Brothers, E.; Kudin, K. N.; Staroverov, V. N.; Kobayashi, R.; Normand, J.; Raghavachari, K.; Rendell, A.; Burant, J. C.; Iyengar, S. S.; Tomasi, J.; Cossi, M.; Rega, N.; Millam, J. M.; Klene, M.; Knox, J. E.; Cross, J. B.; Bakken, V.; Adamo, C.; Jaramillo, J.; Gomperts, R.; Stratmann, R. E.; Yazyev, O.; Austin, A. J.; Cammi, R.; Pomelli, C.; Ochterski, J. W.; Martin, R. L.; Morokuma, K.; Zakrzewski, V. G.; Voth, G. A.; Salvador, P.; Dannenberg, J. J.; Dapprich, S.; Daniels, A. D.; Farkas, Ö.; Foresman, J. B.; Ortiz, J. V.; Cioslowski, J.; Fox, D. J. Gaussian, Inc., Wallingford CT, 2009.
20. Sakurai, H. “Phanes bridged by group 14 heavy elements” In *Adv. Inorg. Chem*. Sykes, A. G.; Cowley, A. H., Eds. Academic Press, San Diego, 2000, volume 50, 359−407.
21. (a) Hesse, M.; Meier, H.; Zeeh, B. *Spectroscopic Methods in Organic Chemistry 2nd ed.*; Georg Thieme Verlag, Stuttgart, 2007.
(b) Friebolin, H. *Basic One- and Two-Dimensional NMR Spectroscopy*, 5*th ed.*;Wiley-VCH: Weinheim, 2011.
22. (a) Izatt, R. M.; Pawlak, K.; Bradshaw, J. S. *Chem. Rev*. **1991**, *91*, 1721–2085.
(b) Yordanov, A. T.; Roundhill, D. M. *Coordin. Chem. Rev*. **1998**, *170*, 93–124.
23. (a) Korom, S.; Martin, E.; Serapian, S. A.; Bo, C.; Ballester, P. *J. Am. Chem. Soc.* **2016**, *138*, 2273–2279.
(b) Wang, Q. C.; Qu, D. H.; Ren, J.; Chen, K.; Tian, H. *Angew. Chem. Int. Ed*. **2004**, *43*, 2661–2665.

24. (a) Kuritani, M.; Tashiro, S.; Shionoya, M. *Chem. –Asian J.* **2013**, 8, 1368–1371.
(b) Kuritani, M.; Tashiro, S.; Shionoya, M. *Inorg. Chem.* **2012**, 51, 1508–1515.
(c) Omoto, K.; Tashiro, S.; Kuritani, M.; Shionoya, M. *J. Am. Chem. Soc.* **2014**, *136*, 17946–17949.
25. (a) Baier, M.; Gleiter, R.; Rominger, F. *Eur. J. Org. Chem.* **2006**, *2006*, 5264–5278.
(b) Zhao, L.; Mak, T. C. W. *Organometallics* **2007**, *26*, 4439–4448.
26. Lindeman, S. V.; Rathore, R.; Kochi, J. K. *Inorg. Chem.* **2000**, *39*, 5707–5716.
27. Pommerehne, J.; Vestweber, H.; Guss, W.; Mahrt. R. F.; Bässler, H.; Porsch, M.; Daub, J. *Adv. Mater.* **1995**, *7*, 551–554.
28. (a) Ikai, M.; Tokito, S.; Sakamoto, Y.; Suzuki, T.; Taga, Y. *Appl. Phys. Lett*. **2001**, *79*, 156–158.
(b) Ren, X.; Li, J.; Holmes, R. J.; Djurovich, P. I.; Forrest, S. R.; Thompson, M. E. *Chem. Mater.*, **2004**, *16*, 4743–4747.
29. Hosokawa, C.; Higashi, H.; Nakamura, H.; Kusamoto, T. *Appl. Phys. Lett*. **1995**, *67*, 3853–3855.
30. (a) Uchida, Y.; Hirose, T.; Nakashima, T.; Kawai, T.; Matsuda, K. *Org. Lett*. **2016**, *18*, 2118–2121.
(b) Kawai, T.; Kawamura, K.; Tsumatori, H.; Ishikawa, M.; Naito, M.; Fujiki, M.; Nakashima, T. *ChemPhysChem* **2007**, *8*, 1465–1468.
(c) Maeda, H.; Bando, Y.; Shimomura, K.; Yamada, I.; Naito, M.; Nobusawa, K.; Tsumatori, H.; Kawai, T. *J. Am. Chem. Soc*. **2011**, *133*, 9266–9269.
31. Iwamura, M.; Kimura, Y.; Miyamoto, R.; Nozaki, K. *Inorg. Chem*. **2012**, *51*, 4094–4098.
32. Altomare, A.; Cascarano, G.; Giacovazzo, C.; Guagliardi, A.; Burla, M. C.; Polidori, G.; Camalli, M. *J. Appl. Cryst*. **1994**, *27*, 435.
33. Sheldrick, G. M. *Acta Cryst*. **2008**, *A64*, 112–122.
34. Burla, M. C.; Caliandro, R.; Camalli, M.; Carrozzini, B.; Cascarano, G. L.; De Caro, L.; Giacovazzo, C.; Polidori, G.; Spagna R. *J. Appl. Cryst.* **2005**, *38*, 381–388.
35. Gruene, T.; Hahn, H. W.; Luebben, A. V.; Meilleur, F.; Sheldrick. G. M. *J. Appl. Cryst.* **2014**, *47*, 462–466.

Chapter 4

Conclusion and Prospects

Conclusion and Prospects

Throughout this thesis, the development of multifunctional disilane-bridged arenes was carried out. I have prepared and evaluated the various disilane-bridged arenes with functionalities such as solid-state emission, aggregation-induced emission, molecular inversion, inclusion into macrocycles, electroluminescence, and circular polarized luminescence.

In Chapter 1, the importance and the applications of functional molecules, in particular emissive organic D–A molecules, were described. Then the emissive properties of oligosilane–arene molecules derived from σ–π conjugation were mentioned, and Pd-catalyzed arylation, the reaction to prepare oligosilane–arene molecules, was explained. And photofunctional D–Si–Si–A molecules were described to emphasize the utilities and perspectives of inserting disilane unit into organic molecules.

In Chapter 2, disilane-bridged donor–acceptor–donor (D–Si–Si–A–Si–Si–D) and acceptor–donor–acceptor (A–Si–Si–D–Si–Si–A) triads were developed. These compounds were prepared *via* Pd-catalyzed arylation of hydrosilanes in moderate yields. They absorbed UV–vis region assigned to ICT and/or π–π* transition according to DFT calculation, and by the excitation of these bands, weak emission in the solution state whereas strong emission in the solid state (up to 85% quantum yield) arising from the aggregation effect (AIE). X-ray diffraction revealed that there were no π–π stacking in crystalline phase owing to the bulkiness of the disilane unit, which suppressed the intermolecular interaction.

In Chapter 3, multifunctional octamethyltetrasila[2.2]cyclophane derivatives were investigated. Desired products, containing donor–acceptor and planar chiral ones, were synthesized *via* Pd-catalyzed cyclization reaction. The structural studies were carried out with XRD, NMR, and DFT calculation. VT-NMR results revealed that the molecular inversion occurred in solution phase, and this inversion could be controlled by the bulkiness of substituents. By the inclusion with macrocycles, this inversion motion was suppressed because of the strong Ag–π interaction. Donor–acceptor tetrasila[2.2]cyclophanes showed broad absorption bands and green-colored emission assignable to ICT transition, and one compound showed solid state emission with 49% quantum yield. OLED containing a donor–acceptor tetrasila[2.2]cyclophane was fabricated, which displayed green electroluminescence with 0.36% external quantum efficiency. Moreover, the development of a planar chiral tetrasila[2.2]cyclophane with CPL activity ($|g_{lum}|$ = ca. 0.002) was achieved.

As future prospects, disilane-bridged D–A oligomers (such as D–A–D–A molecules)

or polymers, which have longer conjugation system, will be investigated for the development of novel OLED materials. In this research, I achieved organosilanes with blue- to green-colored emissive properties in the solid state (D–A–D and A–D–A) in Chapter 2. To enhance the variety of multi-colored emitting organosilanes (especially yellow to red emission in the solid phase or in the film phase), it is necessary to develop the more extended disilane-bridged D–A oligomers and polymers. In addition, disilane-bridged cyclophanes displayed both electroluminescence and CPL properties as described in Chapter 3. For the application to optical devices such as 3D display, it is important to develop the materials showing circularly polarized electroluminescence, the combination of OLED and CPL. Utilizing the features of cyclophane and disilane linkers, tetrasila[2.2]cyclophanes with the high CPL ability and high EL efficiency are excepted to be developed. Moreover, in this research, only tetramethyldisilane was used as a linker. By replacing the methyl groups bonded to Si atoms with bulkier groups (e.g. *tert*-butyl moieties, Figure 4.1.1(a)), the enhancement of solid state emission is expected by the strong suppression of intermolecular interaction compared with methyl groups. By connecting two methyl groups with alkyl chains (e.g. disilacyclohexane moieties, Figure 4.1.1(b)), the improvement of emission in solution is expected owing to the inhibition of non-radiative relaxations (e.g. molecular rotation and vibration).[1]

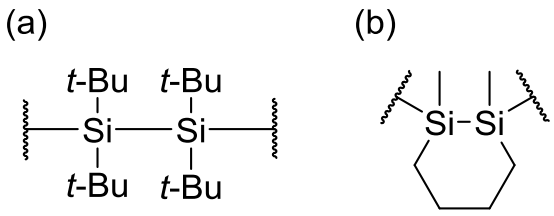

Figure 4.1.1. (a) Structure of tetra-*tert*-butyldisilane linker. (b) Structure of dimethyldisilacyclohexane linker.

To conclude my Ph.D. thesis, a series of disilane-bridged triads and cyclophanes which displayed various functionalities has been developed. Pd-catalyzed coupling reaction provided the preparation of novel disilane-bridged arenes, including donor–acceptor dyads/triads and chiral system. Utilizing the feature of a disilane linker, "nonplanar and flexible structure with σ conjugation system", I developed "multiple functional" aryl-disilane compounds. This research, the development of multifunctional disilane-bridged materials, is expected to contribute to the development of multifunctional silicone-based materials, especially oligosilane-bridged organic molecules.

Reference

1. Karatsu, T. *J. Photochem. Photobiol. C: Photochem. Rev.* **2008**, *9*, 111–137.

Appendix

Copies of ^{1}H and ^{13}C NMR spectra in $CDCl_3$ at 300 K

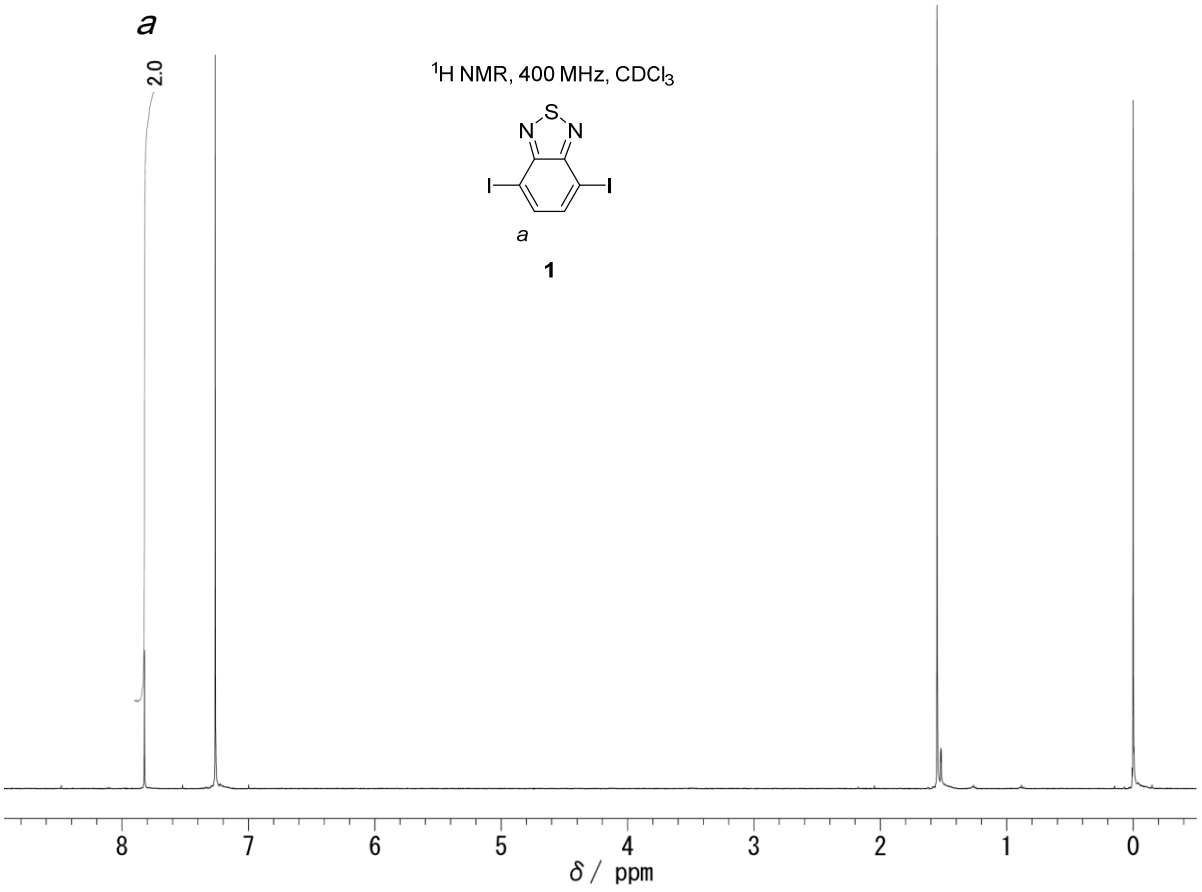
a
2.0
^{1}H NMR, 400 MHz, $CDCl_3$
N
S
N
I
I
a
1
8
7
6
5
4
3
2
1
0
δ / ppm

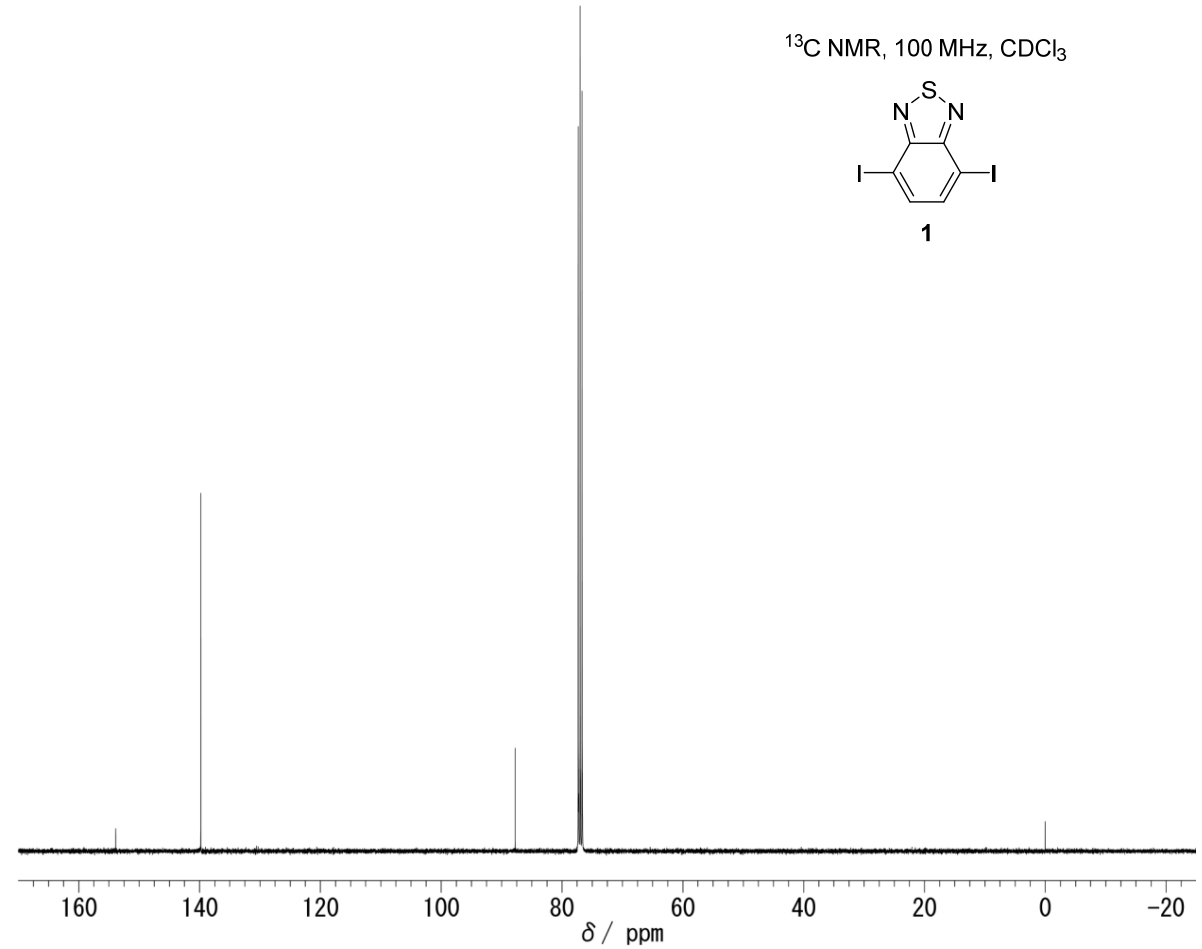
^{13}C NMR, 100 MHz, $CDCl_3$
N
S
N
I
I
1
160
140
120
100
80
60
40
20
0
−20
δ / ppm

^{1}H NMR, 500 MHz, $CDCl_3$

2

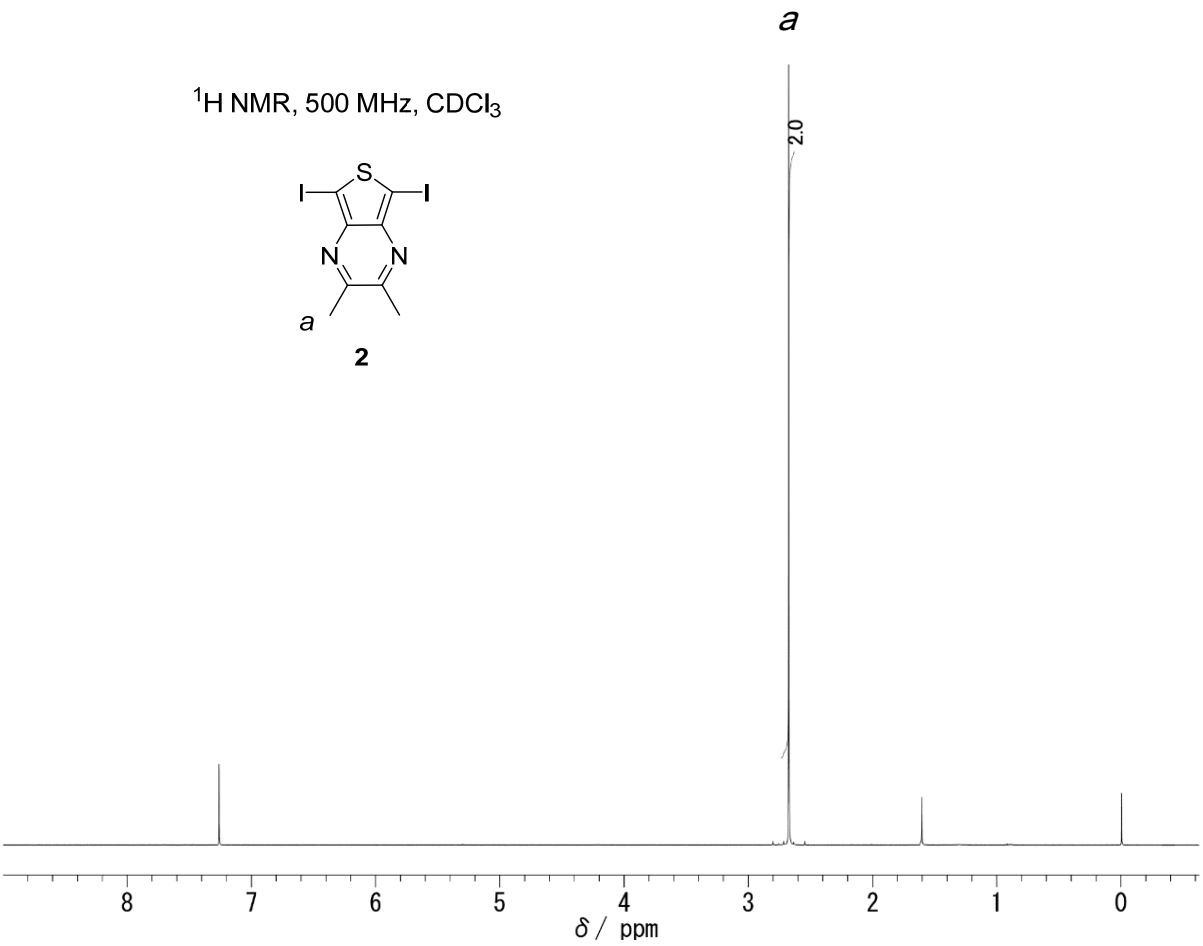

^{13}C NMR, 125 MHz, $CDCl_3$

2

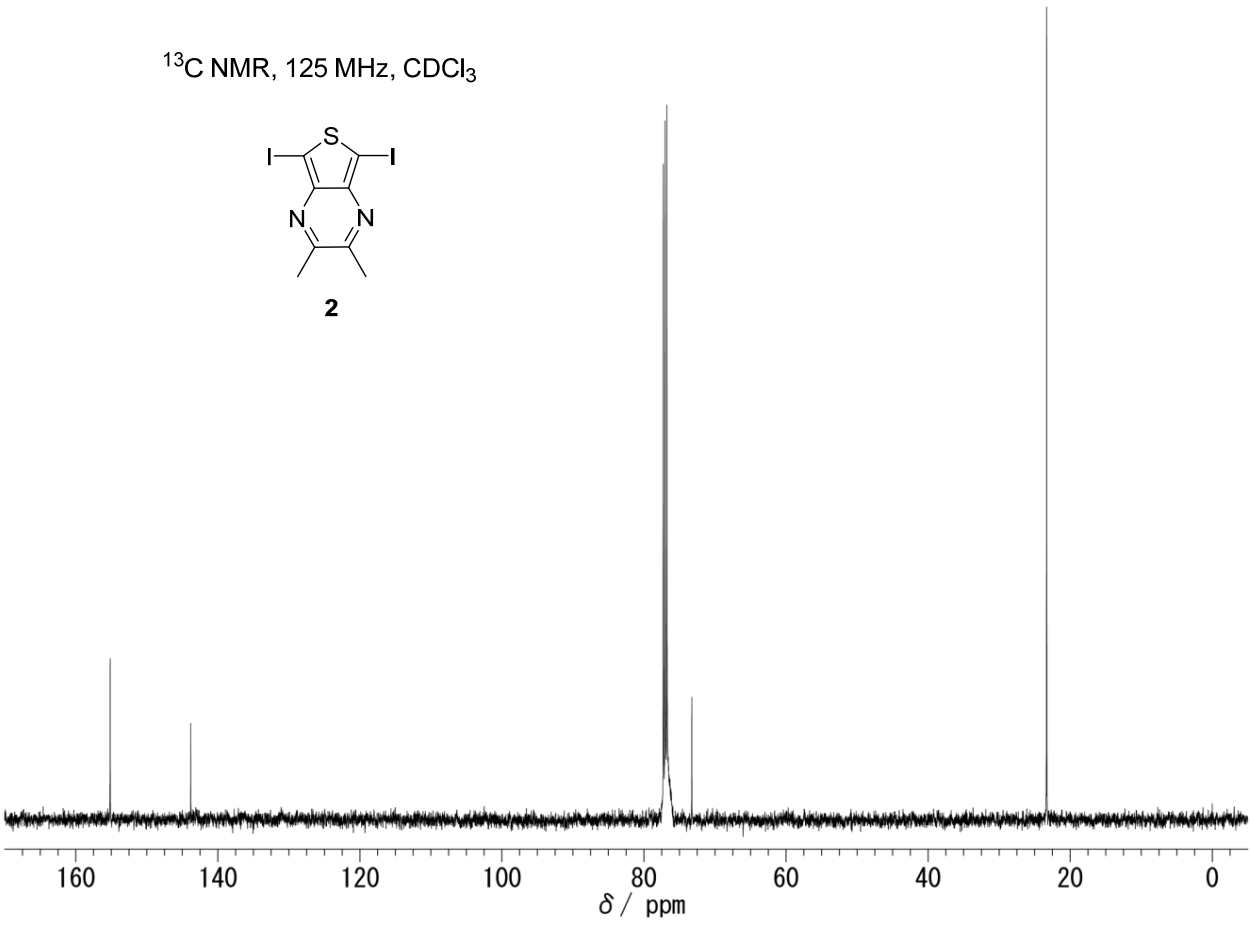

^{1}H NMR, 500 MHz, $CDCl_3$

6

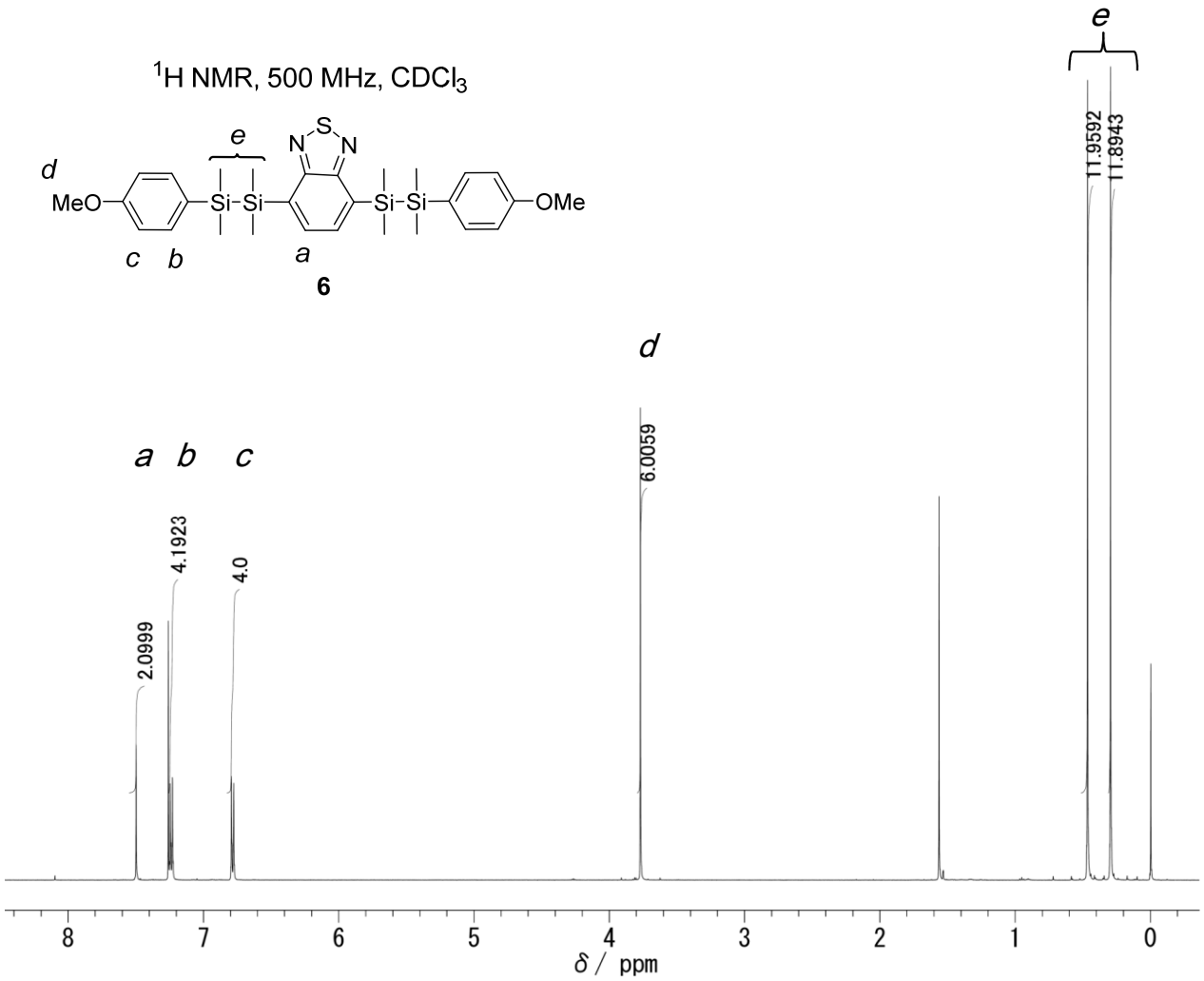

^{13}C NMR, 125 MHz, $CDCl_3$

6

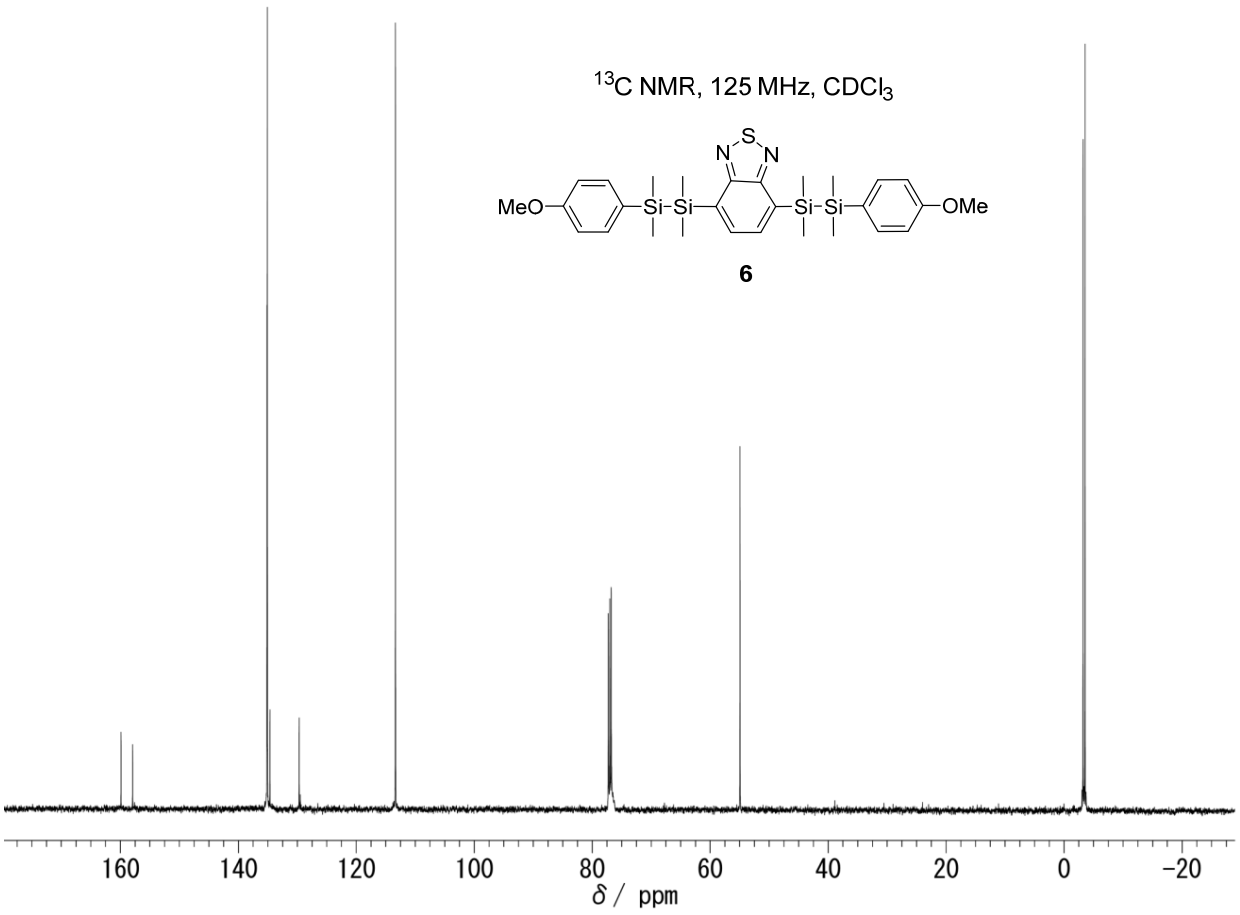

^{1}H NMR, 400 MHz, $CDCl_3$

7

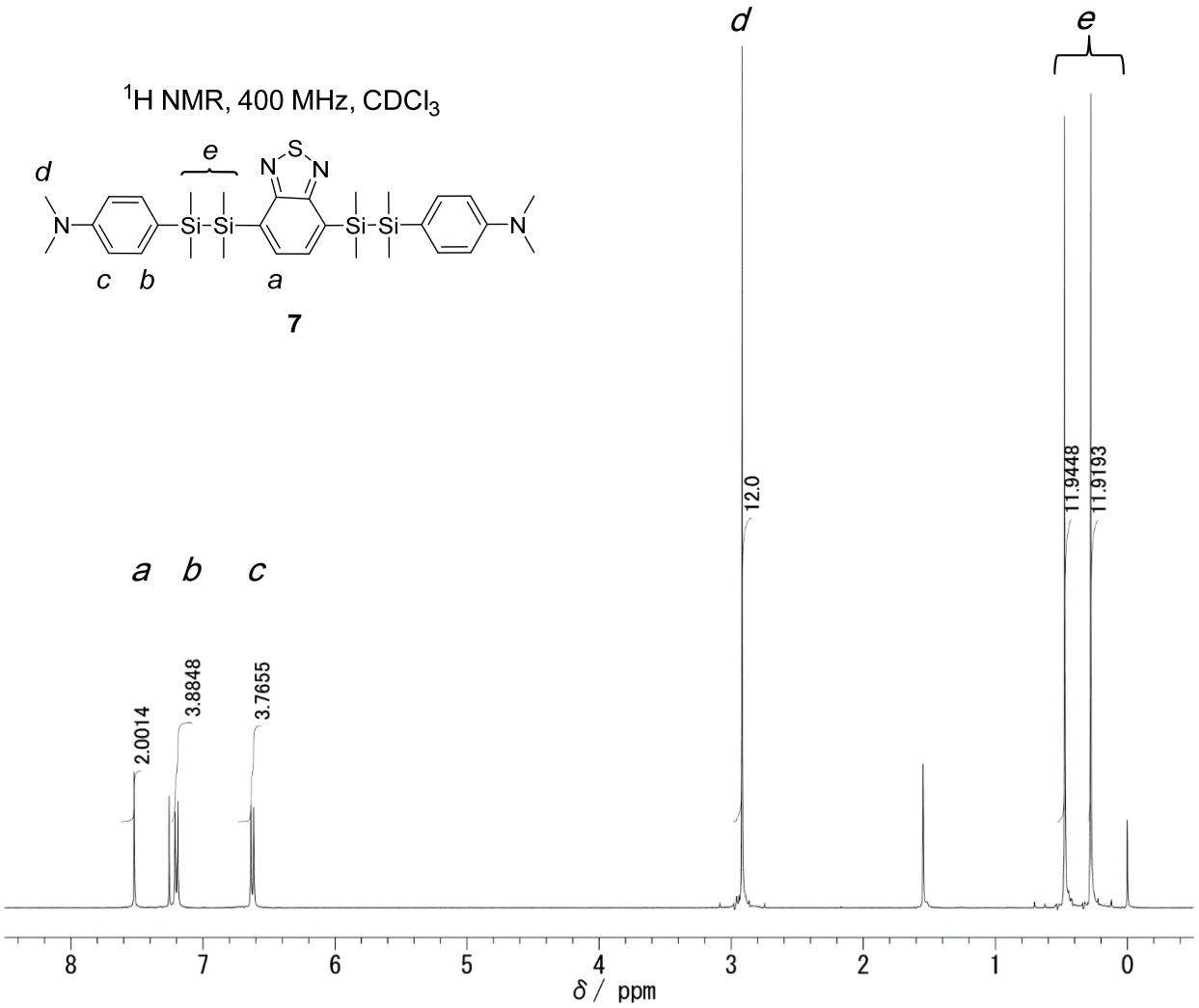

^{13}C NMR, 100 MHz, $CDCl_3$

7

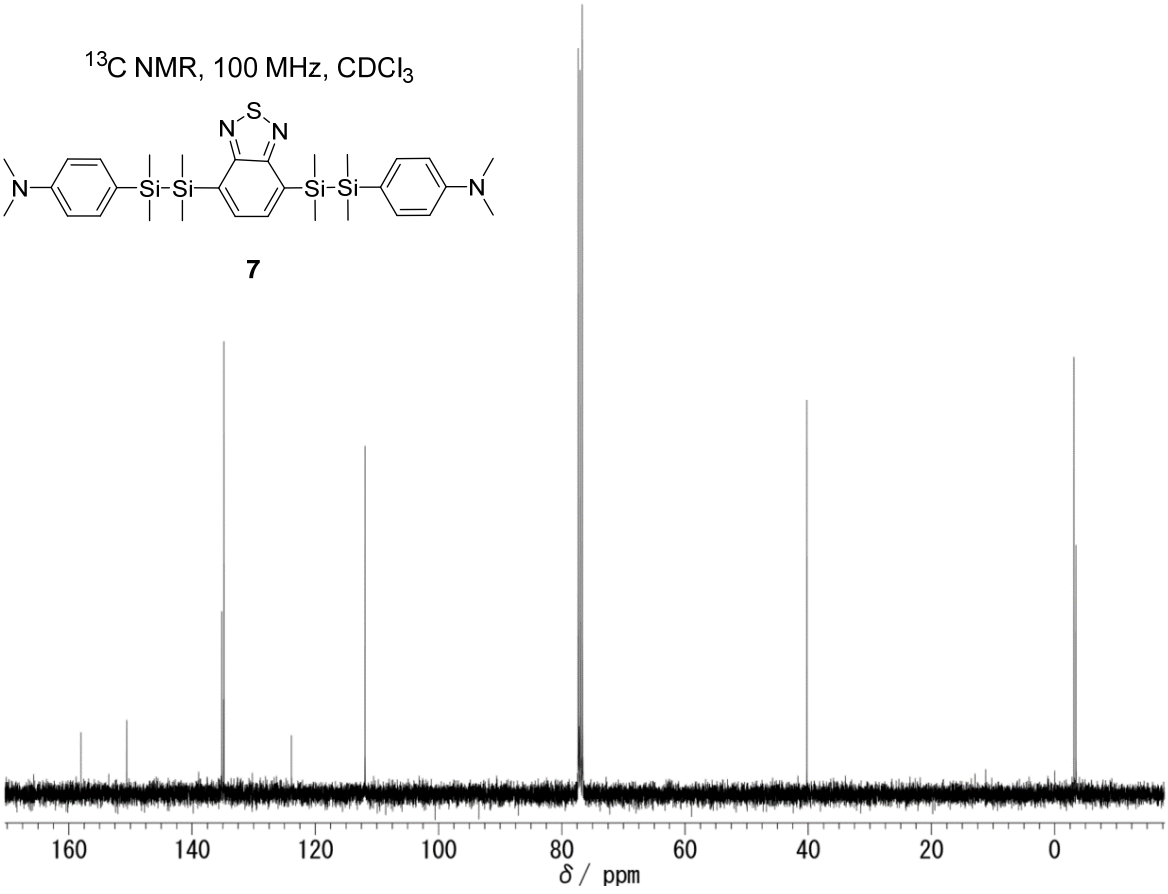

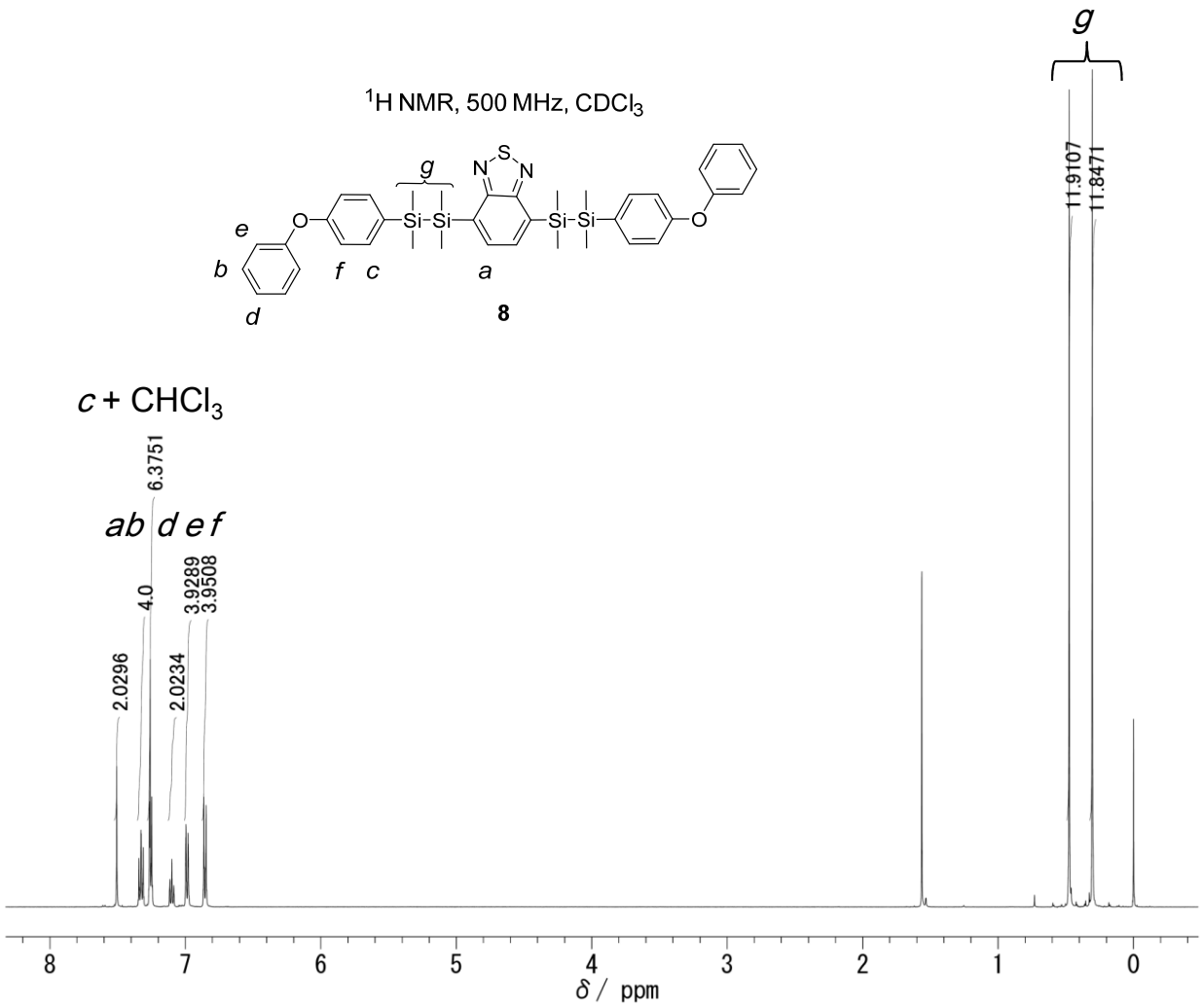
g
^{1}H NMR, 500 MHz, CDCl$_3$
e
b
d
f
c
a
8
11.9107
11.8471
c + CHCl$_3$
6.3751
ab
d
e
f
4.0
3.9289
3.9508
2.0296
2.0234
8
7
6
5
4
3
2
1
0
δ / ppm

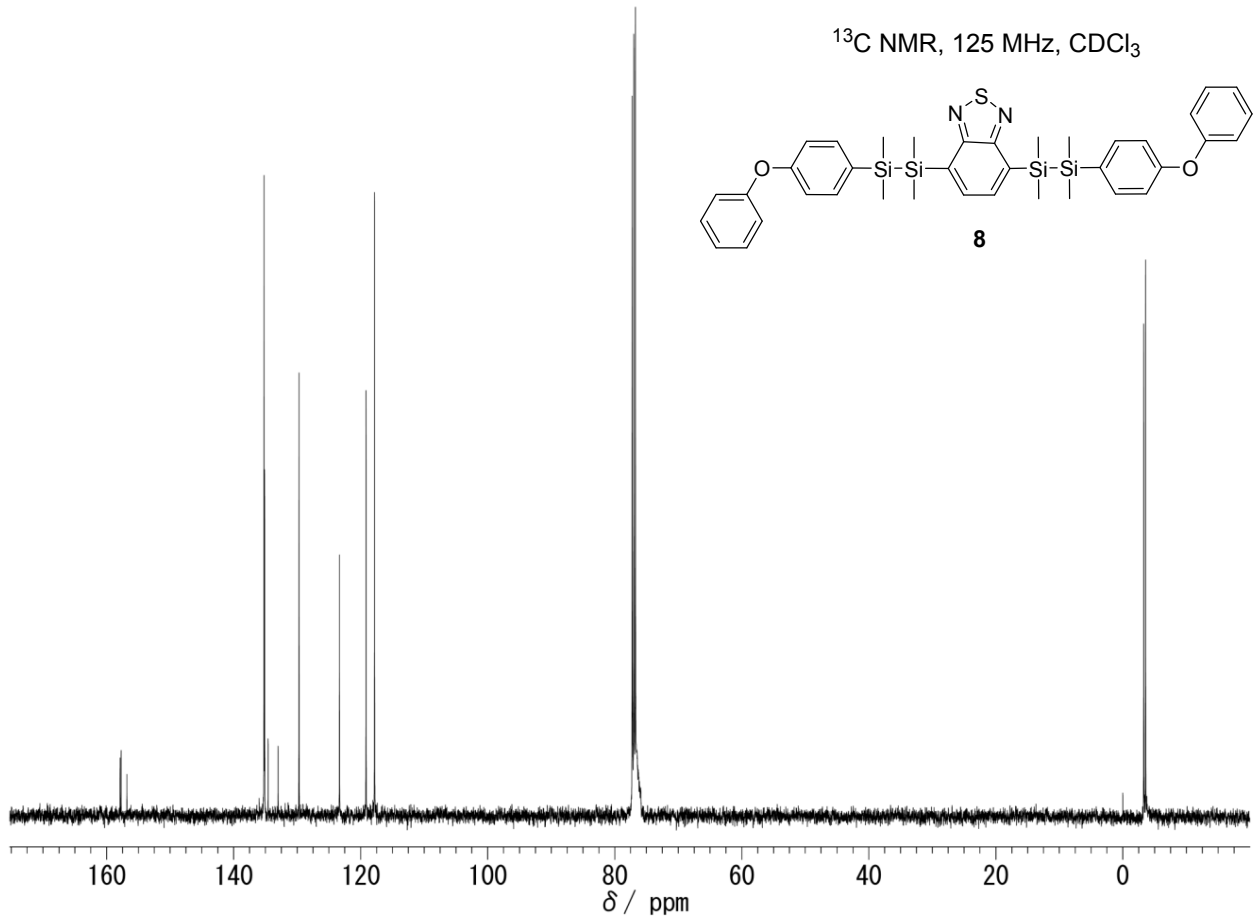
^{13}C NMR, 125 MHz, CDCl$_3$
8
160
140
120
100
80
60
40
20
0
δ / ppm

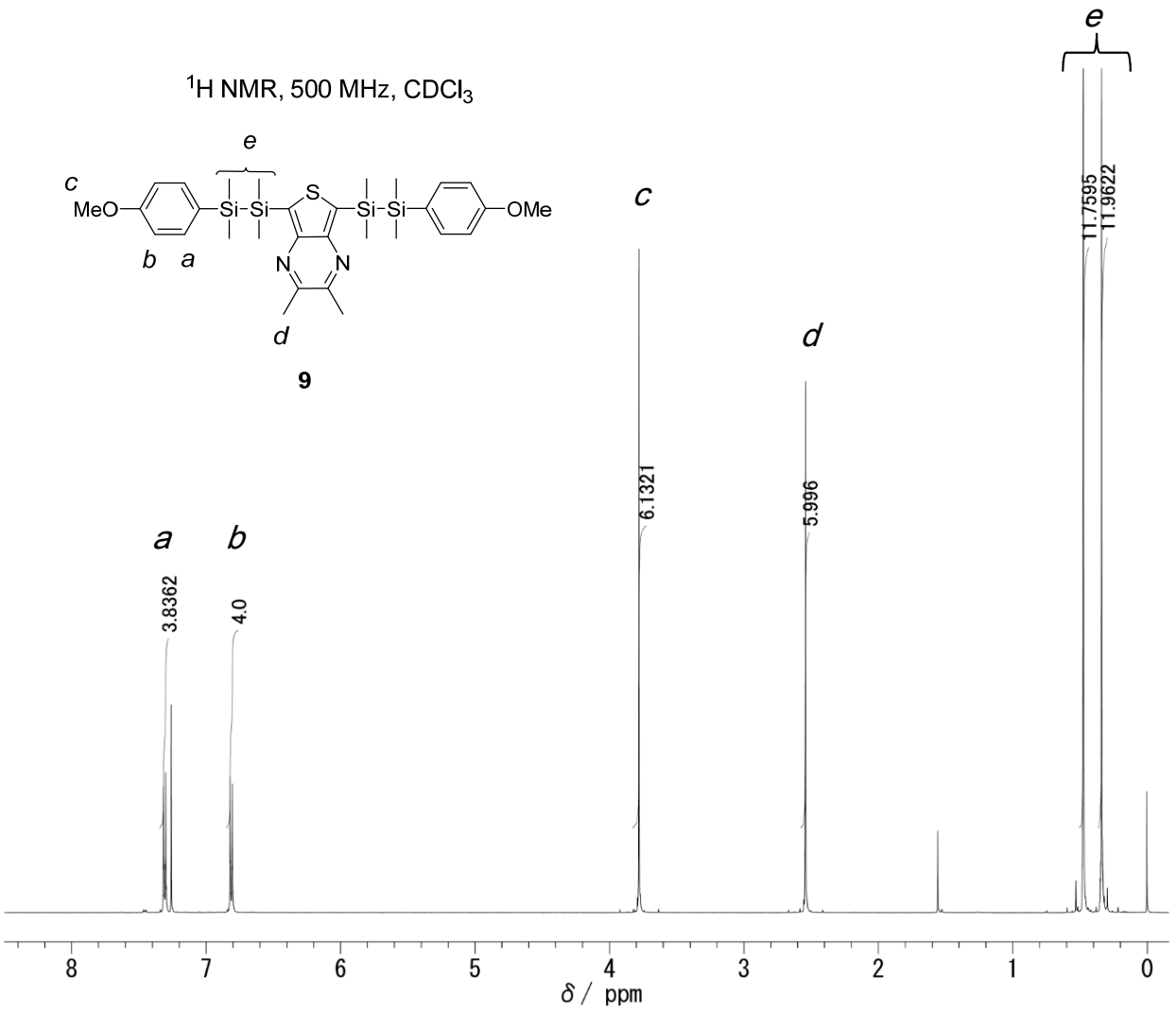
1H NMR, 500 MHz, CDCl3
e
c
MeO
Si-Si
S
Si-Si
OMe
b a
N
N
d
9
a
b
c
d
e
3.8362
4.0
6.1321
5.996
11.7595
11.9622
8
7
6
5
4
3
2
1
0
δ / ppm

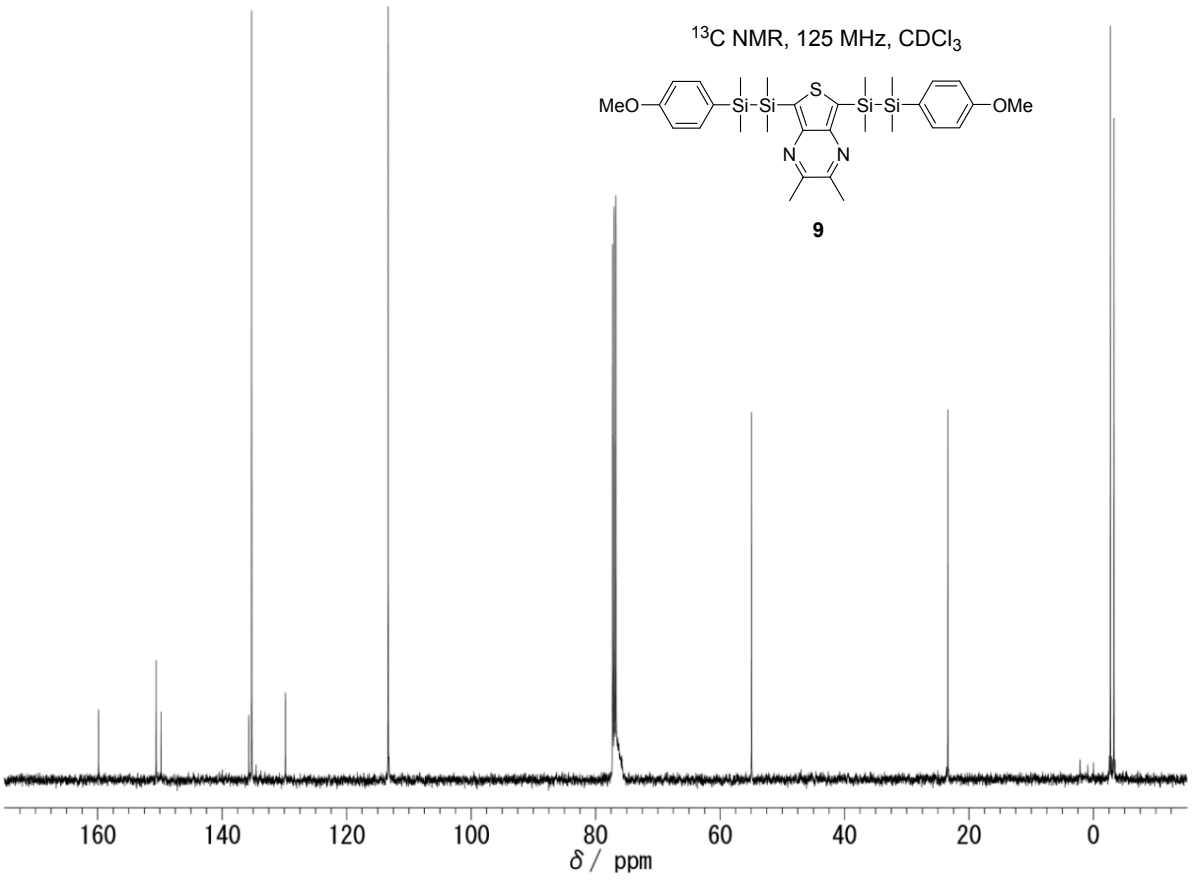
13C NMR, 125 MHz, CDCl3
MeO
Si-Si
S
Si-Si
OMe
N
N
9
160
140
120
100
80
60
40
20
0
δ / ppm

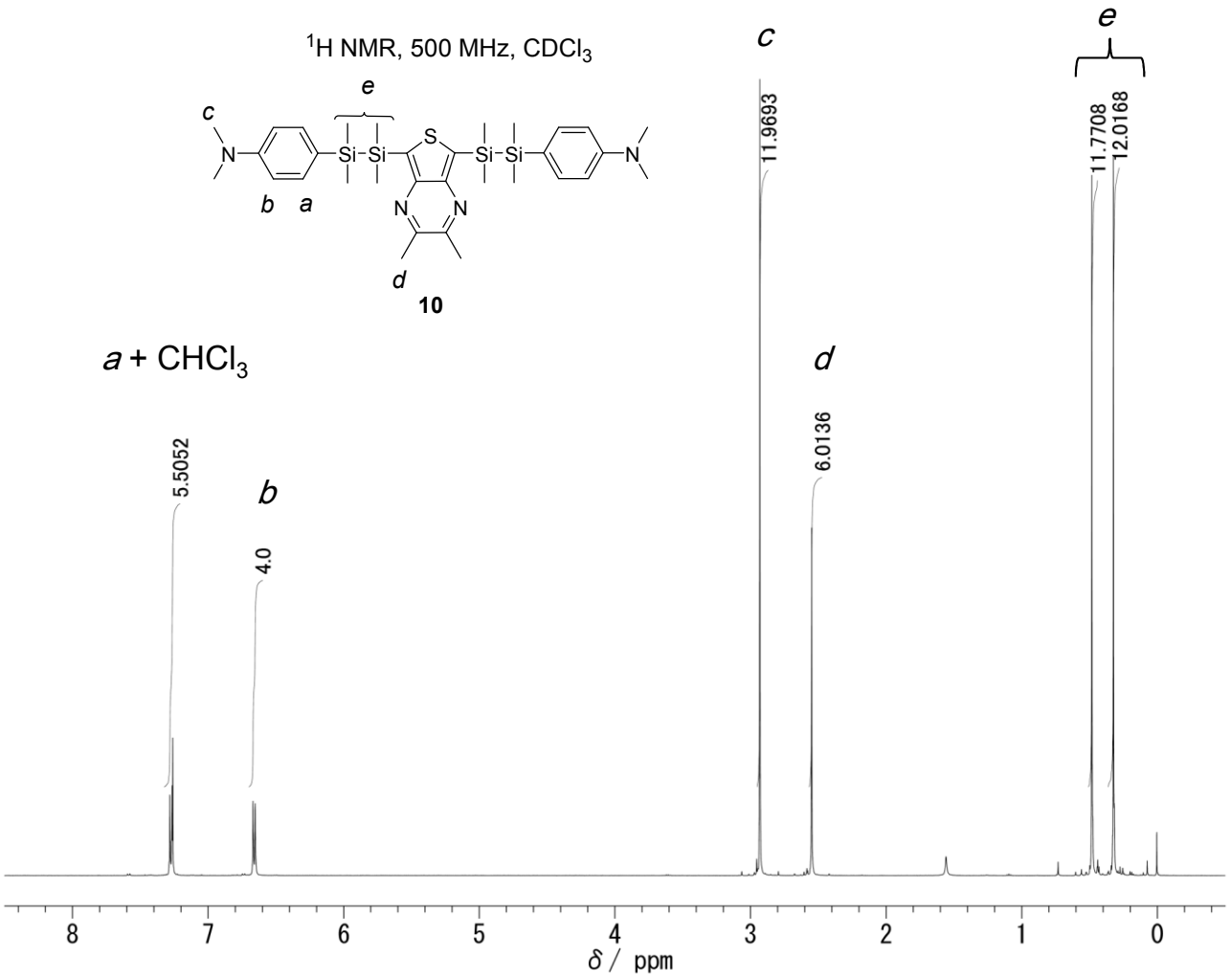
^{1}H NMR, 500 MHz, $CDCl_3$
10
a + $CHCl_3$
5.5052
4.0
11.9693
6.0136
11.7708
12.0168
δ / ppm

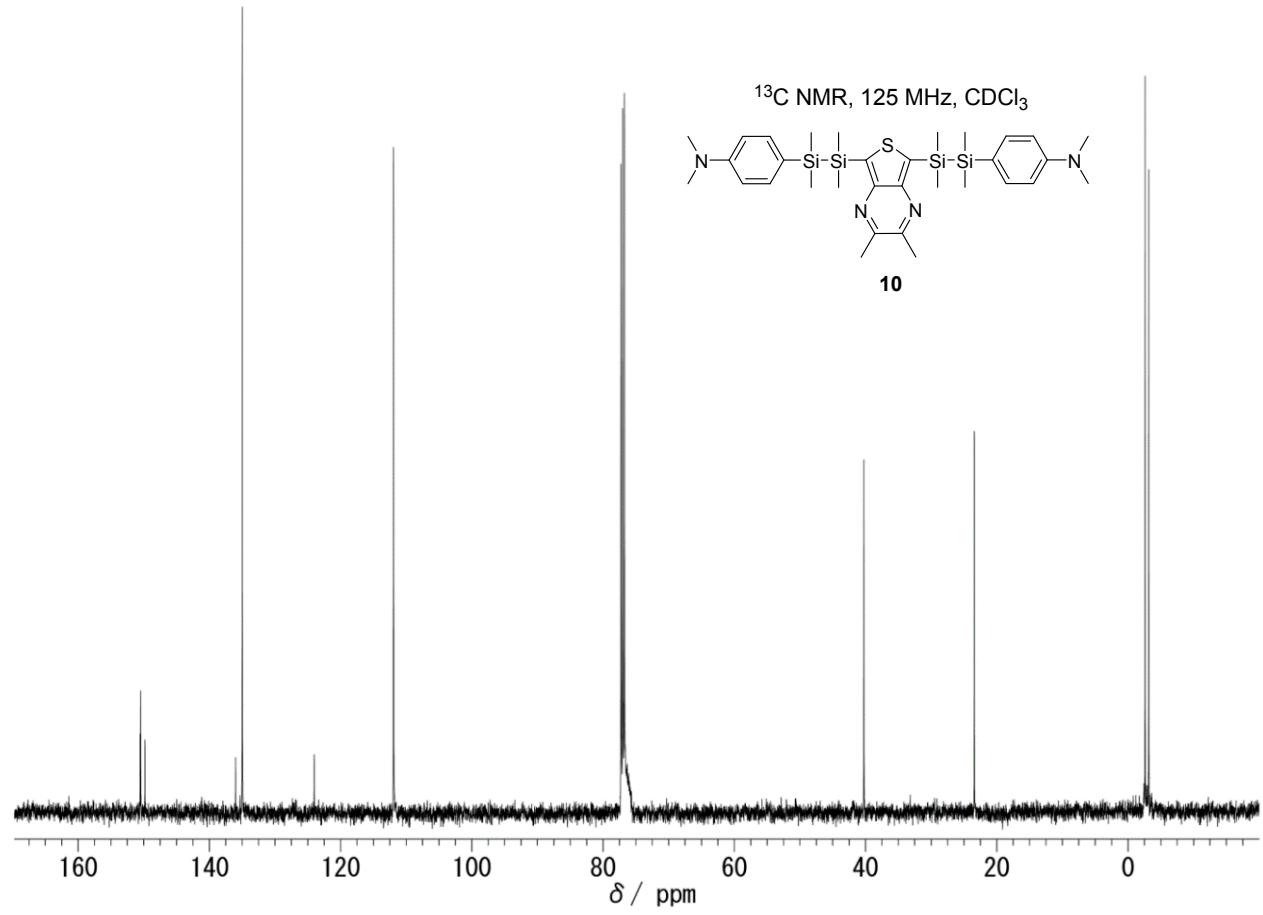
^{13}C NMR, 125 MHz, $CDCl_3$
10
δ / ppm

^{1}H NMR, 400 MHz, $CDCl_3$

11

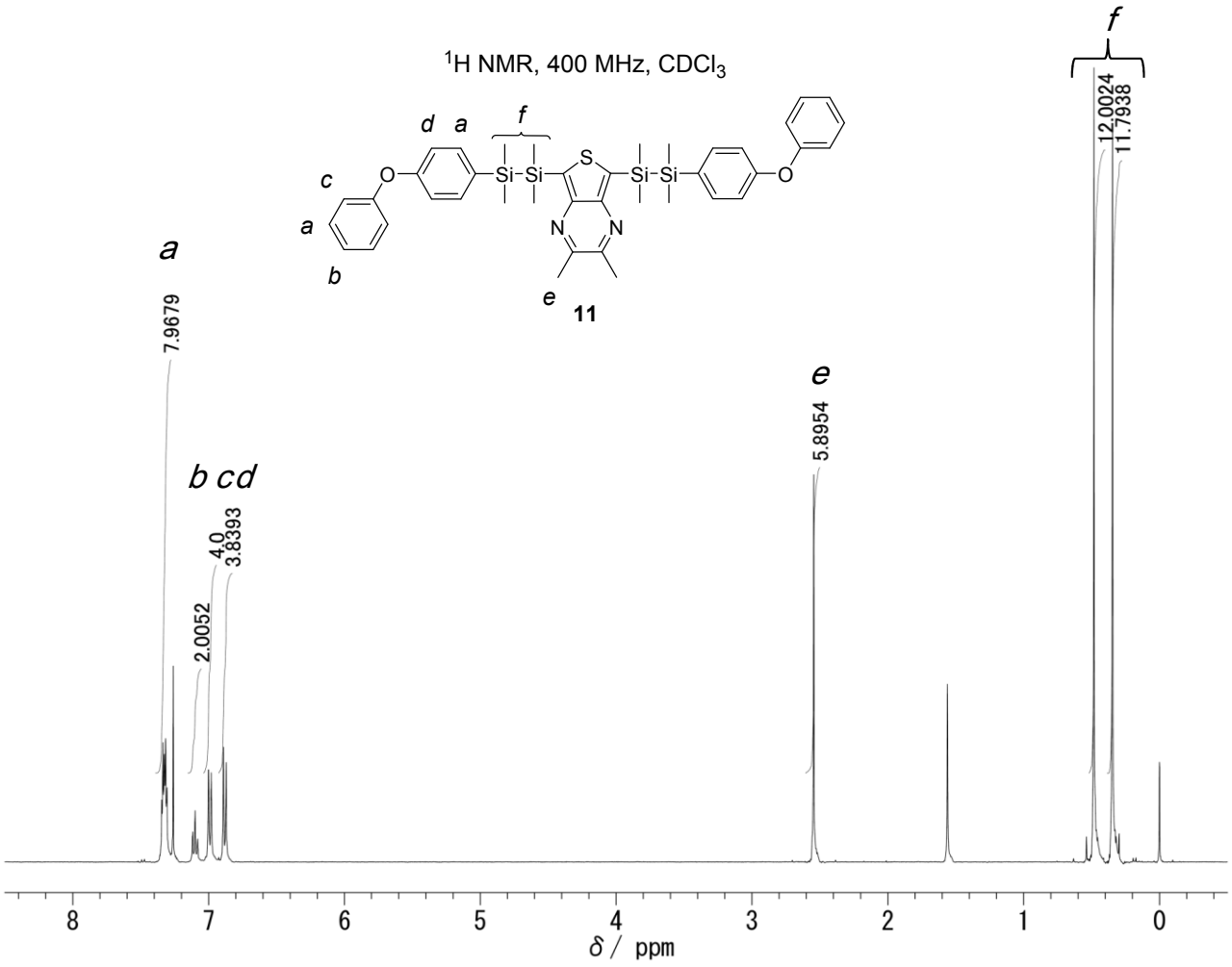

^{13}C NMR, 100 MHz, $CDCl_3$

11

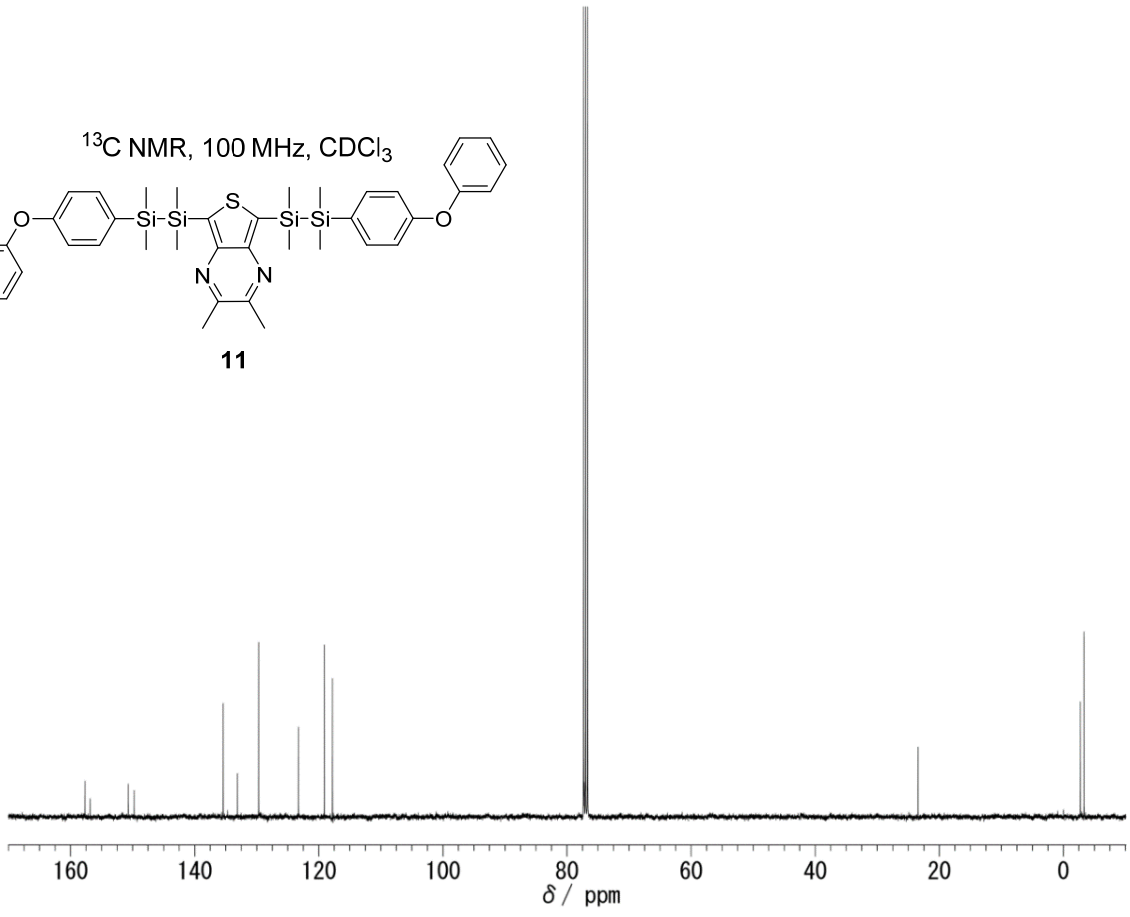

^{1}H NMR, 500 MHz, $CDCl_3$

12

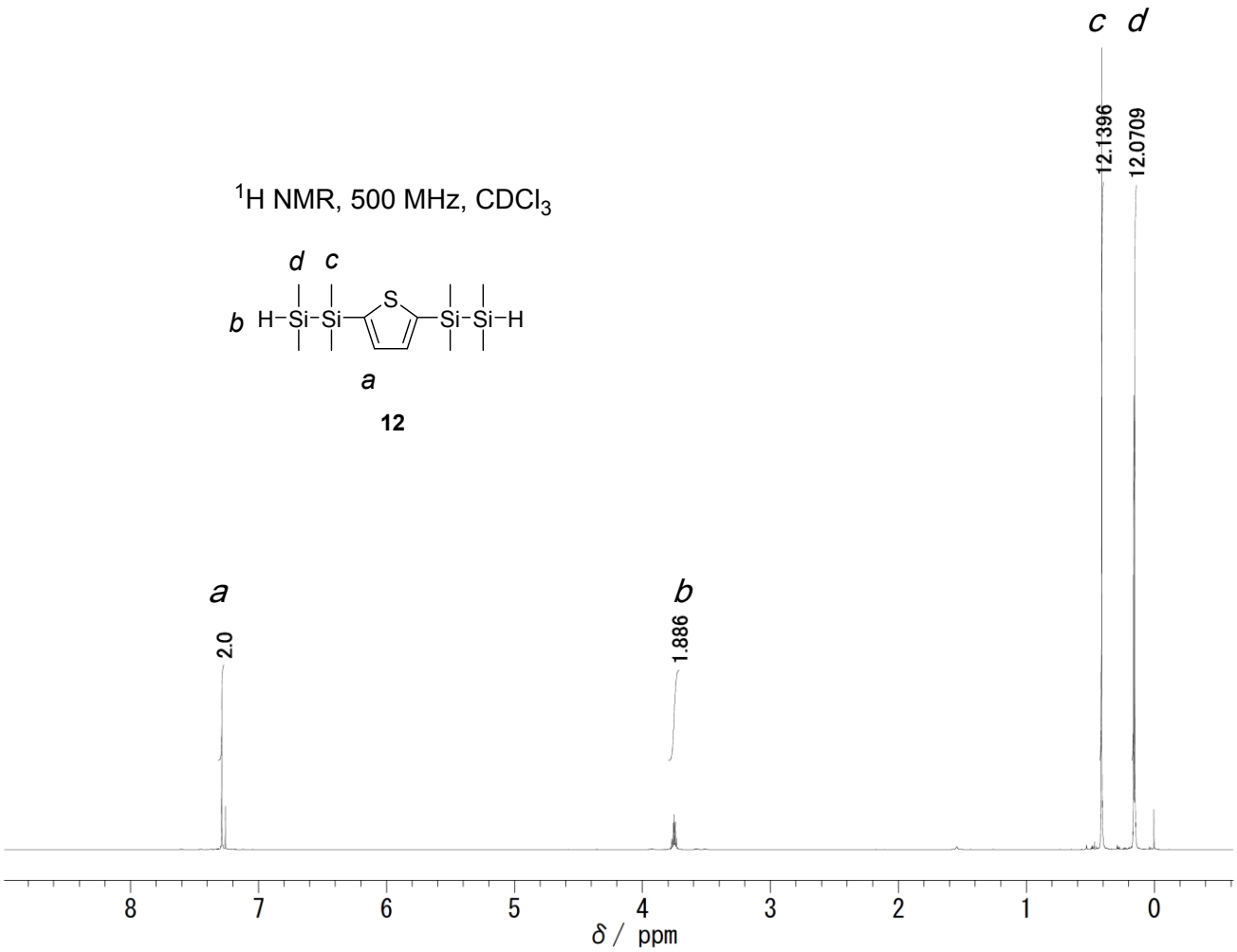

^{13}C NMR, 125 MHz, $CDCl_3$

12

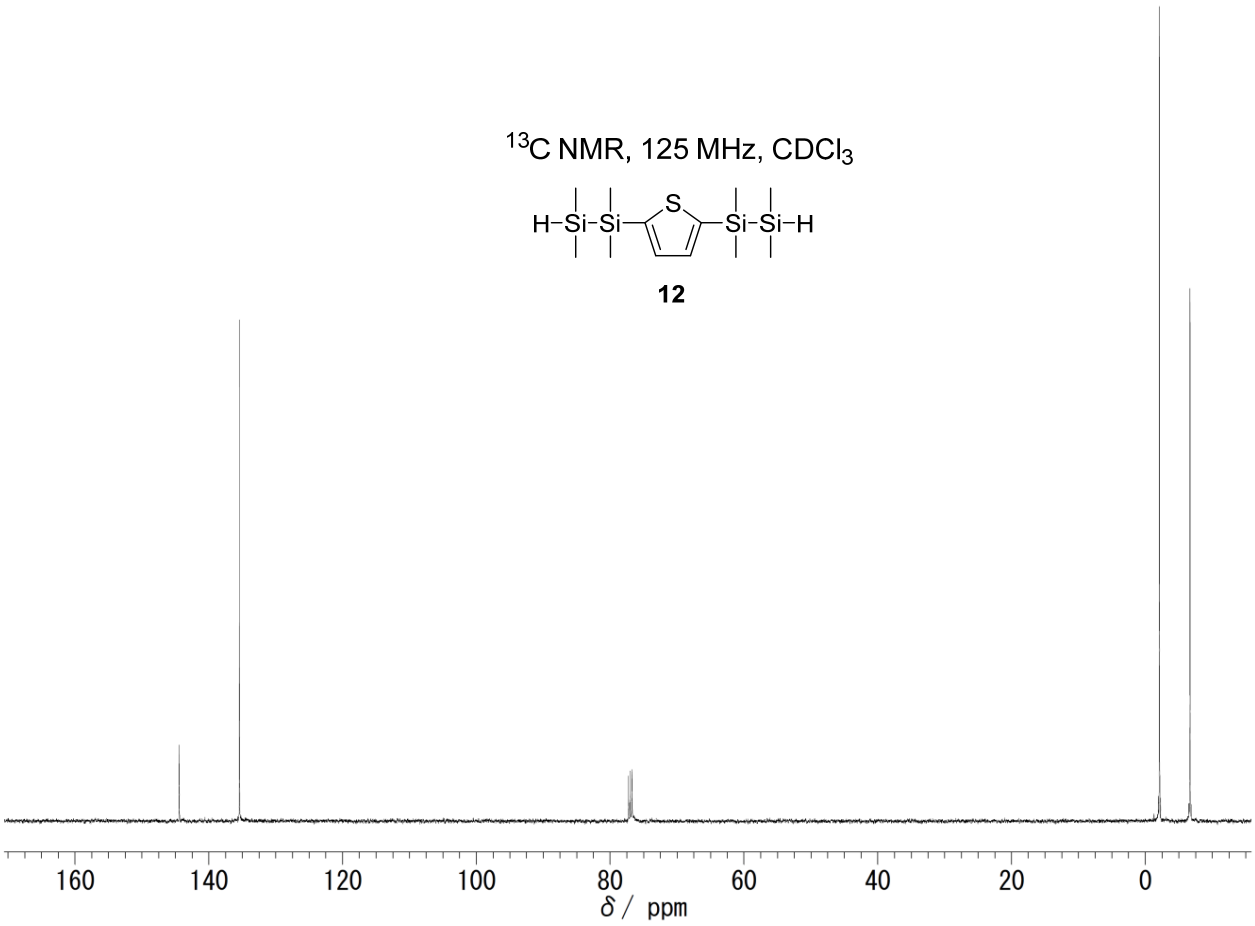

^{1}H NMR, 500 MHz, $CDCl_3$

13

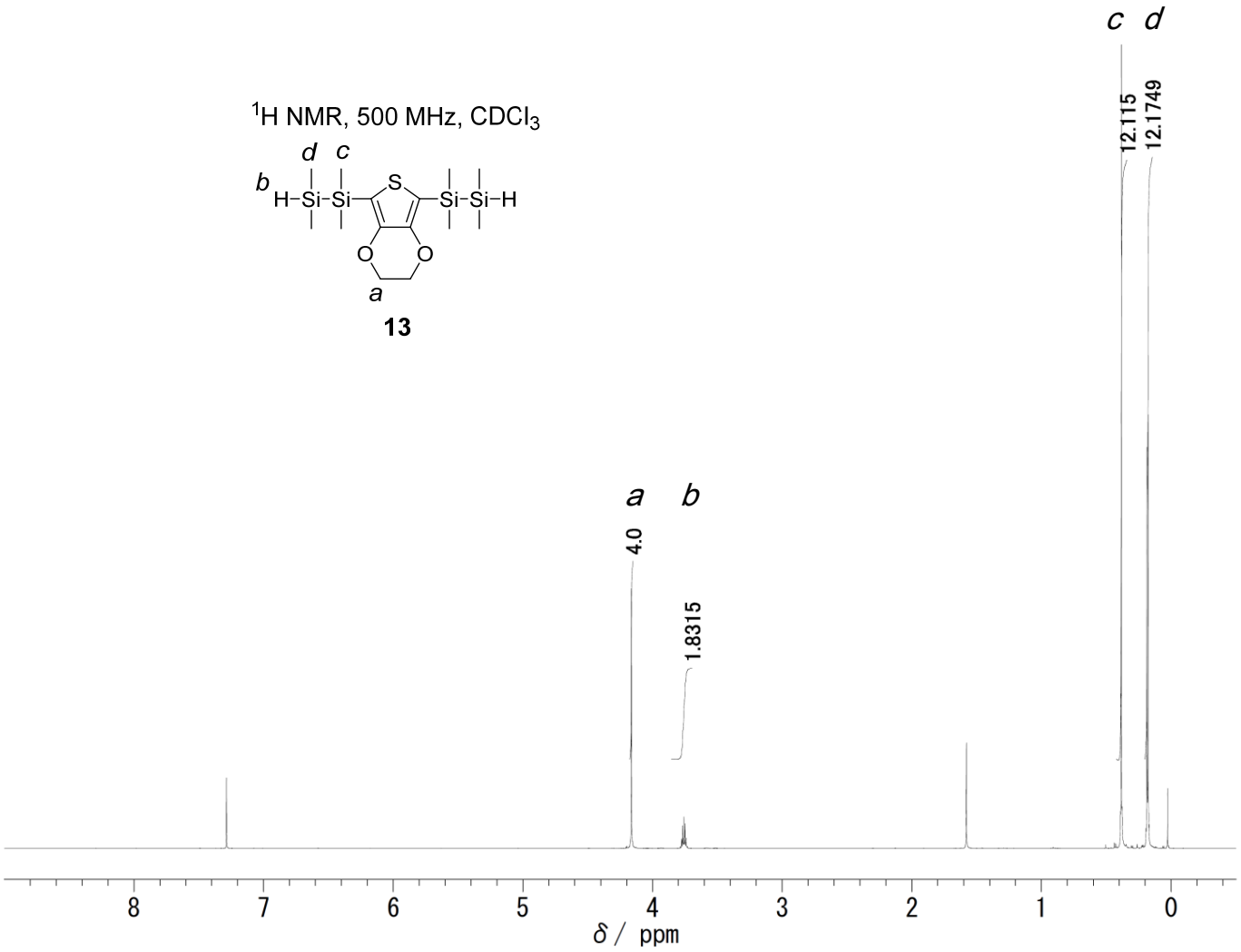

^{13}C NMR, 125 MHz, $CDCl_3$

13

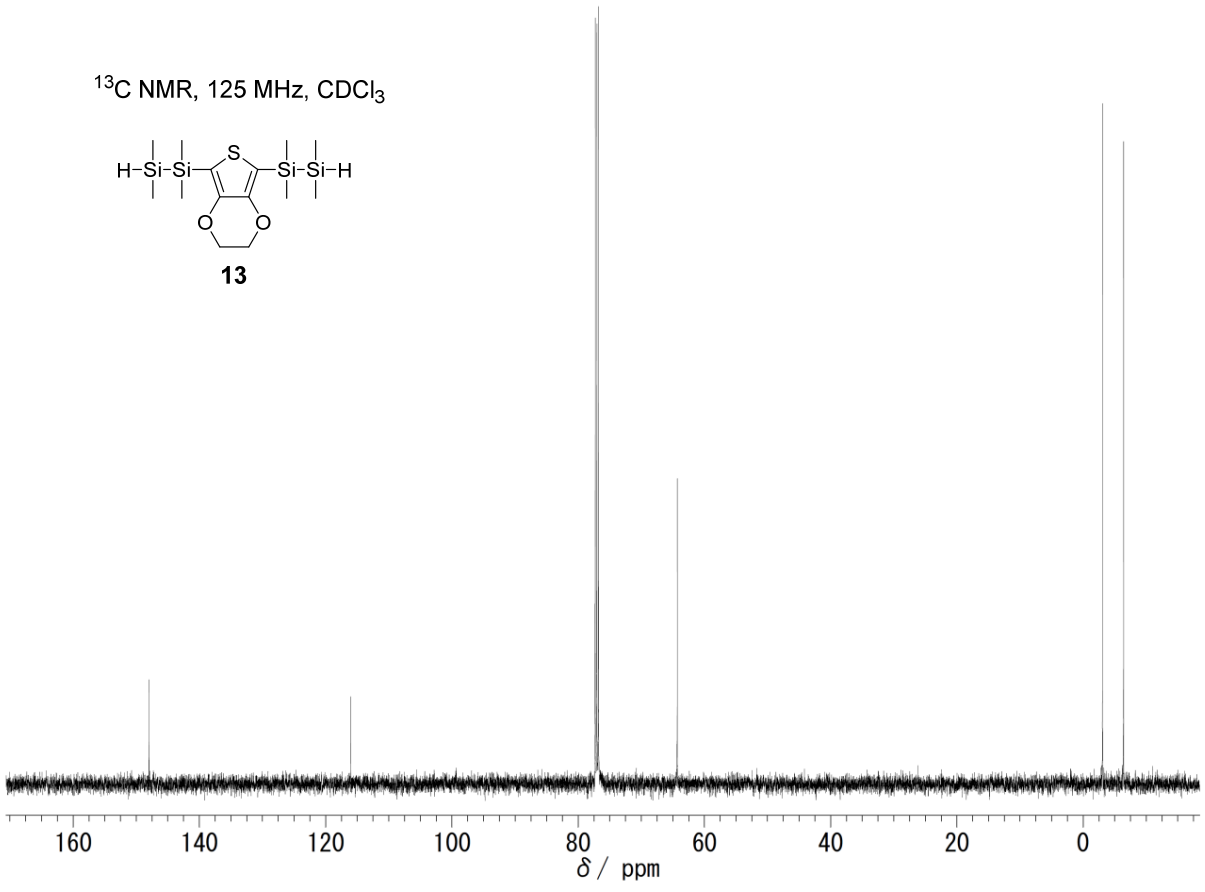

^{1}H NMR, 500 MHz, $CDCl_3$

14

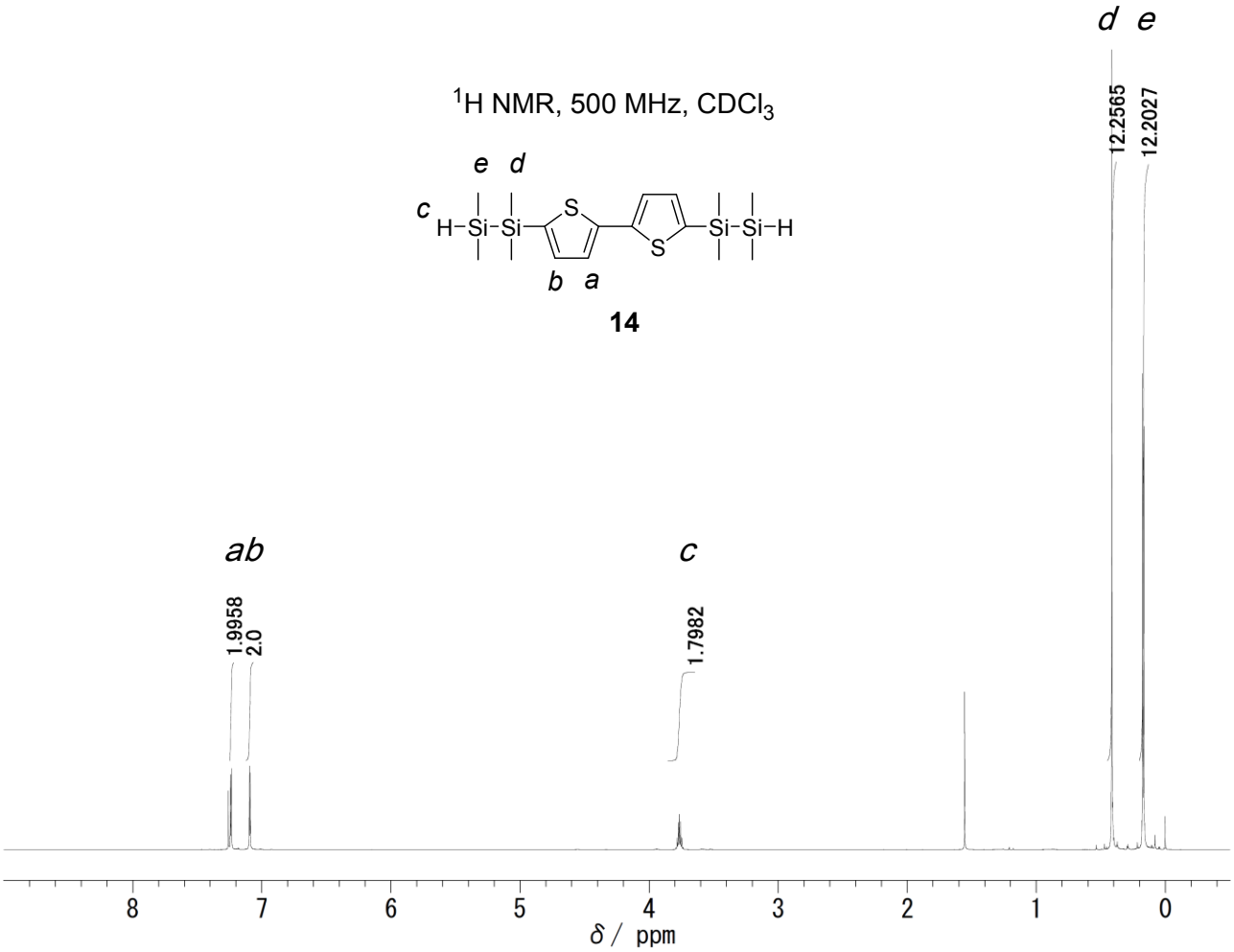

^{13}C NMR, 125 MHz, $CDCl_3$

14

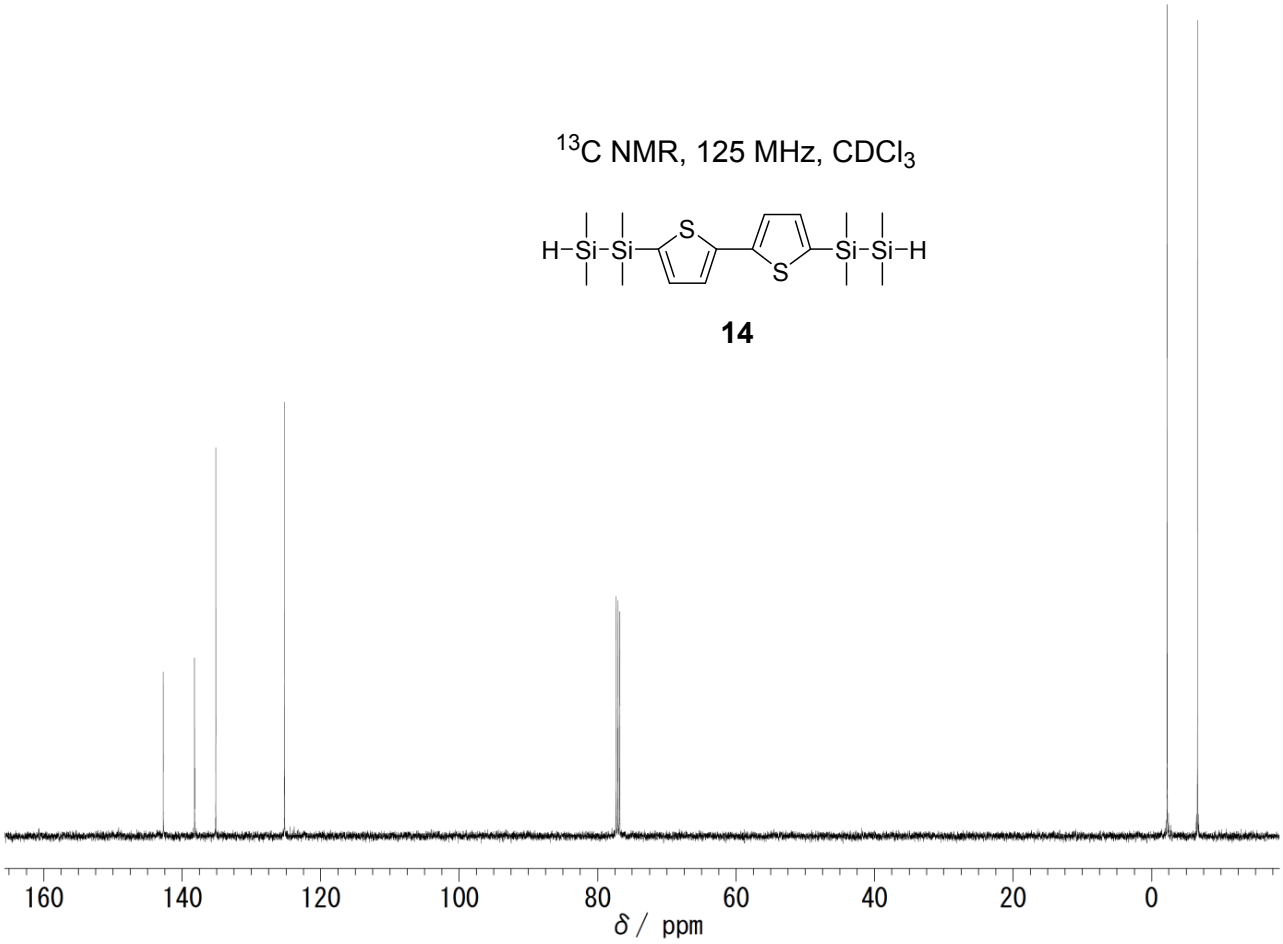

^{1}H NMR, 500 MHz, $CDCl_3$

15

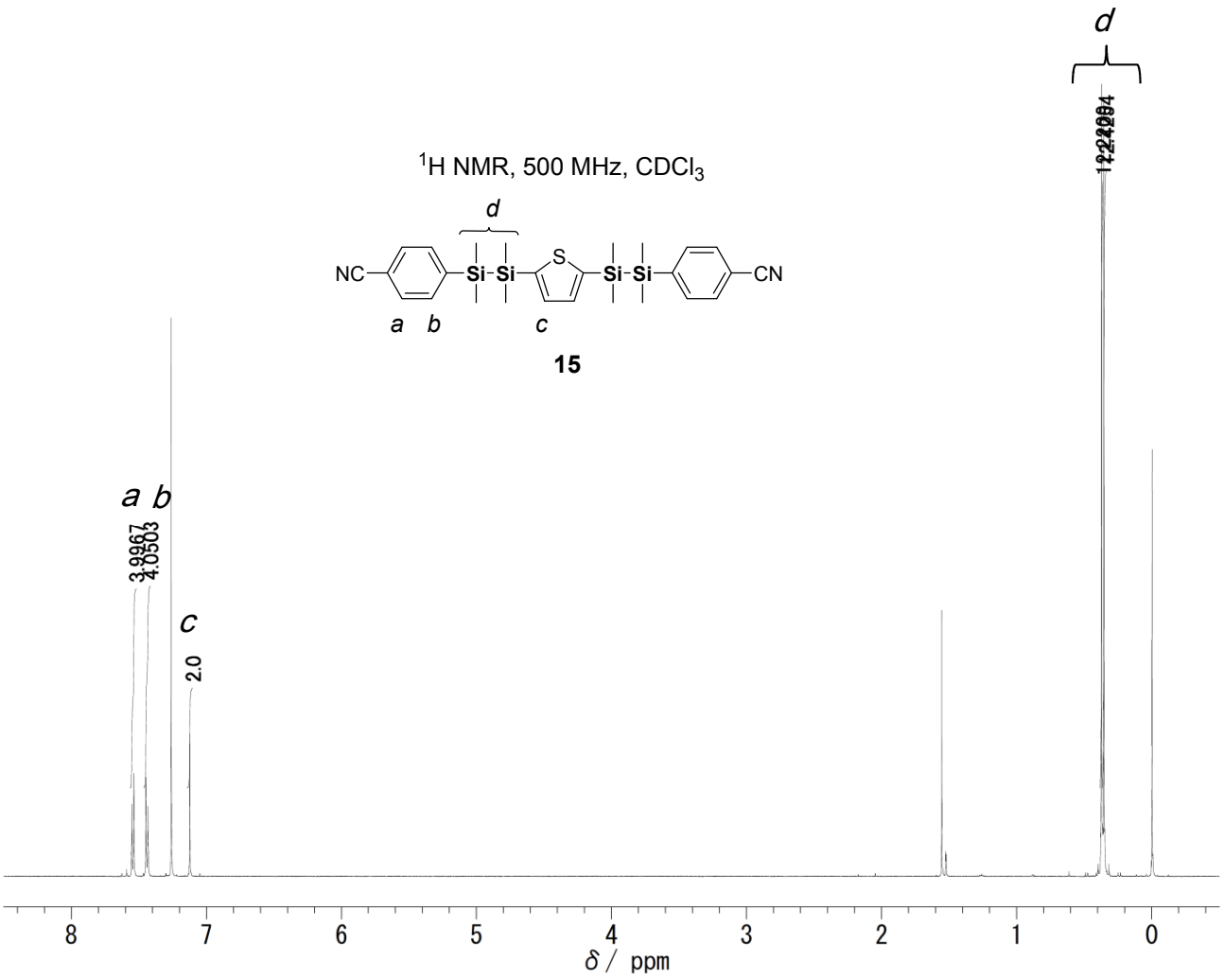

^{13}C NMR, 125 MHz, $CDCl_3$

15

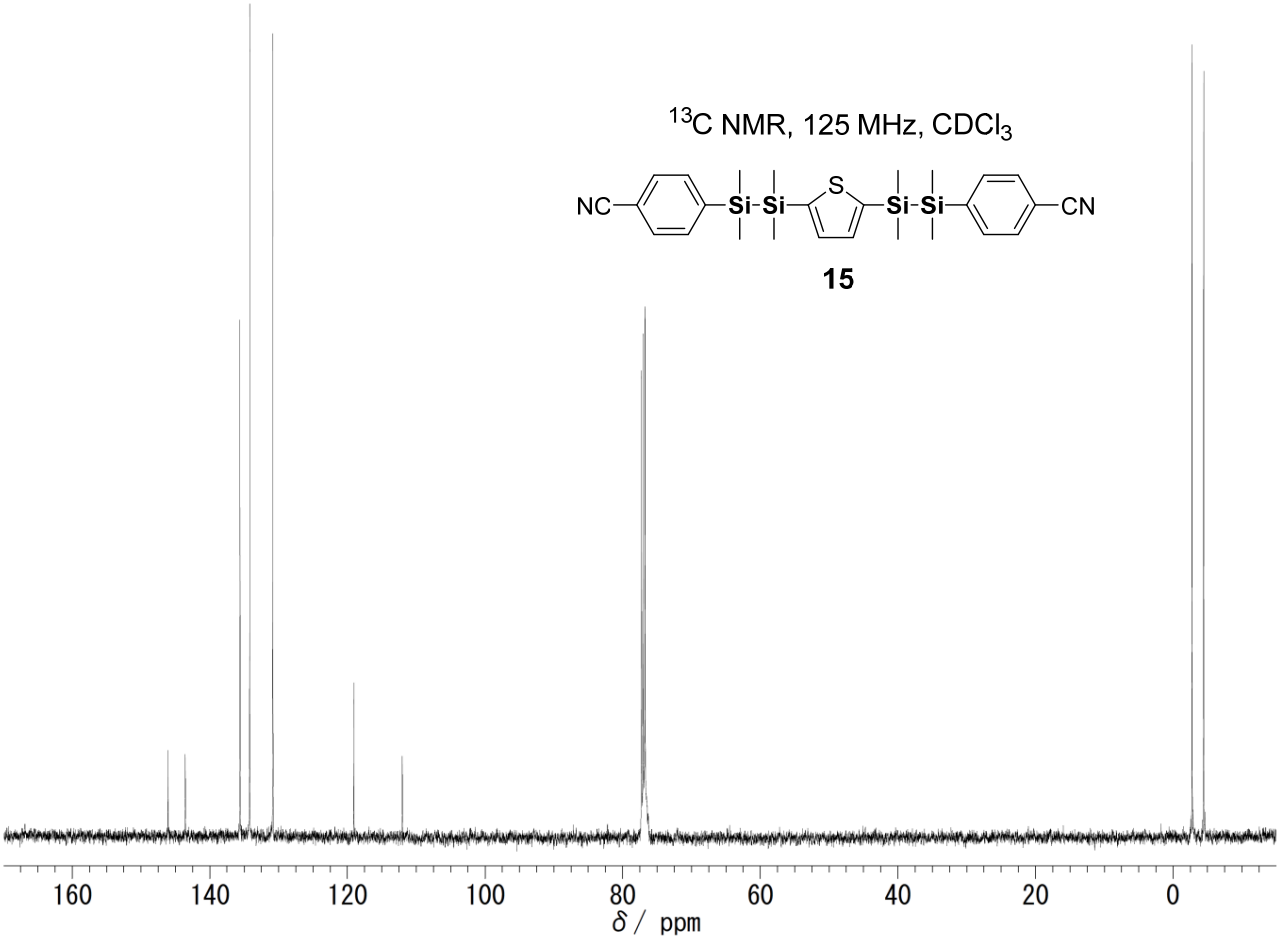

^{1}H NMR, 500 MHz, $CDCl_3$

16

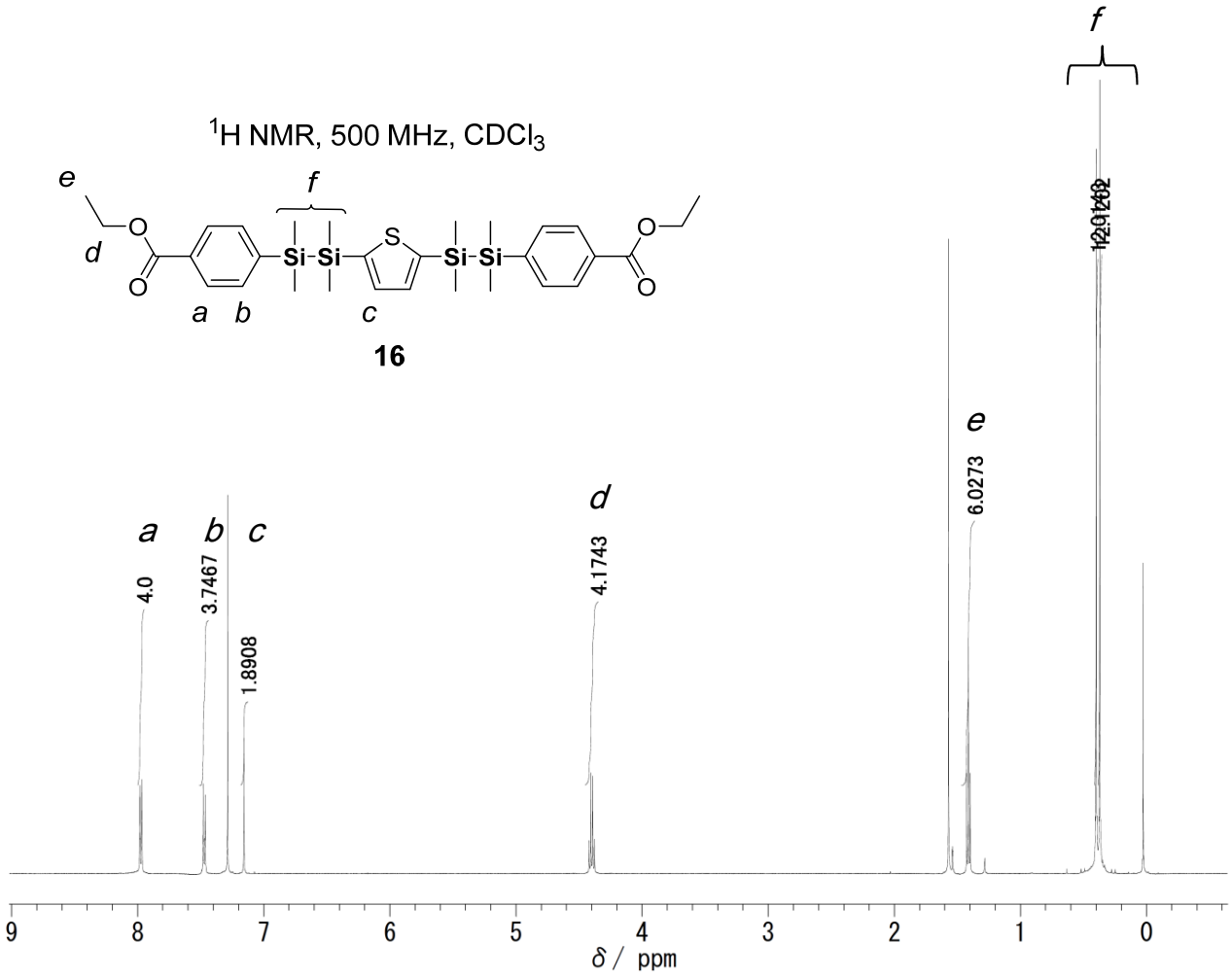

^{13}C NMR, 125 MHz, $CDCl_3$

16

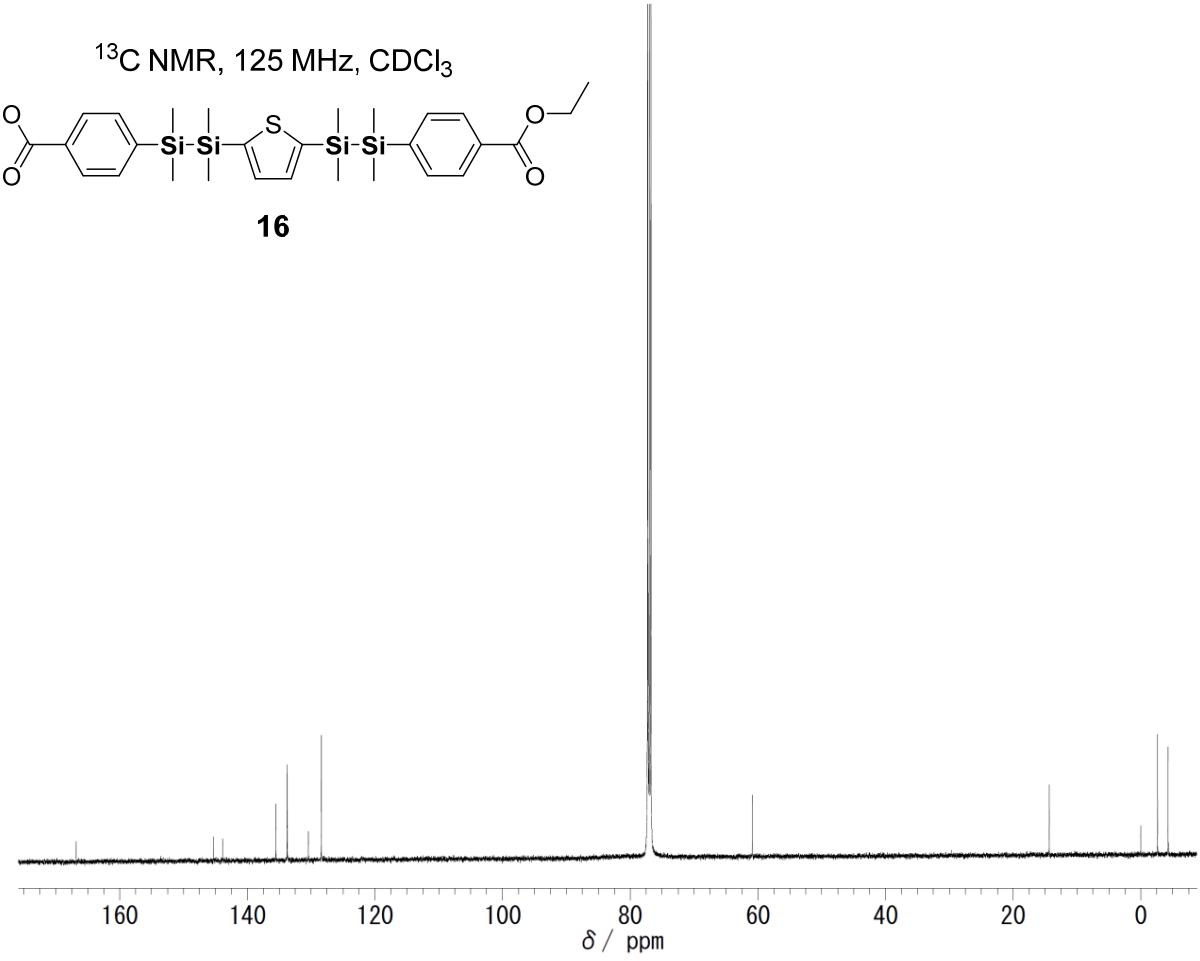

^{1}H NMR, 500 MHz, $CDCl_3$

17

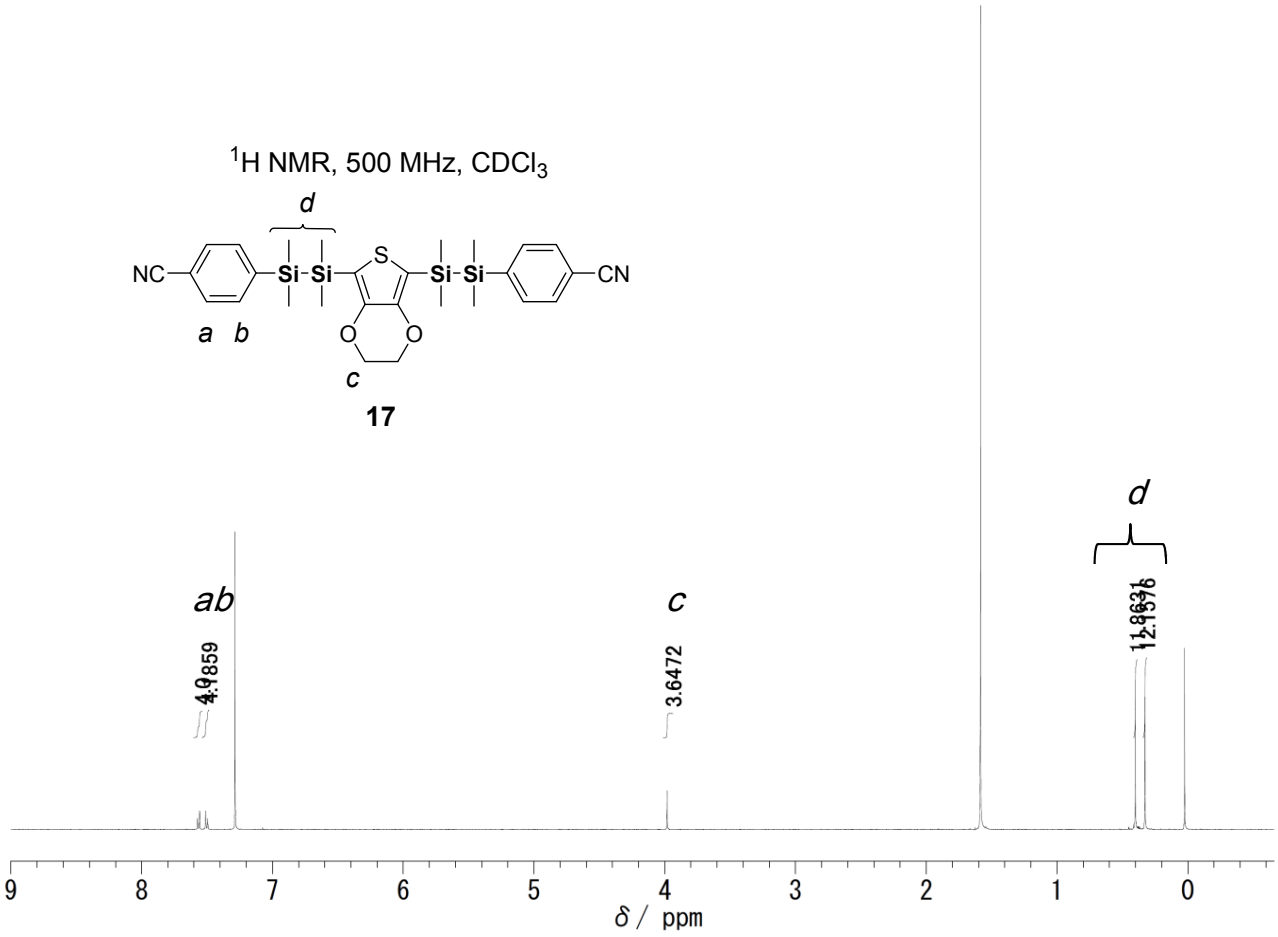

^{13}C NMR, 125 MHz, $CDCl_3$

17

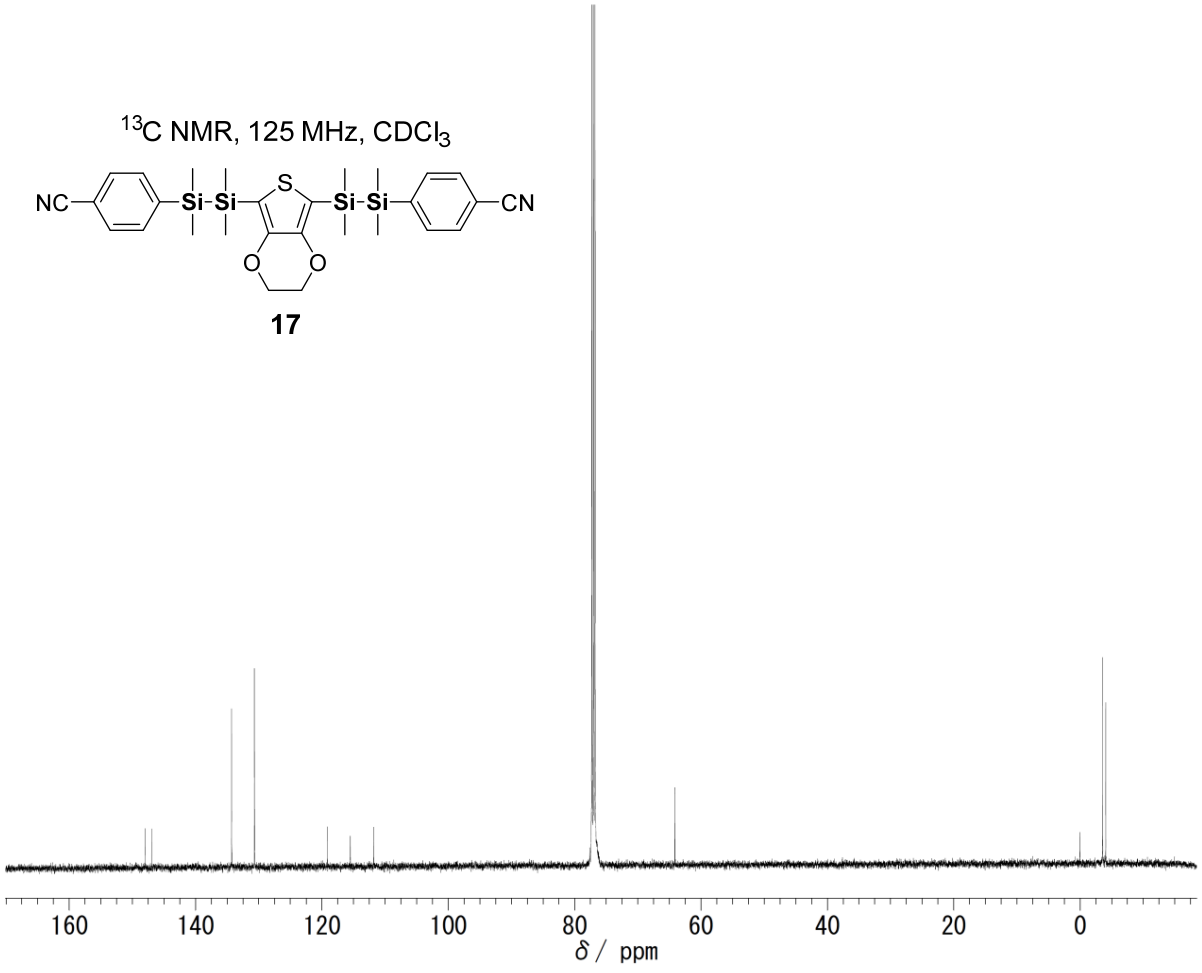

^{1}H NMR, 500 MHz, $CDCl_3$

18

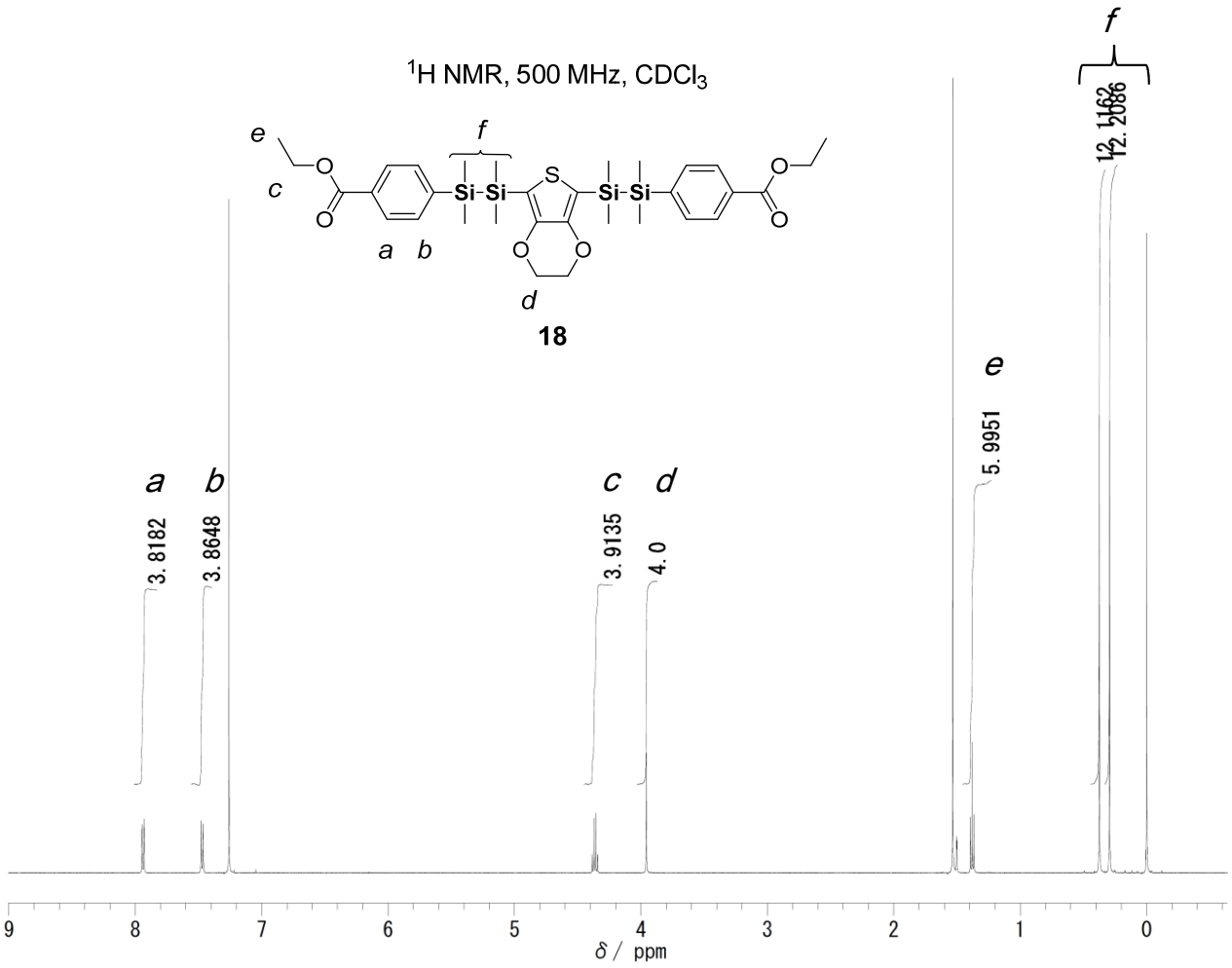

^{13}C NMR, 125 MHz, $CDCl_3$

18

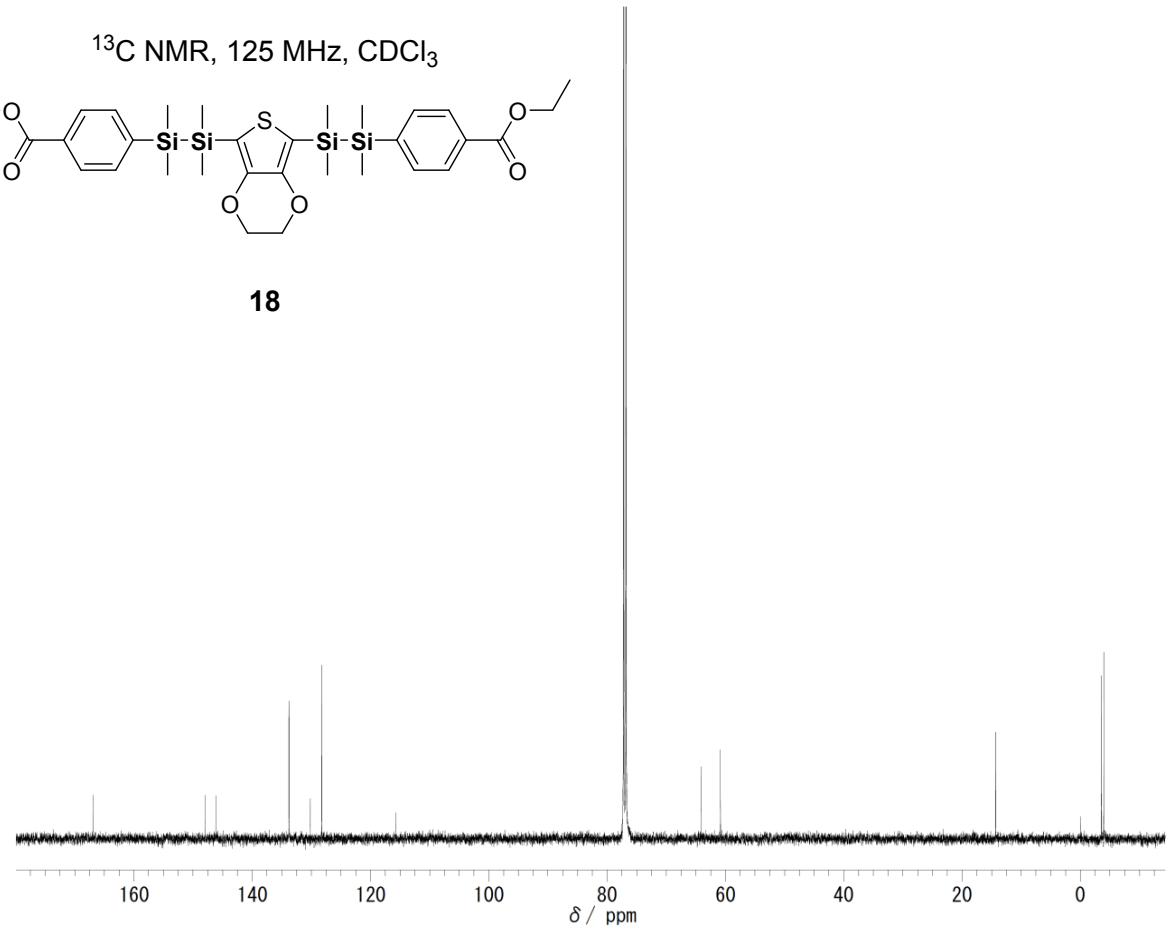

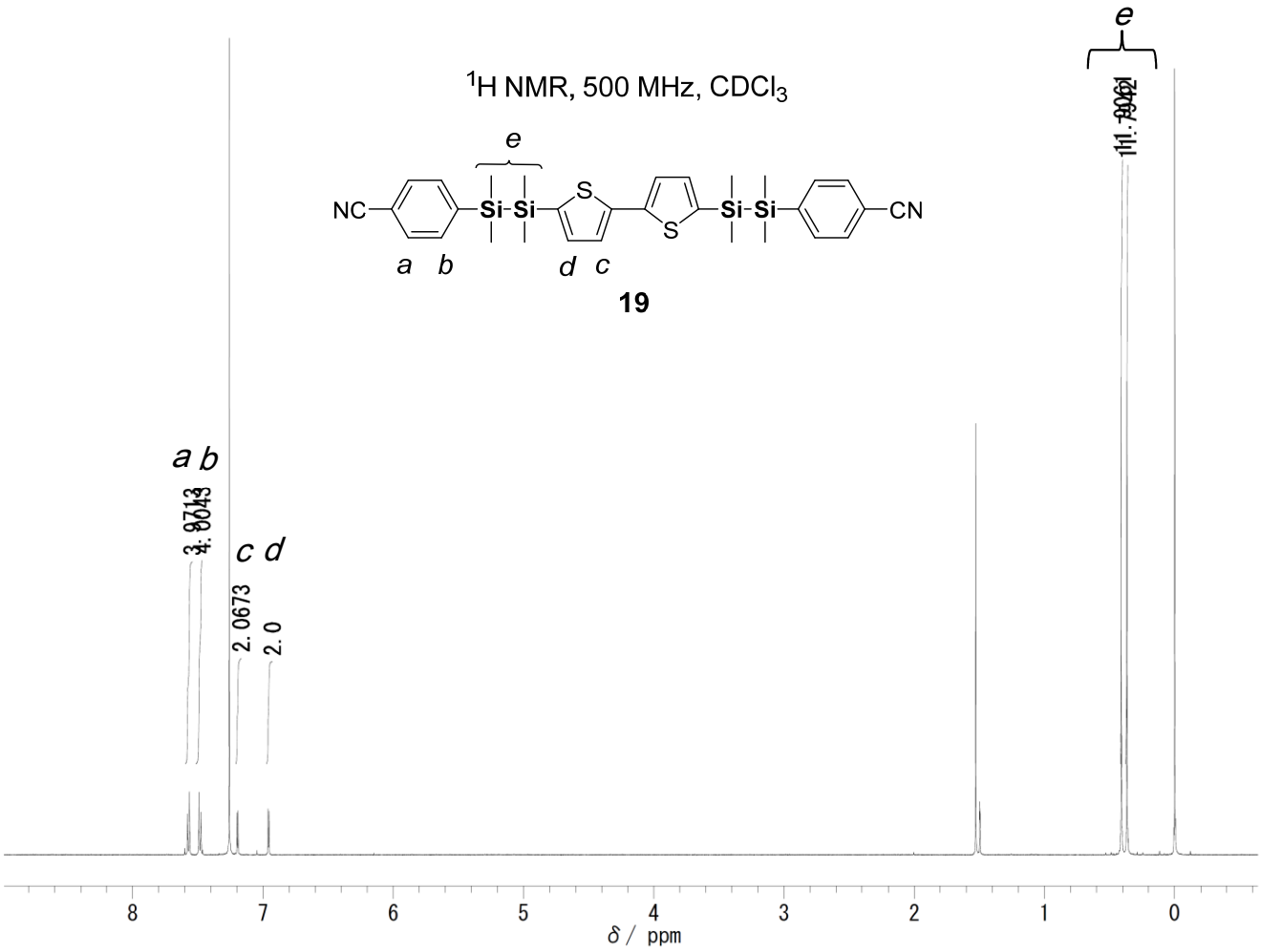
^{1}H NMR, 500 MHz, $CDCl_3$
e
NC
Si-Si
S
S
Si-Si
CN
a b
d c
19
a b
c d
2.0673
2.0
δ / ppm

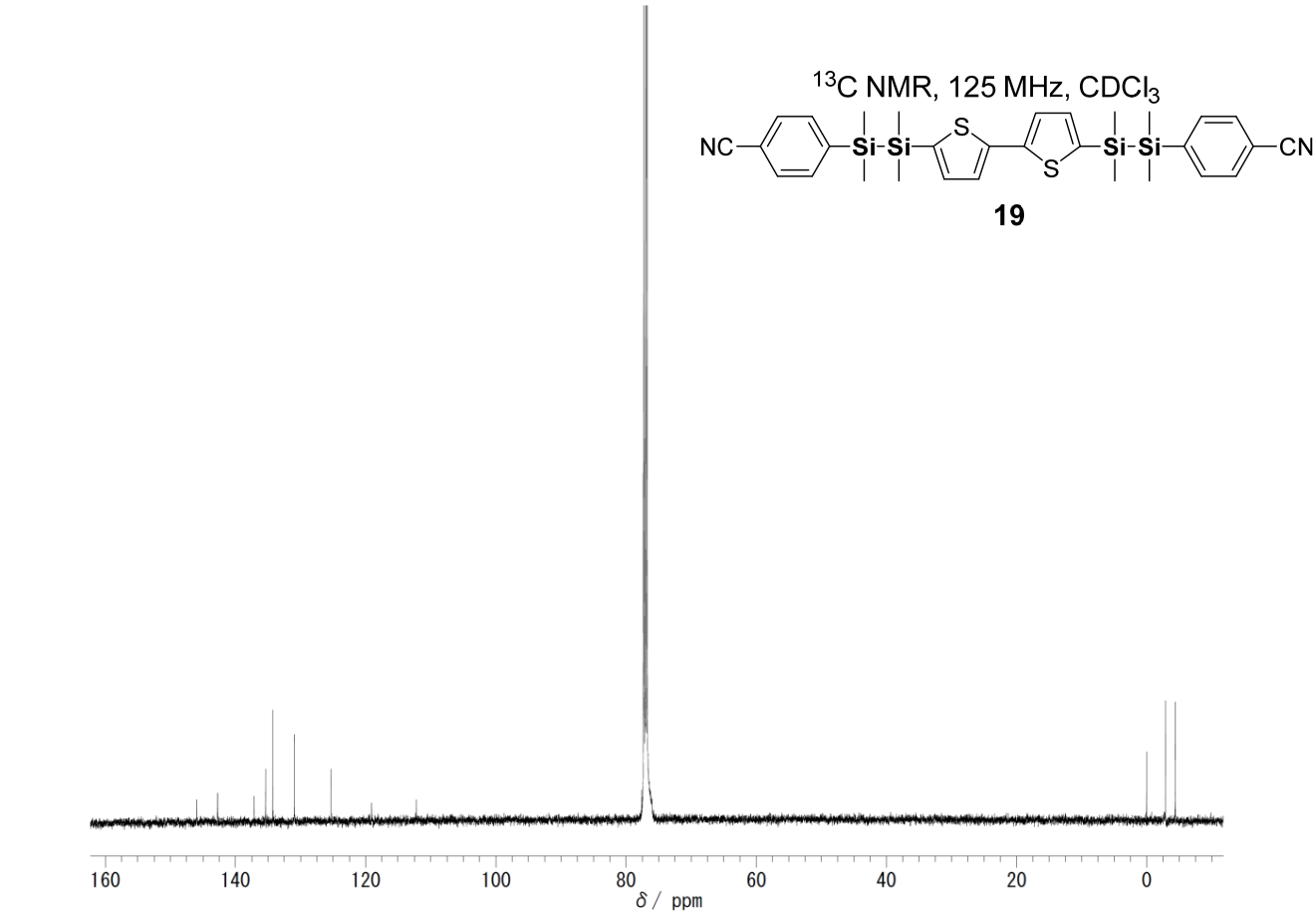
^{13}C NMR, 125 MHz, $CDCl_3$
NC
Si-Si
S
S
Si-Si
CN
19
δ / ppm

^{1}H NMR, 500 MHz, $CDCl_3$

20

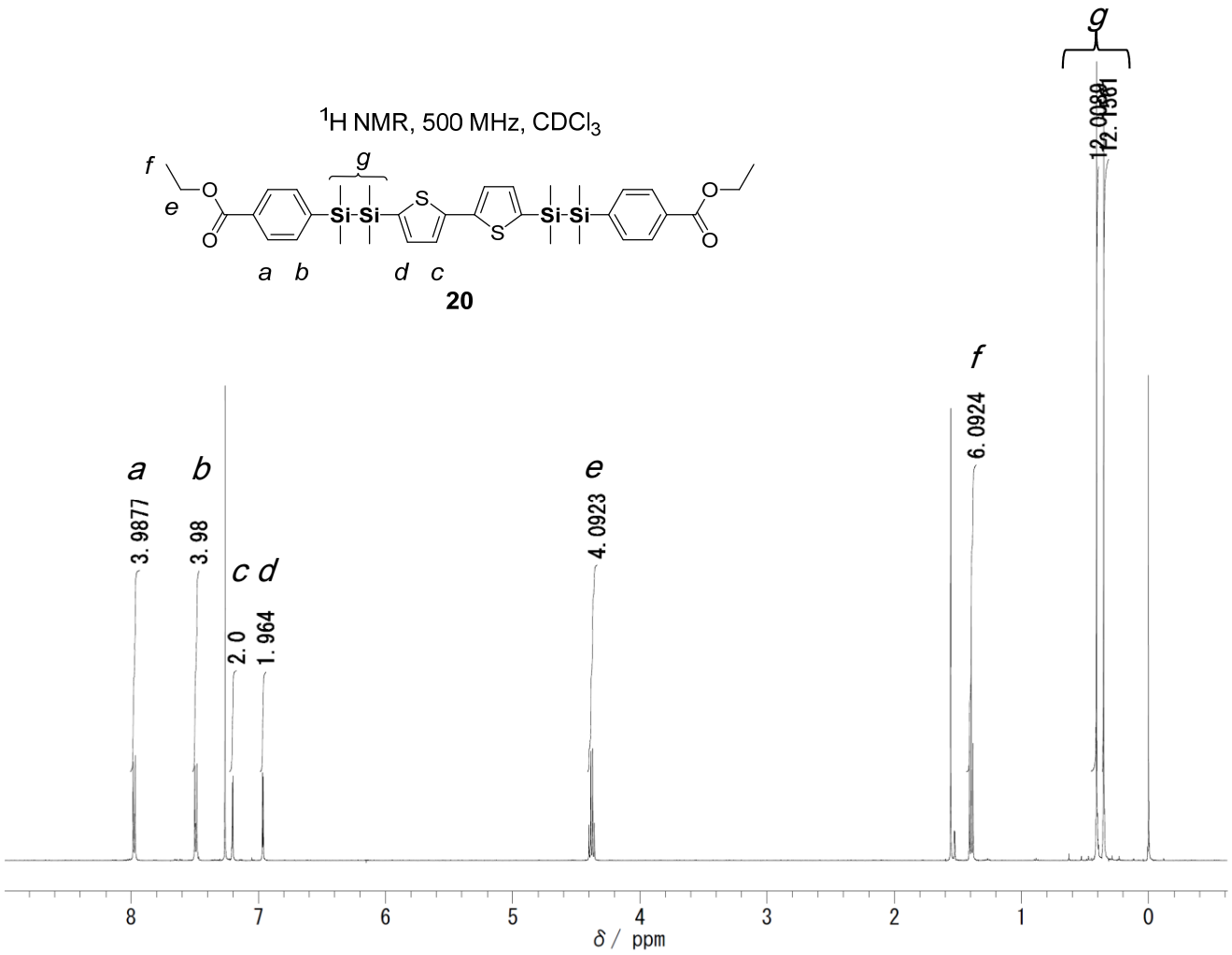

^{13}C NMR, 125 MHz, $CDCl_3$

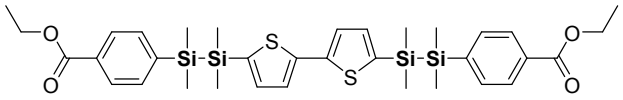

20

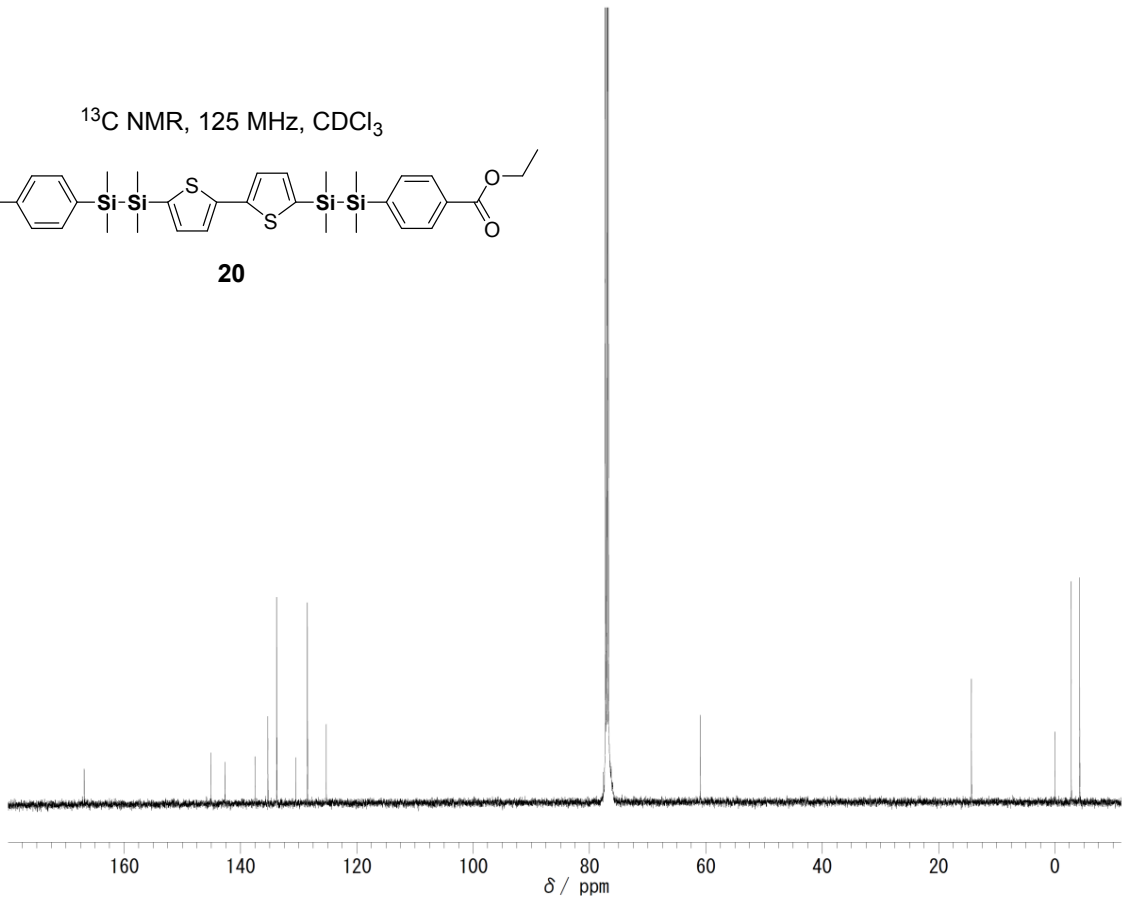

^{1}H NMR, 500 MHz, $CDCl_3$

21

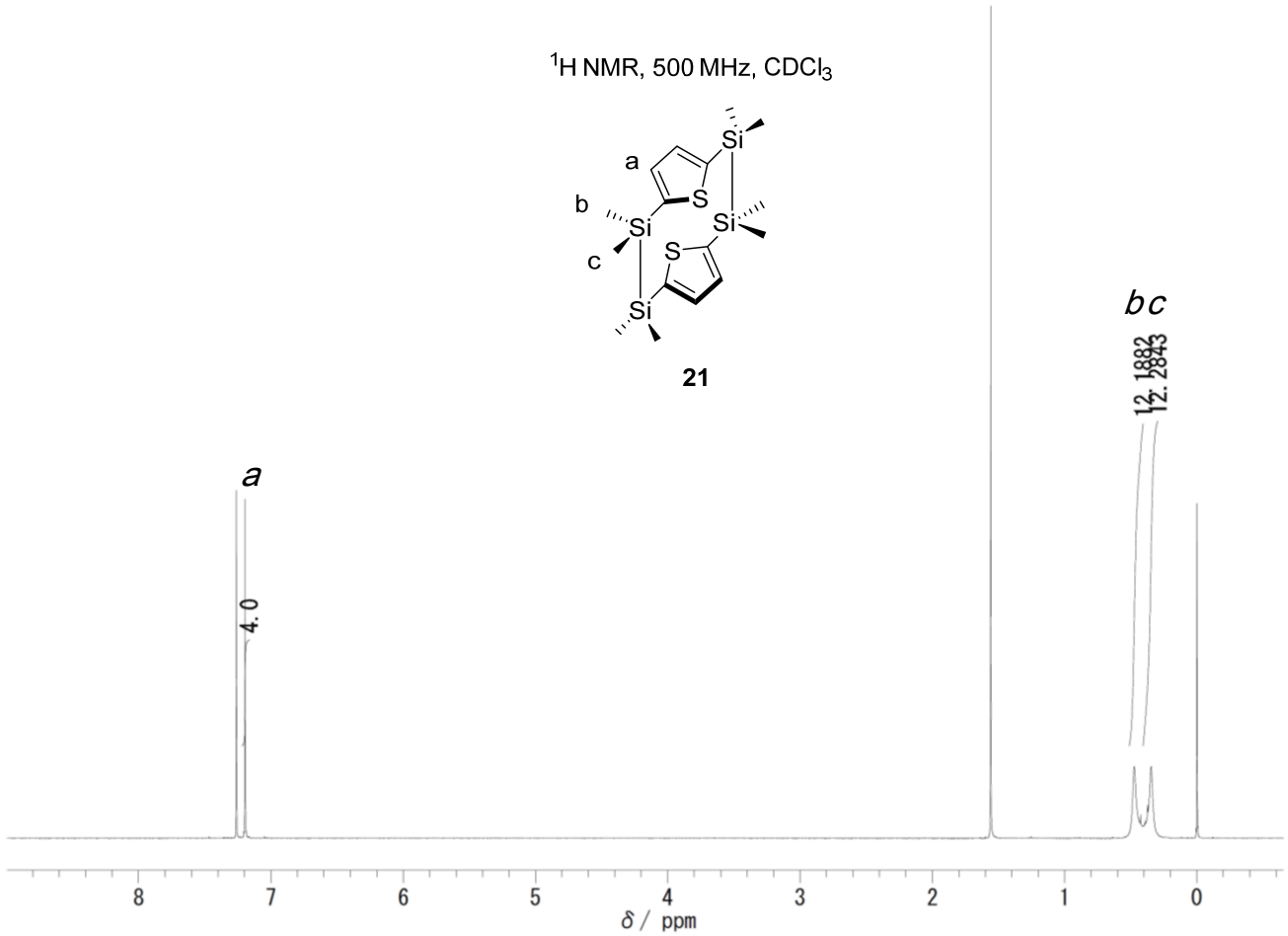

^{13}C NMR, 125 MHz, $CDCl_3$

21

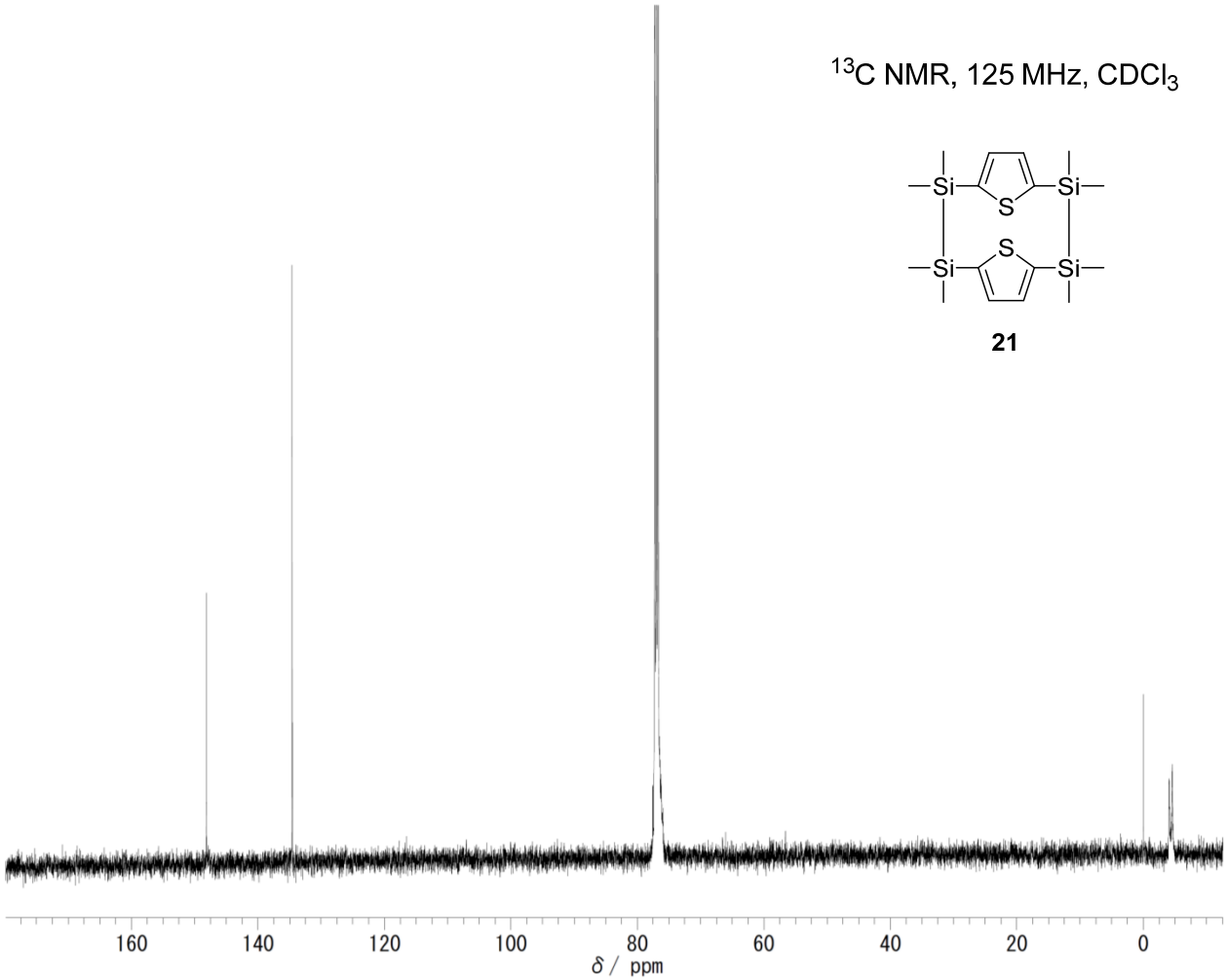

^{1}H NMR, 500 MHz, $CDCl_3$

22

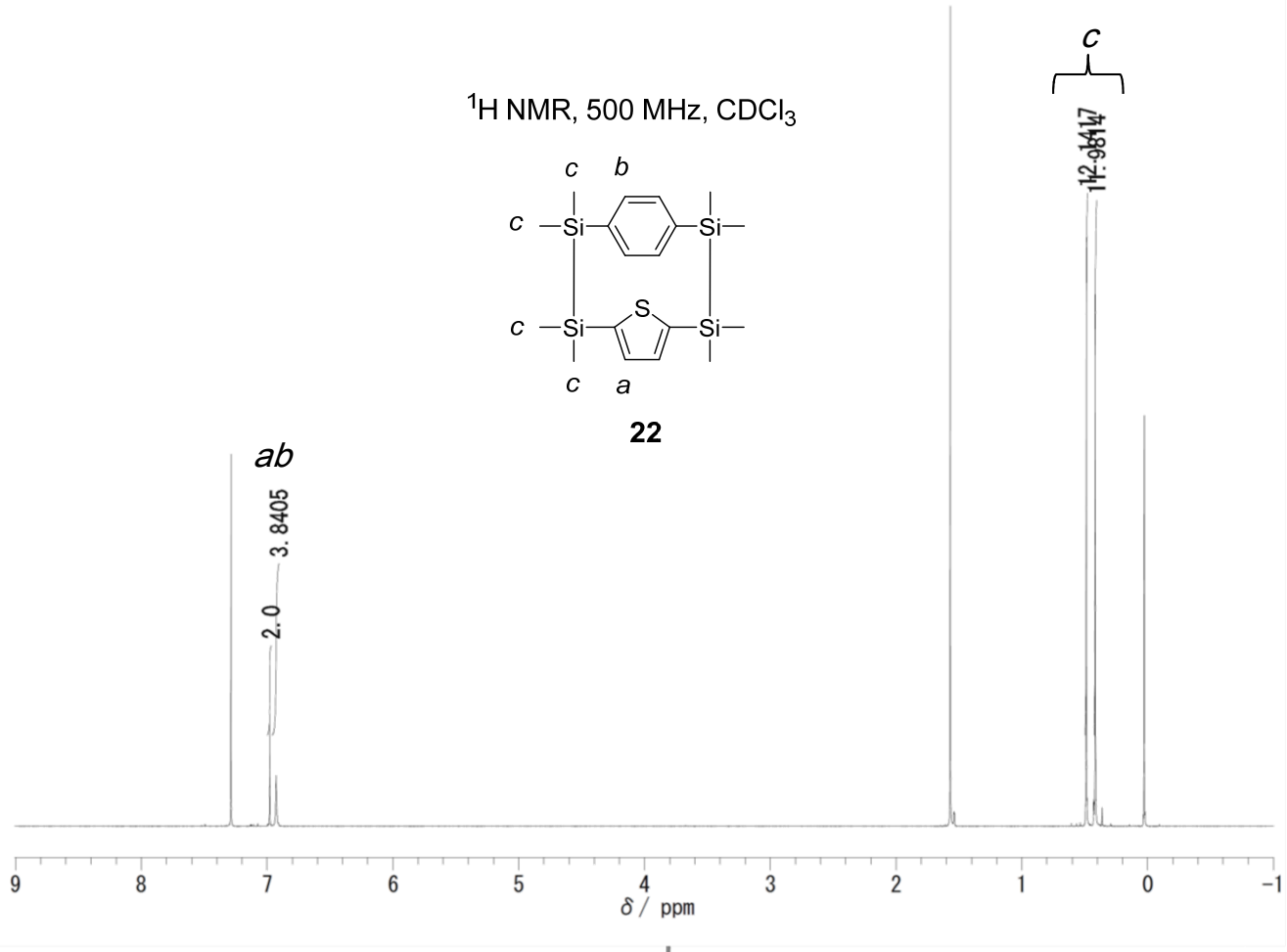

^{13}C NMR, 125 MHz, $CDCl_3$

22

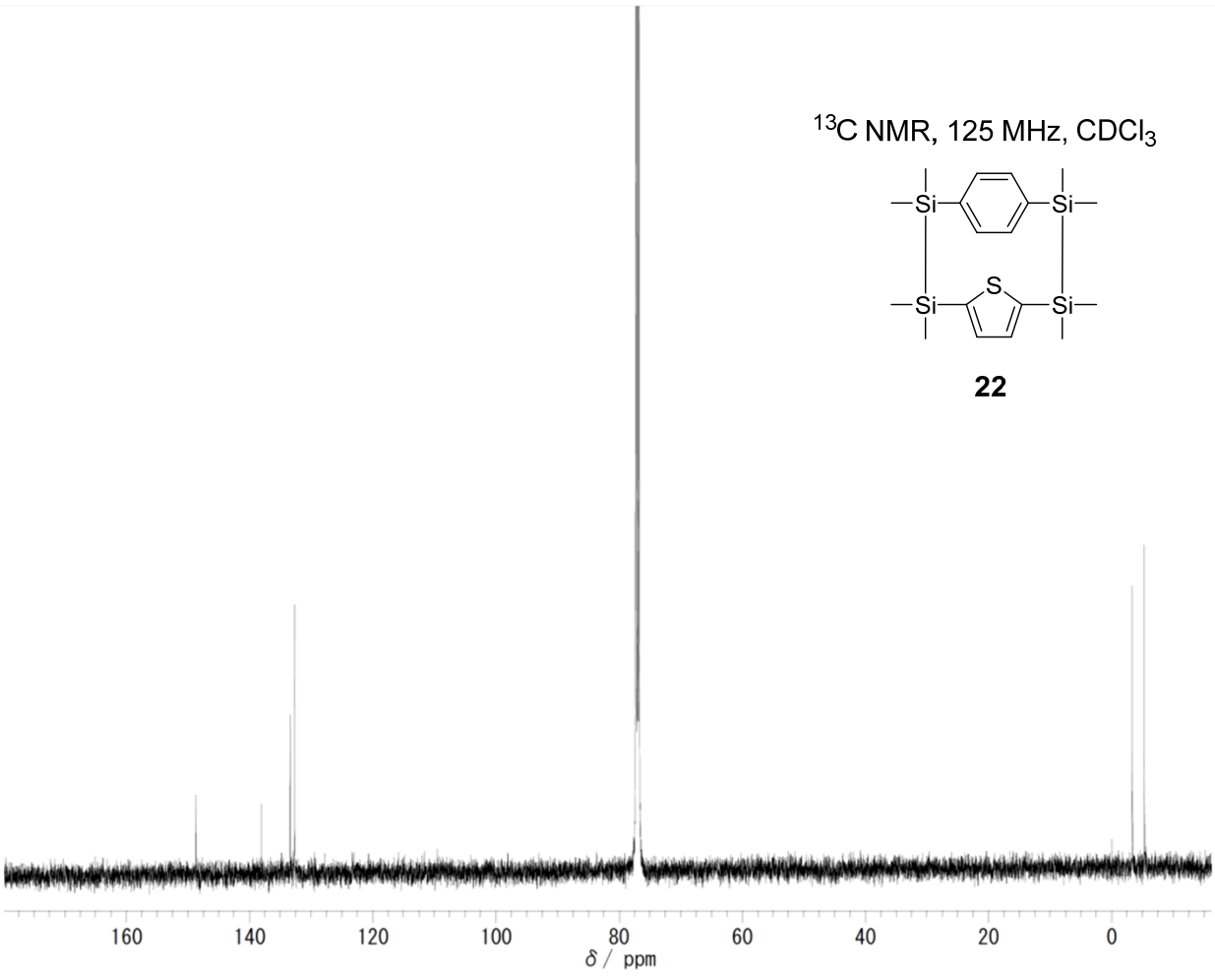

^{1}H NMR, 500 MHz, $CDCl_3$

23

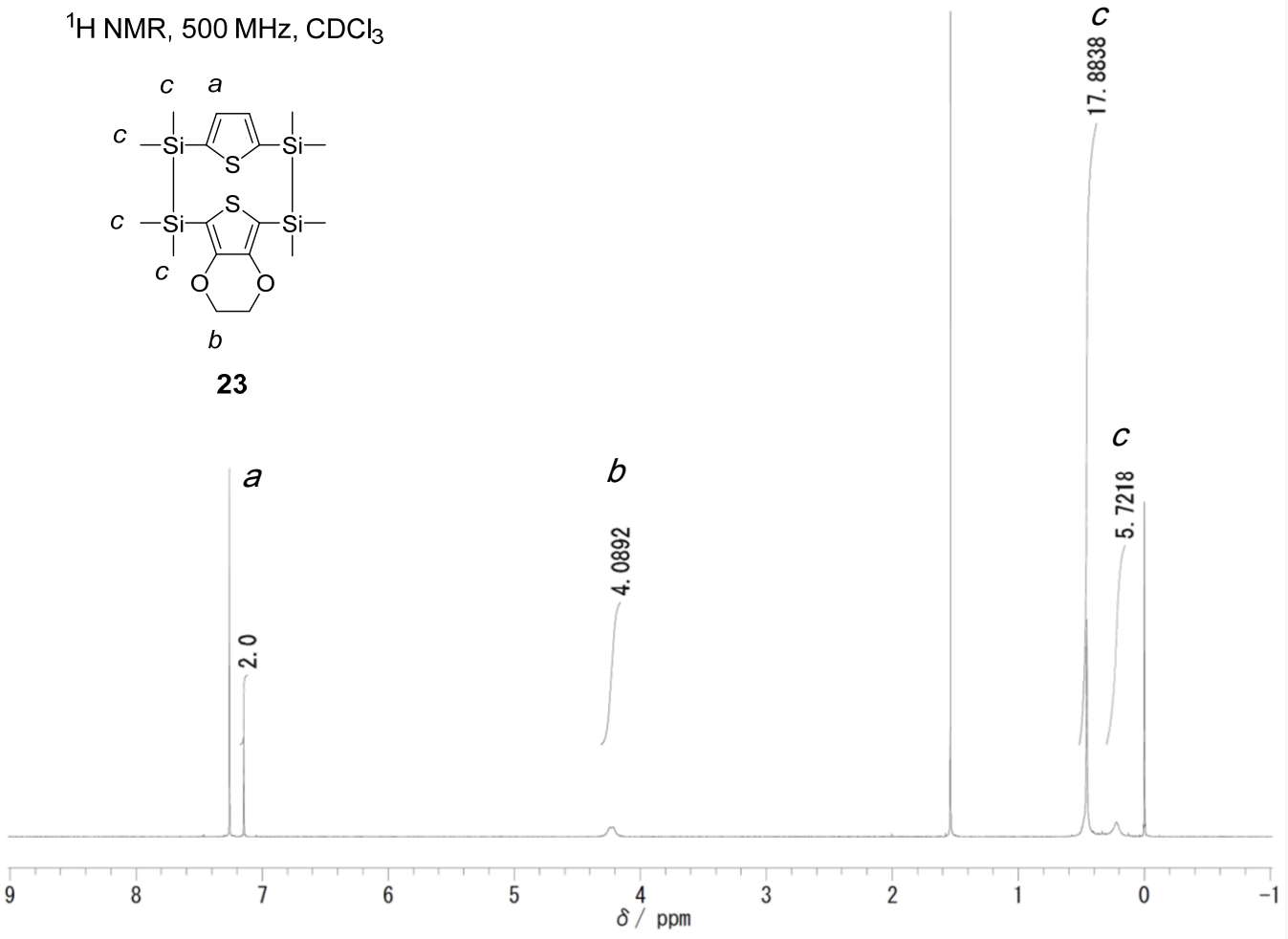

^{13}C NMR, 125 MHz, $CDCl_3$

23

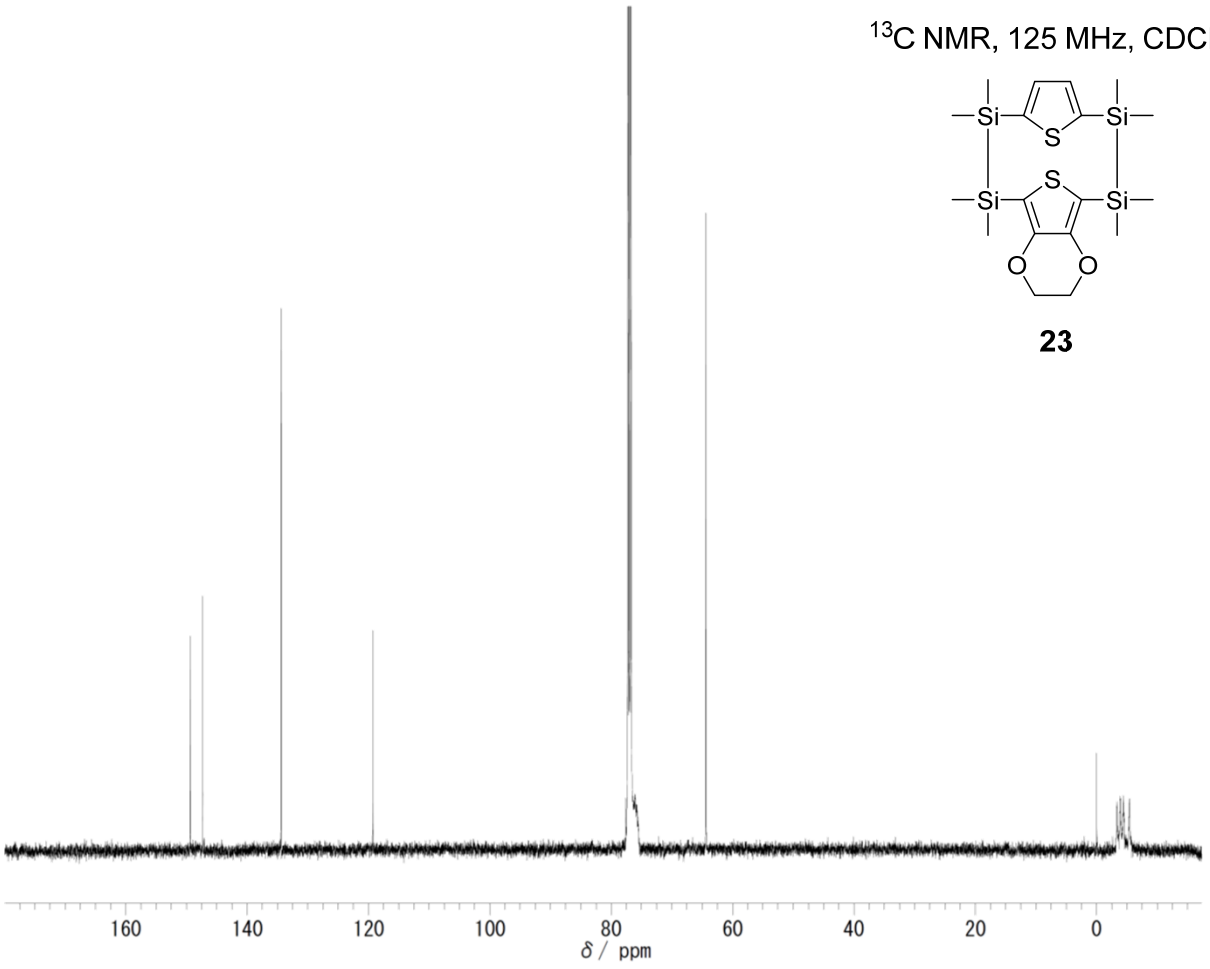

^{1}H NMR, 500 MHz, $CDCl_3$

24

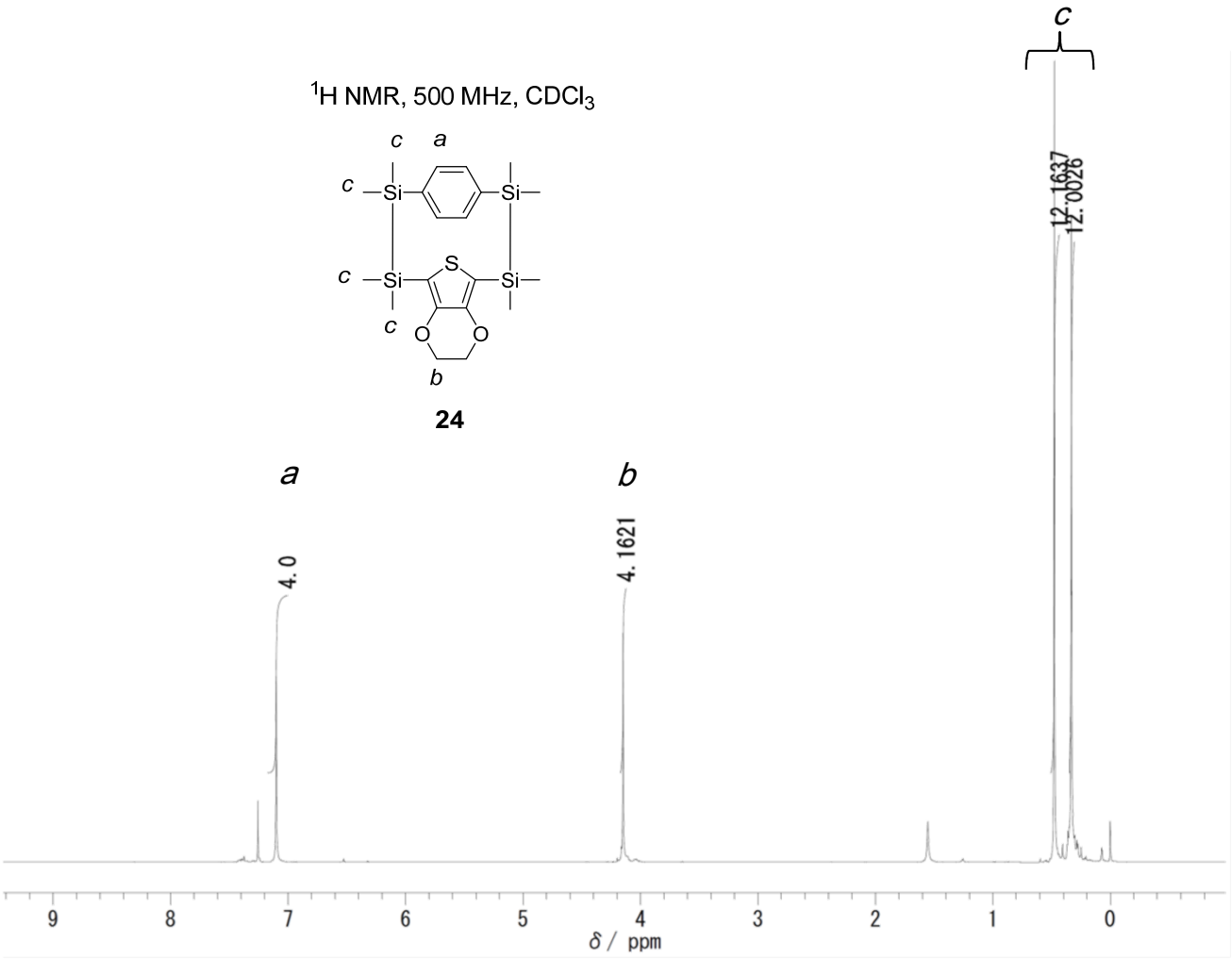

^{13}C NMR, 125 MHz, $CDCl_3$

24

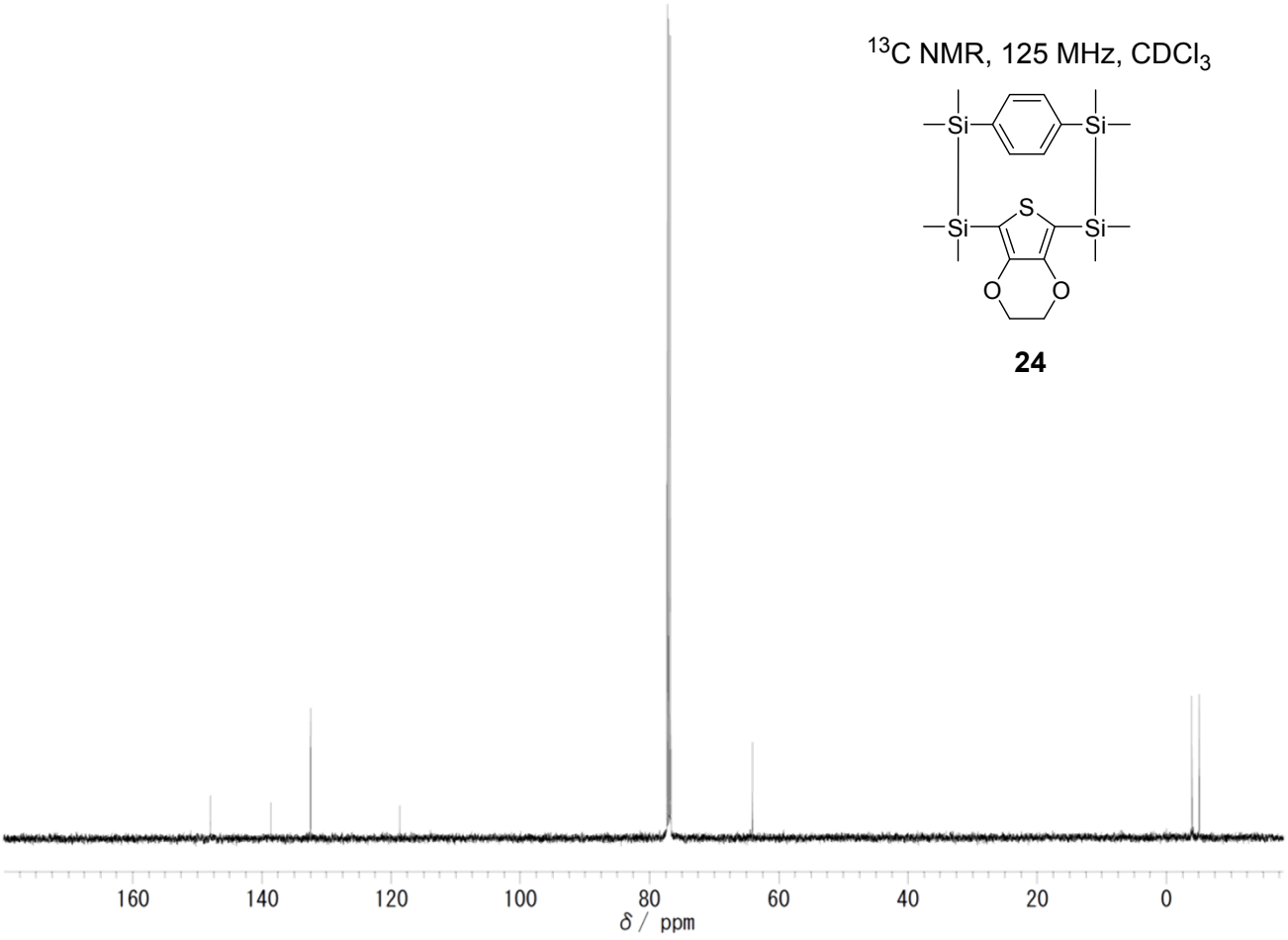

^{1}H NMR, 500 MHz, $CDCl_3$

25

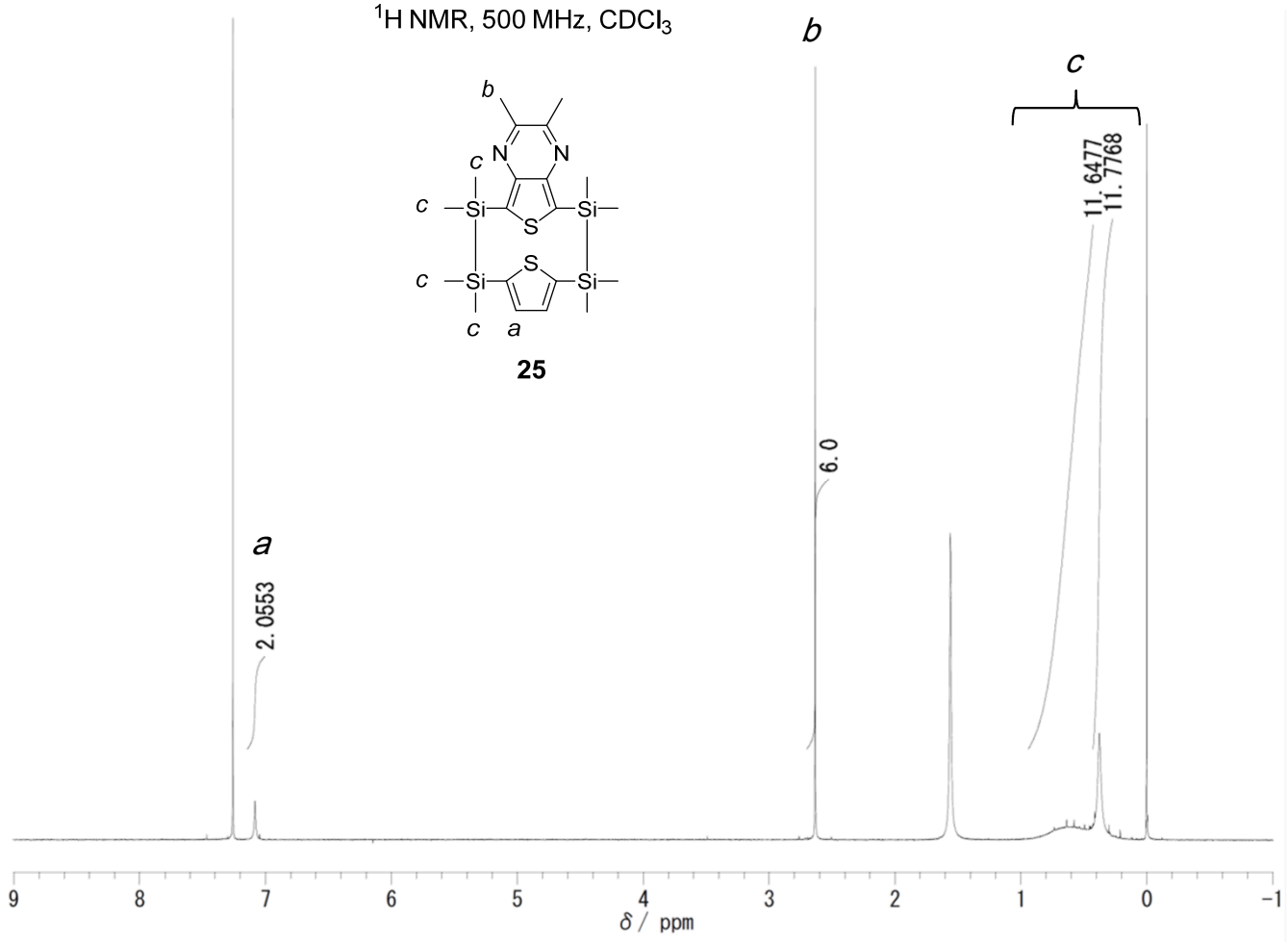

^{13}C NMR, 125 MHz, $CDCl_3$

25

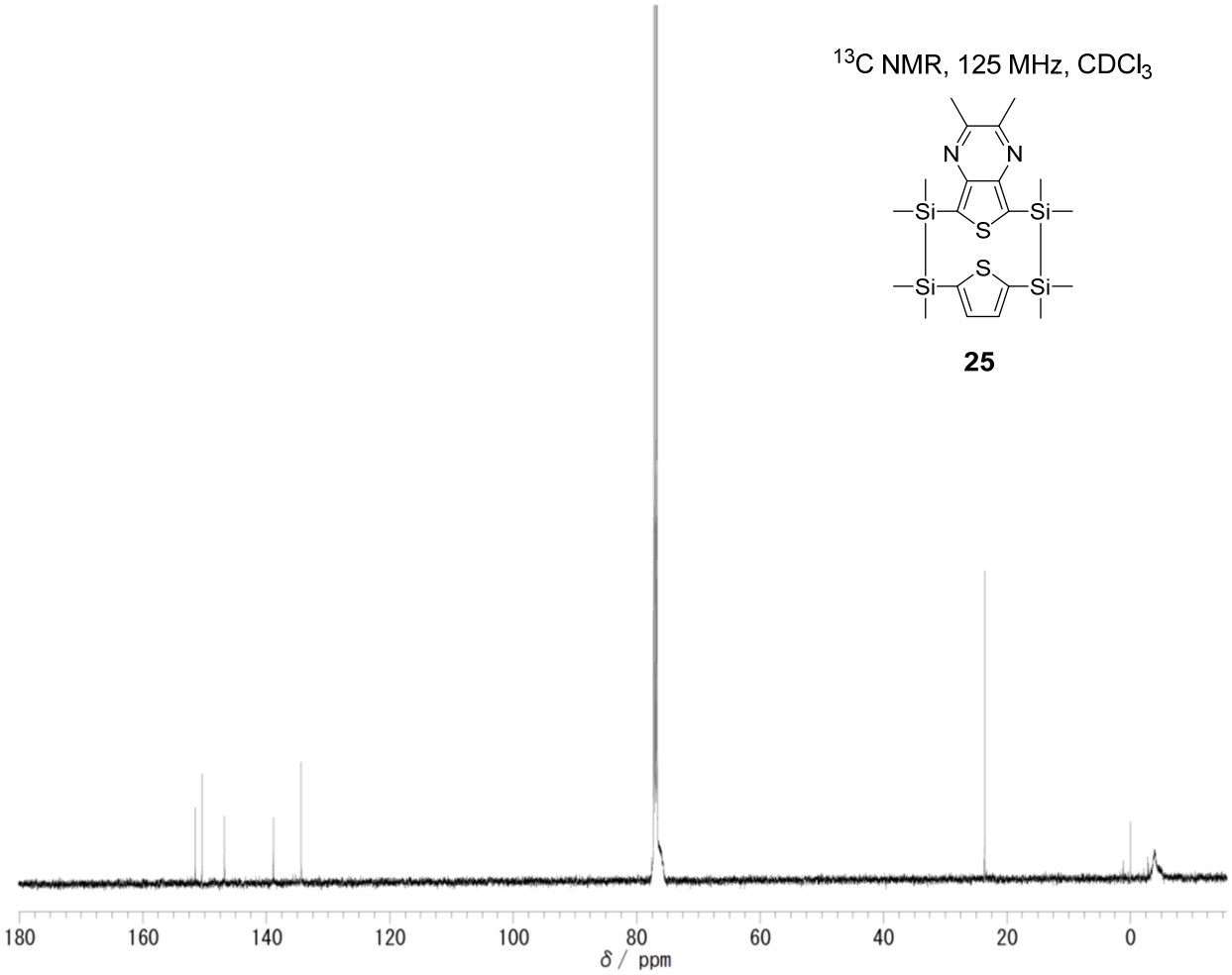

^{1}H NMR, 500 MHz, $CDCl_3$

26

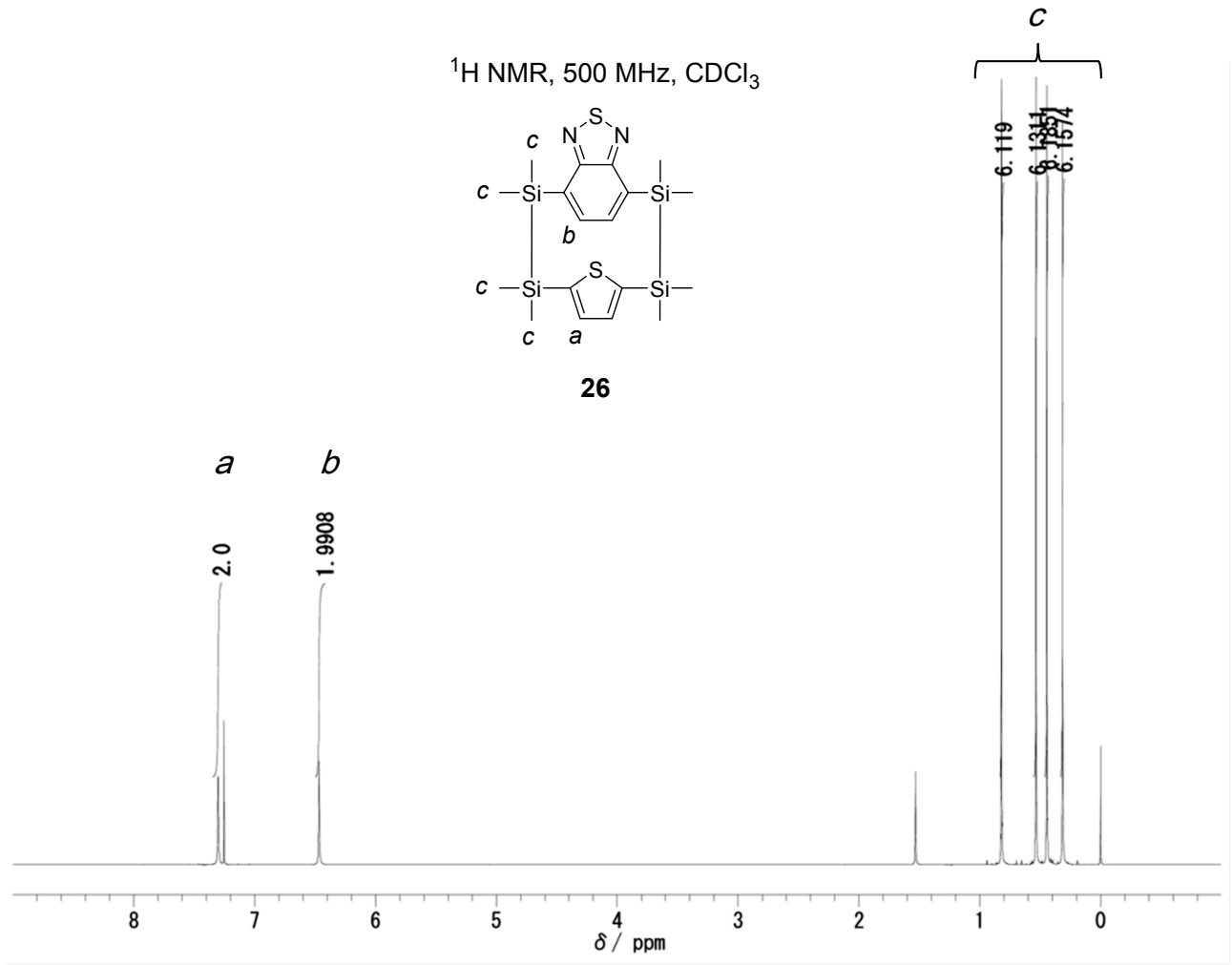

^{13}C NMR, 125 MHz, $CDCl_3$

26

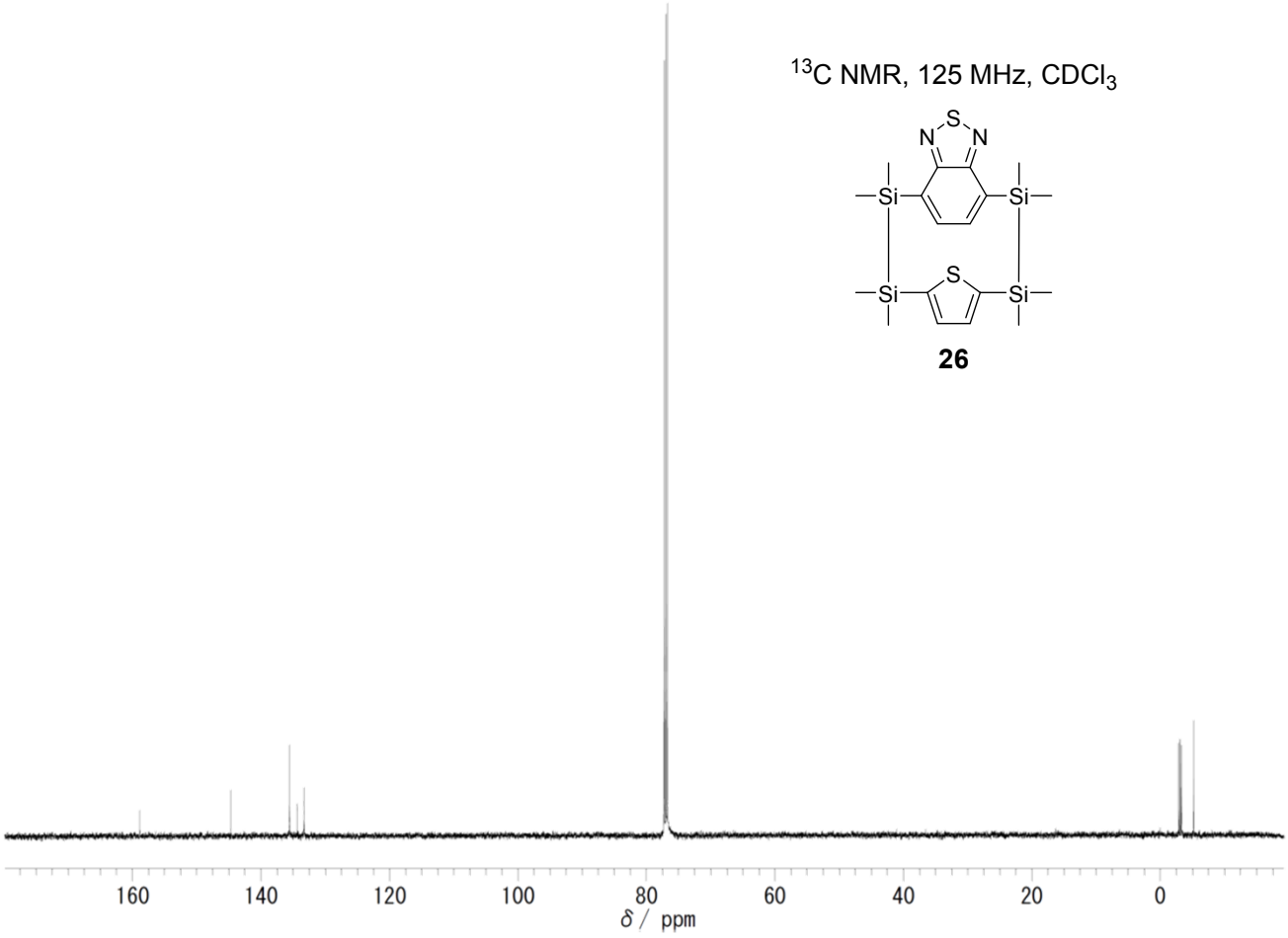

^{1}H NMR, 500 MHz, $CDCl_3$

27

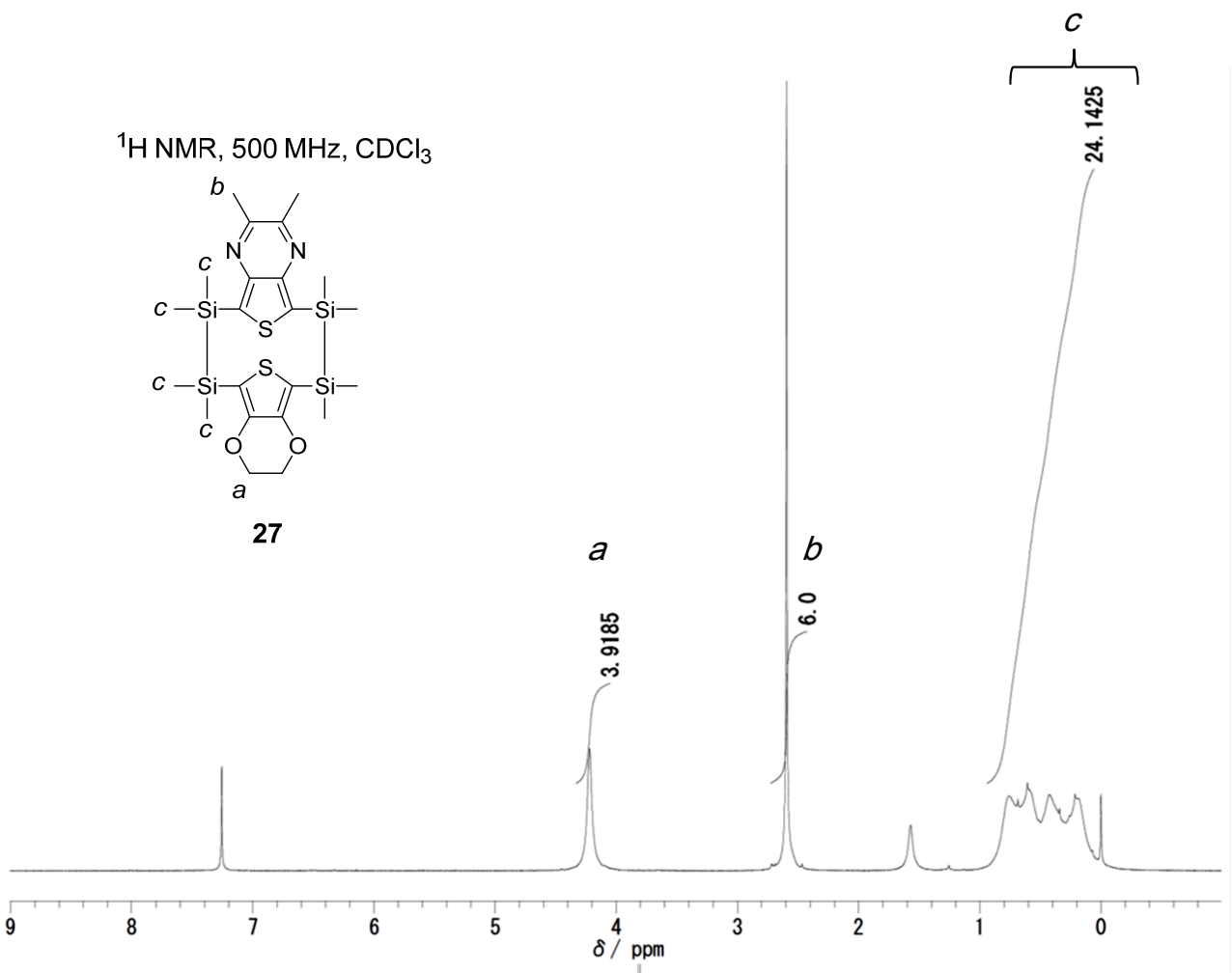

^{13}C NMR, 125 MHz, $CDCl_3$

27

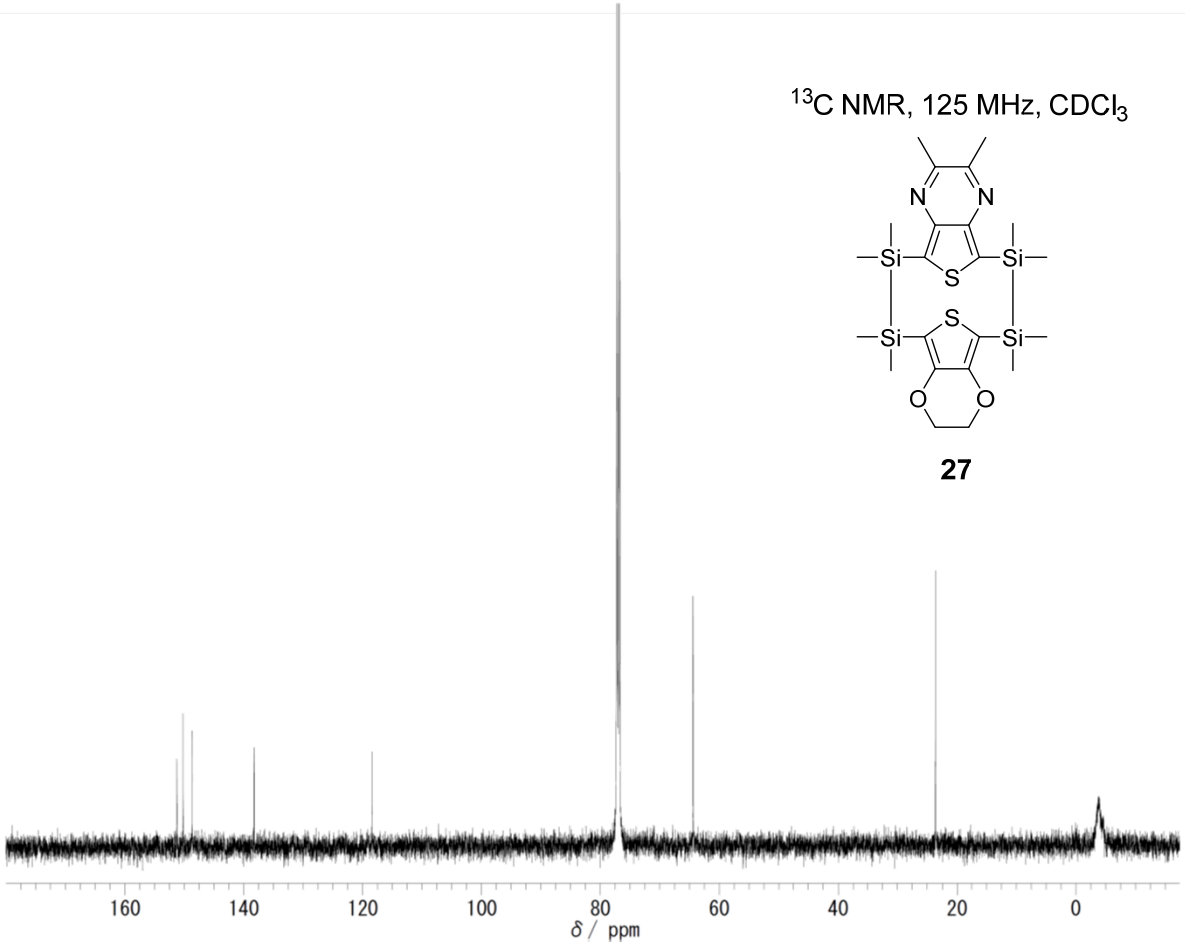

^{1}H NMR, 500 MHz, $CDCl_3$

28

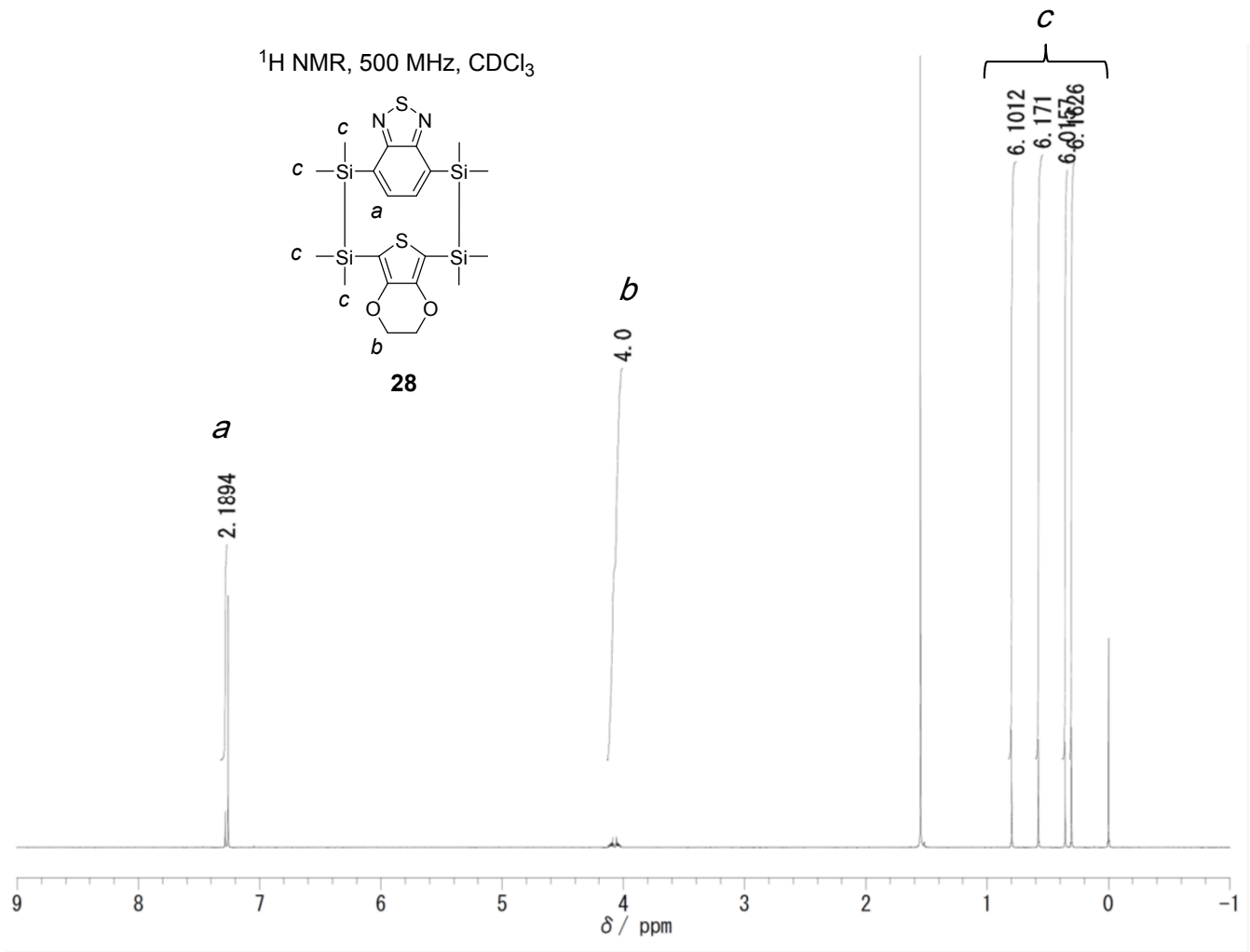

^{13}C NMR, 125 MHz, $CDCl_3$

28

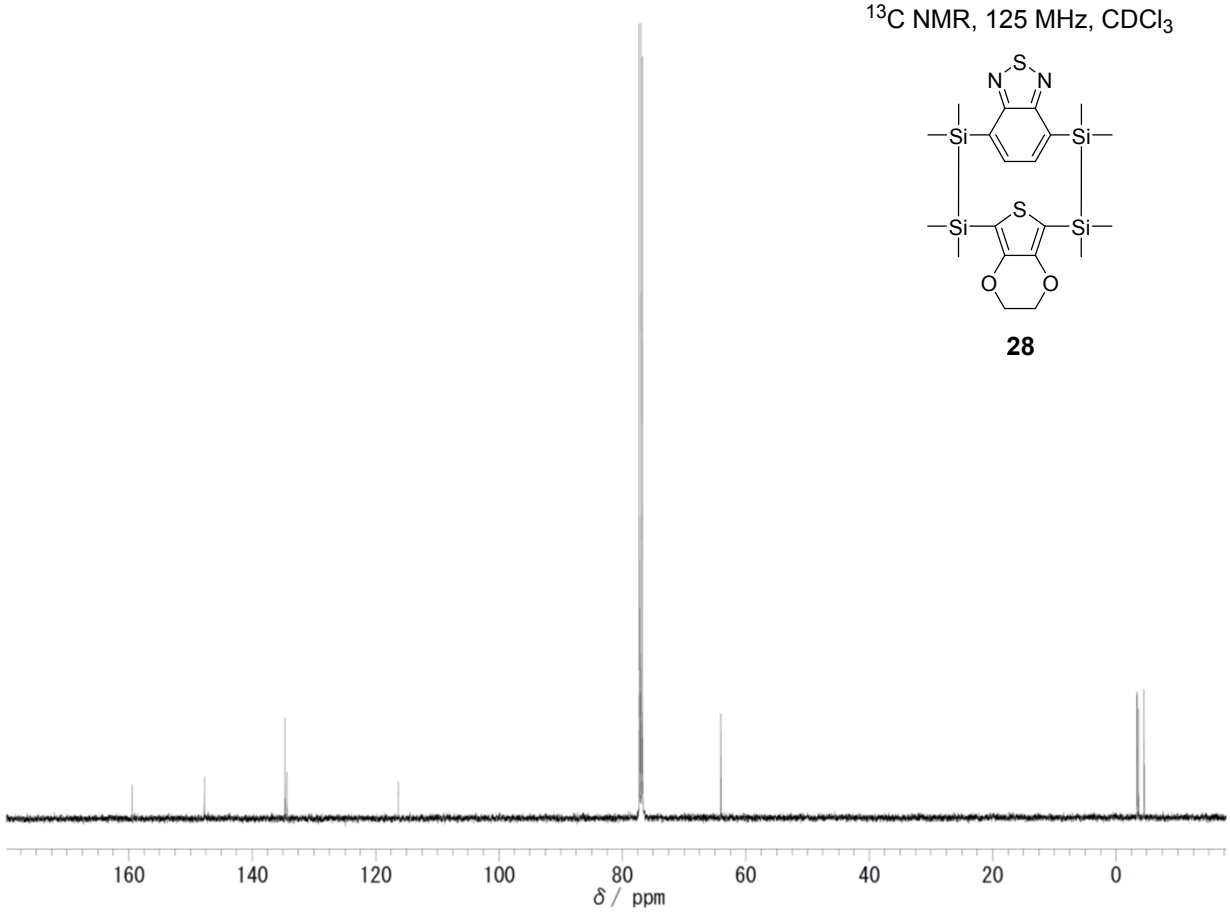

^{1}H NMR, 500 MHz, $CDCl_3$

30

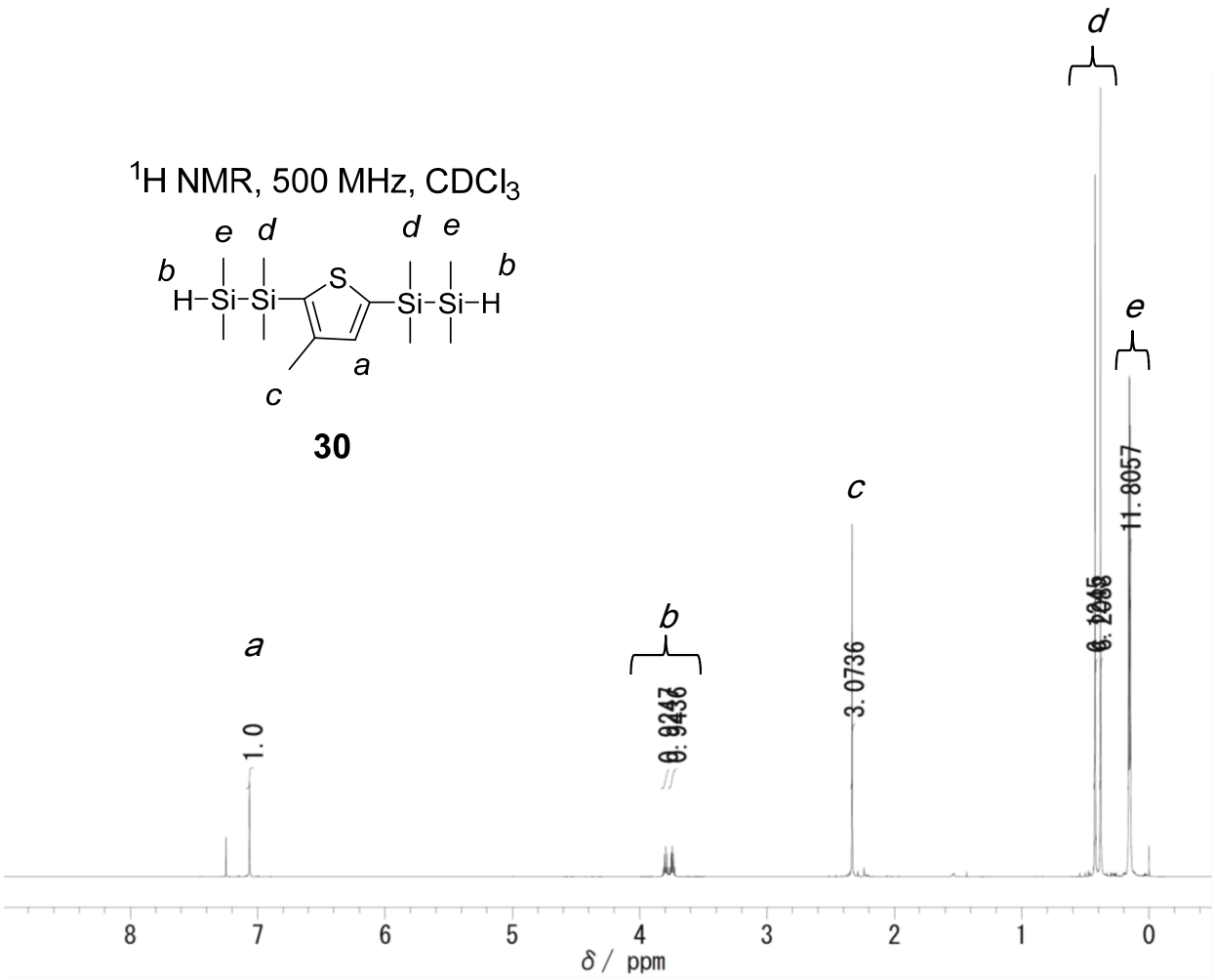

^{13}C NMR, 125 MHz, $CDCl_3$

30

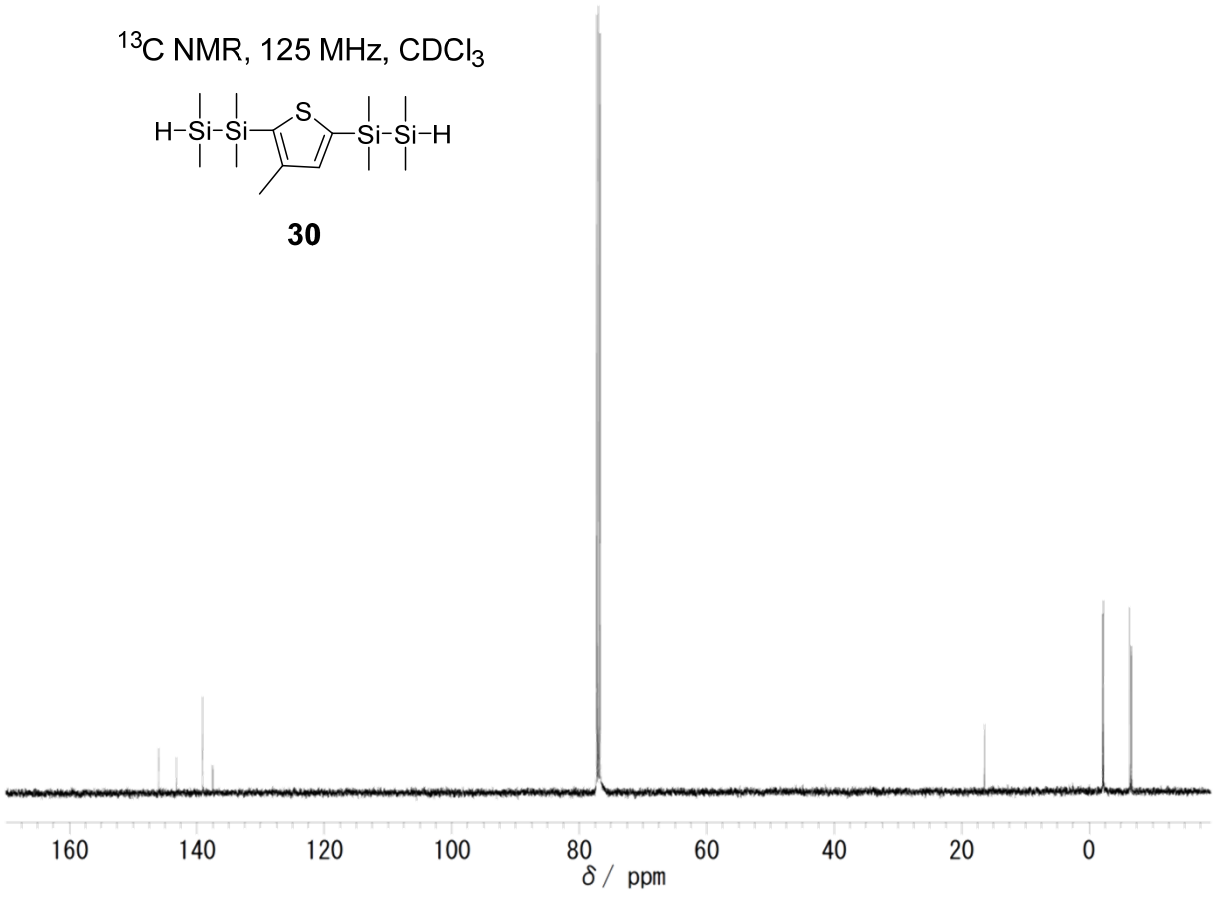

^{1}H NMR, 500 MHz, $CDCl_3$

31

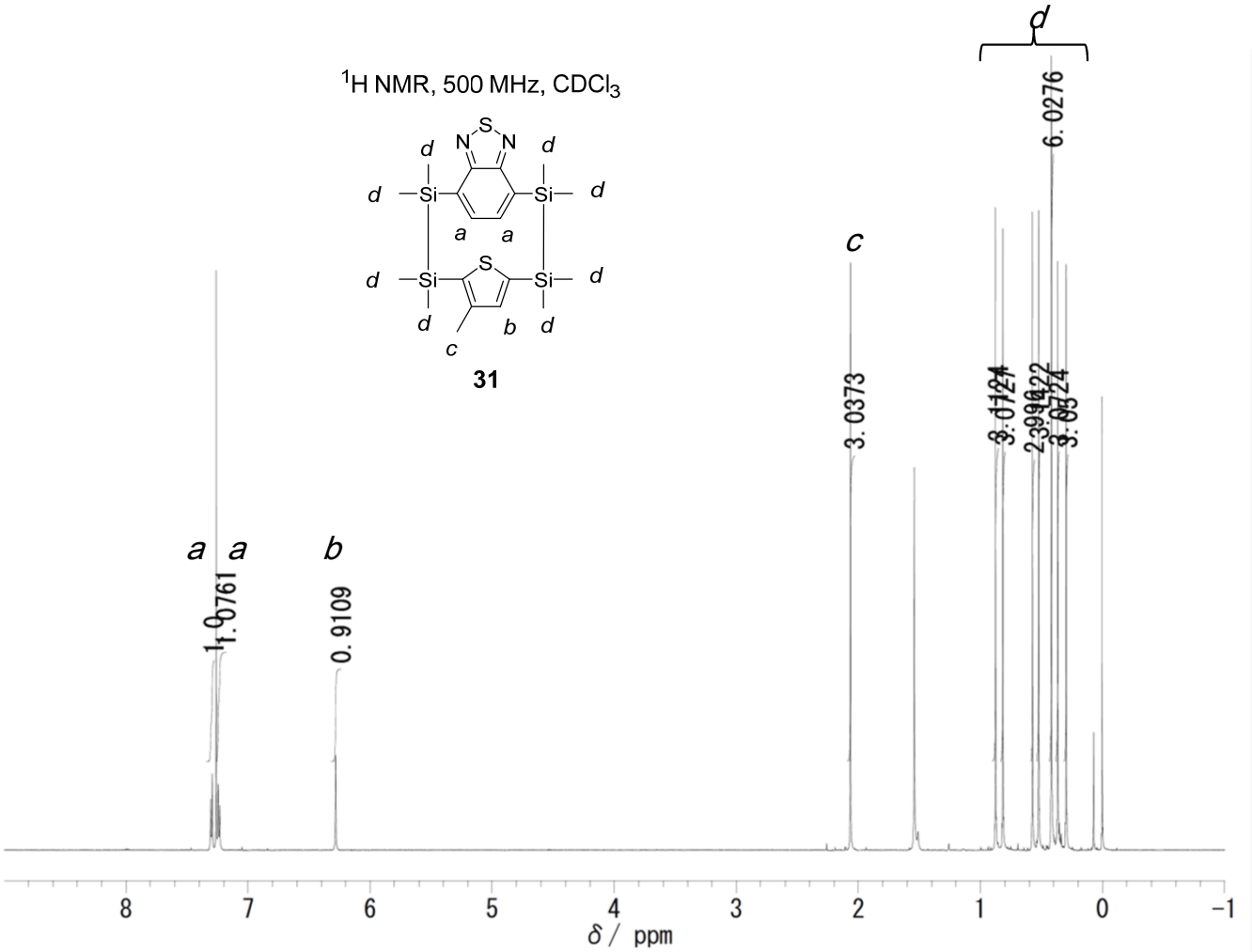

^{13}C NMR, 125 MHz, $CDCl_3$

31

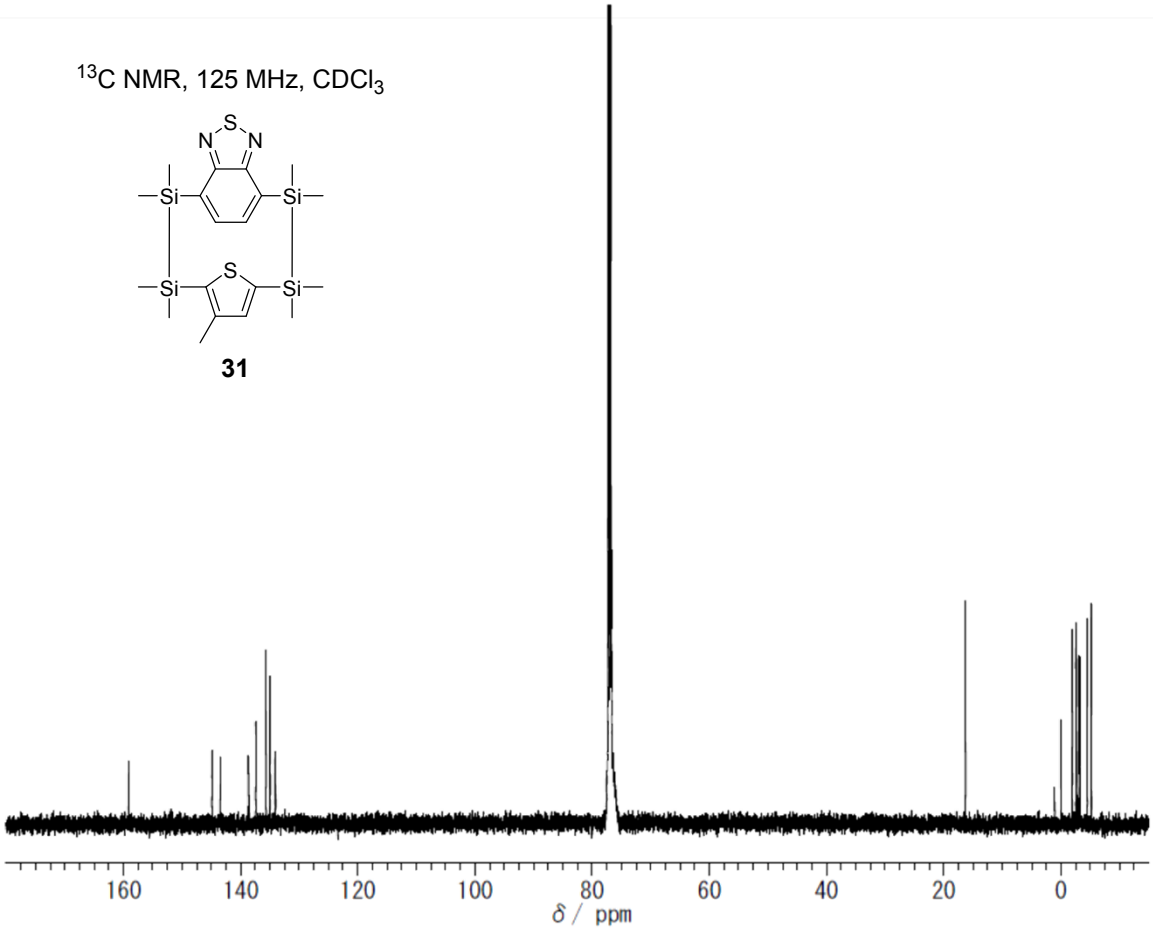

Acknowledgement

I would like to show my gratitude to those who supported the accomplishment of my Ph.D. course research.

I am greatly thankful to Prof. Hiroshi Nishihara for his kind and useful advice, hearty discussions and encouragements, and giving me the opportunity to research in my Ph.D. course. I also thank to Associate Prof. Yoshinori Yamanoi for his kind direction and discussion for my research. Assistant Prof. Ryota Sakamoto, Assistant Prof. Tetsuro Kusamoto, Project Assistant Prof. Mariko Miyachi, Project Assistant Prof. Kuo Hui Wu, and Project Assistant Prof. Hiroaki Maeda helped and advised me in my research.

I would like to express my gratitude to all the members in Nishihara laboratory. I give special thanks to Mr. Takayuki Nakashima, Mr. Shuhei Ueki, Mr. Shinya Koga, and Mr. Tsukasa Usuki, the members of the organosilicon group. And I also show my gratitude to Dr. Takamasa Tsukamoto, Dr. Yohei Hattori, and Dr. Mizuho Tsuchiya for the fruitful discussion about measurements. I also appreciate my contemporary, Ms. Eunice Jia Han Phua.

There are researchers who supported my Ph.D. course study technically. I appreciate Prof. Eiji Nishibori (Division of Physics, Faculty of Pure and Applied Sciences, Tsukuba Research Center for Interdisciplinary Materials Science & Center for Integrated Research in Fundamental Science and Engineering, University of Tsukuba) and Dr. Kunihisa Sugimoto (Japan Synchrotron Radiation Research Institute) for the measurement of synchrotron radiation X-ray diffraction at SPring-8; Prof. Hirokazu Tada, Associate Prof. Ryo Yamada, Assistant Prof. Tatsuhiko Ohto, and Assistant Prof Song-Toan Pham (Graduate School of Engineering Science, Osaka University) for the fabrication and measurement of electroluminescence devices; Prof. Mitsuhiko Shionoya, Associate Prof. Shohei Tashiro, and Dr. Kenichiro Omoto (School of Science, The University of Tokyo) for the inclusion measurement of guest compound and macrocycles; Dr. Mineyuki Hattori, Ms. Keiko Jimura, and Dr. Shigenobu Hayashi (National Institute of Advanced Industrial Science and Technology) for the measurement of solid state NMR; Prof. Koichi Nozaki, Assistant Prof. Munetaka Iwamura, and Ms. Hikaru Koike (Graduate School of Science and Engineering, University of Toyama) for CPL measurement; Dr. Aiko Kamitsubo (The Elemental Analysis Center, The University of Tokyo) for the elemental analysis measurements; and Mr. Hideki Waragai (The University of Tokyo) for the measurement of fluorescence quantum yield in the solid state.

I am indebted to the Japan Chemical Industry Association (JCIA) for financial support and providing opportunities of my Ph.D. research.

Schemes, Figures and Tables in Chapter 2 and Chapter 3 are reproduced from my publications in *Angewandte Chemie International Edition* published in 2016 and *Journal of the American Chemical Society* published in 2017, respectively. Several Figures in Chapter 1, Chapter 2, and Chapter 3 are also reproduced from articles published by the John Wiley & Sons, Inc. and the American Chemical Society. I also show my gratitude to the John Wiley & Sons, Inc. and the American Chemical Society for giving permission to reuse them in this thesis.

Finally, I would like to express deep gratitude to my family, who supported me physically, mentally, and financially.

December 2017

Masaki Shimada

List of Publications

【Publications related to the thesis】

1. "Bright Solid-state Emission of Disilane-bridged Donor–Acceptor–Donor and Acceptor–Donor–Acceptor Chromophores" Masaki Shimada, Mizuho Tsuchiya, Ryota Sakamoto, Yoshinori Yamanoi, Eiji Nishibori, Kunihisa Sugimoto, Hiroshi Nishihara, *Angew. Chem. Int. Ed.* **2016**, *55*, 3022–3026.
2. "Unusual Reactivity of Group 14 Hydrides toward Organic Halides: Synthetic Studies and Application to Functional Materials" Masaki Shimada, Yoshinori Yamanoi, Hiroshi Nishihara, *J. Synth. Org. Chem. Jpn.* **2016**, *74*, 1098–1107.
3. "Multifunctional Octamethyltetrasila[2.2]cyclophanes: Conformational Variations, Circularly Polarized Luminescence, and Organic Electroluminescence" Masaki Shimada, Yoshinori Yamanoi, Tatsuhiko Ohto, Song-Toan Pham, Ryo Yamada, Hirokazu Tada, Kenichiro Omoto, Shohei Tashiro, Mitsuhiko Shionoya, Mineyuki Hattori, Keiko Jimura, Shigenobu Hayashi, Hikaru Koike, Munetaka Iwamura, Koichi Nozaki, Hiroshi Nishihara, *J. Am. Chem. Soc.* **2017**, *139*, 11214–11221.

【Publications not related to the thesis】

1. "Fluorescence and phosphorescence of a series of silicon-containing six-membered-ring molecules" Takayuki Nakashima, Masaki Shimada, Yu Kurihara, Mizuho Tsuchiya, Yoshinori Yamanoi, Eiji Nishibori, Kunihisa Sugimoto, Hiroshi Nishihara, *J. Organomet. Chem.* **2016**, *805*, 27–33.
2. "Homoleptic Bis(dipyrrinato)zinc(II) Complexes: Emission in the Solid State" Mizuho Tsuchiya, Ryota Sakamoto, Masaki Shimada, Yoshinori Yamanoi, Yohei Hattori, Kunihisa Sugimoto, Eiji Nishibori, Hiroshi Nishihara, *Inorg. Chem.* **2016**, *55*, 5732–5734.
3. "Effects of Substitution on Solid-State Fluorescence in 9-Aryl-9-methyl-9*H*-9-silafluorenes" Yoshinori Yamanoi, Takayuki Nakashima, Masaki Shimada, Hiroaki Maeda, Hiroshi Nishihara, *Molecules* **2016**, *21*, 1173.
4. "A simple zinc(II) complex that features multi-functional luminochromism induced by reversible ligand dissociation" Takamasa Tsukamoto, Risa Aoki, Ryota Sakamoto, Ryojun Toyoda, Masaki Shimada, Yohei Hattori, Mizuki Asaoka, Yasutaka Kitagawa, Eiji Nishibori, Masayoshi Nakano, Hiroshi Nishihara, *Chem. Commun.* **2017**, *53*, 3657–3660.

5. "Solvent-Controlled Doublet Emission of an Organometallic Gold(I) Complex with a Polychlorinated Diphenyl(4-pyridyl)methyl Radical Ligand: Dual Fluorescence and Enhanced Emission Efficiency" Yasuyo Ogino, Tetsuro Kusamoto, Yohei Hattori, Masaki Shimada, Mizuho Tsuchiya, Yoshinori Yamanoi, Eiji Nishibori, Kunihisa Sugimoto, Hiroshi Nishihara, *Inorg. Chem.* **2017**, *56*, 3909–3915.
6. "Access to Chiral Silicon Centers for Application to Circularly Polarized Luminescence Materials" Shinya Koga, Shuhei Ueki, Masaki Shimada, Ryoma Ishii, Yu Kurihara, Yoshinori Yamanoi, Junpei Yuasa, Tsuyoshi Kawai, Taka-aki Uchida, Munetaka Iwamura, Koichi Nozaki, and Hiroshi Nishihara, *J. Org. Chem.* **2017**, *82*, 6108–6117.
7. "β-IminoBODIPY Oligomers: Facilely Accessible π-Conjugated Luminescent BODIPY Arrays" Mizuho Tsuchiya, Ryota Sakamoto, Masaki Shimada, Yoshinori Yamanoi, Yohei Hattori, Kunihisa Sugimoto, Eiji Nishibori, Hiroshi Nishihara, *Chem. Commun.* **2017**, 53, 7509–7512.
8. "Mechano-, thermo-, solvato-, and vapochromism in bis(acetato-κ^1O)[4'-(4-(diphenylamino)phenyl)-] (2,2':6',2"-terpyridine-κ^3N,N',N'')zinc(II) and its polymer" Takamasa Tsukamoto, Risa Aoki, Ryota Sakamoto, Ryojun Toyoda, Masaki Shimada, Yohei Hattori, Yasutaka Kitagawa, Eiji Nishibori, Masayoshi Nakano, Hiroshi Nishihara, *Chem. Commun.* **2017**, *53*, 9805–9808.
9. "Aggregation-induced Emission Enhancement from Disilane-Bridged Donor–Acceptor–Donor Luminogens Based on the Triarylamine Functionality" Ushiki Tsukasa, Masaki Shimada, Yoshinori Yamanoi, Tatsuhiko Ohto, Hirokazu Tada, Hidetaka Kasai, Eiji Nishibori, Hiroshi Nishihara, *ACS Appl. Mater. Interfaces* **2018**, *in press*.
10. "Binuclear diphosphine complexes of gold(I) alkynyls, the effects of alkynyl substituents onto photophysical behavior" Yulia R. Shakirova, Masaki Shimada, Dmitrii A. Olisov, Galina L. Starova, Hiroshi Nishihara, Sergey P. Tunik, *Z. Anorg. Allg. Chem.* **2018**, *in press*.